Antarctic Glacial Chronology:
New constraints from surface exposure dating

by

Robert P. Ackert Jr.

B.A., University of Maine, 1979
M.S., University of Maine, 1990

Submitted in partial fulfillment of the requirements for the degree of

DOCTOR OF PHILOSOPHY

at the

MASSACHUSETTS INSTITUTE OF TECHNOLOGY

and the

WOODS HOLE OCEANOGRAPHIC INSTITUTION

JUNE 2000

Signature of Author_____

Joint Program in Oceanography
Massachusetts Institute of Technology
And Woods Hole Oceanographic Institution
May 5, 2000

Certified by_____

Dr. Mark D. Kurz
Thesis Supervisor

Accepted by_____

Dr. Timohty L. Grove
Chairman, Joint Committee for Marine Geology and Geophysics
Massachusetts Institute of Technology /
Woods Hole Oceanographic Institution

Antarctic Glacial Chronology:
New constraints from surface exposure dating

by

Robert P. Ackert Jr.

Submitted to the Massachusetts Institute of Technology –
Woods Hole Oceanographic Institution
Joint Program in Oceanography
on May 5, 2000, in partial fulfillment of the
requirements for the degree of
Doctor of Philosophy

Abstract

Surface exposure dating, using the concentration of cosmogenic nuclides (^{3}He, ^{21}Ne, and ^{36}Cl) in moraine boulders, combined with mapping of glacial moraines from three key locations, is used to provide new constraints to Antarctic glacial chronology. The results are used to reconstruct past West Antarctic Ice Sheet (WAIS) geometry and test models of WAIS behavior. Mount Waesche is a volcanic nunatak near the dome of the WAIS in Marie Byrd Land. The Dominion Range is at the head of the Beardmore Glacier, an outlet glacier of the East Antarctic Ice Sheet in the Transantarctic Mountains. Dromedary Platform is a bench along the Koettlitz Glacier which flows into southern McMurdo Sound. In addition, a new ^{3}He production rate calibration, and determination of initial ^{3}He/^{4}He in Ferrar Dolerite and Beacon Sandstone, substantially reduce uncertainties in Antarctic exposure ages.

^{3}He production rates of 129 ± 4 atoms/g/yr (olivine) and 124 ± 4 atoms/g/yr (clinopyroxene) at sea level, high latitude, are determined from an independently dated 125 ka lava flow in Patagonia (46°S). Paired ^{3}He and ^{36}Cl measurements are consistent with negligible surface erosion which is inferred from flow morphology. These mid-latitude, long term, ^{3}He production rates reduce uncertainties previously introduced when scaling production rates calibrated at lower latitudes to Antarctica. The results also confirm the compositional dependence of ^{3}He production rates predicted by theoretical calculations and are used to scale the production rates to quartz.

Determinations of initial ^{3}He/^{4}He in pyroxene from shielded dolerite and by incremental heating of quartz show that inherited (nucleogenic) ^{3}He concentrations are very low (^{3}He/^{4}He <.010 R/Ra). For exposures longer than about 30,000 years the inherited component can be ignored. These results enable correction for inherited ^{3}He in less than 30,000 year exposures of these common Antarctic lithologies. Exposure ages of less than 6000 years were obtained on moraine boulders in the Dominion Range.

At Mt. Waesche, a moraine band on the flank of the volcano records past ice elevations up to 85 meters above the present ice elevation. ^{3}He and ^{36}Cl surface exposure ages of basalt boulders up to 45 meters above the present ice level indicate that the last highstand of the WAIS occurred about 10 ± 1 ka , several thousand years after maximum extent of the WAIS in the Ross Sea. These data, suggest that the WAIS was out of equilibrium during the last glacial maximum (LGM). This conclusion is supported by results from a time-dependent ice sheet model. The new

chronology and model also place constraints on past WAIS ice volume and the WAIS contribution to sea level rise during the last deglaciation. Surface exposure ages from the upper part of the moraine band are scattered (10-282 ka), but consistently fall within glacial (low sea level) stages in the marine isotope record, including an interstadial during the last interglacial stage. Paired ^{3}He and ^{36}Cl data are consistent with negligible erosion.

^{3}He and ^{21}Ne surface exposure ages from six drifts of Beardmore Glacier are presented. Ages on Beardmore 1 drift range from 6 to 13 ka and record the most recent damming of the Beardmore Glacier by an expanded WAIS. The exposure ages on the older Beardmore 2 drift are more scattered (6-56 ka). This drift probably records thickening of the upper Beardmore Glacier during the LGM. The Meyer drift records at least four expansions of the upper Beardmore Glacier. Because Meyer drift geometry is similar to that of the Beardmore drift, these drifts also likely record an expanded WAIS. ^{3}He and ^{21}Ne ages on Meyer 1 drift (~600 ka) clearly distinguish it from Meyer 4 drift (~1 Ma). ^{21}Ne ages on the Dominion drift are ~2 Ma. The Meyer 4 drift and Dominion drift are correlated with Taylor Glacier moraines in Arena Valley on the basis of surface exposure ages and moraine morphology. These results indicate that expansions of the WAIS similar to that of the LGM have occurred throughout the Pleistocene.

On Dromedary Platform, lateral moraines record advances of grounded ice from McMurdo Sound during stage 2, damming of the lower Koettlitz Glacier by grounded WAIS during stage 6 and thickening during the Holocene and stage 5. The ^{3}He exposure ages are widely scattered, but independent stratigraphic control provided by ^{14}C, U series, and surface exposure dates of correlative drifts in McMurdo Sound allows evaluation of prior exposure and cover. Older moraines up to 350 meters above the stage 2 ice limit record earlier thickening of lower Koettlitz Glacier. Stratigraphic control provided by ^{40}Ar/^{39}Ar dated lava flows show the surface exposure ages are probably effected by cover and erosion and provide only minimum ages for the moraines. The oldest moraines are older than 400 ka and require grounded ice in McMurdo Sound, implying mid-Pleistocene advances of the WAIS similar to or larger than that of Stage 2. Surface exposure ages on a 1.68 Ma volcanic cone require erosion rates of ~65 cm /Myr, an order of magnitude higher than those previously obtained using cosmogenic nuclides in Antarctica. The ^{40}Ar/^{39}Ar age limits uplift of Dromedary Platform to <450 m/Myr.

These results show that surface exposure dating, combined with careful field observations, is a powerful tool for constraining Antarctic glacial history, and can be used to date moraines from 5 to 2,000 ka. The results are consistent with models in which the WAIS extent is largely determined by relative sea level and implies that the WAIS has fluctuated synchronously with the Northern Hemisphere ice sheets for at least the last 1 million years.

Thesis Supervisor: Mark D. Kurz
Title: Senior Scientist, Woods Hole Oceanographic Institution

Acknowledgements

This thesis represents the culmination of my graduate career which, including my Master's Degree and a break, has spanned 17 years. Indeed, my background in Antarctic glacial geology, which I drew heavily on for this work, extends back 25 years. Consequently, I have a great many people to thank. First of all, I must acknowledge my wife, Ruby Ackert-Herzig, who has provided steadfast support during this long process and edited the final document. We began our family just before I entered the MIT/WHOI Joint Program and we have also renovated an old Cape Cod house. She has endured the rigors of single parenthood during my numerous long field seasons, my long work hours and erratic schedule, and living with unfinished projects at home. Our children, Freeland and Adele, have been a great source of comfort and provided needed distraction. They also put up gallantly with my absences. My parents have provided encouragement and generous financial support, and never asked when I was going to get a real job. The freedom to do work that I love has been a cherished gift from my family.

My advisor, Mark Kurz has walked the sometimes fine line of being a true friend, colleague, field companion, and mentor. He has had the task of teaching a pick and shovel field geologist ("just give me the age") quantitative isotope geochemistry. He has also raised the funding necessary for most of my financial support and given me tremendous freedom to continue to follow my various (non-geochemical) interests.

George Denton introduced me to the Antarctic while I was an undergraduate at the University of Maine and started me on the path which lead ultimately to this thesis. He showed me how one can address big scientific questions by using detailed geologic field work in key areas. His knowledge of Antarctic glacial geology, which he passed on to me, is the foundation of this work. My association with Harold Borns also spans 25 years. He first introduced me to the field of glacial geology as an undergraduate and supplied the inspiration and samples for the Mount Waesche chapter.

Many people were involved in the sometimes tedious and demanding sampling necessary for this work. Dave Kammer, Gera Pantalev, Tim Kenna, Becky Weed, Paul Rappaport ,and Ken Sims assisted in the Antarctic work. The Mt. Waesche field party, in particular, Harold Borns and Parker Calkin and Dave Barclay supplied the samples, geologic map, and valuable feedback. Nelia Dunbar generously supplied a GPS map and samples of the tephra layers near Mt. Waesche and critical input concerning the formation of the moraine bands. Jim Fastook provided the output from his WAIS model, which provided the context for the Mt. Waesche results.

Brad Singer provided the initial impetus for the Patagonian work and provided logistical support (primarily a Ford Falcon station wagon) and the Cerro Volcán $^{40}Ar/^{39}Ar$ dates. Lynn Gualterri assisted in sample collection. The Ocean Ventures Fund provided additional financial support for the Patagonian field work and ^{36}Cl dates.

Here at WHOI, Stephanie Murphy, Lisa Max and Josh Curtice helped process samples. Many thanks to Dempsey Lott for maintaining the mass spectrometers necessary for making these measurements and for passing on some of his knowledge of high vacuum systems. Manuel Moreira, a post-doc in Mark's lab, provided the impetus and valuable expertise necessary to make neon isotope measurements. Robin Singer, an occasional office mate, provided encouragement and was instumental in automating the new mass spectrometer, faciliting the neon measurements. Almost everyone at the WHOI graphic department had a hand in some of the beautiful figures. Many thanks also to Lynn Woodward for graphic design, especially the classy posters which presented these results at meetings. Many thanks to Sheila Clifford who managed to format all of my various files into an attractive single document. She and Joanna Ireland have also be a great help over the years navigating the various paper trails necessity to get things done.

Finally, I gratefully acknowledge John Farrington and the Education Department for their unqualified support and patience during some trying times I encountered while completing the final draft of this dissertation.

Antarctic Glacial Chronology:
New constraints from surface exposure dating

Table of Contents

List of Figures

List of Tables

CHAPTER 1

Surface exposure dating using cosmogenic nuclides and application to Antarctic glacial chronology

1.1 Introduction

Global climate change is an area of intense research as scientists struggle to predict the global climatic effects of anthropogenic greenhouse gases. Climate reconstructions provide targets for evaluating global climate models and determine the limits of natural climate variability. While high resolution climate records from deep-sea cores and ice cores are beginning to allow more detailed reconstruction of past oceanic and atmospheric circulation, the continental glacial record remains much less known. Glaciers are sensitive recorders of climate change and are important feedbacks to the climate system. Glaciers leave records of past ice extent and volume through a variety of land forms, from which past climate parameters can be inferred. Dating of glacial moraines has been dominated by ^{14}C measurements of organic sediments which usually produce limiting (maximum or minimum) ages. Unfortunately, in many arid areas where erosion rates are low and the glacial record is most complete, suitable organic deposits have not been preserved. In addition, the glacial record often extends beyond the limit of radiocarbon dating (~45 kyr). Surface exposure dating using *in situ* produced cosmogenic nuclides in surficial rocks is allowing dating of many glacial systems for the first time. This thesis presents new mapping and surface exposure age constraints on glacial moraines in Antarctica. The uncertainties in the surface exposure dates have been reduced by a new calibration on a 125 ka lava flow in Patagonia.

1.2 Surface exposure dating using cosmogenic nuclides

Cosmogenic nuclides are formed by cosmic ray induced nuclear reactions in the Earth's atmosphere or in materials at the Earth's surface. The dominant reaction in the upper 2 m of a rock surface is neutron induced spallation (Kurz, 1986a; Lal, 1991; Lal and Peters, 1967). In spallation reactions, the target nucleus is broken into fragments by collision with a high energy particle. For spallation to occur, the energy of the incident particle must be greater than the binding energy of the nucleus, several 10's of MeV. When the resultant nuclides are rare (^{3}He, ^{21}Ne), or have short half lives (^{10}Be, ^{26}Al, ^{36}Cl) and reside in a closed system, the concentration of the nuclides is a function of the exposure time to cosmic rays. For stable nuclides (^{3}He, ^{21}Ne) this function is linear.

1) $$N = Pt$$

where N is the number of atoms/g, P is the production rate (atoms/g/yr) and t is time (years). For radioactive nuclides (*e.g.*, ^{10}Be, ^{26}Al, ^{36}Cl) the function is exponential due to loss resulting from radioactive decay.

2) $$N = \frac{P}{\lambda}\left(1 - e^{-\lambda t}\right)$$

where l (yr^{-1}) is the decay constant for the nuclide. At the top of the atmosphere, the cosmic ray flux is composed primarily of protons (~85%) and alpha particles (~15%) (Lal and Peters, 1967). These particles react with nuclei in the atmosphere to produce a cascade of secondary particles including protons, neutrons, electrons, muons and various other particles. At the Earth's surface, the flux of particles with sufficient energy (20-50 MeV) to cause spallation is dominated by neutrons.

The most common nuclides used for surface exposure dating are listed in Table 1.1.

Table 1.1 Cosmogenic nuclides used for surface exposure dating

Isotope	Half-life (years)	Production rate* (atoms/g/yr)	(Ref.)	Measurement technique	Sample material
^{3}He	stable	129	(1)	MS	olivine
		124	(1)		clinopyroxene
		140	(1)		quartz
^{10}Be	1.5×10^{6}	5	(2)	AMS	quartz
^{21}Ne	stable	21	(3)	MS	quartz
		25	(4)		pyroxene
		37	(5)		olivine
^{26}Al	7.16×10^{5}	37	(2)	AMS	quartz
^{36}Cl	3.08×10^{5}	154 (g K)	(6)	AMS	whole rock
		74 (g Ca)	(6)		calcite
					Ca plagioclase

* at sea level and latitude > 60°. MS is mass spectrometer, AMS is accelerator mass spectrometer.
References: 1) this study; 2) Clark *et al.* (1995); 3) Niedermann *et al.* (1994); 4) Schäfer *et al.* (1999); 5) (Staudacher and Allégre, 1993); 6) Phillips *et al.* (1995).

Each nuclide has various advantages and disadvantages; no nuclide is ideal in all situations. ^{3}He has the highest production rate and the lowest detection limit making it ideal for young samples. Both ^{3}He and ^{21}Ne are stable making them useful for very old samples because the inventory of the nuclide has the potential to increase indefinitely. In contrast, radioactive nuclides eventually reach saturation, a condition analogous to secular equilibrium in radioactive decay chains, where production equals decay and the concentration of the nuclide remains constant (Figure 1.1). Saturation is approached in three to five half lives. One disadvantage of stable cosmogenic nuclides is that correction for initial concentrations must be made which is not always straightforward. These corrections are particularly important for old rocks with short exposure.

An advantage of radioactive nuclides with relatively short half lives (^{10}Be, ^{26}Al and ^{36}Cl) is that corrections for non-cosmogenic inherited components are generally unnecessary (subducted ^{10}Be has been detected in arc volcanics) or minimal (correction for nucleogenic ^{36}Cl can be made from the U , Th and Cl concentrations (Zreda and Phillips, 1994b)). Cosmogenic ^{36}Cl can be measured in whole rock samples and has several unique advantages and disadvantages because the production rate is composition dependent and produced by spallation on Ca and K and neutron capture on ^{35}Cl (Zreda *et al.*, 1991).

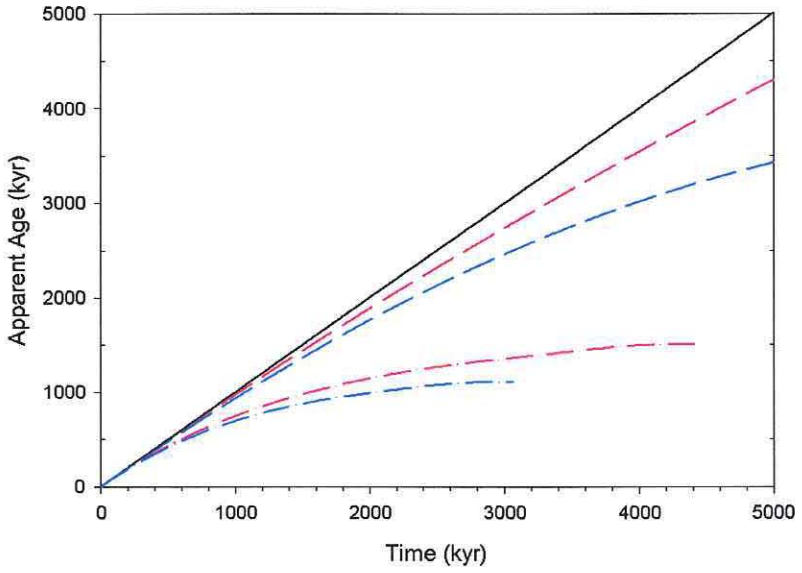

Figure 1.1. Model curves for apparent ^{3}He and ^{10}Be exposure age versus time (true age) calculated assuming the erosion rate is zero. Black solid line is for zero erosion for both isotopes; red lines are ^{3}He and blue lines are ^{10}Be. Dashed lines are when actual erosion rates are $1x10^{-5}$ g/cm^{2}/yr (~4 cm/Myr) and dash-dot lines when actual erosion rates are $1x10^{-4}$ g/cm^{2}/yr (~40 cm/Myr). Stable nuclides (^{3}He) will reach steady-state apparent ages given enough time and high erosion rates. For radioactive nuclides (^{10}Be) erosion effectively reduces the steady state age. Apparent ages are calculated for an elevation of 2000 m, at high latitude similar to the location of samples described in Chapter 3.

Because the production rate by neutron capture increases with depth in the top 10 to 20 centimeters, ^{36}Cl is well suited to studies of erosion rates (Liu *et al.*, 1994). By measuring concentrations of ^{36}Cl in two mineral phases or another cosmogenic nuclide, both the erosion rate and exposure age can be determined (Gillespie and Bierman, 1995; Liu *et al.*, 1994). However, the chemical composition of the rock or mineral separate must be determined and ^{36}Cl is unsuitable for samples over about a million years because of the relatively short half life (~300 kyr). ^{10}Be and ^{26}Al are typically measured in quartz because it is ubiquitous, chemical separation is possible by HF leaching, and the target chemistry (SiO_2) is simple (Brown *et al.*, 1991). When both ^{10}Be and ^{26}Al are measured exposure ages and erosion rates can be determined (Brown *et al.*, 1991; Lal, 1991; Nishiizumi *et al.*, 1991a). ^{10}Be, ^{26}Al, and ^{36}Cl must be measured using accelerator mass spectrometry (Nishiizumi *et al.*, 1986; Phillips *et al.*, 1986). Although these measurements have become routine in the last decade, they remain expensive and time consuming. In contrast, ^{3}He and ^{21}Ne can be measured on conventional mass spectrometers.

A number of fundamental assumptions must be met in order for measured exposure dates to accurately reflect the age of the landform to be dated:

1. The production rates are well known.
2. The sample must remain a closed system during exposure (no loss or contamination).
3. Erosion must be minimal or independently constrained.
4. The sample must not have been shielded from cosmic rays by an obstruction or shielding is independently constrained.
5. The sample must not have been exposed to cosmic rays prior to the exposure of interest.

Although production rates have been calculated based on cosmic ray data and estimated elemental spallation cross sections (for many elements only data for proton induced spallation is available) (Lal, 1991; Masarik and Reedy, 1995), the uncertainties in these calculations are large. Production rates are more commonly determined empirically by measuring the concentration of cosmogenic nuclides in surfaces of "known" age. Uncertainties in the age of calibrated surfaces and in scaling factors discussed below are difficult to quantify (10-15%), but are much greater than the analytical precision of the measurements of nuclide concentration (2-6%). Because the

cosmic ray flux is attenuated by interaction with matter, production rates vary with altitude and depth in the rock (Lal, 1991; Lal and Peters, 1967). In addition, the cosmic ray flux is not uniform over the Earth's surface because the Earth's magnetic field interacts with the charged cosmic ray particles (Lal and Peters, 1967). Near the poles and down to latitude 60°, the steeply dipping lines of the Earth's magnetic field do not deflect incoming cosmic rays. Nearer the equator, the magnetic field lines are more nearly perpendicular to the cosmic ray flux and only the more energetic particles can penetrate the upper atmosphere. This energy barrier (cut off rigidity) varies with time because the intensity of the magnetic field varies over many time scales, ranging from thousands to millions of years, resulting in variations in the cosmic ray flux at low latitudes.

Empirical production rates must be appropriately scaled when applied to samples with differing depth beneath the surface, altitude and/or latitude (Lal, 1991; Lal and Peters, 1967). Scaling for altitude (atmospheric depth) is based on cosmic ray neutron monitor data which are approximated by an exponential relationship.

$$P = P_0 e^{-(1033 - d_a/L)} \qquad 3)$$

P is production rate at altitude (d_a) and P_0 is the production rate at sea level. The apparent vertical attenuation length, L, is equal to 150 to 160 g/cm^2 (Lal, 1991; Lal and Peters, 1967). Lengths are divided by density to normalize for materials of different density. Thus, 1033 is the atmospheric depth at sea level in g/cm^2 and the altitude is converted to these units (d_a) using standard tables or polynomial fits to the tabulated data (Lide, 1998-9). Several studies using drill cores have demonstrated that the attenuation in rock can be approximated by a similar exponential (Brown *et al.*, 1992; Kurz, 1986b; Kurz and Brook, 1994), where d is the depth below the surface (g/cm^2).

$$P = P_0 e^{-d/L} \qquad 4)$$

In rock (ρ~2.5 g/cm^3, L = 165±5 g/cm^2), the production rate is about half the surface value at 50 cm and negligible (~4 %) at 2 m.

Scaling for latitude is also based on cosmic ray neutron monitor data. Lal (1991) presents scaling factors based on the data of Lal (1967) in polynomial form which includes the effects of

both latitude and altitude. These scaling factors predict variations in production rates at various elevations and latitude (Zreda *et al.*, 1991; Chapter 2). Published production rates and measured cosmogenic nuclide concentrations are now universally scaled to high latitude and sea level using the Lal (1991) scaling factors. The uncertainties in the scaling factors are not quantified but are generally assumed to be 10 to 15 percent. Uncertainties in the scaling factors can be minimized by using locally calibrated production rates (Singer *et al.*, 1998; Stone *et al.*, 1998), but in practice this is rarely possible. For surfaces younger than 20,000 years and from latitudes lower than 60°, production rates are expected to be time dependent due to variations in the strength of the Earth's magnetic field (Clark *et al.*, 1995). Studies of ^{14}C dated lava flows show significant variations in production rate which agree in direction with those predicted by changes in field strength (Kurz *et al.*, 1990; Licciardi *et al.*, 1999). For ages older than 20,000 years variations in the integrated production rate are expected to be small.

The assumption of closed system behavior is similar to that of any isotope-based dating system. For gases such as ^{3}He and ^{21}Ne, diffusion out of the sample will lower measured values which limits the mineral phases that can be utilized for surface exposure dating. Laboratory and empirical diffusion studies of olivine and clinopyroxene have shown that these minerals retain helium on geologic time scales and thus most applications of these isotopes have been restricted to basaltic rocks (Hart, 1984; Trull *et al.*, 1991). Unfortunately, helium is generally not retained in quartz (Cerling, 1990; Trull *et al.*, 1995), although in grains greater than 1 mm from polar climates, helium may be retained in quartz for up to 100 kyrs (Brook and Kurz, 1993). In contrast, neon appears to be quantitatively retained in quartz for millions of years (Bruno *et al.*, 1997; Graf *et al.*, 1991; Schäfer *et al.*, 1999; Staudacher and Allegre, 1991). ^{3}He and ^{21}Ne are also produced in small quantities by nucleogenic reactions (from a particles produced by decay of U and Th). As discussed above, corrections for an inherited component are required for older rocks. Meteoric water contains ^{10}Be and ^{36}Cl produced in the atmosphere and samples must be leached to remove this fraction.

Erosion of the sample results in apparent surface exposure dates which are younger than the true exposure age (excluding ^{36}Cl). For this reason, surface exposure dating is most successful in areas where erosion rates are low. In some cases, preservation of surface morphology such as glacial striations or primary surface morphology on lava flows can be used to establish that erosion rates are negligible. The effects of constant erosion rates on the accumulation of a stable nuclide are:

$$N = \frac{PL}{E}\left(1 - e^{-(E/L)t}\right) \quad 5)$$

For radioactive nuclides the equation is:

$$N = \frac{P}{\lambda + E/L}\left(1 - e^{-(\lambda + E/L)t}\right) \quad 6)$$

E is the erosion rate (g/cm^2/yr); P is the production rate (atoms/g/yr); t is time (yr); l is the decay constant (yr^{-1}) and L is the attenuation length (g/cm^2). Equation 5 shows that stable nuclides will also saturate if there is erosion of the surface (Figure 1.1). If steady state erosion is assumed or can be demonstrated (t = ∞in Equation 5 and 6) then maximum erosion rates can be calculated. Measurement of multiple nuclides can place constraints on erosion rates.

Shielding of samples by obstructions can be estimated by measuring azimuth and orientation of the obstruction, and assuming the obstruction has persisted throughout the exposure period. The angular distribution of cosmic ray particles over a wide range of latitudes is given by

$$F(\theta) = \sin^{2.3}\theta \quad 7)$$

F is the directional cosmic ray flux where θ is the angle above the horizon. The "visible" sky can be scaled to an unobstructed horizon and the production rate of the sample adjusted to reflect the decreased cosmic ray flux (Nishiizumi *et al.*, 1989). As a practical matter, obstructions which project less than 10° above the horizontal have negligible effect. Correction for shielding by covering material such as snow or soil can be more difficult. For example, unconsolidated till often erodes to expose striated bedrock long after the glacier retreated. Some studies have made adjustment for snow cover based on average depth and duration of snow cover (*e.g.*, Gosse *et al.*, 1995a; Licciardi *et al.*, 1999). For this reason exposure dates are often interpreted as minimum ages. Antarctica is a desert with low variability in seasonal snow cover in ice-free areas; snow banks tend to be semipermanent features generally in the lee of the prevailing winds. Snow cover over the crests of moraine ridges is generally unlikely.

Prior exposure refers to exposure to cosmic rays before deposition on the landforms from which they were collected. Unfortunately, areas with low erosion rates, where surface exposure dating is most applicable, are also where prior exposure is most likely. Prior exposure is difficult to evaluate in a single sample, unless the age is known independently, but often is indicated by older outliers in a larger data set. If the sample was covered for a significant period between exposures, dates determined by radioactive nuclides will be younger than those on stable

nuclides. The difference in age corresponds to the length of time the sample was covered. Prior exposure is well documented in some glacial deposits in Antarctica (Brook *et al.*, 1993; Brook *et al.*, 1995) where erosion rates are extremely low and surficial debris may have long exposure before incorporation into glacial systems.

Surface exposure dating has been successfully applied to many geologic landforms, including flood deposits, meteor craters and debris fans (Bierman *et al.*, 1995; Cerling *et al.*, 1994; Nishiizumi *et al.*, 1991b). Surface exposure dates on glacial moraines and lava flows are the subject of this dissertation. Lava flows cannot have prior exposure and evaluation of erosion can be made by the degree of preservation of the surface flow morphology. Because lava flows can often be dated by ^{14}C of associated organic deposits, they are commonly used as ^{3}He and ^{21}Ne production rate calibration sites (Cerling and Craig, 1994; Kurz *et al.*, 1990; Licciardi *et al.*, 1999). The same characteristics which make lava flows good calibration surfaces allow them to be accurately dated by surface exposure dating when alternative dating techniques are not feasible. Surface exposure dating is especially valuable for young, or low K, lava flows that have insufficient ^{40}Ar for accurate measurements.

Glacial moraines, deposited at glacier margins, are also amenable to surface exposure dating (Gosse *et al.*, 1995a; Gosse *et al.*, 1995b; Phillips *et al.*, 1997; Phillips *et al.*, 1996a; Phillips *et al.*, 1990) (Brook *et al.*, 1993; Brook *et al.*, 1995). Glaciers are efficient agents of erosion and typically remove many meters of bedrock during a glaciation. Most glacial debris is freshly quarried from the base of the glacier or from rapidly eroding headwalls of cirques. By sampling large boulders on moraine crests problems associated with cover and instability can be avoided and the degree of preservation of original morphology can be evaluated. However, erosion of the unconsolidated matrix material of the moraine (silt, sand and gravel) can substantially alter the age distribution of moraine boulders on older deposits (Hallet and Putkonen, 1994; Zreda and Phillips, 1994a). Potential factors effecting the exposure history of a moraine boulder are shown schematically in Figure 1.2.

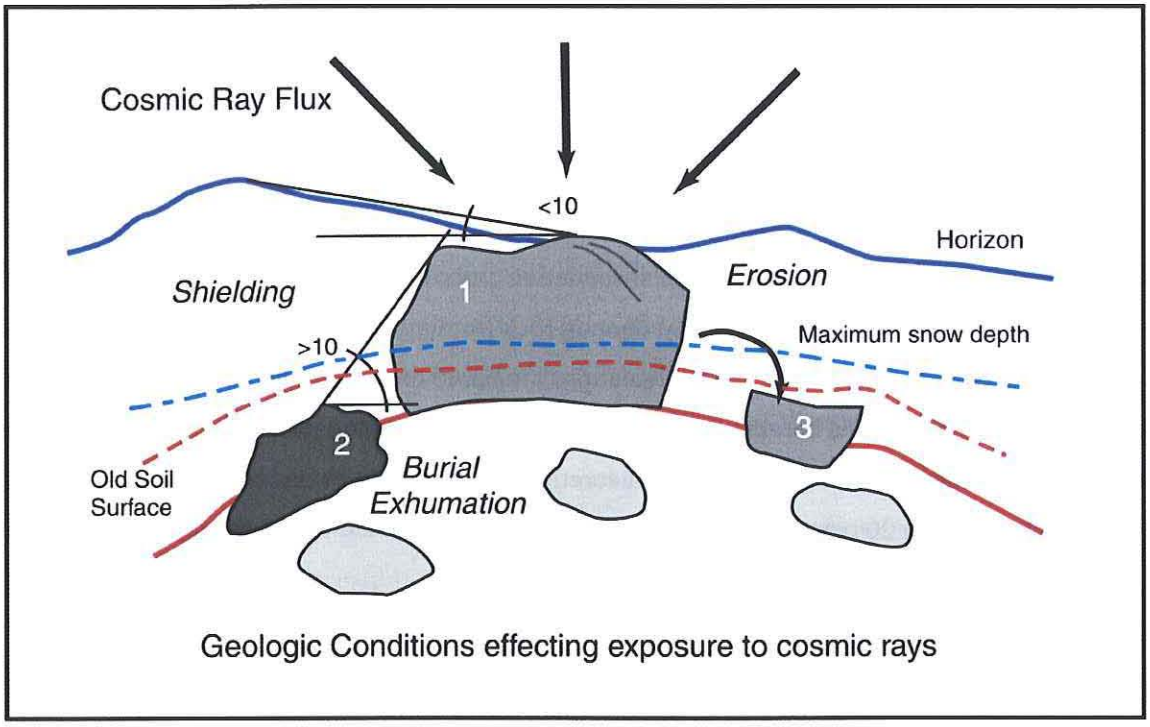

Figure 1.2 Cartoon depicting ideal and problematic boulders for surface exposure dating. Boulder 1 is ideal. The boulder is on the moraine crest in a stable position. The boulder is not shielded by an obstruction and the top surface stands above the seasonal snow cover and past soil surfaces. Striations on the top of the boulder are evidence for negligible surface erosion and indicate erosion at the base of the glacier, minimizing the probability of prior exposure. In contrast, boulder 2 is shielded from the cosmic ray flux by boulder 1 and is covered seasonally by snow. In addition, boulder 2 has been shielded by soil cover in the past and its position on the steep slope makes past reorientation possible. Boulder 3 has broken off boulder 1 and suffers problems similar to Boulder 2. However, if the boulder fractured recently, an accurate exposure age might be obtained from the upper right corner which contains the original top surface.

1.3 Cosmogenic ^{3}He

Cosmogenic ^{3}He was first discovered in Hawaiian lava flows (Kurz, 1986a) and is measured with conventional magnetic sector mass spectrometers. The detection limit (5000-10,000 atoms) for ^{3}He is lower than other cosmogenic nuclides. The low detection limit combined with the high production rate makes it possible to date samples as young as 500 years at sea level. To date, most applications of cosmogenic ^{3}He exposure dating have used olivine or clinopyroxene mineral phases in young basaltic rocks. Limited applications have also been made in quartz (Brook *et al.*, 1993; Brook *et al.*, 1995) and pyroxene from dolerite, an intrusive rock (Bruno *et al.*, 1997; Kurz and Ackert, 1997; Schäfer *et al.*, 1999).

Spallation reactions are the primary production mechanism for ^{3}He (Kurz, 1986a; Kurz, 1986b). In contrast to heavier cosmogenic nuclides, ^{3}He is formed primarily as ejecta. Due to its low atomic number, ^{3}He can be formed from all the major elements in silicate minerals. Therefore, ^{3}He has the highest production rate and the production rate is not strongly dependent on rock composition. Several efforts to calculate ^{3}He production rates based on the cosmic ray flux at the air/rock boundary and elemental spallation cross sections have been made. Lal (1991) calculated ^{3}He production rates in some common rock forming minerals and found differences less than 10 percent (Table 1.2). The calculations are based on the elemental cross sections for ^{3}He production by protons because data for neutrons were not readily available. Acknowledging large uncertainties (25-30 %) and that the theoretical production rates underestimate measured values by more than 20 percent, Lal (1991) suggested the results are useful for comparing relative production rates of different minerals.

Table 1.2 Elemental and mineral ^{3}He production rates*

	Si	O	Mg	Al	Fe	Ca	Fo_{85}	SiO_2
Lal (1991)	66	83	50	47	28	–	64	75
M & R (1996)	111	135	116	107	40	61	114	140

* Production rates are atoms/g-element/yr.

More recently, (Masarik and Reedy, 1995; Masarik and Reedy, 1996) used Monte Carlo simulations to model the spectra of cosmic ray neutron fluxes at the Earth's surface. Production rates were determined by integrating the product of the flux and elemental cross sections over the energy spectrum (Table 1.2). This approach has been well-tested against production rates measured in lunar samples and meteorites (Masarik and Reedy, 1994). Although the cosmic ray flux at the surfaces of these extraterrestrial samples is primarily protons, at 30 cm depth the flux is 70 percent neutrons, so validation of the model on these samples is relevant to terrestrial applications. The elemental production rates and attenuation lengths (L) calculated for the Earth's surface are in good agreement with published values. The uncertainties are estimated to be 10 to 20 percent. The Masarik and Reedy (1996) elemental ^{3}He production rates predict the measured difference in ^{3}He production rate of olivine and clinopyroxene from a lava flow in Patagonia (Chapter 2) and are used to scale ^{3}He production rates measured in olivine to quartz (Chapter 4).

A small proportion of ^{3}He may be produced via thermal neutron capture on lithium: ^{6}Li(n,α)T→^{3}He. Cosmogenic thermal neutrons are produced by thermalization of fast neutrons in the atmosphere and within the rock. The relative importance of this reaction is dependent on the lithium concentration in the rock and the concentration of other elements with high thermal neutron absorption cross sections. Of particular importance are B, Gd and Sm. The fraction of the thermal neutrons that interact with Li is given by:

$$f = \frac{\sigma_{Li} N_{Li}}{\sum_{i=1}^{n} \sigma_i N_i} \qquad 8)$$

N is the number of atoms; σ is the cross section for neutrons; i is each element and n is the total number of different elements in the mineral. Thermal neutrons can also be produced by muon capture reactions; some of these neutrons may have sufficient energy (>10 MeV) to cause spallation reactions. Because muons are only weakly interacting particles they could theoretically produce cosmogenic nuclides at depths greater than 2 m and this production mechanism has been called on to explain deviations from an exponential distribution in ^{3}He concentrations in shallow drill cores (Kurz, 1986b).

In many rocks, there is a non-cosmogenic ^{3}He component and corrections for this inherited ^{3}He must be made. In young volcanic rocks the inherited component is *magmatic*. In older rocks the inherited ^{3}He is primarily *nucleogenic*. Thermal neutrons can also be produced by radioactive decay of U and Th within the rock and produce ^{3}He primarily via the reaction discussed above, but also via other pathways (Lal, 1987). The high background of *radiogenic* ^{4}He (α particles) produced by U and Th decay is what precludes the use of ^{4}He in surface exposure dating; the spallation production ratio of ^{3}He/^{4}He based on studies of meteorites is ~0.2 (Mazor *et al.*, 1970).

In young volcanic rocks the magmatic He is trapped during crystallization. In olivine, most of the magmatic helium (up to 90%) is in fluid or melt inclusions within the crystals while the cosmogenic helium resides in the crystal lattice (Kurz, 1986b; Kurz *et al.*, 1996). This heterogeneous distribution is exploited to determine the initial ^{3}He concentration (Kurz, 1986a). The sample is first crushed *in vacuo* which selectively releases the magmatic component. The residual powder is then melted *in vacuo* to release the cosmogenic component. The cosmogenic ^{3}He is calculated as follows:

9) $^3He_c = {}^3He_t - {}^3He_i$

where ^3He_c is cosmogenic, ^3He_t is total gas released on melting, and ^3He_i is initial (magmatic) ^3He. The ^3He_i and ^3He_t is determined as follows:

10) $^3He_i = {}^3He/{}^4He_{cr} * {}^4He_m$

11) $^3He_t = {}^3He/{}^4He_m * {}^4He_t$

cr denotes values obtained by crushing and m denotes values obtained by melting residual powders. This calculation is valid because only a negligible fraction of ^4He is cosmogenic. While this calculation produces consistent results for typically low U and Th young (<1 Ma) volcanic rocks, it is not applicable to older volcanic rocks because they contain radiogenic ^4He which is not restricted to fluid or melt inclusions. In old (>1 Ma) rocks, the ^4He released by melting has a large radiogenic component. Determination of the inherited (magmatic) ^3He assumes that the ^4He is only magmatic. When the $^3He/^4He_c$ is multiplied by the ^4He released by melting, the inherited ^3He calculated in Equation 10 will be too large. The inherited ^3He concentration calculated in this manner can be larger than the total ^3He released by melting resulting in negative values of ^3He_c in Equation 9.

This technique is not necessarily valid for other lithologies. Experiments on quartz showed that significant quantities of cosmogenic ^3He are released on crushing (Brook *et al.*, 1993). An alternative in samples with low U and Th concentrations and long exposure ages is to assume that all ^3He is cosmogenic. Although, some nucleogenic ^3He is produced depending on the Li, U and Th content of the rock, for long exposures, ^3He_c is much larger than ^3He_i and the overestimation of the age is negligible. Trull (1991) showed that cosmogenic ^3He is preferentially released by step heating at low temperature and the inherited $^3He/^4He$ can be determined from the high temperature heating steps. In an Antarctic sandstone the measured $^3He/^4He$ was .011 ± 004 R/R_a which was similar to estimates based on U, Th, and Li content of the rock. This value can be substituted in Equation 10 for the $^3He/^4He_c$ to calculate the inherited ^3He. This approach is utilized in Chapter 2 to determine inherited $^3He/^4He$ from sandstones in the Beardmore Glacier Region.

Inherited $^{3}He/^{4}He$ can also be measured directly in samples shielded from exposure to cosmic rays. Such samples may be obtained in quarries, road cuts, drilled cores, or from natural exposures. This approach is most practical when a lithology is common and homogeneous. Shielded samples were used to determine the inherited $^{3}He/^{4}He$ of the Ferrar Dolerite, an intrusive rock found throughout the Transantarctic Mountains (Chapter 2).

The ^{3}He production rate was first determined on Hawaiian lava flows (Kurz, 1986b; Kurz *et al.*, 1990). The lava flows (20°N) were well-suited to calibration studies because they were dated by ^{14}C measurements on underlying charcoal, contained abundant olivine and flow morphology could be used to evaluate erosion. Based on the youngest and best preserved flows (<2000 yrs), Kurz (1990) determined a production rate of 125 ± 30 atoms/g/year normalized to sea level using Equation 3. Although production rates calculated from samples greater than 7000 yrs were similar (127 ± 19 atoms/g/yr) production rates on lava flows between 2000 and 7000 years were significantly lower. Kurz *et al.* (1990) attributed the production rate variations to fluctuations in the Earth's magnetic field. Although the age of the minimum in production rate is similar to that predicted by archeomagnetic and sedimentalogic data (McElhinny and Senanayake, 1982), the magnitude is a factor of 2 greater than theoretical predictions.

Cerling (1990) measured a ^{3}He production rate on the Tabernacle Hill lava flow (latitude 39° N) which erupted into the well-dated (17,800 yr) Provo shoreline of glacial lake Bonneville in Utah. A ^{3}He production rate of 118 atoms/g/year is obtained when the data are scaled to high latitude and sea level using Lal (1991). Subsequently, Cerling and Craig (1994) presented data from additional lava flows that support their previous estimates and suggest that production rate variations have been less than 30 percent over the last 18,000 years. Most recently, Licciardi (1999) found evidence for lower production rates 2000 to 4000 yrs ago from lava flows in Oregon supporting the conclusions of Kurz (1990) and concluded that fluctuations in the magnetic field have measurable effects on Holocene mid latitude production rates.

Accurate production rates are necessary to the exposure dating technique. The differences in published ^{3}He production rates probably result from errors in the independent dating of the calibration surfaces, the scaling factors, unidentified erosion problems, or the time dependence of the production rate. Because of the lower uncertainties and higher geomagnetic latitude, the ^{3}He production rate of Cerling (1990) has become generally accepted. A new ^{3}He production rate of 129 ± 4 atoms/g/yr (olivine) is presented in Chapter 2. This production rate was calibrated on a radiometrically dated 125 ka lava flow in Patagonia and is slightly higher than the Cerling (1990)

^{3}He production rate. This calibration has the advantage of being from high latitude, minimizing uncertainties due to fluctuations in the Earth's magnetic field, and also provides a long term average. This ^{3}He production rate is used for calculating surface exposure ages in Antarctica (Chapters 4 and 5).

1.4 Cosmogenic ^{21}Ne

Cosmogenic ^{21}Ne was detected in terrestrial rocks shortly after the discovery of cosmogenic ^{3}He (Marti and Craig, 1987). Ne, like He, is a noble gas that can be measured with magnetic sector mass spectrometers; both elements can be measured on the same sample of gas by selective release from a cryotrap. A significant advantage of Ne over He for surface exposure dating is that Ne is quantitatively retained in quartz. Quartz samples from Antarctica have been shown to retain Ne for millions of years and give concordant ages with ^{10}Be and ^{26}Al measured in the same samples (Bruno *et al.*, 1997; Graf *et al.*, 1991; Niedermann *et al.*, 1993; Schäfer *et al.*, 1999; Staudacher and Allegre, 1991). Cosmogenic ^{21}Ne has also been measured in olivine and co-existing plagioclase (Poreda and Cerling, 1992) and in pyroxene (Bruno *et al.*, 1997; Marti and Craig, 1987; Schäfer *et al.*, 1999).

In contrast to helium, there are three isotopes of neon, ^{20}Ne, ^{21}Ne and ^{22}Ne. The existence of an additional isotope and distinct isotopic ratios for Ne in air, cosmogenic Ne, and mid-ocean ridge basalts (MORB), allows calculation of initial ^{21}Ne concentrations and separation of the cosmogenic component from inherited components (air, nucleogenic, and magmatic) (Table 1.3). The MORB component, derived from depleted mantle, was determined on a global suite of dredged samples (Sarda *et al.*, 1988). The cosmogenic Ne ratios were determined on stony meteorites (Graf *et al.*, 1990) and are characterized by elevated ^{21}Ne/^{22}Ne ratios compared to air and slightly depleted ^{20}Ne/^{22}Ne. Cosmogenic ^{20}Ne, ^{21}Ne and ^{22}Ne are produced in similar amounts in spallation reactions. Cosmogenic ^{20}Ne and ^{22}Ne concentrations are negligible compared to those in inherited components. In contrast, very low ^{21}Ne/^{20}Ne in the inherited Ne allows for measurement of cosmogenic ^{21}Ne in samples as young as 3000 yrs (Sarda *et al.*, 1993).

Table 1.3 Ne isotope ratios of end member components in rocks

	Air	Cosmogenic[1]	MORB[2]
$^{22}Ne/^{20}Ne$	0.102	1.04	.075
$^{21}Ne/^{20}Ne$	.00295	.87	.0053

[1]From (Graf *et al.*, 1990), [2]From (Sarda *et al.*, 1988)

Table 1.4 Nuclear reactions producing neon isotopes

Spallation	Neutron capture	Nucleogenic
Si (n, 4p xn) Ne	^{24}Mg (n, α) ^{20}Ne	^{18}O (α, n) ^{21}Ne
	^{25}Mg (n, α) ^{22}Ne	^{17}O (α, n) ^{20}Ne
	^{19}F (α, n) ^{22}Ne	

Nuclear reactions producing Ne isotopes are listed in Table 1.4. In quartz, Si is the only target for spallation produced Ne. Mg has a high cross section for spallation to Ne and is important in Mg rich phases such as olivine. ^{21}Ne is also produced by nucleogenic reactions on oxygen and F. Although limited cosmogenic Ne can be produced from spallation produced a particles, these reactions are more important for nucleogenic Ne where the a particles are produced by U and Th decay over a time period much greater than potential exposure. Production of ^{22}Ne from ^{19}F could be important in quartz with F-rich fluid inclusions.

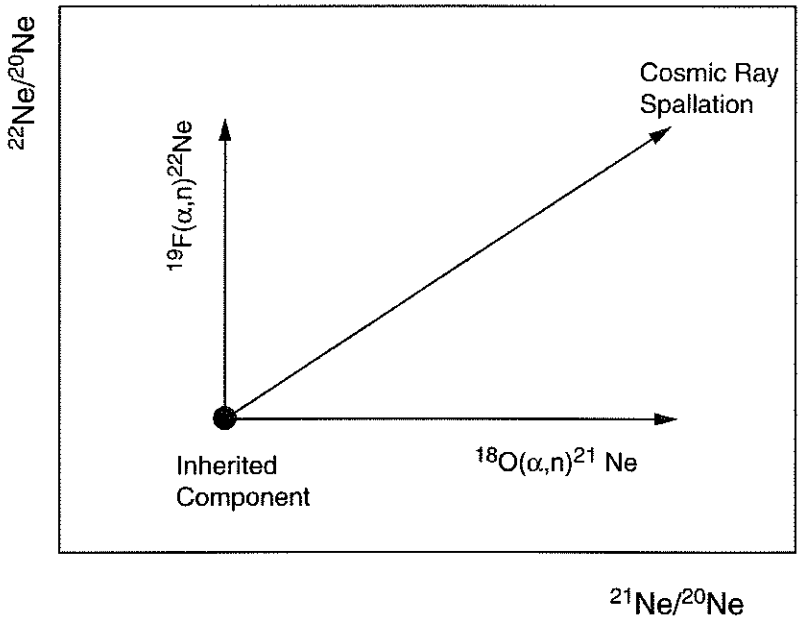

Figure 1.3 Neon 3-isotope schematics showing direction of shifts expected from the addition of different Ne components to trapped Ne. Figure after Niedermann *et al.* (1993). This figure has the advantage of clearly showing the difference between spallation and nucleogenic neon

Ne isotope data is typically plotted on 3-isotope diagrams (Figure 1.3), which allow evaluation of the Ne components present. Step heating of samples (300 - 1500°C) releases different fractions of the Ne components present. Alternatively, data from suites of samples of similar lithology can be plotted. In two-component mixtures with an air-like inherited component, samples containing cosmogenic Ne will plot on a mixing line between air and cosmogenic Ne. In Figure 1.3, which applies to quartz, nucleogenic reactions will move the measured ratios in the directions shown. The spallation $^{22}Ne/^{21}Ne$ can be determined by a best fit line to the data on the plot. If this line intersects the air end members it is strong indication of two component mixing. The spallation $^{22}Ne/^{21}Ne$ varies slightly with chemical composition and is used to calculate cosmogenic ^{21}Ne in samples where the inherited component has magmatic or nucleogenic Ne.

The production rate of ^{21}Ne is dependent on the target composition. The target chemistry for quartz is simple; Si is the only target element for ^{21}Ne production. In quartz, it is often assumed that the sample contains only air Ne and cosmogenic Ne. This assumption is justified when the data fall on the air-cosmogenic mixing line on 3-isotope plots (Figure 1.3). In this case, the calculation of cosmogenic ^{21}Ne is analogous to that of ^{3}He. The inherited Ne is assumed to

have an air-like $^{21}Ne/^{20}Ne$ and all ^{20}Ne is assumed to be derived from air. This assumption is justified by the fact that ^{20}Ne in air is over 300 times more abundant than ^{21}Ne.

12) $$^{21}Ne_c = {}^{21}Ne_t - {}^{21}Ne_i$$

13) $$^{21}Ne_i = (^{21}Ne/{}^{20}Ne)_{air} * {}^{20}Ne_{melt}$$

An example of simple two component mixing is presented for a sample from Antarctica by Niedermann *et al.* (1993). They determined the cosmogenic $^{22}Ne/^{21}Ne$ in quartz = 1.243 ± .022. Ne isotopes measured in moraine boulders (Chapter 4) also fall on the air-cosmogenic mixing line and are modeled as two component mixtures.

However, in some quartz samples nucleogenic Ne components also occur (Table 1.4). Quartz often contains fluid and mineral inclusions which can include F. U and Th may reside in inclusions or adjacent minerals. Because the stopping distance of a particles produced by U and Th is 10 to 40 µm, nucleogenic Ne is concentrated along grain boundaries. Selective dissolution and removal of inclusion rich grain fragments have been shown to reduce the nucleogenic component (Niedermann *et al.*, 1994). Step heating of the samples often selectively releases the various neon components (Niedermann *et al.*, 1993). The concentration of nucleogenic ^{21}Ne can also be calculated by assuming that all ^{4}He is radiogenic (stopped a particles) providing a conservative estimate of diffusive loss of He. An estimate of nucleogenic ^{21}Ne is made using a $^{21}Ne_n/^{4}He_{rad}$ production ratio of (5-10) x 10^{-8} (Eikenberg *et al.*, 1993; Kennedy *et al.*, 1990). In Antarctic samples with long exposures, a maximum of 12 percent nucleogenic ^{21}Ne was calculated in this manner. This was the only sample which plotted substantially off a two component mixing line (Bruno *et al.*, 1997).

Niedermann *et al.* (1994) measured cosmogenic Ne from Sierra Nevada quartz separates previously used to calibrate ^{10}Be and ^{26}Al production rates (Nishiizumi *et al.*, 1989) and obtained a ^{21}Ne production rate of 21 atoms/g/year (quartz) at sea level and high latitude. This corresponds to an elemental production rate of 45 atoms/g (Si)/year. However, the age assumed for the surfaces (11 ka) is probably too young and the production rates were scaled to high latitude from the present geomagnetic latitude rather than the geographic latitude resulting in an overestimate of the production rates (Clark *et al.*, 1995). Because of wander of the geomagnetic pole, over time scales greater than 10 kyr, the geographic pole is a good estimate of the average

geomagnetic pole position (Merrill *et al.*, 1996). A revised value of 18 atoms/g/yr is used to calculate surface exposure ages of sandstone boulders in Chapter 4. The calculated ^{21}Ne ages give good agreement with ^{3}He ages of dolerite (pyroxene) boulders from the same moraine.

Cosmogenic neon has also been measured in olivine and clinopyroxene in young basaltic lava flows, ultramafic xenoliths and intrusive rocks (Bruno *et al.*, 1997; Sarda *et al.*, 1993, Schäfer *et al.*, 1999; Staudacher and Allègre, 1993). In young basalts, the nucleogenic Ne is negligible, but magmatic Ne is present. The ^{21}Ne production rate in olivine is related to the magnesium content and it is necessary to determine the mineral composition in order to utilize appropriate production rates. Poreda and Cerling (1992) demonstrated a correlation between the ^{21}Ne /^{3}He and Mg content of olivine and measured a ^{21}Ne production rate of 45 ± 4 atoms/g/yr (Fo_{81}) in the Tabernacle Hill lava flow (Section 1.3) (Poreda and Cerling, 1992).

In pyroxene, 98 percent of ^{21}Ne production is from spallation on Si, Mg and Al. Schäfer *et al.* (1999) determined theoretical ^{21}Ne production rates from Mg and Al of 196 atoms/g/yr and 55 atoms/g/yr normalized to Si (45 atoms/g/yr). These results are tabulated normalized to Si so values corresponding to lower production by Si are easily determined. Their results are in general agreement with other theoretical calculations (Masarik and Reedy, 1996). Measured ^{3}He/^{21}Ne in the samples analyzed by Schäfer *et al.* (1999) indicates a ^{3}He production rate of 110 ± 5 atoms/g/yr. While this value is reassuringly close to measured ^{3}He production rates considering it reflects an average over millions of years, the calculated ^{3}He production rate is 20 percent lower when a revised ^{21}Ne production rate for Si is used (see above). The discrepancy indicates some ^{3}He loss over millions of years or problems with the theoretical production rate calculations.

Cosmogenic ^{21}Ne has been used to date old glacial surfaces in Antarctica where ^{10}Be has reached saturation concentrations (~3-4 Ma at 2000 m) (Bruno *et al.*, 1997). The ^{21}Ne ages are millions of years older than those obtained by ^{10}Be, demonstrating the unique potential of this nuclide for dating old quartz samples (Bruno *et al.*, 1997; Schäfer *et al.*, 1999). In Antarctica, ^{21}Ne has only been measured in samples with exposure ages greater than 1 Ma where assumptions of two component mixing are most valid. For younger exposures the contribution of nucleogenic ^{21}Ne is potentially more important. In Chapter 4 data are presented from a sample ~600 ka which are consistent with two component mixing. A future research goal is to extend cosmogenic ^{21}Ne dating to younger surfaces by determining initial ^{21}Ne/^{20}Ne from shielded samples.

1.5 Cosmogenic ^{36}Cl

Although the ^{36}Cl dating method was first proposed in 1955 (Davis and Schaeffer, 1955), detection of cosmogenic ^{36}Cl in terrestrial rocks awaited the development of accelerator mass spectrometry (AMS) (Phillips *et al.*, 1986). Cosmogenic ^{36}Cl is produced primarily by spallation reactions with ^{39}K and ^{40}Ca and thermal neutron capture by ^{35}Cl (Phillips *et al.*, 1986). Negative muon capture becomes progressively more important with depth in rock. The major reactions are listed in Table 1.5.

Table 1.5 Major reactions producing ^{36}Cl in surficial rocks

Reaction type	Notation	% of total ^{36}Cl
Spallation	^{39}K (n, 2n2p)^{36}Cl	16-80
	^{40}Ca (n, 2n3p)^{36}Cl	
Thermal neutron activation of Cl	^{35}Cl (n, g) ^{36}Cl	11-80
Negative muon capture by Ca	^{40}Ca (m^-, α)^{36}Cl	0.3-10
Thermal neutron activation of K	^{39}K (n, α)^{36}Cl	0-2
Negative muon capture by K	^{39}K (m^-, p2n)^{36}Cl	0-0.4

Table from Zreda *et al.*, 1994b.

The production rate is strongly dependent on rock composition. In order to calculate ^{36}Cl surface exposure ages, it is therefore necessary to know the major element composition and Cl composition of the rock. In addition, the concentrations of B, Sm and Gd, which have very high cross sections for neutron capture, must be known. In the upper meter of the rock surface, the production rate is

$$14) \qquad P_{36} = \Psi_n + \Psi_{Ca} + \Psi_K$$

where Ψ_{Ca} and Ψ_K are the spallation induced production rates on Ca and K per unit concentration and Ψ_n is the production rate by neutron capture:

15) $$\Psi_n = \phi_n \frac{\sigma_{35} N_{35}}{\sum_i \sigma_i N_i}$$

where ϕ_n is the thermal neutron flux, σ_{35} is the thermal neutron activation cross section of ^{35}Cl, N_{35} is the concentration of ^{35}Cl,σ_i is the thermal neutron activation cross section of element i, and N_i is the concentration of each element.

In practice, the ratio of ^{36}Cl to total Cl (N_{Cl}) is measured by AMS and Cl concentration is typically measured by isotope dilution. Substituting Equations 14 and 15 into the general age equation (2) and dividing by N_{Cl} yields the ^{36}Cl age equation:

16) $$R = \left[\Psi_{Ca} N_{Ca} + \Psi_K N_k + \phi_n \frac{\sigma_{35} N_{35}}{\sum_i \sigma_i N_i} \right] \frac{\left(1 - e^{-\lambda t}\right)}{\lambda N_{Cl}}$$

Where R is $^{36}Cl/Cl$. Correction for inherited, nucleogenic ^{36}Cl produced by neutron activation can be important in young surfaces. Typical $^{36}Cl/Cl$ due to neutrons produced by U and Th decay is 5×10^{-15} to 5×10^{-14} (Phillips *et al.*, 1986).

Unlike cosmogenic nuclides produced primarily by spallation, the production rate of ^{36}Cl by thermal neutron capture (Ψ_n) does not exponentially decrease with depth. In rocks where a substantial fraction of the total cosmogenic ^{36}Cl is produced by neutron capture, there is a sub-surface maximum in the production rate. Because the stopping distance of thermal neutrons in rock is 10 to 20 cm and the absorption cross section of Ar is high, some of the thermal neutrons in the top 20 centimeters escape the rock (Liu *et al.*, 1994). An important outcome is that for rocks with substantial Ψ_n, erosion of the surface will increase the apparent (zero erosion) age, in contrast to spallation produced nuclides in which erosion lowers the apparent age. This property can be used to evaluate erosion rates (Liu *et al.*, 1994). This surface boundary effect complicates calculation of ^{36}Cl exposure ages, and the treatment of the neutron flux depth dependence in age models is still evolving.

Calibration of ^{36}Cl production rates is also complicated by the multiple production pathways. Two methods have been used. The first calibrates elemental production rates on

mineral phases with only one target element. For example, ^{36}Cl production rate due to spallation on Ca (Ψ_{Ca}) was determined on plagioclase feldspar in basalt from the Tabernacle Hill lava flow (Section 1.3) and in calcite (Stone *et al.*, 1996). Unfortunately, calibration surfaces with mineral phases containing only K or Cl have not been located.

Calibration has been also done iteratively in a suite of samples with variable target concentrations and ages (Phillips *et al.*, 1996b; Zreda *et al.*, 1991). The thermal neutron capture rate on ^{35}Cl (Ψ_n) was determined in quartz (high Cl, low K and Ca), the average Ψ_n was used to calculate the ^{36}Cl production rate due to spallation on K (Ψ_K) in microcline feldspar. Finally the average Ψ_n and Ψ_K were used in calculations of the production rate due to spallation on Ca (Ψ_{Ca}). These production rates were used to recalculate Ψ_n, and so forth. Convergence was obtained in eight iterations. Ψ_{ca} was determined on plagioclase feldspar in basalt from the previously described Tabernacle Hill lava flow. Subsequently, Stone *et al.* (1996) reproduced Ψ_{Ca} at Tabernacle Hill and determined Ψ_{Ca} in calcite (Stone *et al.*, 1996). The initial calibration of Ψ_n and Ψ_K were from glacial moraines in the White Mountains of California dated by ^{14}C of rock varnish and by correlation with other moraines stratigraphically constrained by ^{14}C dated sediments (Zreda *et al.*, 1991). The more recent calibration used a larger suite of samples, including data from Meteor Crater, Arizona (Phillips *et al.*, 1996b).

1.6 Applications to Antarctic glacial chronology

The history of the Antarctic ice sheets is fundamental to understanding global climate change. Reconstructions of past ice sheet configurations are an important input to global climate models. Prior to development of large Northern Hemisphere ice sheets (~2.5 Ma) the Antarctic ice sheets were the only significant ice masses on Earth and played a dominant role in eustatic sea level fluctuations. The history of the marine-based West Antarctic Ice Sheet (WAIS) is of particular interest because of its potential instability in the face of global warming. Disintegration of the WAIS would increase sea level by ~5 m with profound effects on society (Hughes, 1987; Mercer, 1978; Oppenheimer, 1998). Detailed records of WAIS behavior during the last deglaciation provide a context for evaluating potential future changes in the ice sheet (Conway *et al.*, 1999). Reconstructions of Antarctic ice sheets during the Pliocene, the most recent period of warmer-than-present climates also provide insight into the potential response of the ice sheets to projected anthropogenic warming. At present, vastly different interpretations of Antarctic

Pliocene climate and ice sheet dynamics exist due to differing interpretations of the age of key fossiliferous deposits in the Transantarctic Mountains (*e.g.,* Denton *et al.*, 1993; Webb *et al.*, 1996). Resolution of this debate requires improved chronologies of the associated deposits and landforms.

The Transantarctic Mountains separate the largely terrestrial East Antarctic Ice Sheet (EAIS) from the marine WAIS. Large outlet glaciers of the EAIS flow through the mountains into the Ross Ice Shelf or the Ross Sea (Figure 1.4).

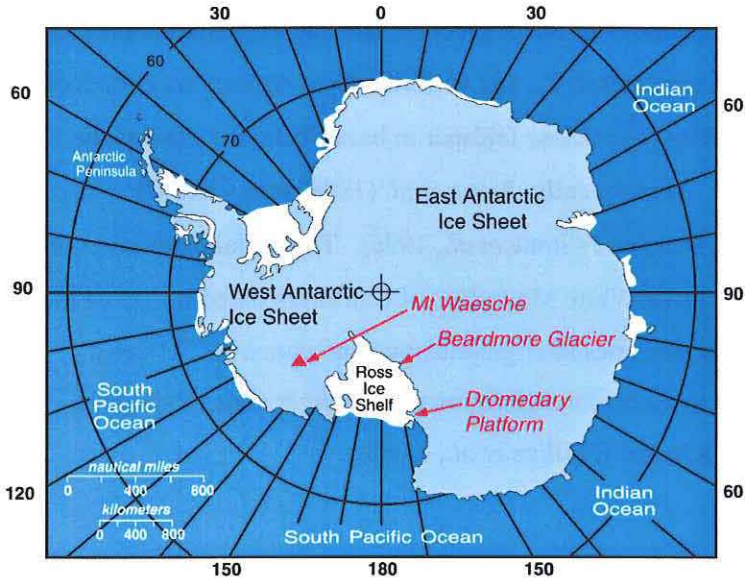

Figure 1.4 Map of Antarctica showing locations of field areas described in this thesis. The locations are well-placed for monitoring fluctuations of the grounding line and dome of the West Antarctic Ice Sheet. McMurdo Sound is just north of Dromedary Platform.

The uplands between the outlet glaciers are subject to alpine glaciation. The cold dry climate of Antarctica has preserved the most complete glacial record in the world. These same conditions have made it difficult to date glacial deposits (with a few notable exceptions) because organic sediments which can be dated by ^{14}C are generally absent. In addition, the glacial record extends back millions of years, far beyond the range of ^{14}C. In Antarctica, glacial moraines which delimit past ice extent range in age from a few hundred years to several million years. Glacial tills as old as 13 Ma are exposed in the Dry Valleys region (Marchant *et al.*, 1996; Marchant *et al.*, 1993). The cold dry climate provides ideal conditions for surface exposure dating because erosion rates are very low. Surface exposure dating using cosmogenic nuclides has been used to provide a

chronology of the ice sheets ranging from the Holocene (Ackert *et al.*, 1999) to the Miocene (Kurz and Ackert, 1997; Schäfer *et al.*, 1999).

Sea level is thought to be the dominant control on the extent of the WAIS (Hollin, 1962; Huybrechts, 1990a; Stuiver *et al.*, 1981). This ice sheet is grounded largely below sea level and is thought to be unstable (Denton *et al.*, 1991; Hughes, 1987; MacAyeal, 1992; Mercer, 1978; Stuiver *et al.*, 1981). The base of the WAIS is more than 2000 m below sea level in some interior basins (Drewry, 1983). To a large extent, the geometry of the ice sheet is controlled by the position of the grounding line (where the ice begins to float) in the Ross and Weddell Seas. At present, large ice shelves exist outboard of the grounding line in both embayments and ablation is almost entirely by iceberg calving.

If all other factors are held constant, a decrease in relative sea level will result in an advance of the ice sheet grounding line over the continental shelf. Because the growth of Northern Hemisphere Ice Sheets (NHIS) lowered eustatic sea level by at least 100 m, it is suggested that the WAIS has fluctuated synchronously with NHIS during the Pleistocene (Denton *et al.*, 1986; Hollin, 1962) . This model is supported in the McMurdo Sound Region (Figure 1.4). There, ^{14}C ages on glacial lacustrine sediments deposited in ice-dammed lakes fringing ice grounded in McMurdo Sound date to the last glacial maximum (LGM) (Denton *et al.*, 1971; Stuiver *et al.*, 1981). These data are supported by geophysical evidence in the Ross Sea which shows that the WAIS extended to near the continental shelf break during the LGM (Anderson *et al.*, 1992; Domack *et al.*, 1999; Licht *et al.*, 1999; Licht *et al.*, 1996; Shipp *et al.*, 1999). This advance occurred despite the fact that accumulation rates decreased due to colder temperatures during this time (Lorius *et al.*, 1979).

In contrast to the behavior of the WAIS, cross cutting relationships suggest that advances of local alpine glaciers and the Taylor Glacier in the Dry Valleys occur during interglacial periods (Denton *et al.*, 1971; Denton *et al.*, 1989b; Marchant *et al.*, 1994; Stuiver *et al.*, 1981). The Taylor Glacier drains a peripheral dome of the EAIS and terminates in Taylor Valley. Apparently these glaciers are responding to accumulation changes which occur over the glacial cycle (Lorius *et al.*, 1979). At present, temperatures remain low enough that ablation is primarily by sublimation, but accumulation rates are substantially higher than during the LGM. This relationship is the basis of the *dual control* hypothesis of the behavior of the Antarctic ice sheets in which the WAIS responds primarily to sea level changes and alpine glaciers and independent ice caps respond primarily to accumulation changes (Figure 1.5) (*e.g.*, Denton *et al.*, 1991). The

EAIS responds to sea level along the marine margins but primarily to accumulation along the margin bounded by the Transantarctic Mountains.

Ice profiles reconstructed from lateral moraines along outlet glaciers which drain EAIS ice into the Ross Ice Shelf south of McMurdo Sound show greater thickening toward the ice shelf. This observation indicates damming of the outlet glaciers by grounded ice in the Ross Embayment (Bockheim *et al.*, 1989; Denton *et al.*, 1989a; Mercer, 1968; Mercer, 1972). The dual control model is used to assign LGM ages to the lateral moraines based on their profiles and on cross cutting relationships with moraines of local alpine glaciers (Figure 1.5). The profiles are then used to constrain reconstructions of interior ice elevations during the LGM (Denton *et al.*, 1991). While this interpretation is reasonable, and is supported by relative age dating based on soil development and rock weathering, direct chronologic control on glacial deposits is lacking.

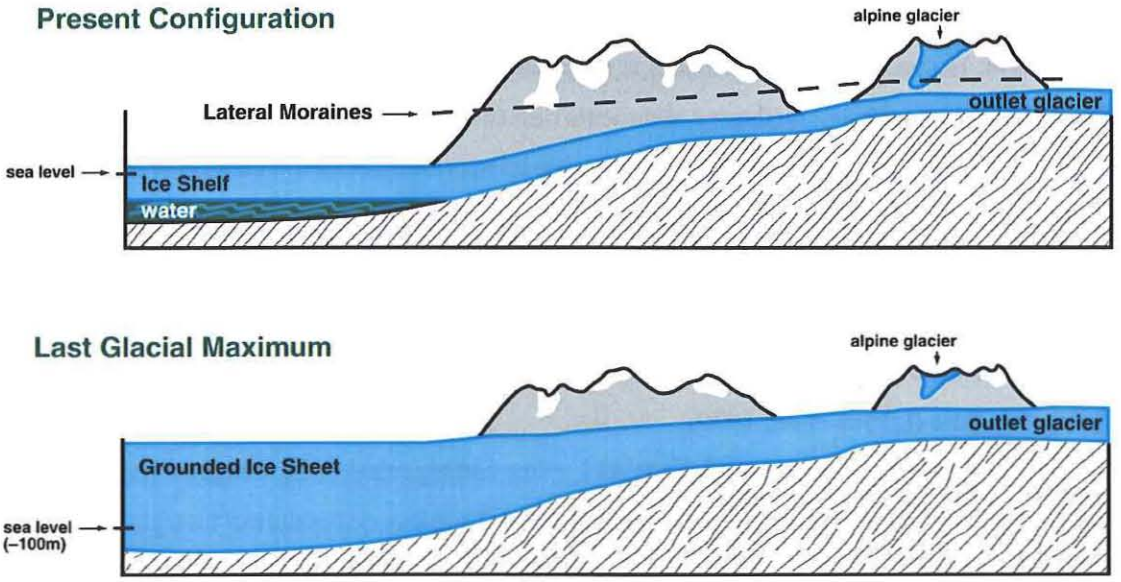

Figure 1.5 Cartoon depicting the dual control hypothesis. Present configuration: The outlet glacier terminates in a floating ice shelf. Alpine glaciers in the Transantarctic Mountains advance due to increased accumulation resulting from warmer temperatures. LGM: the outlet glacier is dammed by grounded ice. Thickening is greatest near the terminus and least near the head. The alpine glaciers retreat due to decreased accumulation. Note that moraines of the alpine glacier cross cuts the lateral moraines of the outlet glacier. Relationships like these have been used to assign an LGM age to the lateral moraines.

In this thesis, glacial chronologies are developed in three key areas of Antarctica to reconstruct past fluctuations of the WAIS and test models of ice sheet behavior (Figure 1.4). At all three locations, maximum ice extent during the last glaciation (stage 2) was determined. At all three areas new mapping of previously undifferentiated glacial moraines and surface exposure chronology has documented fluctuations of the WAIS prior to the LGM. Moraines at Mt. Waesche, a volcanic nunatak in Marie Byrd Land, gauge past ice highstands near the dome of the ice sheet. The results described in Chapter 3 place firm control on WAIS ice volume during the LGM. The surface exposure chronology indicates that maximum ice elevations occurred at ~10 ka, several thousand years after maximum ice extent in the Ross Sea (Ackert *et al.*, 1999). These results suggest that the WAIS never attained an equilibrium profile. This has important implications for modeling the ice sheet and post glacial sea level rise. Limited older surface exposure dates indicate earlier high stands also occurred during glacial periods, including the cold periods during the last interglacial (stage 5b).

The Beardmore Glacier is a major outlet glacier of the EAIS which flows into the Ross Ice Shelf through the Transantarctic Mountains. Lateral moraines indicate that, in the past, the down stream parts of the Beardmore (and other outlet glaciers) thickened preferentially. The moraine geometry indicates that the glacier flowed into grounded ice rather than a floating ice shelf (Denton *et al.*, 1989a; Mercer, 1972). These moraines, previously dated by only relative age techniques (Denton *et al.*, 1989a), provide key constraints of WAIS and EAIS reconstructions during the LGM. The surface exposure chronology presented in Chapter 4 from the Dominion Range, at the head of the Beardmore Glacier, provides the first numerical age control on these important deposits and indicates maximum ice levels occurred during the Early Holocene, consistent with the data from Mt. Waesche.

Older moraines at the Dominion Range, previously attributed to the penultimate glaciation (stage 6) (Denton *et al.*, 1989a), range in age from ~600 ka to ~1 Ma. The ~600 ka moraine is tentatively correlated with stage 16. The ~1 Ma moraine and two older moraines ~2 Ma are correlated with similar age moraines in the Dry Valleys Region (Brook *et al.*, 1993). This correlation implies expansions of the WAIS similar in magnitude to those of the late Pleistocene. The age of the ~1 Ma moraine falls within the mid-Pleistocene Revolution (Berger *et al.*, 1994), when the dominant periodicity of climate fluctuations shifted from 40 kyr to 100 kyr (Raymo *et al.*, 1997). The 100 kyr climate cycle is characterized by maximum global ice volumes in excess

of those of the 40 kyr cycle (Raymo, 1997). These results suggest that expansions of the WAIS are key components of this excess ice volume.

The Dromedary Platform is a bedrock bench adjacent to the Koettlitz Glacier which flows into southern McMurdo Sound (Figure 1.4). Eight lateral moraines at increasing elevation occur between the Koettlitz ice margin and the upper part of the bench. New mapping and a glacial chronology are presented in Chapter 5. The chronology indicates that the moraines range in age from Holocene to at least 450 ka. Some glacial deposits may be older than 1.68 Ma. The moraines record advances of the Koettlitz Glacier during interglacial conditions and damming of the glacier by grounded WAIS ice during glacial periods. In contrast to the other study locations, there is considerable scatter in the surface exposure data. However, the surficial mapping coupled with the $^{40}Ar/^{39}Ar$ chronology and stratigraphic relationships allows evaluations of problems associated with prior exposure and overlying cover and erosion rates of volcanic landforms.

In summary, the results from the three areas strongly support the model of sea level control of WAIS geometry. However, the results from interior locations indicate that the sea level changes during the last glaciation were too rapid for interior elevations of the WAIS to reach equilibrium with the expanded periphery. This result is consistent with time-dependent ice sheet models which predict significantly less ice volume than models of equilibrium conditions (Huybrechts, 1990b; Steig *et al.*, 1999). Results from all three locations document earlier fluctuations of the WAIS. At the Beardmore Glacier the oldest moraines linked to the WAIS are ~1 Ma which suggests that the sea level has exerted the dominant control on the WAIS during the mid to late Pleistocene.

Note added in press:

Several new developments in the field of surface exposure dating have occurred since the final draft of this document was completed. A scheme for scaling production rates which accounts for the non-dipole component of the Earth's magnetic field was published (Dunai, 2000). A long term ^{3}He production rate of 118 atoms/g/yr from Lanzarote, Canary Islands was published consistent with the production rates used in this work (Dunai and Wijbrans, 2000). New unpublished work in this lab by Lindsay Schoenbohm of MIT on sandstone bedrock cores from Antarctica suggests that the ^{21}Ne production rate from Niederman *et al.* (1994) used in Chapter 4 is too low, which could explain the offset observed between the measured ^{21}Ne (quartz) and ^{3}He (pyroxene) ages.

References

Ackert, R.P., Jr., Barclay, D.J., Borns, H.W., Jr., Calkin, P.E., Kurz, M.D., Steig, E.J., and Fastook, J.L., 1999, Measurement of ice sheet elevations in interior West Antarctica.: *Science*, **v. 286**, p. 276-280.

Anderson, J.B., Shipp, S.S., Bartek, L.R., and Reid, D.E., 1992, Evidence for a grounded ice sheet on the Ross Sea continental shelf during the late Pleistocene and preliminary paleodrainage reconstruction, *in* Kennett, J.P., and Warnke, D.A., eds., *The Antarctic Paleoenvironment: A perspective on global change*, **v. 57**: Antarctic Research Series: Washington, D. C., American Geophysical Union, p. 39-62.

Berger, W.H., Yasuda, M.K., Bickert, T., Wefer, G., and Takayama, T., 1994, Quaternary time scale for the Ontong Java Plateau: Milankovitch templete for Ocean Drilling Program Site 806: *Geology*, **v. 2**, p. 463-467.

Bierman, P.R., Gillespie, A.R., and Caffee, M.W., 1995, Cosmogenic ages for earthquake recurrence intervals and debris flow fan deposition, Owens Valley, California: *Science*, **v. 270**, p. 447-450.

Bockheim, J.G., Wilson, S.C., and Denton, G.H., 1989, Late Quaternary ice-surface fluctuations of Hatherton Glacier, Transantarctic Mountains: *Quaternary Research*, **v. 31**, p. 229-254.

Brook, E.J., Kurz, M.D., Ackert, R.P., Jr., Denton, G.H., Brown, E.T., Raisbeck, G.M., and Yiou, F., 1993, Chronology of Taylor Glacier advances in Arena Valley, Antarctica, using *in situ* cosmogenic ^{3}He and ^{10}Be: *Quaternary Research*, **v. 39**, p. 11-23.

Brook, E.J., Kurz, M.D., Ackert, R.P., Jr., Raisbeck, G., and Yiou, F., 1995, Cosmogenic nuclide exposure ages and glacial history of late Quaternary Ross Sea Drift in McMurdo Sound, Antarctica: *Earth and Planetary Science Letters*, **v. 131**, p. 41-56.

Brook, E.J., and Kurz, M.K., 1993, Surface-exposure chronology using *in situ* cosmogenic ^{3}He in Antarctic quartz sandstone boulders: *Quaternary Research*, **v. 39**, p. 1-10.

Brown, E.T., Brook, E.J., Raisbeck, G.M., Yiou, F., and Kurz, M.D., 1992, Effective attenuation lengths of cosmic rays producing ^{10}Be and ^{26}Al in quartz: implications for exposure age dating: .

Brown, E.T., Edmond, J., Raisbeck, G.M., Yiou, F., Kurz, M.D., and Brook, E.J., 1991, Examination of surface exposure ages of Antarctic moraines using in-situ produced ^{10}Be and ^{26}Al: *Geochimica et Cosmochimica Acta*, **v. 55**, p. 2269-2283.

Bruno, L.A., Baur, H., Graf, T., SchlÅcter, C., Signer, P., and Wieler, R., 1997, Dating of Sirius Group tillites in the Antarctic Dry Valleys with cosmogenic ^{3}He and ^{21}Ne: *Earth and Planetary Science Letters*, **v. 147**, p. 37-54.

Cerling, T.E., 1990, Dating Geomorphic Surfaces Using Cosmogenic ^{3}He: *Quaternary Research*, **v. 33**, p. 148-156.

Cerling, T.E., and Craig, H., 1994, Cosmogenic ^{3}He production rates from 39°N to 46°N latitude, western USA and France: *Geochimica Cosmochimica Acta*, **v. 58**, p. 349-255.

Cerling, T.E., Poreda, R.J., and Rathburn, S.L., 1994, Cosmogenic ^{3}He and ^{21}Ne age of the Big Lost River flood, Snake River Plain, Idaho: *Geology*, **v. 22**, p. 227-230.

Clark, D.H., Bierman, P.R., and Larsen, P., 1995, Improving *in situ* cosmogenic chronometers: *Quaternary Research*, **v. 44**, p. 367-377.

Conway, H., Hall, B.L., Denton, G.H., Gades, A.M., and Waddington, E.D., 1999, Past and future grounding-line retreat of the West Antarctic Ice Sheet: *Science*, **v. 286**, p. 280-283.

Davis, R., Jr., and Schaeffer, O.A., 1955, Chlorine-36 in Nature: *Annals of the New York Academy of Science*, **v. 62**, p. 105-122.

Denton, G.H., Armstrong, R.L., and Stuiver, M., 1971, The late Cenozoic glacial history of Antarctica, *in* Turekian, K.K., ed., *The Late Cenozoic Glacial Ages*: New Haven, Yale University Press.

Denton, G.H., Bockheim, J.G., Wilson, S.C., Leide, J.E., and Anderson, B.G., 1989a, Late Quaternary ice-surface fluctuations of Beardmore Glacier, Transantarctic Mountains: *Quaternary Research*, **v. 31**, p. 189-209.

Denton, G.H., Bockheim, J.G., Wilson, S.C., and Stuiver, M., 1989b, Late Wisconsin and early Holocene glacial history, inner Ross Embayment, Antarctica.: *Quaternary Research*, **v. 31**, p. 151-182.

Denton, G.H., Hughes, T.H., and Karlen, W., 1986, Global ice-sheet system interlocked by sea level: *Quaternary Research*, **v. 26**, p. 3-26.

Denton, G.H., Prentice, M.L., and Burkle, L.H., 1991, Cenozoic history of the Antarctic ice sheet, *in* Tingey, R.J., ed., *The Geology of Antarctica: Oxford*, Clarendon Press, p. 365-419.

Denton, G.H., Sugden, D.E., Marchant, D.R., Hall, B.L., and Wilch, T.I., 1993, East Antarctic ice sheet sensitivity to Pliocene climatic change from a Dry Valleys perspective: *Geografiska Annaler*, **v. 75**, p. 155-204.

Domack, E.W., Jacobson, E.A., Shipp, S., and Anderson, J.B., 1999, Late Pleistocene/ Holocene retreat of the West Antarctic Ice Sheet: Part 2- Sedimentologic and stratigraphic signature.: *Geological Society of America Bulletin*, **v. 111**, p. 1517-1536.

Drewry, D.J., 1983, Antarctica: glaciological and geophysical folio: Cambridge, Scott Polar Research Institute.

Dunai, T.J., 2000, Scaling factors for production rates of in situ produced cosmogenic nuclides: a critical evaluation: *Earth and Planetary Science Letters*, **v. 176**, p. 157-169.

Dunai, T.J., and Wijbrans, J.R., 2000, Long-term cosmogenic ^{3}He production rates (152 ka- 1.35 Ma) from ^{40}Ar/^{39}Ar dated basalt flows at 29°N latitude: *Earth and Planetary Science Letters*, **v. 176**, p. 147-156.

Eikenberg, J., Signer, P., and Wieler, R., 1993, U-Xe. U-Kr and U-Pb systematics for dating uranium minerals and investigations of the production of nucleogenic neon and argon: *Geochimica Cosmochimica Acta*, **v. 57**, p. 1053-1069.

Gillespie, A.R., and Bierman, P.R., 1995, Precision of terrestrial exposure ages and erosion rates estimated from analysis of cosmogenic isotopes produced *in situ*: *Journal of Geophysical Research*, **v. 100**, p. 24,637-24,649.

Gosse, J.C., Evenson, E.B., Klein, J., Lawn, B., and Middleton, R., 1995a, Precise cosmogenic ^{10}Be measurements in western North America: support for a global Younger Dryas cooling event: *Geology*, **v. 23**, p. 877-880.

Gosse, J.C., Klein, J., Evenson, E.B., Lawn, B., and Middleton, R., 1995b, Beryllium -10 dating of the last Pinedale glacial sequence: *Science*, **v. 268**, p. 1329-1333.

Graf, T., Buar, H., and Signer, P., 1990, A model for the production of cosmogenic nuclides in chondrites: *Geochimica Cosmochimica Acta*, **v. 54**, p. 2521-2534.

Graf, T., Kohl, C.P., Marti, K., and Nishiizumi, K., 1991, Cosmic-ray produced neon in Antarctic rocks: *Geophysical Research Letters*, **v. 18**, p. 203-206.

Hallet, B., and Putkonen, J., 1994, Surface dating of dynamic landforms: *Science*, **v. 265**, p. 937-940.

Hart, S.R., 1984, Helium diffusion in olivine: *Earth and Planetary Science Letters*, **v. 70**, p. 297-302.

Hollin, J.T., 1962, On the glacial history of Antarctica: *Journal of Glaciology*, **v. 4**, p. 173-195.

Hughes, T.J., 1987, Deluge II and the continent of doom: Rising sea level and collapsing Antarctic ice.: *Boreas*, **v. 16**, p. 89-100.

Huybrechts, P., 1990a, A 3-D model for the Antarctic Ice Sheet: A sensitivity study on the glacial-interglacial contrast: *Climate Dynamics*, **v. 5**, p. 79-92.

Huybrechts, P., 1990b, The Antarctic ice sheet during the last glacial-interglacial cycle: A three dimensional experiment: *Annals of Glaciology*, **v. 5**, p. 115-119.

Kennedy, B.M., Hiyagon, H., and Reynolds, J.H., 1990, Crustal neon: a striking uniformity: *Earth and Planetary Science Letters*, **v. 98**, p. 277-286.

Kurz, M.D., 1986a, Cosmogenic helium in a terrestrial igneous rock: *Nature*, **v. 320**, p. 435-439.

Kurz, M.D., 1986b, *In situ* production of terrestrial cosmogenic helium and some applications to geochronology: *Geochimica et Cosmochimica Acta*, **v. 50**, p. 2855-2862.

Kurz, M.D., and Ackert, R.P., 1997, Stability of the East Antarctic Ice Sheet?: New chronological evidence from Bennett Platform, Antarctica: *EOS*, **v. 78**, p. S185.

Kurz, M.D., and Brook, E.J., 1994, Surface exposure dating with cosmogenic nuclides, *in* Beck, C., ed., *Dating in Exposed and Surface Contexts*: Albuquerque, University of New Mexico Press, p. 139-159.

Kurz, M.D., Colodner, D., Trull, T.W., Moore, R.B., and O'Brien, K., 1990, Cosmic ray exposure dating with *in situ* produced cosmogenic ^{3}He: results from young Hawaiian lava flows: *Earth and Planetary Science Letters*, **v. 97**, p. 177-189.

Kurz, M.D., Kenna, T.C., Lassiter, J.C., and DePaolo, D.J., 1996, Helium isotopic evolution of Mauna Kea Volcano: First results from the 1-km drill core: *Journal of Geophysical Research*, **v. 101**, p. 11,781-11,791.

Lal, D., 1987, Production of ^{3}He in terrestrial rocks: *Chemical Geology* (Isotope Geoscience Section), **v. 66**, p. 89-98.

Lal, D., 1991, Cosmic ray labeling of erosion surfaces: *In situ* nuclide production rates and erosion models: *Earth and Planetary Science Letters*, **v. 104**, p. 424-439.

Lal, D., and Peters, B., 1967, Cosmic ray produced radioactivity on the Earth, *in* Flügge, S., and Sitte, K., eds., *Encyclopedia of physics*, Volume XLVI/2: New York, Springer-Verlag, p. 551-612.

Licciardi, J.M., Kurz, M.D., and Clark, P.U., 1999, Calibration of cosmogenic ^{3}He production rates: Results from Holocene lava flows: *Earth and Planetary Science Letters*, **v. 172**, p. 261-271.

Licht, K.J., Dunbar, N.W., Andrews, J.T., and Jennings, A.E., 1999, Distinguishing subglacial till and glacial marine diamictons in the western Ross Sea, Antarctica: Implications for last glacial maximum grounding line: *Geological Society of America Bulletin*, **v. 111**, p. 91-103.

Licht, K.J., Jennings, A.E., Andrews, J.T., and Williams, K.M., 1996, Chronology of late Wisconsin ice retreat from the western Ross Sea, Antarctica: *Geology*, **v. 24**, p. 223-226.

Lide, D.R., 1998-9, *CRC Handbook of Chemistry and Physics*: Boca Raton, CRC Press, p. 14-16 - 14-22.

Liu, B., Phillips, F.M., Fabryka-Martin, J.T., Fowler, M.M., and Stone, W.D., 1994, Cosmogenic ^{36}Cl accumulation in unstable landforms. 1. Effects of the thermal neutron distribution: *Water Resources Research*, **v. 30**, p. 3115-3125.

Lorius, C., Merlivat, L., Jouzel, J., and Pourchet, M., 1979, A 30,000-year isotope climatic record from Antarctic Ice: *Nature*, **v. 280**, p. 644-648.

MacAyeal, D.R., 1992, Irregular oscillations of the West Antarctic ice sheet: *Nature*, **v. 359**, p. 29-32.

Marchant, D.R., Denton, G.H., Bockheim, J.G., Wilson, S.C., and Kerr, A.J., 1994, Quaternary changes in the level of upper Taylor Glacier, Antarctica: Implications for paleoclimate and ice-sheet dynamics: *Boreas*, **v. 23**, p. 29-43.

Marchant, D.R., Denton, G.H., Swisher III, C.C., and Potter Jr., N., 1996, Late Cenozoic Antarctic paleoclimate reconstructed from volcanic ashes in the Dry Valleys region of southern Victoria Land: *Geological Society of America Bulletin*, **v. 108**, p. 181-194.

Marchant, D.R., Swisher III, C.C., Lux, D.R., West Jr., D.P., and Denton, G.H., 1993, Pliocene paleoclimate and East Antarctic Ice-Sheet history from surficial Ash deposits: *Science*, **v. 260**, p. 667-670.

Marti, K., and Craig, H., 1987, Cosmic-ray-produced neon and helium in the summit lavas of Maui: *Nature*, **v. 325**, p. 335-337.

Masarik, J., and Reedy, R.C., 1994, Effects of bulk chemical composition on nuclide production processes in meteorites: *Geochimica Cosmochimica Acta*, **v. 58**, p. 5307-5317.

Masarik, J., and Reedy, R.C., Terrestrial cosmogenic-nuclide production systematics calculated from numerical simulations: *Earth and Planetary Science Letters*, **v. 136**, p. 381-395.

Masarik, J., and Reedy, R.C., 1996, Monte Carlo simulation of the in-situ-produced cosmogenic nuclides: *Radiocarbon*, **v. 38**, p. 163.

Mazor, E., Heymann, D., and Anders, E., 1970, Noble gases in carbonaceous chondrites: *Geochimica et Cosmochimica Acta*, **v. 34**, p. 781-824.

McElhinny, M.W., and Senanayake, W.E., 1982, Variations in the geomagnetic dipole 1: The past 50,000 years: , **v. 34**, p. 39-51.

Mercer, J.H., 1968, Glacial geology of the Reedy Glacier Area, Antarctica: *Geological Society of America Bulletin*, **v. 79**, p. 471-486.

Mercer, J.H., 1972, Some observations on the glacial geology of the Beardmore Glacier area, *in* Adie, R.J., ed., *Antarctic Geology and Geophysics*: Oslo, Universitetsforlaget, p. 427-433.

Mercer, J.H., 1978, West Antarctic ice sheet and the CO_2 greenhouse effect: A threat of disaster: *Nature*, **v. 271**, p. 321.

Merrill, R.T., McElhinny, M.W., and McFadden, P.L., 1996, The magnetic field of the Earth: *Paleomagnetism, the Core, and the Deep Mantle*: San Diego, Academic Press, 531 p.

Niedermann, S., Graf, T., Kim, J.S., Kohl, C.P., Marti, K., and Nishiizumi, K., 1994, Cosmic-ray-produced ^{21}Ne in terrestrial quartz; the neon inventory of Sierra Nevada quartz separates: *Earth and Planetary Science Letters*, **v. 125**, p. 341-355.

Niedermann, S., Graf, T., and Marti, K., 1993, Mass spectrometric identification of cosmic-ray-produced neon in terrestrial rocks with multiple neon components: *Earth and Planetary Science Letters*, **v. 118**, p. 65-73.

Nishiizumi, K., Kohl, C.P., Arnold, J.R., Klein, J., and Fink, D., 1991a, Cosmic ray produced ^{10}Be and ^{26}Al in Antarctic rocks: Exposure and erosion rates: *Earth and Planetary Science Letters*, **v. 104**, p. 440-454.

Nishiizumi, K., Kohl, C.P., Shoemaker, E.M., Arnold, J.R., Klein, J., Fink, D., and Middleton, R., 1991b, *In situ* ^{10}Be-^{26}Al exposure ages at Meteor Crater, Arizona: *Geochimica et Cosmochimica Acta*, **v. 55**, p. 2699-2703.

Nishiizumi, K., Lal, K., Klein, J., Middleton, R., and Arnold, J., 1986, Production of ^{10}Be and ^{26}Al by cosmic rays in terrestrial quartz *in situ*: *Nature*, **v. 319**, p. 134-136.

Nishiizumi, K., Winterer, E.L., Kohl, C., P., Klein, J., Middleton, R., Lal, D., and Arnold, J.R., 1989, Cosmic ray production rates of 10-Be and 26-Al in quartz from glacially polished rocks: *Journal of Geophysical Research*, **v. 94**, p. 17907-17915.

Oppenheimer, M., 1998, Global warming and the stability of the West Antarctic Ice Sheet: *Nature*, **v. 393**, p. 325-332.

Phillips, F.M., Leavy, B.D., Jannik, N.O., Elmore, D., and Kubik, P.W., 1986, Accumulation of cosmogenic chlorine-36 in rocks: A method for surface exposure dating: *Science*, **v. 231**, p. 41-43.

Phillips, F.M., Zreda, G.M., Gosse, C.J., Klein, J., Evenson, E.B., Hall, R.D., Chadwick, O.A., and Sharma, P., 1997, Cosmogenic ^{36}Cl and ^{10}Be ages of Quaternary glacial and fluvial deposits of the Wind River Range, Wyoming: *Geological Society of America Bulletin*, **v. 109**, p. 1453-1463.

Phillips, F.M., Zreda, M.G., Benson, L.V., Plummer, M.A., Elmore, D., and Sharma, P., 1996a, Chronology for fluctuations in Late Pleistocene Sierra Nevada Glaciers and Lakes: *Science*, **v. 274**, p. 749-751.

Phillips, F.M., Zreda, M.G., and Flinsch, M.R., 1996b, A reevaluation of cosmogenic ^{36}Cl production rates in terrestrial rocks: *Geophysical Research Letters*, **v. 23**, p. 949-952.

Phillips, F.M., Zreda, M.G., Smith, S.S., Elmore, D., Kubik, P.W., and P., S., 1990, Cosmogenic chorine-36 chronology for glacial deposits at Bloody Canyon, Eastern Sierra Nevada: *Science*, **v. 248**, p. 1529-1532.

Poreda, R.J., and Cerling, T.E., 1992, Cosmogenic neon in recent lavas from the western United States: *Geophysical Research Letters*, **v. 19**, p. 1863-1866.

Raymo, M.E., 1997, The timing of major climate terminations: *Paleoceanography*, **v. 12**, p. 577-585.

Raymo, M.E., Oppo, D.W., and Curry, W., 1997, The mid Pleistocene climate transition: A deep sea carbon isotopic perspective: *Paleoceanography*, **v. 12**, p. 546-559.

Sarda, P., Staudacher, T., and Allägre, C.J., 1988, Neon isotopes in submarine basalts: *Earth and Planetary Science Letters*, **v. 91**, p. 73-88.

Sarda, P., Staudacher, T., Allegre, C.J., and Lecompte, A., 1993, Cosmogenic neon and helium at Reunion: measurement of erosion rate: *Earth and Planetary Science Letters*, **v. 119**, p. 405-417.

Schäfer, J.M., Ivy-Ochs, S., Wieler, R., Leya, I., Baur, H., Denton, G.H., and SchlÅchter, C., 1999, Cosmogenic noble gas studies in the oldest landscape on earth: surface exposure ages of the Dry Valleys, Antarctica: *Earth and Planetary Science Letters*, **v. 167**, p. 215-226.

Shipp, S., Anderson, J.B., and Domack, E.W., 1999, Late Pleistocene/Holocene Retreat of the West Antarctic Ice-sheet System in the Ross Sea: *Geological Society of America Bulletin*, **v. 111**, p. 1486-1516.

Singer, B.S., Ackert, R.P., Jr., Kurz, M.D., Guillou, H., and Ton-That, T., 1998, Chronology of Pleistocene Glaciations in Patagonia: A ^{3}He, $^{40}Ar/^{39}Ar$, & K-Ar study of lavas and moraines at Lago Buenous Aires, 46° S, Argentina: Geological Society of America, 1998 annual meeting, Abstracts with Programs, **v. 30**, p. 299.

Staudacher, T., and Allegre, C.J., 1991, Cosmogenic Neon in ultramafic Nodules from Asia and in Quartzite from Antarctica: *Earth and Planetary Science Letters*, **v. 106**, p. 87-102.

Staudacher, T., and Allägre, C.J., 1993, The cosmic ray produced $^{3}He/^{21}Ne$ ratio in ultramafic rocks: *Geophysical Research Letters*, **v. 20**, p. 1075-1078.

Steig, E.J., Fastook, J.L., Ackert, R.P., Jr., White, J.W.C., Licht, K.L., Zweck, C., and Goodwin, I., 1999, West Antarctic Ice Sheet elevation changes, *Antarctic Research Series*, American Geophysical Union, p. in press.

Stone, J.O., Allan, G.L., Fifield, K.L., and Cresswell, R.G., 1996, Cosmogenic chorine-36 from calcium spallation: *Geochimica et Cosmochimica Act*a, **v. 60**, p. 679-692.

Stone, J.O., Ballantyne, C.K., and Fifield, K.L., 1998, Exposure dating and validation of periglacial weathering limits, northwest Scotland: *Geology*, **v. 26**, p. 587-590.

Stuiver, M., Denton, G.H., Hughes, T.J., and Fastook, J.L., 1981, History of the marine ice sheet in West Antarctica during the last glaciation, a working hypothesis, *in* Denton, G.H., and Hughes, T.J., eds., *The Last Great Ice Sheets*: New York, Wiley-Interscience, p. 319-436.

Trull, T.W., Brown, E.T., Marty, B., Raisbeck, G.M., and Yiou, F., 1995, Cosmogenic ^{10}Be and ^{3}He accumulation in Pleistocene beach terraces in Death Valley, California, U.S.A.: Implications for cosmic-ray exposure dating of young surfaces in hot climates: *Chemical Geology*, **v. 119**, p. 191-207.

Trull, T.W., Kurz, M.D., and Jenkins, W.J., 1991, Diffusion of cosmogenic ^{3}He in olivine and quartz: implications for surface exposure dating: *Earth and Planetary Science Letters*, **v. 103**, p. 241-256.

Webb, P.-N., Harwood, D.M., Mabin, M.G.C., and McKelvey, B.C., 1996, A marine and terrestrial Sirius Group succession, middle Beardmore Glacier-Queen Alexandra Range, Transantarctic Mountains, Antarctica: *Marine Micropaleontology*, **v. 27**, p. 273-297.

Zreda, M.G., and Phillips, F.M., 1994a, Cosmogenic ^{36}Cl accumulation in unstable landforms 2. Simulations and measurements on eroding moraines: *Water Resources Research*, **v. 30**, p. 3127-3136.

Zreda, M.G., and Phillips, F.M., 1994b, Surface exposure dating by cosmogenic chorine-36 accumulation, *in* Beck, C., ed., Dating in Exposed and Surface Contexts: *Dating in Exposed and Surface Contexts*, University of New Mexico Press, p. 161-183.

Zreda, M.G., Phillips, F.M., Elmore, D., Kubik, P.W., Sharma, P., and Dorn, R.I., 1991, Cosmogenic chlorine-36 production rates in terrestrial rocks: *Earth and Planetary Science Letters*, **v. 105**, p. 94-109.

CHAPTER 2

Determination of ^{3}He production rate in olivine and clinopyroxene and inherited $^{3}He/^{4}He$ of quartz and pyroxene

2.1 Introduction

The utility of ^{3}He surface exposure ages to studies of past climate change critically depends on the accuracy and precision of the calculated ages. The uncertainties are mainly related to the production rate calibrations and the altitude and latitude scaling of the production rates. In lithologies other than young volcanic rocks, correction for the inherited (non-cosmogenic) ^{3}He component also adds uncertainty. The analytical uncertainties in the ^{3}He measurements are typically only 2 to 3 percent. In contrast, uncertainties in production rates and scaling factors, which apply to all cosmogenic nuclides, are estimated to be 10 to 15 percent. These large uncertainties inhibit the application of surface exposure dating to many paleoclimatic problems. In this chapter, a new ^{3}He production rate calibration is presented from a 125 ka lava flow at 46° S latitude independently dated by K-Ar and $^{40}Ar/^{39}Ar$ methods. This long term, mid-latitude production rate calibration minimizes problems with scaling existing low-latitude production rate calibrations to high latitude and lowers uncertainties when applied to older exposure samples.

The importance of the inherited ^{3}He component is related to the exposure age and lithology of the samples. Although the systematics of this correction are well understood for the young volcanic samples on which the ^{3}He surface exposure technique was pioneered (*e.g.*, Kurz *et al.*, 1996), the correction is more complicated for rocks in which the formation age is many orders of magnitude greater than the exposure age. The inherited component can either be trapped during formation of the rock or be the result of radiogenic production. For samples with long exposure, the inherited component is small relative to the cosmogenic component and the calculated ages are relatively insensitive to the value adopted. However, for younger samples (<20 ka) the inherited component becomes increasingly important. This chapter presents new data on the inherited $^{3}He/^{4}He$ of pyroxene from the Ferrar Dolerite and quartz from the Beacon Sandstones in Antarctica. These results allow these ubiquitous lithologies to be used to date surfaces as young as ~10 ka in the Transantarctic Mountains.

2.2 Measurement of inherited $^{3}He/^{4}He$ in quartz and pyroxene

Introduction

The short half lives of the radioactive cosmogenic nuclides (^{10}Be, ^{26}Al and ^{36}Cl) relative to the formation age of the rocks often sampled for exposure dating means that correction for an inherited component is generally unnecessary (^{10}Be and ^{26}Al), or is a constant value determined by secular equilibrium (nucleogenic ^{36}Cl produced by U and Th decay) (Zreda and Phillips, 1994). In contrast, the inventory of the stable cosmogenic nuclides (^{3}He and ^{21}Ne) will increase over time due to nucleogenic reactions. In these reactions, nuclear reactions between a particles (^{4}He) from U and Th decay and target nuclei result in new nuclides. For ^{3}He the principal reaction is ^{6}Li (α,n) $T \rightarrow {}^{3}He$ (Lal, 1987; Morrison and Pine, 1955). Because the cosmogenic ^{3}He component is calculated by subtracting the inherited component from the total ^{3}He measured (Chapter 1), accurate measurement of the inherited component is necessary (Kurz and Brook, 1994).

In young extrusive volcanic phenocrysts (olivine and clinopyroxene), the inherited component is primarily magmatic helium which is released from fluid and melt inclusions by crushing the sample (Kurz, 1986b). The $^{3}He/^{4}He$ measured on crushing is multiplied by the ^{4}He concentration measured when the sample is melted to determine the initial concentration. This value is then subtracted from the total ^{3}He measured on melting the sample (Equations 9 to 11, Chapter 1). This calculation assumes that all the ^{4}He is magmatic (there is no radiogenic or cosmogenic ^{4}He). This approximation is valid in young rocks because the magmatic ^{4}He concentrations in olivine are ~105 times higher than cosmogenic ^{4}He and olivine has low U and Th concentrations (Kurz and Brook, 1994). Typically, about 90 percent of the ^{4}He is released in the crushing step. However, even in volcanic rocks, radiogenic production of ^{4}He may become important for rocks older than 1 Ma. The presence of radiogenic ^{4}He results in an overestimates of the inherited ^{3}He and underestimates of, or even negative, exposure ages (see Chapter 1 for details).

Quartz is an attractive mineral for surface exposure dating because it is ubiquitous and has a simple target chemistry. Unfortunately, diffusion rates of cosmogenic helium in quartz are relatively high (Trull *et al.*, 1991) and substantial diffusive loss has been demonstrated in hot climates (Trull *et al.*, 1995) and in samples with long exposure (Brook and Kurz, 1993; Graf *et al.*, 1991; Niedermann *et al.*, 1994). However, in Antarctica, cosmogenic helium may be

quantitatively retained for up to 100 kyr in quartz grains greater than 1 mm in diameter (Brook and Kurz, 1993). Crushing quartz yields only a small fraction of the He and highly variable $^3He/^4He$, indicating that some of the cosmogenic component is released (Brook and Kurz, 1993). Crushing old pyroxene, such as from the Ferrar Dolerite, yields more consistent results, but repeated crushing of individual samples indicates that some of the cosmogenic component can also be released (Kurz, unpublished data).

Alternative methods for determining the $^3He/^4He$ of the inherited component include step heating experiments and measurements in shielded samples with no cosmogenic component. Because of the variety of sandstone lithologies utilized, it was not feasible to find equivalent shielded samples. However, because cosmogenic ^3He is selectively released at low temperatures in quartz, an estimate of the initial ratio can be determined by step heating (Trull *et al.*, 1991). In contrast, the Ferrar Dolerite is more uniform in chemical composition (Hergt *et al.*, 1991) and results from shielded samples should be applicable to all samples. Shielded samples may be obtained from drill cores greater than 2 m deep, from rapidly eroding outcrops or from fresh rockfall debris.

Measurement of inherited $^3He/^4He$ in quartz

For quartz grains in the Beacon Sandstones, all ^4He is assumed to be radiogenic. The Beacon Sandstones range in age from Devonian to Permian (Elliot *et al.*, 1974). The age of the quartz grains must be significantly older to allow for erosion of the original igneous rocks and subsequent redeposition. Staudacher (1991) calculated K-Ar and U-Xe ages of the quartz in Devonian Beacon Sandstones of greater than 1 Ga. Helium trapped during crystallization would be lost by diffusion over the great age of the quartz. The ^4He concentration is variable among replicate samples (Table 4.2, Chapter 4), consistent with previous studies (Brook and Kurz, 1993). The stopping distance of an a particle in quartz is ~40 mm (Friedlander *et al.*, 1981). U and Th are probably concentrated within accessory minerals in the cement; variable ^4He concentrations probably result from varying proportions of the outermost part of the quartz grains and inhomogeneous distributions of U and Th.

The assumption that there is no cosmogenic ^4He in quartz (all ^4He is radiogenic) is justified by the fact that the measured ^4He is many orders of magnitude greater than expected from the $^3He/^4He$ measured if the He was primarily cosmogenic. This assumption allows calculation of the cosmogenic ^3He in a manner similar to that used for olivine, with the inherited

$^3He/^4He$ substituted for the magmatic (crush) $^3He/^4He$. This inherited helium is a mixture of the radiogenic ^4He and nucleogenic ^3He. Nucleogenic ^3He is produced primarily by the reaction ^6Li (α,n) $T \rightarrow {}^3He$ (Lal, 1987; Morrison and Pine, 1955) and therefore nucleogenic ^3He concentrations are dependent on Li, Th and U concentrations and the distribution of those elements.

In an experiment designed to determine ^3He and ^4He diffusion rates in quartz, Trull (1991) incrementally heated quartz grains from a moraine boulder in Antarctica with 1 Ma exposure to 622°C and then melted the grains. Almost all the cosmogenic ^3He was released at temperatures less than 400°C. The $^3He/^4He$ of the melted grains (>622°C step) was .011 ± .004 R/R_a (R_a is the $^3He/^4He$ of air = 1.384×10^{-6}) and was interpreted as the inherited ratio of the sample. This value is similar to the $^3He/^4He$ of the last heating step (.02±.01 R/R_a) and consistent with values calculated from the Li, Th, and U concentrations and the age of the rock (Brown *et al.*, 1991). This result, from a single sample, indicates that the inherited ^3He concentration is very low and, to a first approximation, all ^3He can be assumed to be cosmogenic.

In this work, He and Ne isotopes were measured in gas released by step heating eight quartz samples from sandstone moraine boulders in the Dominion Range (Figure 2.1). Neon isotope data are presented in Chapter 4. The automated gas extraction line includes a titanium sponge getter, a SAES getter and a cryogenic charcoal trap for separating noble gases (cooled to 7°K, He released at 35°K, Ne released a 70°K). Extracted gas was analyzed for isotopic composition on a MAP215-50 mass spectrometer with a Nier type source. All neon isotopes and ^3He were measured with an electron multiplier and ^4He was measured with a Faraday collector. The samples were progressively heated to 300, 600,and 1500°C. A blank was analyzed for each temperature step, and air standards were analyzed between each sample and blank run. The mass spectrometer was tuned to optimize sensitivity for neon isotopes. All He released at each step was inlet to the mass spectrometer in order to measure the relatively small ^3He concentrations.

During these experiments, the ^4He sensitivity was found to be strongly pressure-dependent and non-linear. For signals less than 0.1 volts, ^4He concentrations were determined by a quadratic fit to the voltage measured on standard aliquots (one to ten; ^4He of 5 to 50 $\times 10^{-9}$ ccSTP) and uncertainties are estimated to be less than 10 percent. For signals greater than 0.1 volts ^4He concentrations were determined by linear interpolation between the 0.1 volt value and the signal obtained from a single large standard (2.03 volts, ~43 times the standard aliquot). Uncertainties are correspondingly larger, but do not effect the qualitative conclusions drawn.

However, the $^3He/^4He$ ratio was insensitive over the wide dynamic range of the measured standards

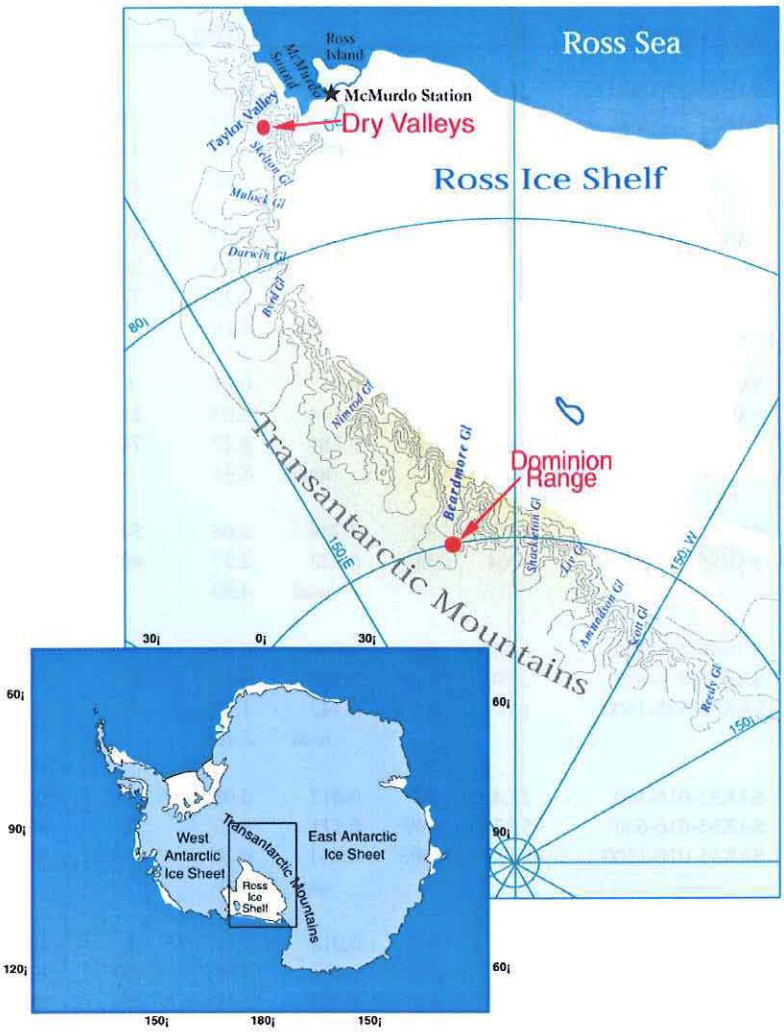

Figure 2.1 Map showing location of the Dry Valleys, where the Taylor Glacier cliff and Kukri Hills shielded dolerite samples were collected, and the Dominion Range, where the quartz samples used in the step heating experiment were collected.

Helium isotope data are presented in Table 2.1. Typically, almost all of the ^3He is released in the 300°C and the 600°C steps (Figure 2.2). The quartz grains are melted in the 1500°C step. Very little ^3He remains in the 1500° step although more than half of ^4He is typically released (Figure 2.2). The weighted mean $^3He/^4He$ of the six samples in which the ^3He concentration was above blank levels in the 1500°C step is .003 ± .0004 R/R_a. This value is interpreted as the inherited $^3He/^4He$ of the quartz samples.

Table 2.1 Helium isotope data of step heated quartz

sample-temp °C	$^3He/^4He$ R/Ra	± 1sig	^4He Volts	^4He x 10^6 ccSTP/g	^4He % released	^3He % released
SAK95-235-300	21.2	0.3	0.021	0.06	3	14
SAK95-235-600	8.09	0.072	0.101	0.94	52	86
SAK95-235-1500	0.002	0.001	0.098	0.81	45	0
			total	*1.82*		
SAK95-445-300	52.7	0.3	0.019	0.05	1	14
SAK95-445-600	17.1	3.1	0.022	0.84	26	86
SAK95-445-1500	0.002	0.001	0.220	2.33	72	0
			total	*3.21*		
SAK95-446-300	43.6	0.5	0.017	0.07	1	19
SAK95-446-600	5.94	0.06	0.144	2.09	25	81
SAK95-446-1500	n.d.	n.d.	0.284	6.27	74	0
			total	*8.44*		
SAK95-245-600	10.9	0.1	0.244	2.66	54	100
SAK95-245-1500	0.004	0.001	0.223	2.27	46	0
			total	4.94		
SAK95-435-300	8.64	0.1	0.014	0.05	2	19
SAK95-435-600	2.70	0.03	0.092	0.68	27	81
SAK95-435-1500	n.d.	n.d.	0.142	1.76	71	0
			total	*2.48*		
SAK95-016-300	28.4	0.3	0.017	0.05	1	5
SAK95-016-600	5.32	0.09	0.111	4.33	95	95
SAK95-016-1500	0.008	0.003	0.063	0.20	4	0
			total	*4.58*		
SAK95-246-300	35.0	0.3	0.018	0.05	2	17
SAK95-246-600	9.00	0.07	0.102	0.93	43	83
SAK95-246-1500	n.d.	n.d.	0.125	1.19	55	0
			total	*2.17*		
SAK95-036-300	38.8	1.000	0.039	0.10	7	72
SAK95-036-600	7.04	0.25	0.068	0.22	16	28
SAK95-036-1500	0.004	0.001	0.102	1.05	76	0
			total	*1.38*		
Weighted mean-1500	0.003	0.0004				

n.d. = not detectable; ^3He detection limit is ~1 count/sec. Ra is the $^3He/^4He$ of air = 1.384×10^{-6}. R is measured $^3He/^4He$. Uncertainties in ^4He are <10% for signals < 0.1 volts. For signals >0.1 uncertainties are greater. See text for discussion. Voltages measured on a DVM with 10^{-11} ohm resistor.

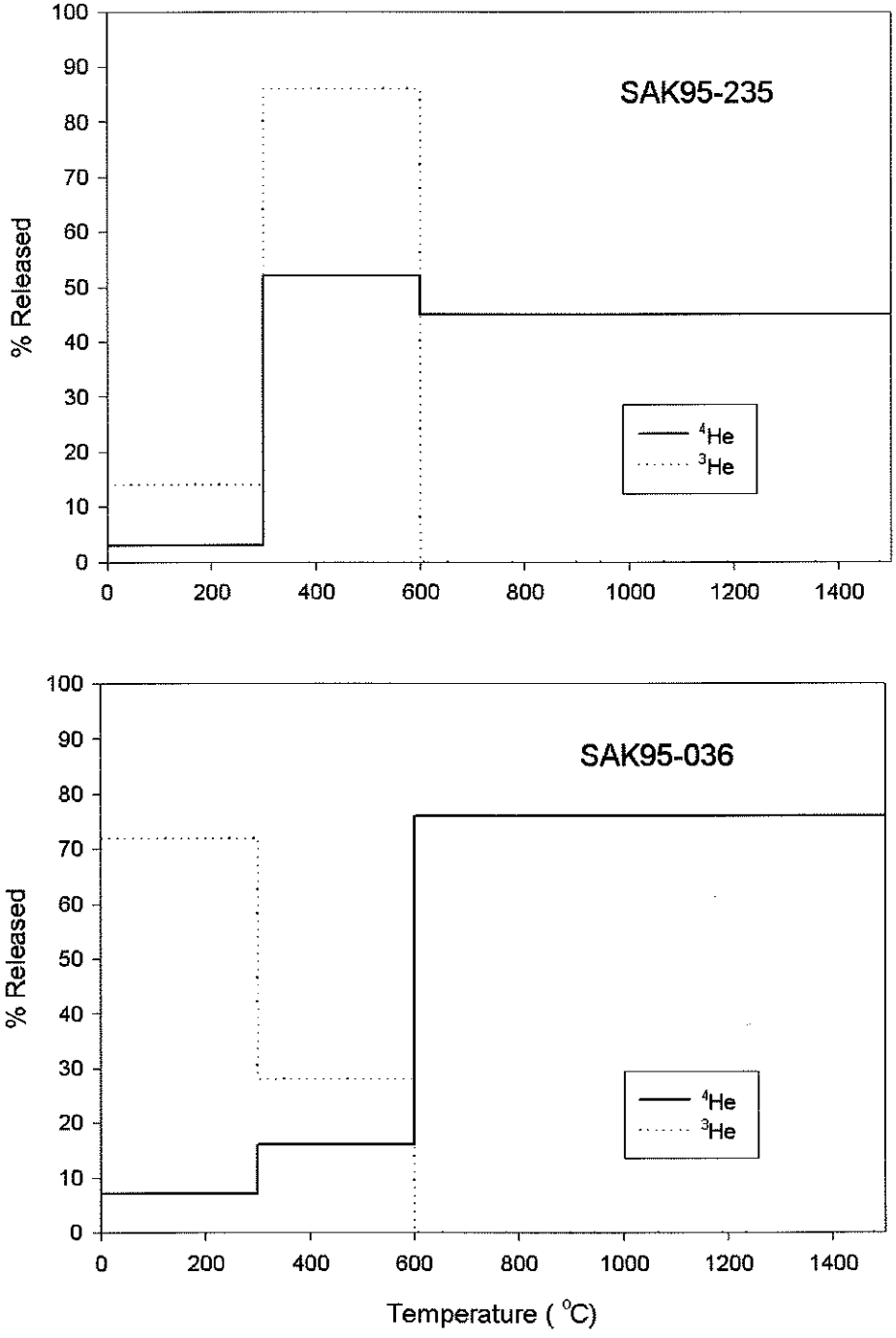

Figure 2.2 Release pattern of ^{3}He and ^{4}He during the 300°, 600° and 1500° heating steps of sample SAK95-036 and 235. Other samples show similar patterns. 100 percent of the cosmogenic ^{3}He is released in the 300° and 600°C heating steps. In contrast, only a few percent of the ^{4}He is released in the first step and almost 50 to 80 percent of the ^{4}He is released in the last step. The $^{3}He/^{4}He$ of the last step characterizes the inherited (radiogenic and nucleogenic) component.

The diffusivity of ^{3}He is estimated by theory and measurement in glasses to be 10 to 20 percent greater than that of ^{4}He due to the difference in mass (Shelby, 1971; Trull, 1989). Therefore, this value is a lower limit because a small fraction of the radiogenic ^{3}He could have been preferentially lost by diffusion in the lower temperature steps. Such low values imply very low Li, U and Th concentrations in the samples. This result is similar to that of Trull (1991) and indicates that all ^{3}He can be assumed to be cosmogenic for samples greater than 30,000 years (cosmogenic ^{3}He <1%). However, in young samples (<10,000 years) the correction for inherited ^{3}He using an inherited ratio of .003 ± .0004 R/R_a results in corrections up to 5 percent.

An independent estimate of the inherited ^{3}He/^{4}He comes from the lowest ^{3}He/^{4}He measured on sandstone boulders from young moraines at the Beardmore Glacier (Chapter 4). The ^{3}He/^{4}He of .017 R/R_a measured on sample SAK95-205 (Table 4.2) is the maximum inherited value because the sample has had some exposure to cosmic rays and a higher inherited ^{3}He/^{4}He results in a negative age. Moreover, scatter in the exposure ages calculated increases when initial ^{3}He/^{4}He higher than .003 R/R_a is used in the age calculations. Thus, the data from moraine boulders are consistent with the step heating results.

The ^{3}He/^{4}He measured in the 1500°C steps of the six samples agree within 2 analytical uncertainties suggesting that the inherited value does not vary substantially between the lithologies measured and the assumption of a uniform inherited value appears valid for the Beardmore Glacier Area. However, the mean inherited ^{3}He/^{4}He measured here may not be appropriate for other quartz rich lithologies; step heating to determine inherited ^{3}He/^{4}He of representative quartz samples will be necessary. The results provide additional evidence that substantial cosmogenic ^{3}He is retained in quartz in the cold climate of Antarctica. The inherited ^{3}He/^{4}He determined here allows calculation of exposure ages on young (<30,000 yr) quartz samples.

Measurement of inherited ^{3}He/^{4}He in pyroxene

The Ferrar Dolerite (176.6±1.8 Ma) (Heimann *et al.*, 1994) occurs as massive horizontal sills and dikes which outcrop along the length of the Transantarctic Mountains (~3000 km) and is the dominant boulder lithology of many moraines. In the Dry Valleys Region (Figure 2.1), the Ferrar consists of 3 massive sills (lower, middle and upper) (McKelvey and Webb, 1962) and many subsidiary dikes. The dolerite is composed primarily of plagioclase and pyroxene. Because pyroxene quantitatively retains helium on million year time scales, the lithology has

great potential for exposure dating in Antarctica. The Ferrar Dolerite has been used to date old (>1 Ma) surfaces in Antarctica using helium and neon isotopes (Bruno *et al.*, 1997; Kurz and Ackert, 1997; Schäfer *et al.*, 1999). In those samples, the cosmogenic component is large and the contribution of the inherited ^{3}He is negligible. However, for late Pleistocene moraines, accurate inherited ^{3}He concentrations are necessary because the cosmogenic contribution is much smaller.

The Ferrar Dolerite is dark gray when freshly exposed but acquires a red-brown stain of iron oxides (desert varnish) within a few thousand years. Dolerite boulders on Holocene moraines typically have some staining and unstained dolerite outcrops are rare. Unstained boulders and bedrock outcrops imply relatively rapid erosion and are assumed here to have little exposure to cosmic rays. Two dolerite outcrops with fresh (unstained) rock exposed were located in the Dry Valleys Region during the 1995-1996 field season. The first outcrop occurs along the upper Taylor Glacier, just east of Arena Valley in the middle sill which intrudes the basement granite complex. The second outcrop was on the headwall of an alpine glacier in the Kukri Hills in the upper sill which intrudes the Beacon Sandstones (Figure 2.3).

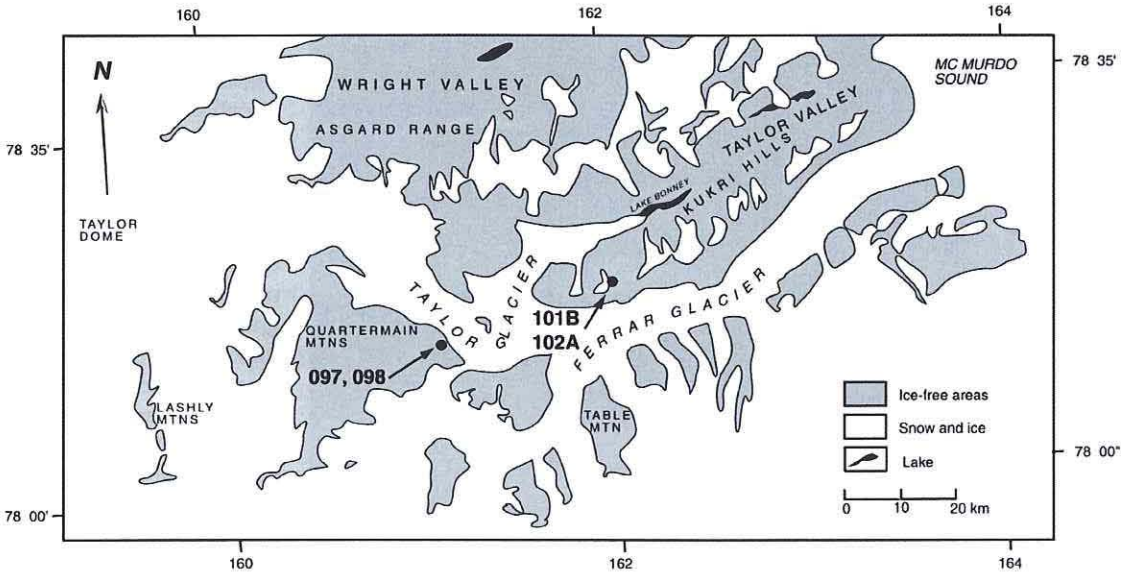

Figure 2.3 Map of the Dry Valleys showing location of the shielded dolerite samples. Location 1: Taylor Glacier (RAK96FF097 and RAK96-098). Location 2: Kukri Hills (RAK96-101B and RAK96-102A). GPS co-ordinates appear in Appendix 2.1.

The first location is at the top of a couloir which extends from the Taylor Glacier margin roughly 100 m from the base of the cliff face (Figure 2.4). At the top of the couloir, an amphitheater shaped outcrop of columnar-jointed dolerite is exposed. The base of the couloir is

covered with fresh (unstained) granite and dolerite talus. The granite exposed in the couloir and the dolerite outcrop at the top are also unweathered. The surficial morphology and lack of weathering indicate recent erosion has exposed fresh rock. Two samples were collected: RAK96-097 is from a flake which had fallen from a low 1 meter overhang and RAK96-098 is from 1 meter inside a narrow crevice formed where the outcrop was failing along joint planes (Figure 2.5). Both samples were well-shielded by the present outcrop geometry. Given evidence for recent cliff retreat (unweathered talus and bedrock), shielding was greater in the past and the field observations suggest complete shielding.

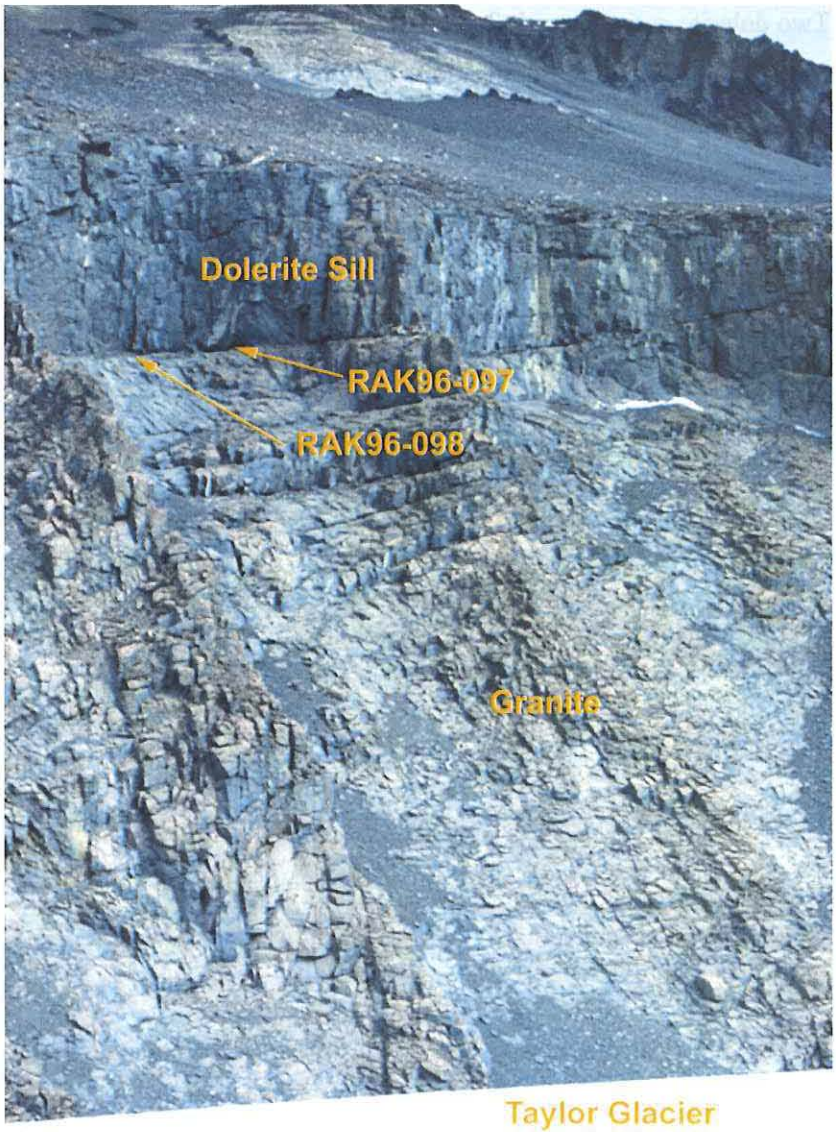

Figure 2.4 Photograph of Location 1 beside the Taylor Glacier. Shielded samples (RAK96-097 and RAK96-098) were collected near the top of the couloir, from the base of the dolerite sill. The gray color of the outcrop indicates the rock has been recently exposed. Relatively rapid erosion is occurring along columnar joints in the dolerite. Relief is ~120 m.

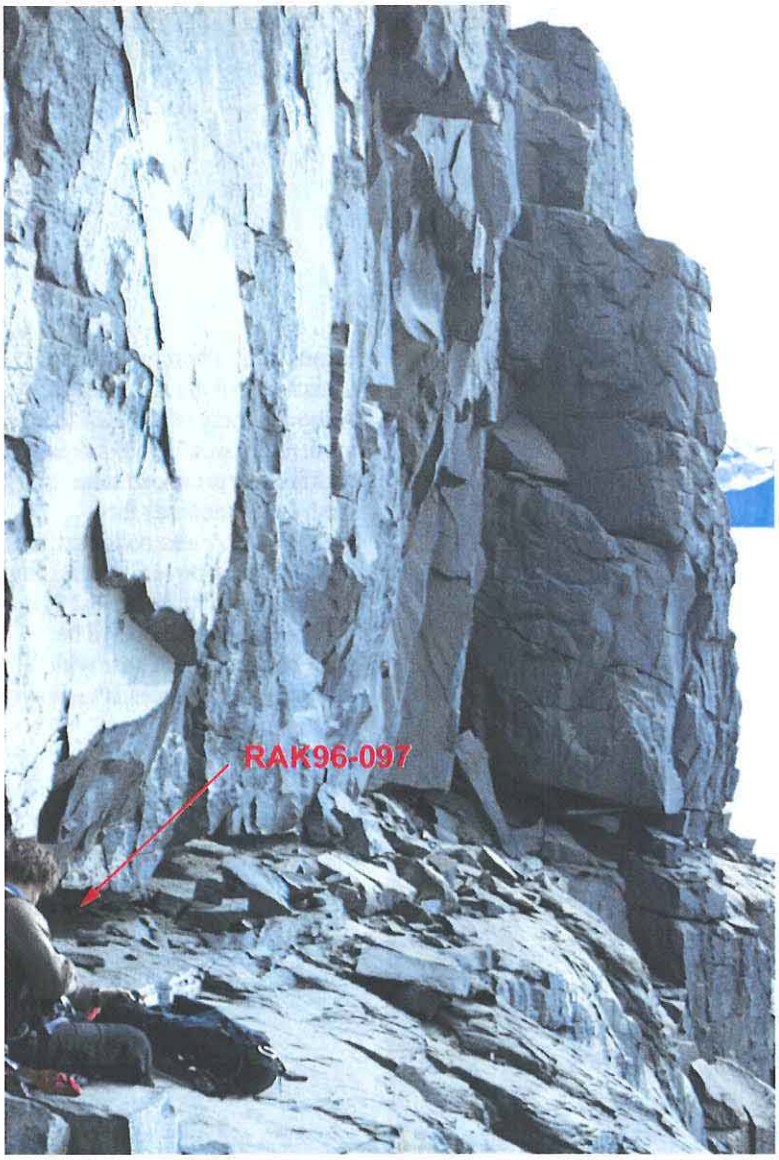

Figure 2.5
Photograph of outcrop at Location 1 beside the Taylor Glacier. RAK96-097 was collected from a block from under the overhang. RAK96-098 was collected from a block >1 m from the outside of a large vertical crack. USAP mountaineer S. Dunbar for scale at lower left.

The outcrop sampled in the Kukri Hills also consisted of columnar jointed dolerite. Large dolerite blocks occur in the talus at the base of a 20 m cliff (Figure 2.6). Both fresh talus blocks and the cliff face were sampled. Sample RAK96-102A from the cliff face was collected from under a small overhang about 40 cm in from the vertical cliff face (Figure 2.7). Sample RAK96-101B was from a greater than 1 m diameter block in the talus. One side had slight staining and is inferred to have been exposed on the cliff face. The sample is from the opposite, unweathered side of the block.

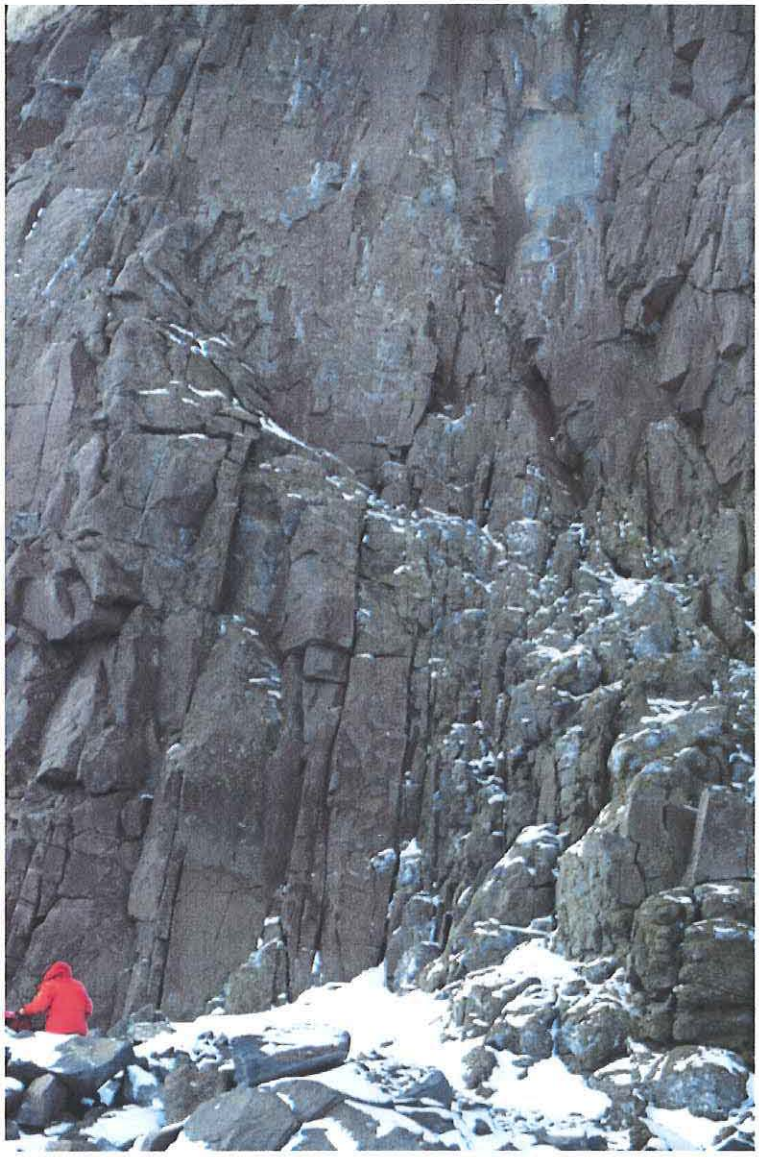

Figure 2.6 Photograph of Location 2 in the Kukri Hills. Although most of the cliff face is moderately weathered, a recent rockfall has produced talus with fresh (unweathered) face. RAK96-102A was collected from the cliff face above field assistant Paul Rappaport. RAK96-101B is from a 1 m talus block. The associated rock fall scar with unweathered surfaces is visible on cliff.

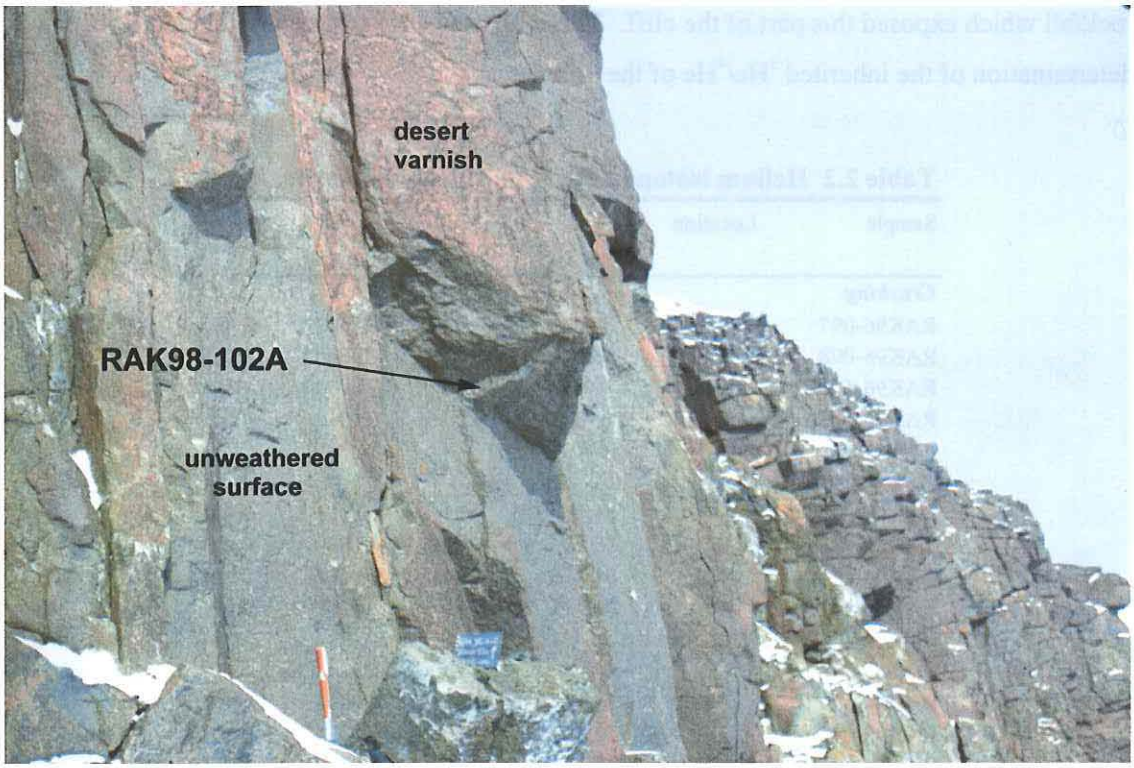

Figure 2.7 Photograph of cliff face at Kukri Hills showing location of RAK96-102A. Sample was collected from beneath the overhang ~40 cm from the cliff face. The less-weathered surface under the overhang indicates the recent fall of ~60 cm thick block.

Helium isotope measurements were made on pyroxene separates crushed *in vacuo* and on the remaining powders melted *in vacuo* following the technique outlined above (see also Chapter 1). Grains of replicate samples were melted *in vacuo* without initial crushing. The results appear in Table 2.2. About 20 percent of the helium from the Taylor Glacier samples was released by crushing. The $^3He/^4He$ of the helium released by crushing is slightly lower than the $^3He/^4He$ of helium released by melting the residual powders, but the measurements agree within 2σ analytical uncertainty. The grains melted without crushing yielded similar $^3He/^4He$ to the melted powders. In contrast, only about 5 percent of the helium was released by crushing the samples from the Kukri Hills and these samples have higher $^3He/^4He$ on crushing (.019 and .035 vs. .006 and .007 R/R_a). The $^3He/^4He$ of melted grains and residual powder are similar. The $^3He/^4He$ of melted whole grains from the talus block is similar to the $^3He/^4He$ of melted whole grains from the Taylor Glacier outcrop, while $^3He/^4He$ measured on the cliff sample (RAK96-102A) was four times higher. The cliff face sample RAK96-102A had a slight red-brown stain (Figure 2.7), indicating some surface weathering and exposure to cosmic rays occurred subsequent to the

rockfall which exposed this part of the cliff. Therefore, the cliff sample is excluded from determination of the inherited $^3He/^4He$ of the dolerite.

Table 2.2 Helium isotope data from shielded dolerite.

Sample	Location	^4He cc/g x 10^{-6}	±1 sig	$^3He/^4He$ R/Ra	±1 sig
Crushing					
RAK96-097	T G	3.11	0.01	0.007	0.002
RAK96-098	T G	3.96	0.01	0.006	0.003
RAK96-101B	K H	1.01	0.00	0.035	0.01
RAK96-102A	K H	0.98	0.07	0.019	0.009
Melted powder					
RAK96-097	T G	14.13	0.03	0.011	0.001
RAK96-098	T G	16.10	0.04	0.008	0.001
RAK96-101B	K H	18.14	0.04	0.012	0.001
RAK96-102A	K H	24.59	0.04	0.04	0.001
Melted grains					
RAK96-097	T G	16.10	0.06	0.0093*	0.0012
RAK96-098	T G	19.05	0.06	0.0075*	0.001
RAK96-101B	K H	21.17	0.07	0.012	0.001
RAK96-102A	K H	22.44	0.09	0.044	0.002
			Weighted mean	**0.010**	**0.001**

Measurements were made on pyroxene mineral separates. R is the measured $^3He/^4He$. Ra is the $^3He/^4He$ of air = 1.384 x 10^{-6}. Sample RAK96-102A has a cosmogenic component and is not used for the weighted mean. * mean of two or more measurements. T G = Taylor Glacier; K H = Kukri Hills.

The data from the Taylor Glacier site and the talus block from the Kukri Hills confirm that there is not a cosmogenic ^4He component. The cosmogenic $^3He/^4He$ as inferred from meteorites is ~0.2 (Mazor *et al.*, 1970). Even if all the ^3He is assumed cosmogenic, the ratio of cosmogenic/inherited ^4He would be about 10^{-8}. Although the measured helium could be a mixture from magmatic and radiogenic sources, it is most likely radiogenic. The dolerite sills probably degassed during slow crystallization and there was ample time (176 Ma) for substantial radioactive production of ^4He. A primarily radiogenic origin is consistent with the very low measured $^3He/^4He$. The weighted mean $^3He/^4He$ of the melted grains from the shielded samples, .010 ± .001 (R/R_a), is the best estimate of the inherited $^3He/^4He$ of the Ferrar Dolerite. This value is similar to the inherited $^3He/^4He$ obtained from step heating of quartz from the Dry Valleys (.011±.004 R/R_a) (Trull *et al.*, 1991), but is about three times greater than the inherited $^3He/^4He$ of quartz measured by step heating quartz from the Beardmore Glacier Area (see above).

The exposure age calculated for the Kukri Hills cliff sample (RAK96-102A) is 44 ka, using an initial $^3He/^4He$ of .010 R/R_a. This is a minimum age estimate, because it does not include shielding due to the vertical orientation of the cliff face or thickness (40 cm) to the cliff face. This result, suggestive of only intermittent cliff erosion by rock falls, is consistent with the lack of evidence for recent rock falls along the cliff (other than at the sample location). The cliff sample was collected near, but not from, the scar on the cliff face related to the sampled talus block. The unweathered surface rock fall scar was not accessible for sampling. The old surface exposure age demonstrates the potential for prior exposure in Antarctica. Almost all debris entering this glacier from the cirque headwall will have some prior exposure to cosmic rays.

Dolerite boulders on last glacial maximum moraines at the Beardmore Glacier (Chapter 4) provide maximum values for inherited $^3He/^4He$. The measured $^3He/^4He$ of three samples ranges from .016 to .059 R/R_a (Table 4.2). The lowest ratio measured in the moraine boulders (.016 R/R_a) places an upper limit on the inherited value because the sample has had exposure to cosmic rays. The calculated surface exposure ages are sensitive the inherited $^3He/^4He$ assumed. When .010 R/R_a is used as the inherited value, the surface exposure ages of the samples with the highest and lowest measured $^3He/^4He$ agree within analytical error. The third sample has a similar age and the calculated ages diverge when higher values are used. The well grouped surface exposure ages obtained when using this inherited $^3He/^4He$ of pyroxene (.010 R/R_a) provide independent evidence that this inherited value is appropriate. The consistency of the surface exposure ages from moraine boulders at the Beardmore Glacier, calculated using the inherited dolerite pyroxene $^3He/^4He$ determined from shielded samples in the Dry Valleys 800 km to the north, indicates that this inherited value is applicable far from the Dry Valleys. This result is consistent with the unusually uniform compositions of the Ferrar Dolerite (Hergt *et al.*, 1991).

Summary

The inherited $^3He/^4He$ of Beacon Sandstone quartz (.003±.0004 R/R_a) was determined by step heating and the inherited $^3He/^4He$ of Ferrar Dolerite pyroxene (.010±.001 R/R_a) was determined from shielded samples. In both cases, the inherited $^3He/^4He$ is very low implying low Li contents of the rocks. In samples with long exposure, all ^3He can be assumed to be cosmogenic. In samples with shorter exposure (measured $^3He/^4He < 0.3$ R/R_a), correction for the inherited component can now be made. The results extend the range of ^3He exposure dating of these common Antarctic lithologies to samples as young as several thousand years.

2.3 Calibration of the ^{3}He production rate over the last 125 kyrs against a ^{40}Ar/^{39}Ar and unspiked K-Ar dated lava flow

Introduction

Over the last decade, surface exposure dating using cosmogenic nuclides has proven to be a powerful new technique for geochronology and geomorphology. A fundamental assumption of the technique is that production rates are well-known. Although considerable progress in calibrating production rates has been made, the uncertainties in the production rates are conservatively estimated to be 10 to 15 percent (Clark *et al.*, 1995; Gillespie and Bierman, 1995; Lal, 1991). In contrast, the analytical uncertainties for measuring ^{3}He are 2 to 3 percent. Production rate uncertainties of this magnitude (10-15%) inhibit the application of surface exposure dating to many fundamental paleoclimate problems. For example, in the 100 kyr age range, the uncertainties are of the same order as the orbital precession half-cycle (~10 kyr). Therefore, it has not been possible to correlate a glacial event dated by surface exposure ages with specific warm or cold events in the marine isotope record. Similarly, on 10 kyr time scales, it has not been possible to correlate dated surfaces with millennial-scale climate events.

The uncertainties in production rates arise from the precision and accuracy of the independent age constraints of the calibration sites, from scaling production rates obtained at calibration sites to sample locations, and from time dependent fluctuations in production rates due to changes in the Earth's magnetic field (Cerling and Craig, 1994b; Clark *et al.*, 1995; Kurz *et al.*, 1990; Sarda *et al.*, 1993). Unless exposure ages are measured near calibration sites, scaling is required because production rates vary with altitude and latitude (Lal and Peters, 1967) (see Chapter 1). Presently, the scaling factors of Lal (1991) are used almost universally by workers in this field. However, the scaling uncertainties are not quantified. Conservative estimates of 10 to 15 percent are commonly used, but they may be lower.

Published ^{3}He calibration surfaces are all less than 18,000 years old (Cerling and Craig, 1994a; Kurz *et al.*, 1990; Licciardi *et al.*, 1999). The production rate at low latitudes should vary over this time interval because variations in the strength of the Earth's magnetic dipole modulates the cosmic ray flux striking the Earth at low latitudes (Clark *et al.*, 1995; Lal and Peters, 1967). Data from Hawaii (Kurz *et al.*, 1990) and Oregon (Licciardi *et al.*, 1999) are consistent with this idea. Thus, the integrated production rate over the last 18 ka may not be the same as the longer-term average. It is important to know if production rates calibrated at younger sites are

appropriate for older surfaces, particularly because the surface exposure dating technique extends far beyond the limit of radiocarbon dating (~45 kyr).

Independent age constraints on calibration surfaces have primarily come from radiocarbon dating. The radiocarbon time scale does not correspond to calendar years due to changes in the global carbon budget and in the production rate of ^{14}C in the atmosphere due to changes in the strength of the Earth's dipole. Although the radiocarbon time scale for the last 20,000 yrs has been calibrated to calendar years (*e.g.,* Stuiver and Reimer, 1993) and is being continuously refined, there is more uncertainty in the older part of the time scale. High precision radiometric dating of lava flows by $^{40}Ar/^{39}Ar$ and unspiked K-Ar methods provide alternative methods of constraining the age of calibration sites. In appropriate samples, ages of ~20 kyr with uncertainties of ± 5 percent are obtainable (Singer *et al.*, 1997). In some K-rich minerals, $^{40}Ar/^{39}Ar$ ages of less than 2000 years have been measured (Renne *et al.*, 1997). Lava flows are ideal sites for calibration studies because there is no possibility of prior exposure to cosmic rays and erosion of the surfaces can be evaluated by the degree of preservation of primary flow morphology. New results presented here show that production rates for ^{3}He obtained from a 125 ± 5 ka Patagonian lava flow are similar to previous estimates scaled from younger sites at lower latitudes. The results imply that the uncertainties in scaling factors of Lal (1991) are less than 5 percent and the production rates calibrated on ~18,000 year old surfaces are similar to long term averages.

Background

Cosmogenic ^{3}He production rates were first determined on Hawaiian lava flows (Kurz, 1986a; Kurz, 1986b). For the purpose of discussion, all production rates are those normalized by Licciardi (1999) by scaling the measured *in situ* production rates to sea level and high latitude (Lal, 1991) and using the same ^{14}C years to calendar years calibration (Stuiver and Reimer, 1993). Based on the youngest and best preserved flows (<2000 yrs), Kurz (1990) determined a production rate of 195 ± 30 atoms/g/yr. Measured production rates were 76 ± 6 atoms/g/yr between 2000 and 7000 years ago and 138 ± 6 atoms/g/yr between 7000 and 15,000 years ago. Cerling (1990) measured a production rate of 121 ± 4 atoms/g/year on the Tabernacle Hill lava flow which erupted into the well-dated (17,800 yr) Provo shore line of glacial Lake Bonneville, Utah. Subsequently, Cerling and Craig (1994a) presented data from lava flows at other locations and ages which support the estimate from the Tabernacle flow, but the independent ages of the

surfaces were not as well constrained. The published ^{3}He production rate in olivine (115±4 atoms/g/year) of Cerling (1994a) has been widely adopted.

Cerro Volcán (46° 45' S, 70° 45' W) is located in Patagonia, east of the Andes near Lago Buenos Aries (Figure 2.8). The region lies in the belt of the prevailing westerlies and in the rain shadow of the Andes. As a result, the climate is extremely arid and cool. Winter snow cover is rare. Cerro Volcán is a basaltic cone reaching 660 m above sea level (Figure 2.9). Lavas emanating from the cone and adjacent fissures were first mapped by Caldenius (1932). The flows cover ~70 km^2 and overlie glacial outwash and moraines deposited by Pleistocene expansions of the Patagonian ice fields. Parts of the flow descend into Cañadon del Deseado where the most distal parts are covered by late Pleistocene (LGM) outwash (Figure 2.10).

Figure 2.8 Location map of Patagonia. Cerro Volcán lies near Lago Buenos Aires on the dry eastern side of the Andes in Patagonia. The lava flows overlie late Pleistocene moraines and outwash deposited during expansions of the Northern Patagonian Ice Field.

Figure 2.9 Photograph of Cerro Volcán to the northwest, taken from a light aircraft. Lago Buenos Aires and the snow-covered Andes can be seen in the background. The flows cover ~70 km^2 and were deposited during a single eruptive event.

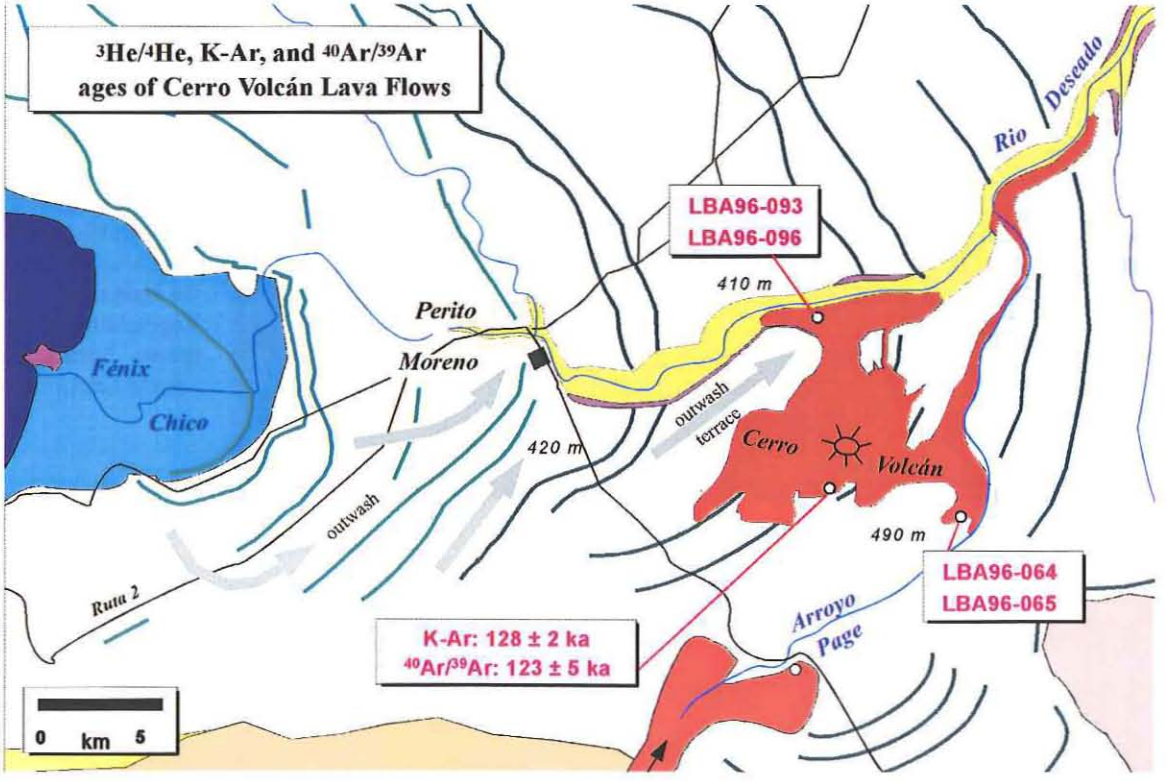

Figure 2.10 Geologic sketch map of Cerro Volcán and surrounding area. Red indicates lava flows, green lines are moraines, bright yellow is outwash from the last glacial maximum, and light yellow is older outwash. Sample locations are marked. GPS coordinates appear in Appendix 2.1.

The lava flows are extremely well-preserved and very sparsely vegetated. The surface morphology is characterized by ropey pahoehoe structures and pressure ridges with up to 4 m relief. The summits of the pressure ridges typically have a crack up to 2 m wide and 1.5 m deep which follows the axis of the ridge (Figure 2.11). The walls of the cracks expose layers of basalt 15 to 20 cm thick which emanated from the crack (Figure 2.12). The vesicular lava is alkali basalt with large (1 to 2 mm) clinopyroxene (cpx) and smaller olivine and plagioclase (0.5-1 mm) in a glassy matrix. The lithology is similar in all locations examined, including a transect to the summit of the cone. The lavas appear to have been emplaced during a single eruptive event. There is no evidence for past cover by loess within the local region. Rather than aeolian deposition, persistent high winds have left a desert pavement in many places.

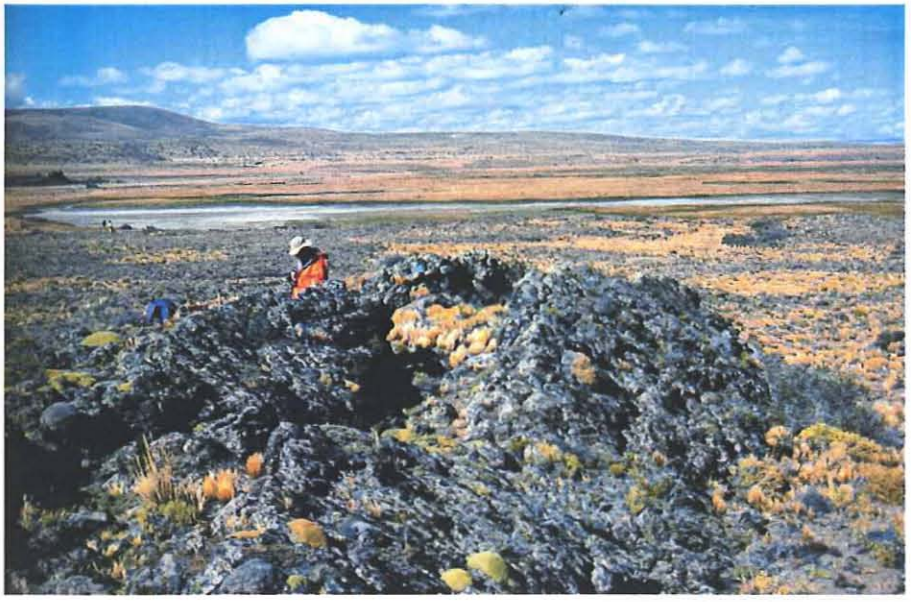

Figure 2.11 Photograph of pressure ridge on Cerro Volcán lava flow. The pressure ridges are typically 1 to 4 m high with a large crack along the center. Vegetation is very sparse. Location of sample LBA98-064.

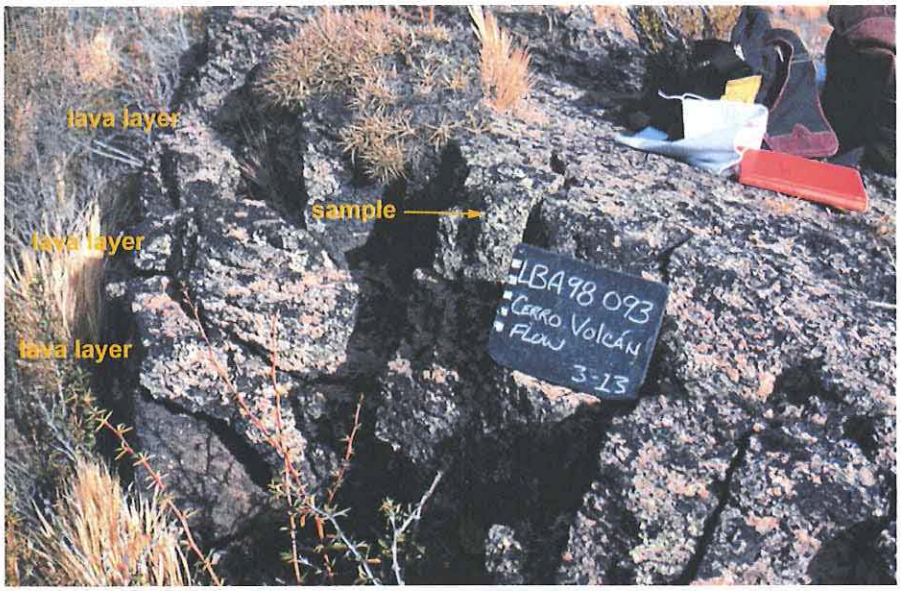

Figure 2.12
Photograph of inner wall of crack in pressure ridge showing three lava layers. Scale bars on chalkboard are 1 cm. The lava layers are about 20 cm thick.

Mercer (1982) reported an imprecise whole rock K-Ar date of 177 ± 56 ka from the Cerro Volcán lava flow. Ton-That (1997) obtained an $^{40}Ar/^{39}Ar$ date of 4.3 ± .7 Ma on a plagioclase separate, but concluded from the strongly discordant age spectrum and field relationships that excess argon was present in the sample and that excess argon may also have affected the whole rock date of Mercer. Subsequently, Guillou (1997) determined two high precision, unspiked K-Ar dates on matrix glass separates with a weighted mean age of 128 ± 4 (Figure 2.13). This technique calibrates the ^{40}Ar peak height measured in the mass spectrometer with an air standard, removing uncertainties associated with addition of an isotope spike, which can be large with young samples (Guillou *et al.*, 1996). Successful dating of matrix glass by K-Ar prompted Singer (1998) to make $^{40}Ar/^{39}Ar$ measurements on matrix glass of the basalt. This experiment yielded a well-defined plateau with a weighted mean age of 123 ± 5 (Figure 2.13). The inverse isochron age calculated from the data was 116 ± 16. The relatively high uncertainty in the isochron age was due to the small spread in measured $^{40}Ar/^{39}Ar$ ratios and the plateau age is considered a better age estimate. Concordance of the two independent methods is good evidence that the ages are accurate. The average (excluding the inverse isochron age) of these analyses, (125.5 ± 3.5 ka) is used for calibration of the ^{3}He production rate.

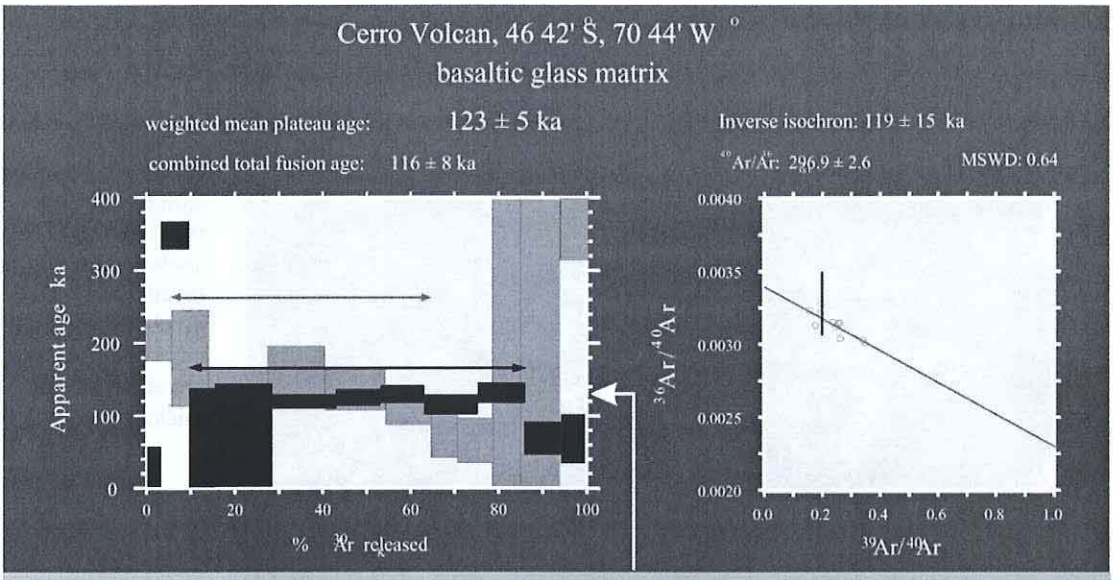

Unspiked K-Ar measurements:

K (wt.%)	weight (g)	Ar^{*} (%)	$^{40}Ar^{*}$ (10^{-12} mol/g)	Age (ka) ± 1mean age	weighted
2.170 ± 0.022	0.79914	1.341	4.913	131±3	128±2
	0.85804	1.169	4.693	125±3	

Figure 2.13 $^{40}Ar/^{39}Ar$ and unspiked K-Ar data for Cerro Volcán lava flow. Upper panel shows release pattern and well defined plateau from $^{40}Ar/^{39}Ar$ step heating experiment and inverse isochron plot. Lower panel shows data from unspiked K-Ar measurements. The figure is from Singer *et al.* (1998).

Methods

Samples for surface exposure dating were collected with hammer and chisel from the upper edge of cracks at the top of pressure ridges (Figure 2.12). In some sites, exfoliation of the uppermost lava layer has exposed lower layers which retain typical surface flow morphology. The samples were collected where the surface of the sampled basalt layer was continuous over at least several square meters. Several samples, less than 100 m apart, were collected at two locations about 10 km apart with an elevation difference of ~80 m (Figure 2.10). The southernmost samples were near the location of the $^{40}Ar/^{39}Ar$ samples (Figure 2.10). Measurements were made on two samples from separate outcrops from each location. Olivine and clinopyroxene (cpx) were separated by hand picking after crushing and sieving. The two samples from the northern location were also analyzed for ^{36}Cl.

Helium isotopes were measured in the cpx and olivine mineral separates on the helium mass spectrometer at the Woods Hole Oceanographic Institution using previously described

techniques (Kurz, 1986b; Kurz *et al.*, 1996). Cosmogenic ^{3}He concentrations were determined as outlined in section 2.1 (see also Chapter 1). Cosmogenic ^{36}Cl was measured on AgCl targets prepared from hand picked 1 to 2 mm whole rock fractions at PRIME lab, Purdue University. Measurement of ^{36}Cl allows evaluation of the assumption of no erosion and provides a test of the ^{36}Cl production rates used. Because ^{36}Cl is produced by spallation on Ca, K and neutron capture on ^{35}Cl, the cosmogenic ^{36}Cl concentration is dependent on the concentration of the target elements as well as the length of exposure. Major element composition was measured by XRF. The trace elements B, Gd and Sm, which have high neutron absorption cross sections and compete for neutrons with ^{35}Cl, were measured by prompt gamma (B and Gd) and NAA (Sm). The major and trace element measurements were made at XRAL Laboratories, Don Mills, Ontario, Canada. Major and trace elements were measured in olivine and cpx by electron probe at MIT.

Determination of the ^{3}He production rate

The helium isotope data from the Cerro Volcán Lava flow appear in Table 2.3. The ^{4}He released by crushing the cpx is ~100 times lower than that released by crushing olivine. The difference probably results from the lower concentration of fluid and melt inclusions in the cpx compared to olivine. Due to the relatively small amount of helium released, the ^{3}He/^{4}He measured on crushing the cpx is variable but agrees with the values obtained from olivine within relatively large uncertainties. It is reasonable to assume the inherited (trapped magmatic) ^{3}He/^{4}He is the same for both minerals. The average obtained from crushing olivine (7.7 ± 0.15 R/R_a; R_a is the ^{3}He/^{4}He of air = 1.384×10^{-6}) was used to correct for the inherited ^{3}He in the cpx samples (Chapter 1) (Kurz, 1986b). The cosmogenic ^{3}He concentration in the two olivine and cpx separates from each location agree within analytical error. However, at each location, the sample that has higher (or lower) cosmogenic ^{3}He in olivine also has the higher (or lower) cosmogenic ^{3}He in cpx when compared to the other sample from the location (Table 2.3). This pattern, which persists in the scaled production rates of all four samples, suggests that the differences are not due to random analytical error alone, but actual (small) differences in the exposure of the samples. The pattern also suggests that the estimates of analytical uncertainty are conservative.

Table 2.3 Helium isotope data from Cerro Volcán

sample	depth (cm)	density g/cm^2	Elev. (m)	^{4}He (crush) cc/gram	±1 sig x 10^{-10}	3/4 (crush) R/Ra	±1 sig	^{4}He (melt) cc/gram	±1 sig x 10^{-10}	3/4 (melt) R/Ra	±1 sig	^{3}He cosmo atm/g	±1 sig x 10^6
clinopyroxene													
LBA-98-064	1.5	2.4	490	2.29	0.02	2.52	1.32	35.6	0.03	183	1	23.2	0.1
LBA-98-065	1.8	2.3	490	3.44	0.04	5.07	1.92	30.6	0.04	219	2	24.1	0.2
LBA-98-093	1.8	2.2	410	6.42	0.06	6.03	1.00	24.2	0.04	245	2	21.3	0.1
LBA-98-096	2.3	2.3	410	66.5	0.4	7.13	0.16	29.0	0.04	208	2	21.6	0.2
olivine													
LBA-98-064	1.5	2.4	490	109	3	7.47	0.17	75.0	0.2	96.7	0.9	24.9	0.3
LBA-98-065	1.8	2.3	490	354	5	7.81	0.10	73.0	0.1	101	1	25.4	0.2
LBA-98-093	1.8	2.2	410	160	1	7.75	0.10	67.3	0.1	95.5	0.5	22.0	0.1
LBA-98-096	2.3	2.3	410	172	2	7.68	0.07	30.6	0.1	206	2	22.6	0.2

R is the measured ^{3}He/^{4}He of the sample. Ra is the ^{3}He/^{4}He of air = 1.384 x 10^{-6}.

The calculated production rates using an age of 125.5 ± 3.5 ka for the lava flow and assuming no erosion appear in Table 2.4. The measured *in situ* production rate is scaled to the surface value using the exponential relationship of production rate with depth determined from drill cores (Kurz, 1986b) (Chapter 1). When the *in situ* production rates are scaled to sea level and high latitude using the polynomial formulation of Lal (1991), the measured ^{3}He production rates for each mineral agree within the 2 σ propagated analytical uncertainties. This result supports the assumption of very low erosion rates; if erosion rates were significant, it is unlikely that the erosion rates would be uniform as required by the similar ^{3}He concentrations. The mean ^{3}He production rate is 123 ± 3 atoms/g/yr in clinopyroxene and 129 ± 4 atoms/g/yr in olivine (scaled to high latitude and sea level).

Table 2.4 ^{3}He production rates at Cerro Volcán

	^{3}He atom/g	± 1 sig x 10^6	Prod rate* *in situ* atom/g/yr	± 1 sig	Prod Rate** *scaled* atom/g/yr
olivine					
LBA-98-064	24.9	0.3	203	6	130
LBA-98-065	25.4	0.2	207	6	133
LBA-98-093	22.0	0.1	179	5	124
LBA-98-096	22.6	0.2	186	5	128
			Mean production rat		**129±4**
clinopyroxene					
LBA-98-064	23.2	0.1	189	5	121
LBA-98-065	24.1	0.2	197	5	127
LBA-98-093	21.3	0.1	174	5	120
LBA-98-096	21.6	0.2	178	5	123
			Mean production rat		**123±3**

**In situ* production rate calculated using 125.5±3.5 ka as eruption age of the flow.

***Production rate scaled to sea level and high latitude (Lal, 1991).

Although the difference in altitude is only ~80 m, the dependence of production rate on altitude is apparent in the significant difference in the ^{3}He production rates between the two sample sites. Because the error introduced by scaling is systematic, propagation of the scaling uncertainty is unnecessary for comparison of samples from the two locations. The normalized ^{3}He concentrations from the southern sampling site (LBA98-064 and 065) are slightly higher than the northern site for both olivine and cpx. The slight offset between the sites could be due to error in the relative elevations (~10 m), slight erosion or analytical error. Although the scaling of Lal (1991) incorporates both latitude and altitude effects, in this case, the scaling largely reflects the effect of altitude; the scaling from latitude 46° to 60° is only 1.5 percent. These results suggest that the error in the scaling for altitude is of the same order as the errors in the measurements and calibration ages (~5%). Previous studies have shown the Lal (1991) scaling accurately predicts the effects of altitude (Zreda and Phillips, 1994). Concordant production rates are also obtained from using a simple exponential scaling for altitude (Chapter 1) (Kurz and Brook, 1994).

The ^{3}He production rate is weakly dependent on composition; average chemical compositions obtained by electron microprobe of eight olivine and eight cpx grains (two per sample) appear in Table 2.5. ^{3}He is produced by spallation reactions with all common rock forming elements. In common silicate minerals, differences in ^{3}He production rates are largely due to variations in Fe and Ca concentrations. Production of ^{3}He by spallation on Fe or Ca is about half that of other common elements in silicates (Table 2.5). Theoretical estimates of elemental production rates (Lal, 1991; Masarik and Reedy, 1995; Masarik and Reedy, 1996) (Table 2.5) suggest that variations in the ^{3}He production rate of typical olivine and cpx is less than 10 percent. Measurements of ^{3}He in olivine and cpx from the same sample (Table 2.3; see also Table 3.1) support this conclusion.

Table 2.5 Major element composition and theoretical ^{3}He production rates from Cerro Volcán

	Si	Ti	Al	Cr	Fe	Mn	Mg	Ca	Na	O	^{3}He production rate atom/g/yr
clinopyroxene											
weight fraction	0.217	0.017	0.043	0.002	0.052	0.001	0.076	0.161	0.004	0.428	
production rate	24.1		4.6		2.1		8.8	9.8		57.8	**107.1**
olivine											
weight fraction	0.185	0.0001	0.0001	0.0003	0.111	0.002	0.274	0.002	0.0004	0.425	
production rate	20.6		0.01		4.4		31.8	0.1		57.4	**114.3**
elemental production rate	111.0		107.0		40.0		116.0	61.0		135.0	

The weight fractions are the mean of electron microprobe measurements of four to five spots on two mineral grains from each sample (n ≥32). The elemental production rates (atom/g-element/yr) are from Masarik and Reedy (1996).

Masarik (1995) used Monte Carlo simulations to model the spectra of cosmic ray neutron fluxes at the Earth's surface with an estimated error of ~8 percent. Production rates were determined by integrating the product of the flux and experimental and evaluated elemental cross sections over the energy spectrum. This approach has been tested against production rates measured in lunar samples and meteorites (Masarik and Reedy, 1994). Although the neutron cross-sections are estimated from proton data and the cosmic ray flux in the lunar samples and meteorites is largely protons, the model results agree well with published terrestrial production rates. Uncertainties in the theoretical production rates are estimated to be 10 to 20 percent. In contrast, the elemental production rates of Lal (1991) are consistently lower than measured production rates. The relative difference in production rates for different mineral compositions is likely more accurate than the absolute production rates because errors in the calculations are systematic. Lal (1991) suggested that the elemental production rates could be used to scale calibrated production rates to different mineral compositions.

The ^{3}He concentration measured in olivine at Cerro Volcán is consistently ~5 percent higher than that of cpx from the same sample (Table 2.3). This offset is consistent with the compositional dependence of the production rate predicted by the theoretical models. Theoretical ^{3}He production rates for the olivine (Fo_{85}) of 114 atoms/g/yr and 107 atoms/g/yr for the cpx are calculated using the elemental production rates of Masarik and Reedy (1996) and the chemical composition of the minerals (Table 2.5). Although the calculated production rates underestimate those measured, the difference (~6%) between the olivine and cpx is similar to that observed, suggesting that scaling ^{3}He production rates for composition using theoretical elemental production rates is a valid approach. This technique is adopted in Chapter 4 to scale the Cerro Volcán production rates for quartz and pyroxene, but additional calibrations are needed.

Evaluation of erosion rates using ^{36}Cl

The ^{3}He production rates (Table 2.4) calculated from the Cerro Volcán data assume no erosion of the lava flow surface. If some erosion has occurred, the ^{3}He production rate will be underestimated. The assumption of no erosion was based on the well-preserved lava flow morphology and careful choice of sample location and is supported by the similar production rates determined from each sample. The assumption of no erosion was further evaluated by measuring cosmogenic ^{36}Cl in two samples (LBA98-093 and 096). If the age of the surface is known, one cosmogenic isotope (with a known production rate) can be used to constrain the erosion rate (Gillespie and Bierman, 1995). ^{36}Cl is well-suited to phenocryst-poor rocks such as basalt because it can be measured in whole rocks.

In theory, ^{36}Cl is well-suited to evaluating erosion rates. In practice, large uncertainties limit the resolution of the technique. Erosion increases the apparent (zero erosion) age of Cl-rich samples because the production rate of ^{36}Cl produced by neutron capture ($^{36}Cl_{nc}$) reaches a maximum within the upper 10 to 20 cm (Liu *et al.*, 1994). The $^{36}Cl_{nc}$ production rate increases with depth because some thermal neutrons produced within the uppermost 10 to 20 cm (stopping distance of thermal neutrons in rock) escape into the atmosphere before interacting with ^{35}Cl (Chapter 1). Cosmogenic ^{36}Cl ages older than a surface of known age would be unambiguous evidence for erosion.

The ^{36}Cl data appear in Table 2.6. Erosion dependent exposure ages were calculated using both the CHLOE program (Phillips and Plummer, 1996) and RICH program (rich@primelab.physics.purdue.edu). The zero erosion CHLOE ages are consistently older than the RICH ages by about 5 percent. The RICH output includes propagated 1σ analytical errors; the uncertainties in the CHLOE ages are estimated at 10 percent. The zero erosion ^{36}Cl ages of the two samples overlap within the 2σ analytical uncertainties in both age models (Table 2.6). The eruptive age of the flow (125.5 ± 4 ka) falls within the overlap. The large spread in the ^{36}Cl ages is due to the large analytical uncertainties in ^{36}Cl measurements which at 2σ are ~20 percent. The reason for the high uncertainties is due to poor counting statistics in the AMS.

Table 2.6 ^{36}Cl data and exposure ages from Cerro Volcán

Sample	K_2O %	CaO %	Cl (ppm)	Abs. X-sect. cm^2/kg	$^{36}Cl/Cl$ x 10^{-15}	RICH Age (kyr)	CHLOE Age (kyr)
LBA98-093	1.66	7.36	316	8.7	376	145 ± 15	153 ±15
LBA98-096	1.5	7.29	354	8.6	506	110 ±11	114 ± 11

Abs. X-sect. is the macroscopic absorption cross section of the rock.
Exposure ages were calculated assuming no erosion and no correction for outcrop geometry.

The erosion dependent RICH ^{36}Cl ages and the radiometric ages are plotted in Figure 2.14. The ^{36}Cl exposure ages are not strongly dependent on the erosion rate. Although the data are consistent with no erosion, the data are also consistent with high (>5 mm/kyr) erosion rates. Sample LBA98-096 apparently falls within the tail of the probability distribution of the counting statistics because a zero erosion ^{36}Cl age should be equal to (no erosion) or greater than (low erosion) the radiometric age of the flow. However, this interpretation is probably not correct because the ^{36}Cl ages have been calculated assuming a flat surface. On rough surfaces (on scales of 10's of cm) neutrons can escape the rock horizontally as well as vertically. This decrease in neutron flux and $^{36}Cl_{nc}$ production rate results in underestimates of the exposure age. A correction for outcrop geometry is probably required because the samples were collected at the edges of cracks on the top of pressure ridges (Figure 2.11) (Zreda *et al.*, 1993).

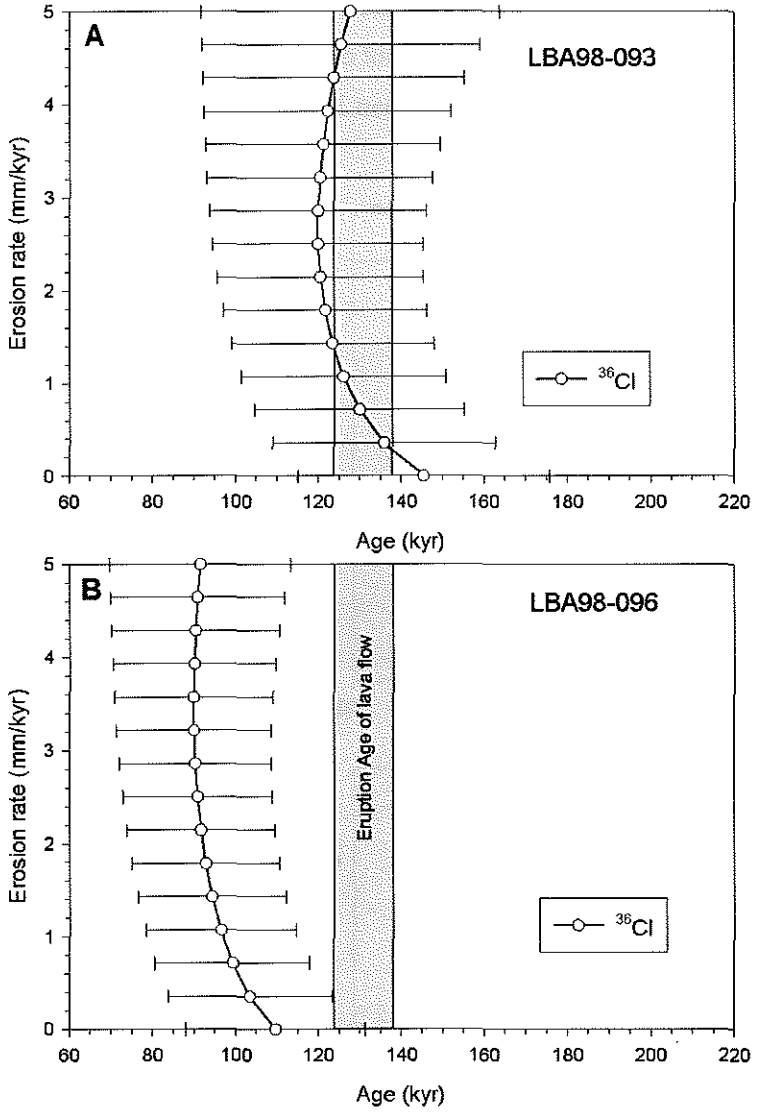

Figure 2.14 ^{36}Cl surface exposure ages calculated by RICH program plotted as function of erosion rate. Gray region is the eruption age determined by unspiked K-Ar and ^{40}Ar/^{39}Ar. Permitted ages and erosion rates fall within the area of overlap of the two data sets. Uncertainties are 2 sigma. A) The erosion rate is not constrained by the data. B) The erosion rate is constrained to less than 0.8 mm/kyr, but the position of the curve to the left (younger) of the eruptive age of the flow suggests a systematic error in the ^{36}Cl ages.

The input to the CHLOE program includes a scaling factor that adjusts the ^{36}Cl production rate based on outcrop geometry. A 30 percent decrease in the neutron flux for a pyramid shaped structure relative to a flat surface was measured by Fabryka-Martin (1990). The geometry of the sample sites is approximated by an angular ridge (Figure 2.12). The reduction in the sub-surface neutron flux for this geometry is estimated to be 20 percent. CHLOE ages, adjusted for outcrop geometry and with 20 percent (~2σ) uncertainties are plotted in Figure 2.15. The geometry scaling factor increases the zero erosion age of sample LBA98-096 from 114 ka to 127 ka and results in a reasonable (older) zero erosion age. The same correction is made to

LBA98-093 which has similar geometry. The greater curvature of the age-erosion rate curves compared to the RICH output results from a different treatment of the $^{36}Cl_{nc}$ production. The data from sample LBA98-093 constrains the erosion rate to less than 3.5 mm/kyr in this model.

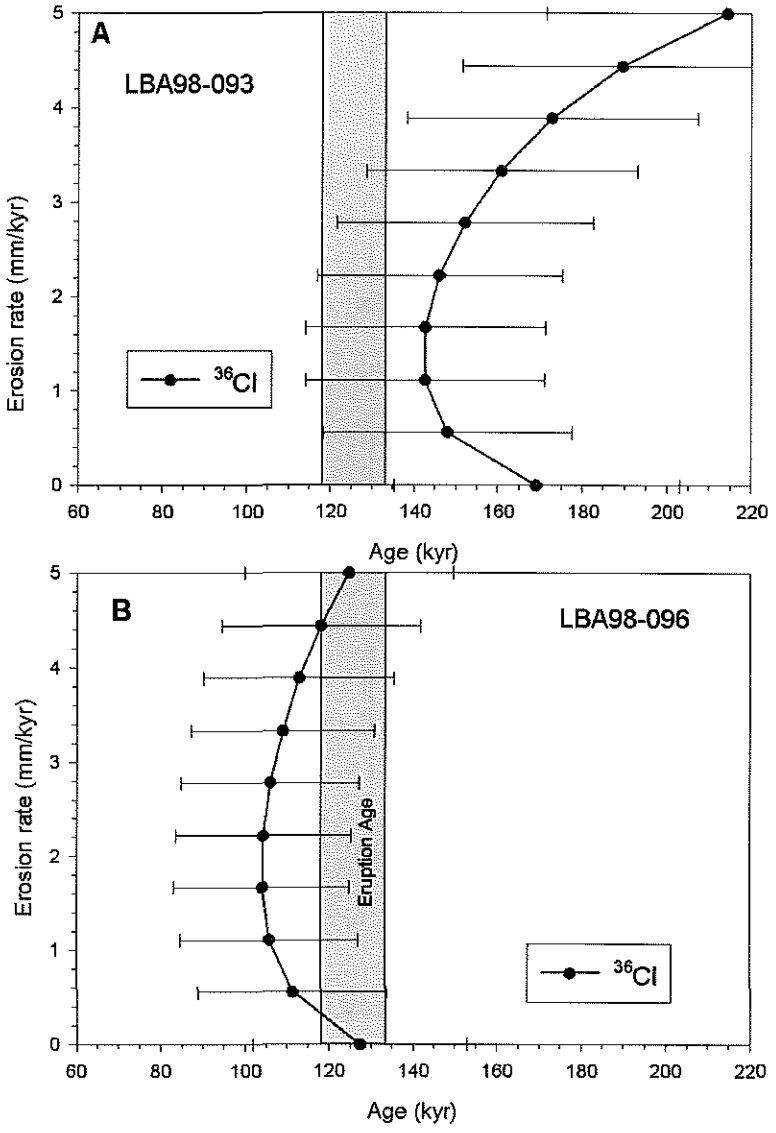

Figure 2.15 ^{36}Cl surface exposure ages calculated by CHLOE program plotted as function of erosion rate. The calculations include the effects of outcrop geometry on ^{36}Cl production rate. The greater curvature of the plots results from different treatment of production of ^{36}Cl by neutron capture. The curves are shifted to the right (older) compared to those in Figure 2.14. Gray region is the eruption age determined by unspiked K-Ar and ^{40}Ar/^{39}Ar. Permitted ages and erosion rates fall within the area of overlap of the two data sets. Plotted uncertainties are 20%. A) Erosion rates are constrained to between 0.2 and 3.6 mm/kyr. B) Erosion rates are not constrained.

In summary, the ^{36}Cl data are compatible with the low erosion rates inferred from the geomorphology but do not independently confirm them. The failure to do so stems from the uncertainties in the ^{36}Cl measurements, uncertainties in the correction for outcrop geometry and from the fact that there is not consensus on the calculation of $^{36}Cl_{nc}$ production rates. It should be

possible to improve the resolution of the technique. The uncertainties in the ^{36}Cl measurements could be improved by increasing the measurement time on the AMS (improved counting statistics) and replicate samples. Uncertainties due to outcrop geometry could be minimized and evaluated by samples collected with simpler (flat) geometries. ^{36}Cl measurements on surfaces of known age and erosion rates such as Cerro Volcán could then be used to evaluate the age models.

2.4 Discussion

The integrated ^{3}He production rates determined over the last 125 ka at Cerro Volcán (129 ± 4 atoms/g/yr in olivine) fall between those determined from younger calibration surfaces at low and mid latitudes (Cerling, 1990; Cerling and Craig, 1994a; Kurz, 1986b; Kurz *et al.*, 1990), when the published ^{3}He production rates are scaled to high latitude and sea level and an updated conversion of ^{14}C to calender years is used (Licciardi *et al.*, 1999). Both the average ^{3}He production rate determined from Hawaiian lava flows between 7000 and 15,000 years old (138 ± 6 atoms/g/yr) (Kurz *et al.*, 1990) and the ^{3}He production rates (121 ± 3 atoms/g/yr) determined at the Tabernacle Hill lava flow (Cerling, 1990) agree within 2σ uncertainties with the value obtained here. However, the data suggest that the ^{3}He production rate at Cerro Volcán is slightly higher than at Tabernacle Hill.

Production rates of cosmogenic nuclides determined from calibrated surfaces integrate over the entire exposure period. At latitudes less than 60°, fluctuations in production rates have occurred over the last 8000 years, most likely due to changes in the strength of the magnetic dipole (Kurz *et al.*, 1990; Licciardi *et al.*, 1999). These results indicate that high latitude sea level production rates scaled from 15 to 18 ka surfaces at low and mid latitudes are within 10 percent of the long term average. Models based on paleomagnetic intensity records suggest that production rates determined at 15 to 18 ka and 125 ka will be similar (Clark *et al.*, 1995). The revised production rate obtained from the Tabernacle Hill lava flow (Cerling, 1990; Cerling and Craig, 1994a) is probably a better estimate of the ^{3}He production rate at 18 ka than the Hawaiian data because the eruption age of the flow is better determined and the Hawaiian production rate is an average over a period of substantial magnetic intensity changes.

The results also provide verification that the scaling of Lal (1991) is substantially correct although it is remotely possible the production rates at 18 ka and 125 ka only appear consistent because of a compensatory inaccuracy in the scaling parameters. The scaling factors of Lal (1991) are based on the Standard Atmosphere and may not be appropriate in areas of anomalous

average atmospheric pressure (Stone, 1999). At present, the calibration sites do not lie in anomalous areas and average pressure at the sites only deviates from the Standard Atmosphere by about 2 percent. Based on present values, which probably characterize interglacial conditions, production rates in Patagonia are predicted to be slightly higher (~4%) than those in Utah. During glacial conditions production rates in Patagonia could be higher as the strong gradient in atmospheric pressure associated with the circumpolar circulation migrates north with the polar front.

The ^{3}He production rate determined at Cerro Volcán substantially reduces the uncertainties in exposure ages attached to ^{3}He production rates and to scaling factors. The uncertainties resulting from scaling have previously been conservatively assumed to be 10 to 15 percent (Lal, 1991). These results are particularly applicable to Antarctica where surface exposure ages are often much older than those of the published calibration sites and where scaling of production rates from low-middle latitude was required. Scaling to high latitude (>60°) from Cerro Volcán at 46° S latitude is only 1.5 percent. The older age of the calibration surface provides a better estimate of long term averages and can be applied with greater confidence to old samples. Fluctuations of the production rate due to variations in field strength are minimal so the Cerro Volcán production rate is also applicable to young (high latitude) samples and provides a baseline for correcting production rates at mid to low latitudes for variations in the magnetic field. The ^{3}He production rate of 123 ± 3 atoms/g/yr measured in clinopyroxene from the Cerro Volcán lava flow and scaled for chemical composition is used in Chapters 4 and 5. The uncertainty in the ^{3}He production rate at high latitude is estimated to be less than 5 percent.

References

Brook, E.J., and Kurz, M.D., 1993, Surface-exposure chronology using *in situ* cosmogenic ^{3}He in Antarctic quartz sandstone boulders: *Quaternary Research*, **v. 39**, p. 1-10.

Brown, E.T., Edmond, J., Raisbeck, G.M., Yiou, F., Kurz, M.D., and Brook, E.J., 1991, Examination of surface exposure ages of Antarctic moraines using *in-situ* produced ^{10}Be and ^{26}Al: *Geochimica et Cosmochimica Acta*, **v. 55**, p. 2269-2283.

Bruno, L.A., Baur, H., Graf, T., Schlücter, C., Signer, P., and Wieler, R., 1997, Dating of Sirius Group tillites in the Antarctic Dry Valleys with cosmogenic ^{3}He and ^{21}Ne: *Earth and Planetary Science Letters*, **v. 147**, p. 37-54.

Caldenius, C.G., 1932, Las glaciaciones Cuaternarias en la Patagonia y Tierra del Fuego: *Geografiska Annaler*, **v. 14**, p. 1-164.

Cerling, T.E., 1990, Dating Geomorphic Surfaces Using Cosmogenic ^{3}He: *Quaternary Research*, **v. 33**, p. 148-156.

Cerling, T.E., and Craig, H., 1994a, Cosmogenic ^{3}He production rates from 39°N to 46°N latitude, western USA and France: *Geochimica Cosmochimica Acta*, **v. 58**, p. 349-255.

Cerling, T.E., and Craig, H., 1994b, Geomorphology and *in-situ* cosmogenic isotopes: *Annual Review of Earth and Planetary Science*, **v. 22**, p. 273-317.

Clark, D.H., Bierman, P.R., and Larsen, P., 1995, Improving *in situ* cosmogenic chronometers: *Quaternary Research*, **v. 44**, p. 367-377.

Elliot, D.H., Barrett, P.J., and Mayewski, P.A., 1974, Reconnaissance geologic map of the Plunket Point Quadrangle, Transantarctic Mountains, Antarctica: Washington, D. C.: U. S. Government Printing Office, U. S. Geological Survey.

Fabryka-Martin, J.F., Fowler, M.M., and Biddle, R., 1990, Study of neutron fluxes underground, Los Alamos National Laboratory.

Friedlander, G., Kennedy, J.W., Macias, E.S., and Miller, J.M., 1981, *Nuclear and Radiochemistry*: New York, Wiley, 684 p.

Gillespie, A.R., and Bierman, P.R., 1995, Precision of terrestrial exposure ages and erosion rates estimated from analysis of cosmogenic isotopes produced *in situ*: *Journal of Geophysical Research*, **v. 100**, p. 24,637-24,649.

Graf, T., Kohl, C.P., Marti, K., and Nishiizumi, K., 1991, Cosmic-ray produced neon in Antarctic rocks: *Geophysical Research Letters*, **v. 18**, p. 203-206.

Guillou, H., Carrcedo, J.C., and Torrado, P., 1996, K-Ar ages and magnetic stratigraphy of a hot spot-induced, fast growing oceanic island: El Hierro, Canary Islands: *Journal of Volcanology and Geothermal Research*, **v. 73**, p. 141-155.

Guillou, H., and Singer, B.S., 1997, Combined Unspiked K-Ar and ^{40}Ar-^{39}Ar dating of Late Quaternary lavas: *Eos, transactions, AGU*, **v. 78**, p. F771.

Heimann, A., Fleming, T.H., Elliot, D.H., and Foland, K.A., 1994, A short interval of Jurassic continental flood basalt volcanism in Antarctica as demonstrated by $^{40}Ar/^{39}Ar$ geochronology: *Earth and Planetary Science Letters*, **v. 121**, p. 19-41.

Hergt, J.M., Peate, D.W., and Hawkesworth, C.J., 1991, The petrogenesis of Mesozoic Gondwana low-Ti flood basalts: *Earth and Planetary Science Letters*, **v. 105**, p. 134-148.

Kurz, M.D., 1986a, Cosmogenic helium in a terrestrial igneous rock: *Nature*, **v. 320**, p. 435-439.

Kurz, M.D., 1986b, *In situ* production of terrestrial cosmogenic helium and some applications to geochronology: *Geochimica et Cosmochimica Acta*, **v. 50**, p. 2855-2862.

Kurz, M.D., and Ackert, R.P., 1997, Stability of the East Antarctic Ice Sheet?: New chronological evidence from Bennett Platform, Antarctica: *EOS, trans. AGU*, **v. 78**, p. S185.

Kurz, M.D., and Brook, E.J., 1994, Surface exposure dating with cosmogenic nuclides, in Beck, C., ed., *Dating in Exposed and Surface Contexts*: Albuquerque, University of New Mexico Press, p. 139-159.

Kurz, M.D., Colodner, D., Trull, T.W., Moore, R.B., and O'Brien, K., 1990, Cosmic ray exposure dating with *in situ* produced cosmogenic ^{3}He: results from young Hawaiian lava flows: *Earth and Planetary Science Letters*, **v. 97**, p. 177-189.

Kurz, M.D., Kenna, T.C., Lassiter, J.C., and DePaolo, D.J., 1996, Helium isotopic evolution of Mauna Kea Volcano: First results from the 1-km drill core: *Journal of Geophysical Research*, **v. 101**, p. 11,781-11,791.

Lal, D., 1987, Production of ^{3}He in terrestrial rocks: *Chemical Geology* (Isotope Geoscience Section), **v. 66**, p. 89-98.

Lal, D., 1991, Cosmic ray labeling of erosion surfaces: *In situ* nuclide production rates and erosion models: *Earth and Planetary Science Letters*, **v. 104**, p. 424-439.

Lal, D., and Peters, B., 1967, Cosmic ray produced radioactivity on the Earth, in Flügge, S., and Sitte, K., eds., *Encyclopedia of physics*, Volume XLVI/2: New York, Springer-Verlag, p. 551-612.

Licciardi, J.M., Kurz, M.D., and Clark, P.U., 1999, Calibration of cosmogenic ^{3}He production rates: Results from Holocene lava flows: *Earth and Planetary Science Letters*, **v. 172**, p. 261-271.

Liu, B., Phillips, F.M., Fabryka-Martin, J.T., Fowler, M.M., and Stone, W.D., 1994, Cosmogenic ^{36}Cl accumulation in unstable landforms 1. Effects of the thermal neutron distribution: *Water Resources Research*, **v. 30**, p. 3115-3125.

Masarik, J., and Reedy, R.C., 1994, Effects of bulk chemical composition on nuclide production processes in meteorites: *Geochimica Cosmochimica Acta*, **v. 58**, p. 5307-5317.

Masarik, J., and Reedy, R.C., 1995, Terrestrial cosmogenic-nuclide production systematics calculated from numerical simulations: *Earth and Planetary Science Letters*, **v. 136**, p. 381-395.

Masarik, J., and Reedy, R.C., 1996, Monte Carlo simulation of the *in-situ*-produced cosmogenic nuclides: *Radiocarbon*, **v. 38**, p. 163.

Mazor, E., Heymann, D., and Anders, E., 1970, Noble gases in carbonaceous chondrites: *Geochimica et Cosmochimica Acta*, **v. 34**, p. 781-824.

McKelvey, B.C., and Webb, P.N., 1962, Geological investigations in southern Victoria Land, Antarctica: Part 3-Geology of Wright Valley: *New Zealand Journal of Geology and Geophysics*, **v. 5**, p. 143-162.

Mercer, J.H., 1982, Holocene glacier variations in southern South America: *Striae*, **v. 18**, p. 35-40.

Morrison, P., and Pine, J., 1955, Radiogenic origin of the helium isotopes in rocks: *Annals of the New York Academy of Sciences*, **v. 62**, p. 71-92.

Niedermann, S., Graf, T., Kim, J.S., Kohl, C.P., Marti, K., and Nishiizumi, K., 1994, Cosmic-ray-produced 21 Ne in terrestrial quartz; the neon inventory of Sierra Nevada quartz separates: *Earth and Planetary Science Letters*, **v. 125**, p. 341-355.

Phillips, F.M., and Plummer, M.A., 1996, CHLOE: A program for interpreting *in situ* cosmogenic nuclide data for surface exposure dating and erosion studies. (abstr.): *Radiocarbon*, **v. 38**, p. 98.

Renne, P.R., Sharp, W.D., Deino, A.L., Orsi, G., and Civetta, L., 1997, $^{40}Ar/^{39}Ar$ dating into the historical realm: Calibration against Pliny the younger: *Science*, **v. 277**, p. 1279.

Sarda, P., Staudacher, T., Allegre, C.J., and Lecompte, A., 1993, Cosmogenic neon and helium at Reunion: measurement of erosion rate: *Earth and Planetary Science Letters*, **v. 119**, p. 405-417.

Schäfer, J.M., Ivy-Ochs, S., Wieler, R., Leya, I., Baur, H., Denton, G.H., and Schlüchter, C., 1999, Cosmogenic noble gas studies in the oldest landscape on earth: surface exposure ages of the Dry Valleys, Antarctica: *Earth and Planetary Science Letters*, **v. 167**, p. 215-226.

Shelby, J.E., 1971, Diffusion of helium isotopes in vitreous silica: *Phys. Rev. Lett.*, **v. 1**, p. 138-140.

Singer, B.S., Ackert, R.P., Jr., Kurz, M.D., Guillou, H., and Ton-That, T., 1998, Chronology of Pleistocene Glaciations in Patagonia: A ^{3}He, $^{40}Ar/^{39}Ar$, & K-Ar study of lavas and moraines at Lago Buenos Aires, 46° S, Argentina: Geological Society of America, 1998 annual meeting, Abstracts with Programs, **v. 30**, p. 299.

Singer, B.S., Vincze, Y., and Hildreth, W., 1997, Timing of Glacial retreat in the Southern Andes from $^{40}Ar/^{39}Ar$ dating of pre- and post-glacial lavas: *Eos, transactions, AGU*, **v. 78**, p. F771.

Staudacher, T., and Allegre, C.J., 1991, Cosmogenic Neon in ultramafic Nodules from Asia and in Quartzite from Antarctica: *Earth and Planetary Science Letters*, **v. 106**, p. 87-102.

Stone, J.O., 1999, Air pressure and cosmogenic isotope production: *Journal of Geophysical Reviews*, p. in review.

Stuiver, M., and Reimer, P.J., 1993, Extended ^{14}C data base and revised Calib 3.0 ^{14}C age calibration program: *Radiocarbon*, **v. 25**, p. 215-230.

Ton-That, T., 1997, $^{40}Ar/^{39}Ar$ dating of basaltic lava flows and the geology of the Lago Buenos Aires region Santa Cruz Province, Argentina [M.S. thesis]: Genève, University of Genève.

Trull, T.W., 1989, Diffusion of helium isotopes in silicate glasses and minerals: Implications for petrogenesis and geochronology [Ph. D. thesis], MIT/WHOI Joint program in Oceanography.

Trull, T.W., Brown, E.T., Marty, B., Raisbeck, G.M., and Yiou, F., 1995, Cosmogenic ^{10}Be and ^{3}He accumulation in Pleistocene beach terraces in Death Valley, California, U.S.A.:Implications for cosmic-ray exposure dating of young surfaces in hot climates: *Chemical Geology*, **v. 119**, p. 191-207.

Trull, T.W., Kurz, M.D., and Jenkins, W.J., 1991, Diffusion of cosmogenic ^{3}He in olivine and quartz: implications for surface exposure dating: *Earth and Planetary Science Letters*, **v. 103**, p. 241-256.

Zreda, M.G., and Phillips, F.M., 1994, Surface exposure dating by cosmogenic chorine-36 accumulation, in Beck, C., ed., *Dating in Exposed and Surface Contexts*, University of New Mexico Press, p. 161-183.

Zreda, M.G., Phillips, F.M., Kubik, P.W., Sharma, P., and Elmore, D., 1993, Cosmogenic ^{36}Cl dating of a young basaltic eruption complex, Lathrop Wells, Nevada: *Geology*, **v. 21**, p. 57-60.

Appendix 2.1 Samples used for ^{3}He production rate determination and initial ^{3}He concentrations

Sample	Location	Deposit/surface	Lithology	Elev. (m)	Latitude	Longitude
Cerro Volcán Lava Flow						
LBA98-064	Estancia Laürabat	pressure ridge	basalt; cpx, ol	490	46° 42.098' S	70° 44.932' W
LBA98-065	Estancia Laürabat	pressure ridge	basalt; cpx, ol	490	46° 42.098' S	70° 44.932' W
LBA98-093	Canadón del Deseado	pressure ridge	basalt; cpx, ol	410	46° 37.093' S	70° 47.799' W
LBA98-096	Canadón del Deseado	pressure ridge	basalt; cpx, ol	410	46° 37.174' S	70° 47.714' W
Shielded Ferrar Dolerite Samples						
RAK96-097	Taylor Glacier Cliff	bedrock overhang	dolerite; px	1119	77° 50.283' S	161° 10.256' E
RAK96-098	Taylor Glacier Cliff	bedrock cleft	dolerite; px	1119	77° 50.283' S	161° 10.256' E
RAK96-101B	Kukri Hills	talus	dolerite; px	1832	77° 47.762' S	161° 56.944' E
RAK96-102A	Kukri Hills	cliff face	dolerite; px	1832	77° 47.762' S	161° 56.944' E

cpx = clinopyroxene; ol = olivine; px = pyroxene. Longitude and latitude determined by handheld GPS. Elevation by altimeter and topographic maps.

CHAPTER 3

Measurements of past ice sheet elevations in interior West Antarctica: Surface exposure chronology of moraines at Mt. Waesche

3.1 Introduction

The history of the marine-based West Antarctic Ice Sheet (WAIS) is of interest because it is potentially unstable in the face of anthropogenic warming (*e.g.,* Mercer, 1978; Oppenheimer, 1998). The WAIS may also be subject to irregular, internally-driven collapse (MacAyeal, 1992). A knowledge of the past configurations and behavior of the WAIS is necessary to both calibrate glaciological models that predict future ice sheet responses and to quantify the Antarctic ice sheet contribution to eustatic sea level rise during the last deglaciation.

Studies of moraines in the Transantarctic Mountains indicate that outlet glaciers were once dammed by thick grounded ice in the Ross Embayment, where only a floating ice shelf occurs today (Bockheim *et al.*, 1989; Denton *et al.*, 1989a; Mercer, 1968). In the McMurdo Sound Region, ^{14}C and surface exposure ages on drift deposited by ice grounded in the Ross Sea date to the last glacial maximum (LGM) (Brook *et al.*, 1995; Denton *et al.*, 1989b; Hall and Denton, 1999). Geophysical mapping of the Ross Sea floor (Anderson *et al.*, 1992; Shipp *et al.*, 1999) and ^{14}C ages on sediments overlying tills (Domack *et al.*, 1999; Licht *et al.*, 1999; Licht *et al.*, 1996) demonstrate that grounded ice extended to near the continental shelf break at the LGM, over 1000 km beyond the present grounding line.

In contrast to its lateral extent, direct evidence for the interior elevation of the WAIS has been quite uncertain. An ice sheet model constrained by the evidence from the Ross Embayment, trimlines in the Ellsworth Mountains, and striations on the Hobbs coast suggests that the ice sheet domes in West Antarctica were 450 to 600 m higher during the LGM (Denton *et al.*, 1991). However, the ages of the trimlines and striations are uncertain and this reconstruction may overestimate interior elevations (Denton *et al.*, 1991). Total gas content from the Byrd ice core, which is largely a function of past atmospheric pressure (elevation of the site) (Martinerie *et al.*, 1992), provides indirect constraints on ice elevation in interior West Antarctica during the LGM. The total gas data are interpreted to indicate that ice elevations were both ~200 m lower (Raynaud and Lebel, 1979; Raynaud and Whillans, 1982), and 400 to 500 m higher (Jenssen, 1983) during the LGM and early Holocene. Byrd core $\delta^{18}O$ data also imply that ice elevations were ~500 m higher during the LGM (Grootes and Stuiver, 1986). Accurate reconstructions of interior ice

elevations have important implications for modeling the dynamics of the WAIS. New surface exposure ages are presented from a lateral moraine band at Mt. Waesche that directly date the most recent ice highstand in interior West Antarctica.

Mt. Waesche is the southernmost volcano in the Executive Committee Range, a line of volcanoes that projects through the WAIS in Marie Byrd Land (Figure 3.1). Regional ice flow is southward from a dome centered on the northern Executive Committee Range where ice elevations exceed 2200 m. WAIS elevations near Mt. Waesche are about 2000 m. The summit caldera reaches 3200 m and is largely snow-covered; small alpine glaciers terminate ~400 m above the ice sheet surface (Figure 3.2). Extensive rock outcrops on the southwestern flank and an adjacent blue-ice area on the ice sheet indicate local net ice ablation. Parasitic cones consisting of black vesicular lavas, cinders, and bombs, overlie shield-building lava flows (LeMasurier and Kawachi, 1990) predominantly composed of alkali basalts and hawaiites. Limited K/Ar dating indicates that Mt. Waesche is less than 1 Ma (LeMasurier and Rex, 1989).

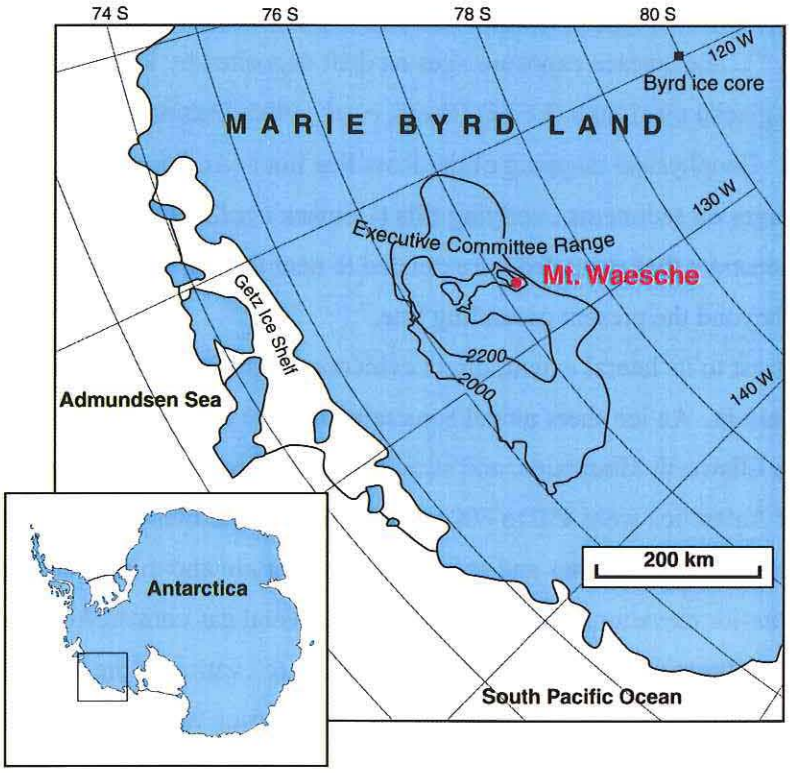

Figure 3.1 Location map of Antarctica and Marie Byrd Land. Mt. Waesche is a volcanic nunatak which projects through the WAIS near a dome of the ice sheet. Ice flows south around Mt. Waesche to the Ross Ice Shelf. Moraines on Mt. Waesche gauge past ice sheet elevations.

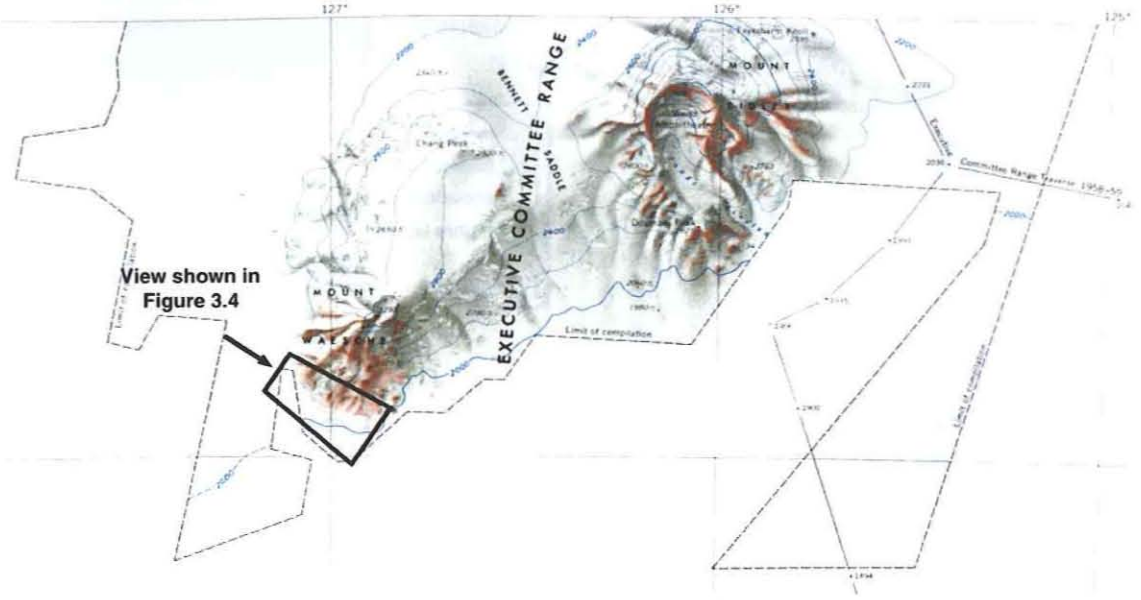

Figure 3.2 Topographic map of Mount Waesche. Ice elevations are ~2000 m. The elevation of the summit caldera is ~3200 m. An area of net ablation is indicated by the bare rock outcrops and an area of blue ice on the southern flank of the volcano. Area shown in Figure 3.4 is marked. Map is reproduced from the USGS Mount Sidley, 1;250000 Antarctic Reconnaissance Series, no. S7700-W12400/1x6, 1960.

3.2 Glacial geology of Mount Waesche

Two lateral moraines of the WAIS occur on the southwestern flank of the volcano (Figures 3.3 and 3.4). An ice-cored lateral moraine adjacent to the present ice margin is composed of tephra and pyroclastic debris. Tephra layers, volcanic debris erupted onto the surface of the ice sheet, are exposed in the ice sheet ablation area on the southwest side of Mt. Waesche. The layers include thin fine-grained trachytic ash from distant volcanoes and locally derived layers of pyroclastic debris and basalt clasts up to 4 m thick (Dunbar *et al.*, 1999). Convergent ice flow downstream of the volcano has folded the tephra layers so that the originally sub-horizontal beds crop out with steep dips (Dunbar *et al.*, 1999) (Figure 3.3). Ice ablation exposes the englacial tephra on the ice sheet surface. Individual tephra layers on the ice sheet can be traced into the ice-cored moraine. The moraine is formed of tephra accumulating along the ice margin (Figure 3.3).

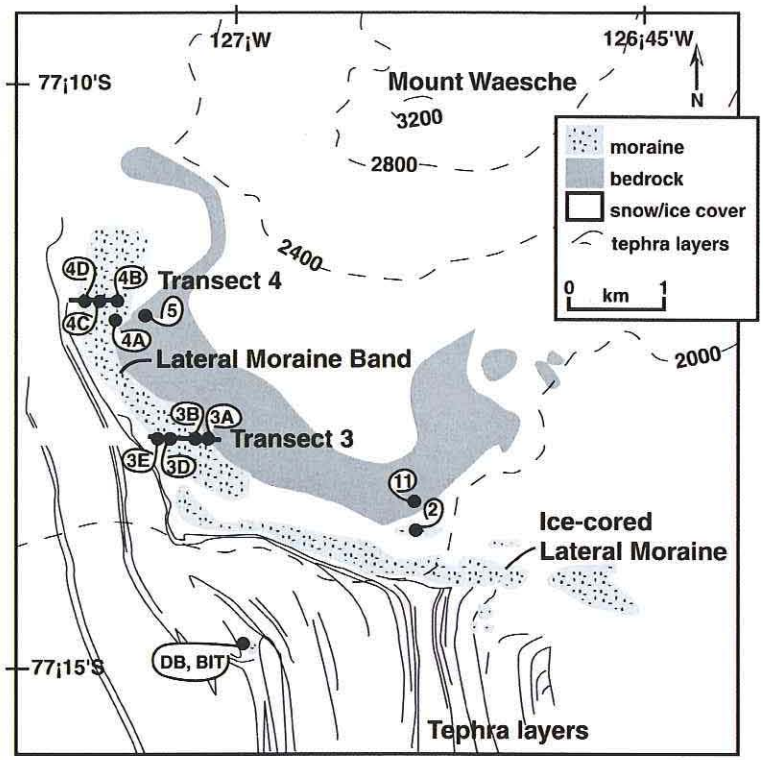

Figure 3.3 Geologic sketch map of the southern flank of Mt. Waesche. The map shows the relationship of englacial tephra layers (solid lines) to the lateral moraines. The ice-cored moraine is formed of tephra which has been concentrated at the ice margin by ablation. Surface exposure sample locations are indicated (WA- prefix omitted). Elevations are in meters. Map is based on Borns *et al.* (1995) and Dunbar *et al.* (1999).

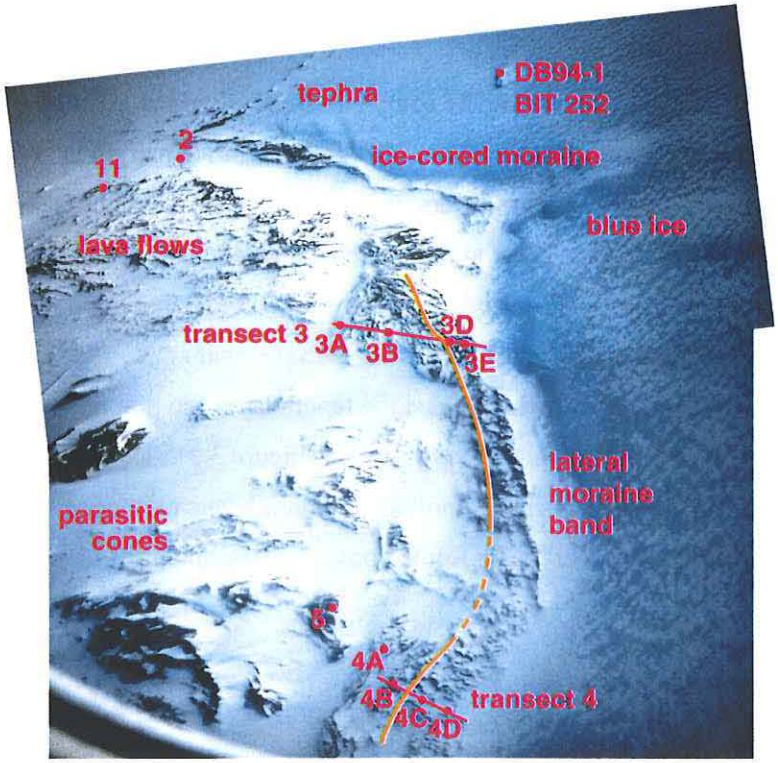

Figure 3.4 Oblique hand-held composite photograph from C-130 aircraft showing the moraines on southwest flank of Mt. Waesche. A geomorphic break dividing the lower and upper parts of moraine band is shown by the yellow line. Concentrations of tephra are visible on the blue ice. Transects and sample locations are indicated (See also Figure 3.3).

A higher lateral moraine band extends from the slope above the western end of the ice-cored moraine northwestward for ~3 km along the base of the volcano. The moraine varies in width from 150 to 300 m and generally increases in elevation to the northwest, rising irregularly to a maximum height of 120 m above the present ice margin. Like the ice-cored moraine, the lateral moraine band is composed of local volcanic rocks. The rocks are primarily basalts containing plagioclase with variable percentages of olivine and clinopyroxene. Clasts are subangular to angular and typically less than 25 cm in length; no striated or glacially molded clasts were observed.

The higher lateral moraine band was likely formed by a process similar to that forming the ice-cored moraine at the ice margin. One difference between the ice-cored moraine and the higher lateral moraine band is that the latter is composed primarily of basalt fragments rather than pyroclastic debris. The greater abundance of basalt clasts on the higher moraine surface may have resulted from lavas that flowed out over the ice surface, along the ice margin, or from preferential weathering of the more friable pyroclastic debris.

The uppermost surface of the lateral moraine band occurs locally as a terrace 20 to 30 m wide, roughly parallel to the present ice margin. The relief is subdued and rarely exceeds 1 m (Figure 3.5). Below this part, the upper moraine surface consists of discontinuous sub-parallel ridges up to 5 m high and 100 to 200 m long that mark former ice margin positions. In general, the surface of the upper part of the moraine band, furthest from the ice margin, is less hummocky than the lower part and the ridges are longer. Clast size is more uniform and smaller on the upper part and fluting of clasts due to wind erosion (ventifaction) is most developed there. The change in character of the moraine surface from the upper parts to the lower parts, closer to the ice margin, suggests that the moraine band is a complex feature and that the upper parts are older than the lower. For the purpose of discussion, the lateral moraine band is divided into higher and lower sections along a subtle morphologic break which occurs between the upper and lower parts (Figure 3.4).

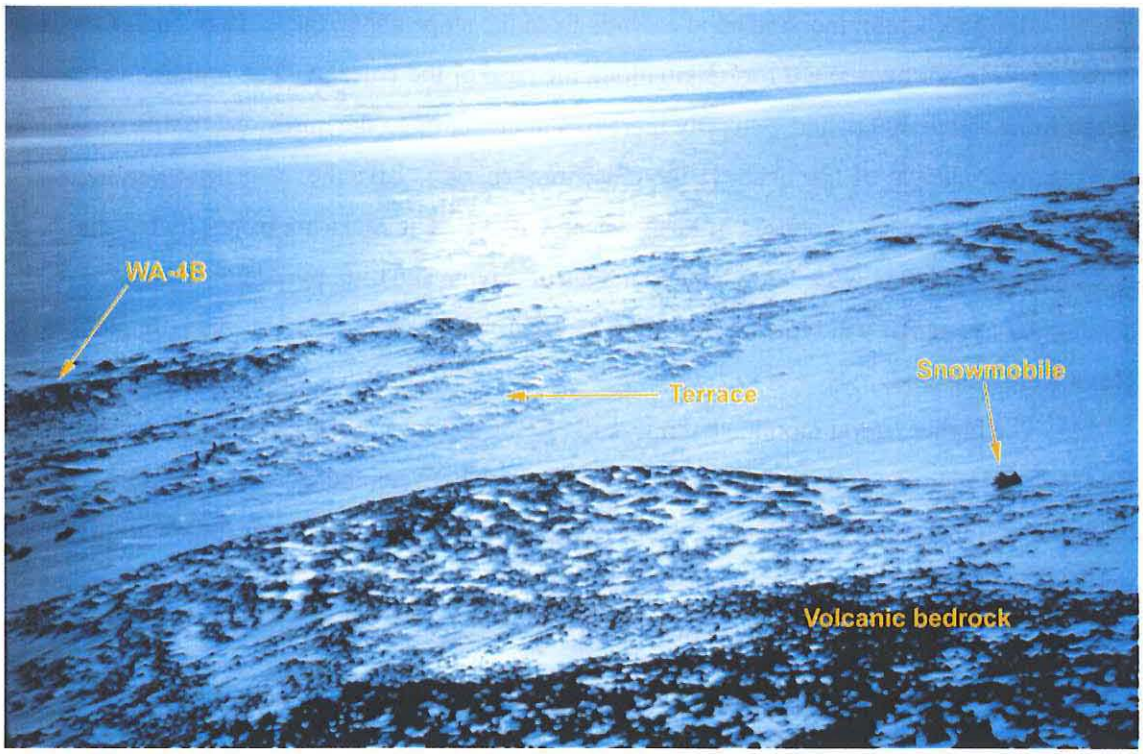

Figure 3.5 Photograph of the moraine band taken from lava flows (foreground) above transect 4 (Figures 3.3 and 3.4). The terrace forming the upper part of the moraine band is well expressed here. Note snowmobile at right for scale. Location of sample site WA-4B is approximate.

Samples for surface exposure dating were collected by a field party led by H. Borns and P. Calkin in 1995. The samples were collected along two transects across the lateral moraine band and from one isolated patch of lateral moraine in a similar setting (Figures 3.3 and 3.4). Clasts 10 to 20 cm in diameter were collected away from patterned ground and shattered boulders. The presence of pedogenic salts beneath the sampled clasts and ventifaction of the exposed surfaces were used as criteria indicating surface stability of the samples. Samples were also taken from *in-situ* lava flow outcrops above the moraines and from a large pile of coarse tephra on the ice sheet surface (Figures 3.3 and 3.4). An additional sample (BIT-252) from the tephra pile was supplied by N. Dunbar. Sample locations were recorded with hand-held GPS; sample elevations were determined by altimeter relative to a base camp on the ice sheet. Relative uncertainties in elevation between sample sites are estimated to be ± 5 m. The relative elevations were tied to geodetic altitude by differential GPS (±20 m) at several locations. Sample elevations, GPS co-ordinates and lithology appear in Appendix 3.1.

3.3 Surface exposure dating

Introduction

Surface exposure dating was used to constrain the age of the lateral moraine band. Details of the technique appear in Chapter 1, with a short summary given here. The surface exposure dating technique relies on the build-up of cosmogenic nuclides (^{3}He, ^{21}Ne, ^{10}Be, ^{26}Al, and ^{36}Cl) in rocks exposed to cosmic rays at the Earth's surface. The nuclides are formed primarily during spallation reactions between cosmic rays and major elements in the rock. A fundamental assumption is that accumulation of cosmogenic nuclides in moraine boulders commenced at deposition and has not been interrupted. In this case, the surface exposure age yields the age of moraine formation and the associated glacial margin. The technique has produced significant results constraining glacial moraine ages where absolute dating was previously impossible (*e.g.,* Brook *et al.*, 1993; Gosse *et al.*, 1995; Phillips *et al.*, 1996a).

Erosion or shielding of a sample after boulder deposition would result in ages younger than the moraine. Exposure to cosmic rays before deposition would result in ages older than the moraine. Prior exposure in a surface exposure data set may be manifested by a scatter of ages older than a cluster of younger ages or ages substantially older than the age anticipated on the basis of other age constraints. Although prior exposure can be a significant problem in Antarctica due to low erosion rates, the data reported here suggest that this is not a pervasive problem at Mt. Waesche. Tephra and lava flows erupted onto the ice sheet will have little prior exposure if burial by ice is rapid and exposure after re-emergence within the ablation zone is short.

In order to calculate accurate surface exposure ages from measured concentrations of cosmogenic nuclides, the production rate must be well known. Production rates calibrated on surfaces of known age must be scaled to the elevation and latitude of the sample (Lal, 1991). Uncertainty in production rates including scaling factors, is conservatively estimated to be 10 to 15 percent. In contrast, analytical error in the ^{3}He measurement is 2 to 3 percent. An additional complication in Antarctica is that anomalous low atmospheric pressure results in production rates that are up to 20 to 30 percent higher than those at latitude 60°. In this study, the high latitude-sea level production rates for ^{3}He (Cerling and Craig, 1994; Licciardi *et al.*, 1999) and ^{36}Cl (Phillips *et al.*, 1996b) were scaled to the appropriate Antarctic altitude using the formulation of Stone (1999) (Chapter 2). This ^{3}He production rate (121±3 atoms/g/yr) is ~6 percent lower than that presented from Cerro Volcán in Chapter 2 and used in Chapters 4 and 5.

Methods

Cosmogenic ^{3}He was measured in 24 olivine and/or clinopyroxene mineral separates from 19 samples. Four whole-rock ^{36}Cl measurements were made: two on porphyritic samples that also had ^{3}He measurements and two on aphanitic basalts in which ^{3}He measurements were not possible. ^{3}He was measured on the helium isotope mass spectrometer at Woods Hole Oceanographic Institution using previously described techniques (Kurz, 1986). The inherited (mantle derived) $^{3}He/^{4}He$ ratio was determined by crushing the mineral separates *in vacuo* which selectively releases gases held in fluid and melt inclusions. The cosmogenic ^{3}He component was calculated by subtracting the inherited ^{3}He component from the ^{3}He released by fusion of the sample powders *in vacuo* (Chapter 1).

Cosmogenic ^{36}Cl was measured in hand-picked 1 to 2 mm grains of fresh ground mass. In order to determine the Ca and K concentration and the macroscopic neutron cross section of the samples, major elements were measured in a sub sample by XRF (Appendix 3.2). B, Gd, and Sm, which have high cross-sections for neutron capture, were measured by NAA (Sm) and prompt gamma (B and Gd). These measurements were made at XRAL Laboratories. AgCl targets were prepared at PRIME lab, Purdue University; Cl concentrations were determined by isotope dilution. ^{36}Cl surface exposure ages were calculated using the CHLOE program (Phillips and Plummer, 1996). Details of the ^{36}Cl technique appear in Chapter 1.

Results

Helium isotope data appear in Table 3.1. The inherited $^{3}He/^{4}He$ determined by the crushed mineral separates is very homogeneous (6.11 ± 0.46 R/R_a, n=21). These are the first helium isotope data for basalts in Marie Byrd Land. The inherited $^{3}He/^{4}He$ is similar to that obtained from the McMurdo Sound Volcanics (6.1 to 7.1 R/R_a) (Brook *et al.*, 1995; see also Table 5.2). The value is lower than that of mid ocean ridge basalts (MORB = ~8 R/R_a) and significantly lower than that of ocean island basalts (OIB) associated with hot spots, but typical of that of basalts erupted through cratonic crust in extensional tectonic regimes. The inherited $^{3}He/^{4}He$ data do not support a hot spot origin for the West Antarctic Rift System (*e.g.*, Behrendt *et al.*, 1992).

Replicate analysis of different mineral separates from the same sample show good reproducibility (Table 3.1). Three olivine replicates and five olivine/cpx pairs all agree within 2σ

analytical uncertainties. The concordance of the olivine and cpx data is consistent with small compositional dependence of the ^{3}He production rate (Lal, 1991).

Table 3.1 ^{3}He surface exposure data from Mt. Waesche.

Sample	Alt (m)	R/R_a* ±1sig (crush)		^{4}He ± 1 sig ccSTP/g x 10^{-9}		R/R_a ±1 sig (melt)		Age ± 1 sig (kyr)		Sample type
DB-94-1	1935	5.90	0.04	47.3	0.6	6.08	0.1	0.4	0.2	supraglacial
BIT-252	1935	6.14	0.10	2.14	0.02	15.2	0.3	0.9	0.0	debris
WA-4D-1	2010	6.27	0.08	44.7	0.3	11.7	0.1	10.6	0.2	lower moraine
WA-4D-3 cpx	2010	5.62	0.41	3.70	0.09	44.0	0.5	6.2	0.2	band
WA-4C-2	2015	6.01	0.12	32.8	0.3	13.0	0.1	10.1	0.2	
WA-4C-2 rep	2015	6.01	0.12	3.79	0.02	63.5	0.5	9.6	0.1	
WA-4C-1	2015	6.13	0.10	4.24	0.04	60.6	0.7	10.2	0.2	
WA-4B-1 cpx	2035	6.10	0.05	31.8	0.3	66.0	0.3	83.2	1.1	upper moraine
WA-4B-1	2035	6.10	0.05	19.4	0.2	104	1	83.2	1.0	band
WA-4B-3 cpx	2035	6.05	0.09	9.13	0.09	226	1	87.8	1.0	
WA-4B-3	2035	6.05	0.09	0.93	0.01	2201	30	87.8	1.5	
WA-4A-1	2040	5.42	0.13	40.9	0.4	40.9	0.2	62.1	0.9	
WA-4A-1 rep	2040	5.42	0.13	4.49	0.09	328	2	62.1	1.3	
WA-3E-1	1945	6.29	0.12	2.27	0.05	485	4	49.5	1.3	lower moraine
WA-3D-1	1985	5.30	0.16	1.81	0.02	120	1	9.2	0.2	band
WA-3D-2	1985	5.91	0.15	1.70	0.01	104	1	7.4	0.1	
WA-3B-1	2025	6.03	0.08	2.23	0.03	174	2	16.1	0.3	upper moraine
WA-3B-2	2025	5.63	0.06	5.45	0.04	198	1	47.0	0.5	band
WA-3B-2 cpx	2025	6.08	0.19	6.37	0.07	169	1	46.5	0.7	
WA-3A-1	2035	7.22	0.18	4.49	0.04	1217	5	233.4	2.4	
WA-3A-2 cpx	2035	5.90	0.05	3.41	0.03	80.4	0.6	10.9	0.1	
WA-3A-2	2035	5.89	0.12	10.3	0.1	28.1	0.3	9.8	0.2	
WA-2-1	1975	6.38	0.05	35.1	0.4	94.5	0.4	140.0	1.8	moraine patch
WA-2-1	1975	6.38	0.05	6.64	0.06	470	2	139.3	1.4	
WA-5-1	2055	6.82	0.07	22.8	0.2	376	2	359.9	4.2	lava flows
WA-5-1 rep	2055	6.64	0.04	6.60	0.12	1290	4	362.3	6.8	
WA-5-1 cpx	2055	6.64	0.06	6.09	0.06	1343	4	348.0	4.0	
WA-11-1	2055	6.67	0.05	3.32	0.04	2547	14	360.2	4.9	

*R/R_a is the ^{3}He/^{4}He ratio relative to the atmospheric ratio (1.384×10^{-6}). R/R_a (crush) is the ratio of the inherited (magmatic) helium component; The mean crush R/R_a (6.11±0.46, n = 21) characterizes the mantle source beneath the ECR. ^{4}He is the gas released on melting *in vacuo*. Samples followed by rep are replicates; typically the initial sample was not crushed, the R/R_a crush value of the replicate was used for both samples. All samples were olivine separates unless denoted by cpx (clinopyroxene). The surface exposure ages were calculated using a ^{3}He production rate of 121 ± 4 atoms/g/yr (high latitude-sea level) (Cerling and Craig, 1994). The higher than published production rate results from an updated ^{14}C years BP to calendar years conversion. Scaling to Antarctic altitudes after Stone (1999). Uncertainties are propagated analytical uncertainties. Scaling and production rate uncertainties are estimated to be <10%.

The ^{3}He surface exposure data are summarized in Table 3.1. In general, the exposure ages on the lateral moraine band increase with distance from, and elevation above, the ice margin (Figure 3.6). The ages of samples from tephra exposed in the ablation area (DB-94-1 and BIT-252), are less than 900 yrs and suggest that prior exposure is minimal. Surface exposure ages of ~360 ka on lava flows (WA-5 and WA-11) are older than any sample from the moraine and are

consistent with K-Ar ages on Mt. Waesche (<1 Ma) (LeMasurier and Rex, 1989). The old lava flow ages indicate erosion rates are low and suggest that mass wasting of material from the volcano slopes above has not supplied substantial amounts of debris to the lateral moraine band.

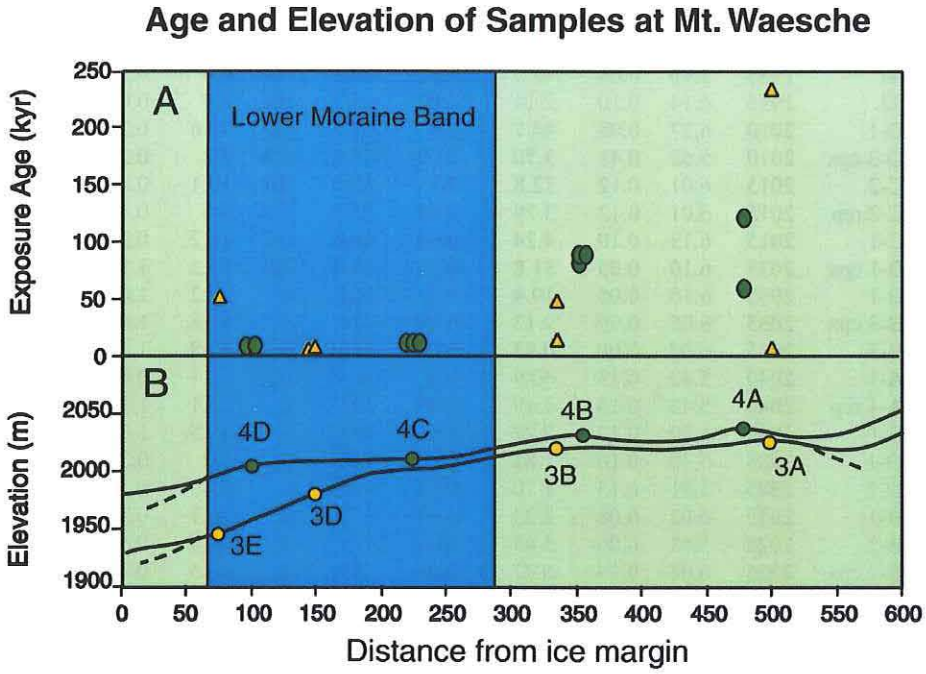

Figure 3.6 (A) Exposure age of samples vs. distance from the ice margin along sample transects. Triangles are samples from transect 3; ovals are samples from transect 4. (B) Elevations and sample locations along transects 3 and 4. Dashed line is the projected moraine surface beneath snow. The samples on the lower moraine band (shaded) range from 6.2 to 10.6 kyr; the best estimate is ~10 ka. The ages of samples from the upper section of the lateral moraine band are older and generally increase in exposure age with elevation and distance from the present ice margin.

The ^{36}Cl surface exposure data are summarized in Table 3.2. The ^{36}Cl ages show good agreement with the ^{3}He ages and demonstrate the utility of ^{36}Cl for dating phenocryst-poor basalts. Because the ^{36}Cl production rate due to neutron capture on ^{35}Cl increases downward within the uppermost 10 cm of rock, erosion effectively increases the ^{36}Cl concentration at the surface (Liu *et al.*, 1994). In Cl-rich rocks, low erosion rates (<5 mm/kyr) can result in apparent ^{36}Cl surface exposure ages that are older than the true surface exposure age if the erosion rate is underestimated (Table 3.2). Paired ^{3}He and ^{36}Cl data can be used to evaluate erosion rates (Phillips *et al.*, 1997). Surface exposure ages can be plotted as function of erosion rate (Figure 3.7). The exposure age determined from spallation-produced nuclides (^{3}He,^{10}Be, ^{21}Ne and ^{26}Al)

decreases with erosion rate. In contrast, the ^{36}Cl age reaches a minimum value for some erosion rates dependent on the relative proportion of production by ^{35}Cl. In the case of no erosion, both nuclides will give the same age. For samples with low erosion rates, the ^{36}Cl age will be higher than the ^{3}He age when no erosion is assumed. For samples that have undergone erosion, the two curves will cross at a point which determines both the age of the sample and the erosion rate. If the ^{36}Cl age is lower than the ^{3}He age when no erosion is assumed, burial of the sample after some initial exposure is possible (Chapter 1).

Table 3.2 ^{36}Cl surface exposure ages from Mt. Waesche.

Sample ID	K_2O (%)	CaO (%)	Cl (ppm)	Σ^* (cm^2/kg)	$^{36}Cl/Cl$ (10^{-15})	Exposure age e=0	(kyr) e=1
WA-4A-2	2.14	6.10	1007	14.1	1365	130	96.1
WA-4B-2	2.10	6.16	761	14.3	1038	88.1	69.3
WA-4C-1	0.78	10.50	201	14.0	254	10.9	10.5
WA-4D-1	0.80	10.50	172	13.6	245	9.4	9.2

*Macroscopic absorption cross section of the rock. Exposure ages were calculated using the CHLOE program (Phillips and Plummer, 1996) that uses ^{36}Cl spallation production rates: $P_{Ca} = 73.3 \pm 4.9$, $P_K = 154 \pm 10$ (Phillips *et al.*, 1996b) and calculates the thermal neutron activation production rate after Liu *et al.* (1994). Exposure ages for erosion rates of zero (e = 0) and 1 mm/kyr (e = 1) are shown. Ages calculated with low erosion rates are younger because the production of ^{36}Cl increases with depth. ^{36}Cl was measured in AgCl targets at PRIME lab, Purdue University. Scaling of the production rates to Antarctic altitudes after Stone (1999). Combined analytical and systematic uncertainties are <15%.

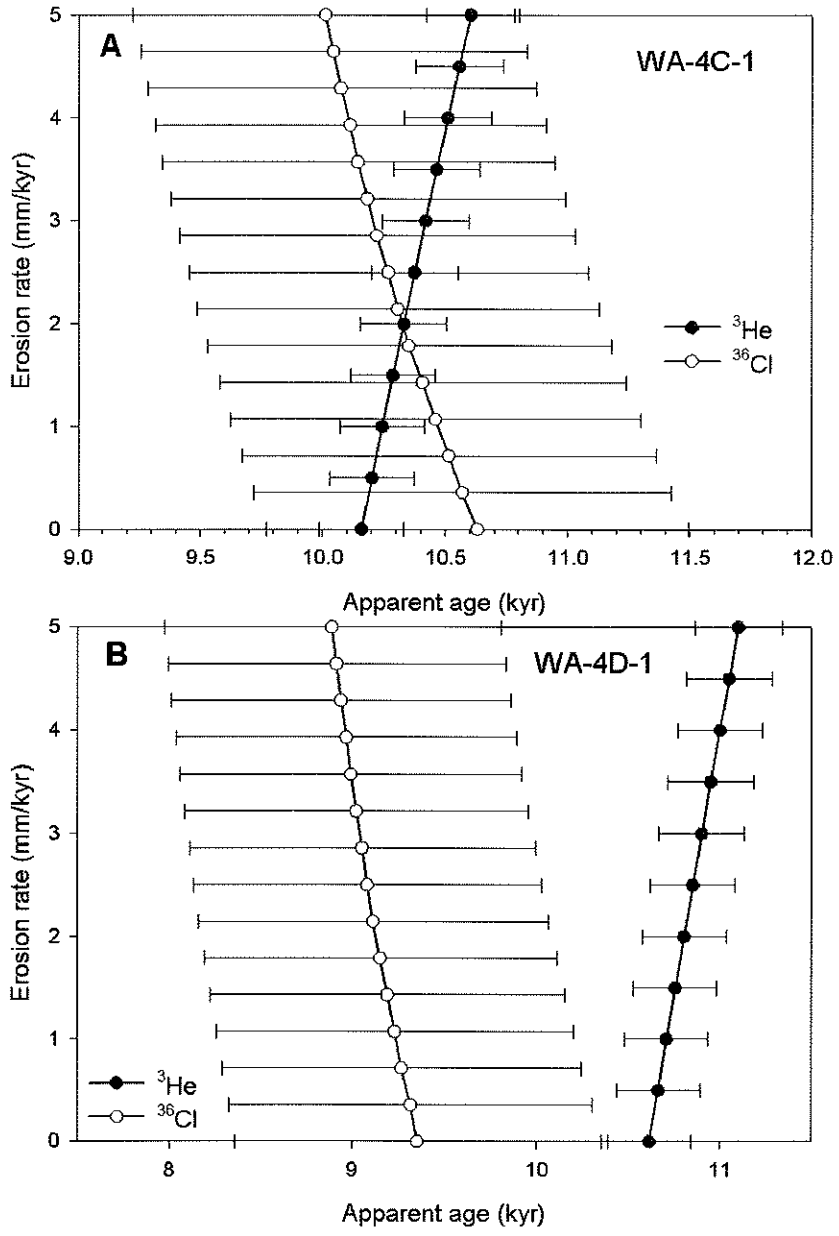

Figure 3.7 ^{3}He and ^{36}Cl ages plotted as a function of erosion rate for two samples from the lower part of the moraine band. The intersection of the apparent age lines determines both the age and erosion rate of the sample. Plotted uncertainties are 1σ analytical uncertainties only. Uncertainties in scaling factors do not effect the relative relationship between the ^{3}He and ^{36}Cl data, but error in the production rates will shift the lines right or left. (A) WA-4C-1. Although the calculated ages indicate the sample is 10.3 ka and the erosion rate is ~2 mm/kyr, the erosion rate is not well-constrained due to the large uncertainty in the ^{36}Cl ages. (B) WA-4D-1. The ages overlap at low erosion rates within the 2σ analytical uncertainties. Alternatively, the ^{36}Cl production rates may be high relative to the ^{3}He or the sample may have experienced long (>100kyr) burial after a short initial exposure.

In practice, uncertainties in the calculations preclude precise determination of both erosion rate and surface exposure age. The paired ^{3}He and ^{36}Cl data from two samples from the lower moraine band are shown in Figure 3.7. The calculated ages for sample WA-4C-1 indicate that the sample age is 10.3 ka and the erosion rate is ~2 mm/kyr. However, the erosion rate could range from 5 mm/kyr to zero within the uncertainties, and the ages are not very sensitive to erosion. The calculated ages for sample WA-4D-1 are suggestive of prolonged burial (~100 kyr) after a brief initial exposure, a scenario which is not impossible in the geologic setting. The age of the oldest (distant source) tephra layers (and the adjacent ice) is > 100 kyr (Dunbar *et al.*, 1999). Alternatively, and more likely because samples of the same lithology with similar ages do not show this pattern (WA-4C-1), the data indicate that the erosion rate is very low. The plotted ^{3}He age uncertainties are 1σ and do not include production rate uncertainties. Taken together, the paired ^{3}He and ^{36}Cl data are consistent with the low erosion rates determined from other Antarctic studies (0.5 to 1 mm/kyr) in quartz (Brown *et al.*, 1991; Nishiizumi *et al.*, 1991) and dolerite (Schäfer *et al.*, 1999). The high Cl concentrations in the older samples (WA-4B-2 and WA-4A-2) makes the ages very sensitive even to very low erosion rates (Table 3.2). Comparison of ^{3}He and ^{36}Cl ages from location WA-4B (but not from the same sample) also suggests that erosion is negligible (Tables 3.1 and 3.2).

The paired ^{3}He and ^{36}Cl data also indicate that the production rates used are consistent. The data from sample WA-4D-1 suggest that the ^{36}Cl production rates used may be 10 percent high relative to that of ^{3}He. However, a similar shift in production rates applied to the ^{36}Cl data from WA-4C-1 would require unreasonably high (>2 mm/kyr) erosion rates when compared to data from other studies (Brown *et al.*, 1991; Nishiizumi *et al.*, 1991; Schäfer *et al.*, 1999).

The surface exposure ages on the seven samples from four localities within the lower proximal section of the moraine band show, with one exception, similar ages (Figure 3.8). The sample nearest the ice margin (WA-3E-1) has an anomalously old age (~50 ka) suggesting prior exposure and is rejected. The mean of the other six samples is 9.0 ± 1.8 ka. There does not appear to be a relation between surface exposure age and position on the lower part of the moraine. The oldest and youngest samples were collected from the same location; the younger samples do not simply represent progressive lowering of the ice margin. Rather, the samples with slightly younger ages probably reflect post-depositional exhumation by frost action or erosion by boulder shattering. Although areas of active cryoturbation were avoided when sampling, exhumation by frost heaving in the past is difficult to rule out. Basalt boulders derived from lava

flows tend to be highly jointed and disintegrate relatively rapidly along these joint surfaces. Subsequent erosion of the fragments is slow, primarily by wind. If the two younger samples are removed, the four remaining samples form a tight cluster of ages (Figure 3.8). The mean of these samples is 10.0 ± 0.6 ka and may be a better age estimate for the lower part of the moraine. The uncertainty in the mean is similar to the 2σ analytical uncertainty. In either case, the mean ages indicate that the interior of the WAIS was up to 45 m thicker ~10 ka. This is the first direct evidence in interior West Antarctica for thicker ice in the past.

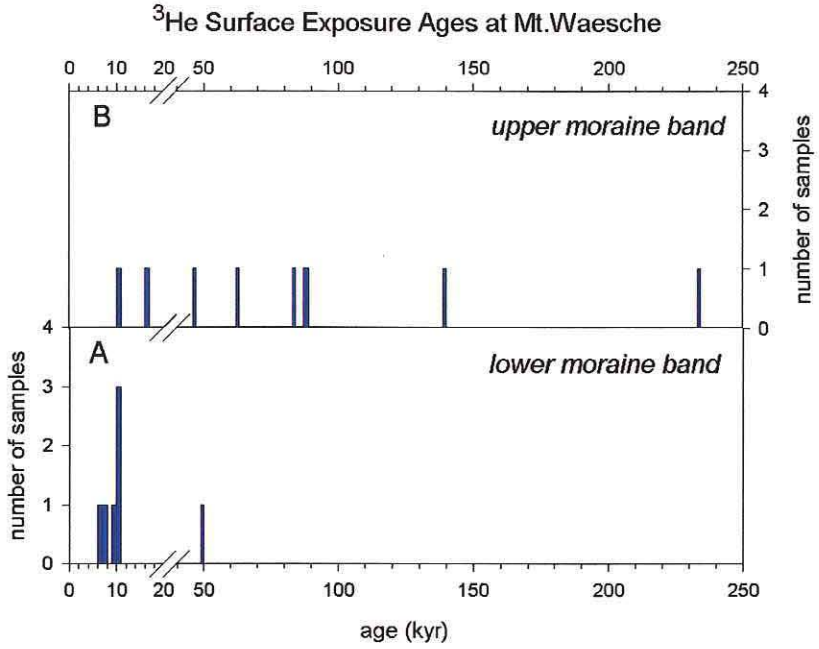

Figure 3.8 Histograms showing distribution of surface exposure ages on the moraine band. Note break of 20 kyr in age axis. (A) The lower part of the moraine band. The old outlier is attributed to prior exposure. The remaining ages cluster around 10 ka which is the best estimate of the moraine age. (B) The upper part of the moraine band. The ages are widely scattered. The scatter likely results from prior exposure, erosion, or multiple glacial events. The youngest age is similar to the ages from the lower moraine band. The age of one sample corresponds to that of the outlier on the lower moraine band.

The exposure ages across the upper distal part of the moraine band and from the isolated moraine outcrop (Figures 3.3 and 3.4), range from 10.8 to 231 ka and vary with location along the moraine (Figures 3.6 and 3.8). An age is not assigned to the upper section of the moraine band because non-concordant exposure ages occur at most sample locations and the ages do not cluster around some value (as is the case on the proximal part of the moraine band). The older surface

exposure ages are consistent with surface morphology observations that indicate an older age for some parts of the upper distal section of the moraine band. The scatter of ages may reflect break-up of boulders after deposition, exhumation by frost action, prior exposure of debris derived from the volcano slopes, or earlier WAIS high stands.

3.4 Discussion

Lower moraine band: Comparison with ice sheet models

The $\delta^{18}O$ record from the Byrd ice core indicates that the age of ~10 ka for the most recent ice sheet high stand at Mt. Waesche falls near the end of a 3000 year period of strong warming in West Antarctica that peaked at the start of the Holocene (Sowers and Bender, 1995). While it is tempting to correlate this high stand with millennial scale climate events of the last deglaciation, the surface exposure ages are not sufficiently precise to be conclusive. As shown below, the WAIS high stand at Mt. Waesche, is probably not simply a response to increased accumulation during deglaciation.

Chronologic data from the Ross Embayment indicates that the WAIS advanced across the Ross Sea to the vicinity of Coulman Island during the LGM and that grounding line retreat was well underway by 11 ka (Domack *et al.*, 1999; Licht *et al.*, 1999; Licht *et al.*, 1996; Shipp *et al.*, 1999) and passed Ross Island ~8 ka (Hall and Denton, 1999). Grounding line retreat may have begun as early as 14 ka, in response to sea level rise resulting from the melting of Northern Hemisphere ice sheets. Apparently, maximum ice elevations around Mt. Waesche occurred several thousand years *after* the maximum ice extent in the Ross Sea.

In order to better understand the implications of these results, the data from Mt. Waesche were compared with a quasi-3D ice sheet model of the WAIS. The model provides a finite element solution of a 2-D (map-plane) time dependent mass continuity equation that integrates ice flow in a vertical column of ice (Fastook and Prentice, 1994; Steig *et al.*, 1999). Ice sheet growth and decay in this model is driven solely by changes in calving rates, which simulates the effects of sea level change on the ice sheet. This simple approach is justified by results from more complex 3-D time-dependent thermomechanical ice sheet models that suggest that eustatic sea level is the primary control on the configuration of the West Antarctic Ice Sheet (Huybrechts, 1990a).

The ice sheet model reproduced the present ice sheet with modern boundary conditions. The model was then tuned to fit the available chronology of ice advance and deglaciation from the Ross Embayment. The calving rate (ablation) was set to zero and the model ice sheet allowed to advance into the Ross Sea for 4900 model years, which resulted in a grounding line near Coleman Island. Calving rates were then increased so that grounding line began to retreat. The calving rate was held constant and adjusted so that the grounding line passed McMurdo Sound after ~3000 model years (~8000 ka). With the calving rate held constant, the present ice configuration was reached after 10,000 model years (~1000 ka). The advance and retreat simulation was repeated twice to eliminate model instabilities.

In the model, the maximum ice elevation at Mt. Waesche occured several thousand years after the start of deglaciation; the difference between the maximum elevation and that at the end of the model run was 40 m (Figure 3.9). An important result of this model is that the WAIS does not have sufficient time to equilibrate with its extended grounding line position during the LGM, which is consistent with the model results of Huybrechts (1990b). As a result, interior elevations are always *lower* than those that would occur if the ice sheet reached equilibrium. During retreat of the grounding line, interior elevations continue to thicken as long as the interior ice elevations are lower than the equilibrium height for the grounding line position at that time. Eventually, the initial wave of thinning reaches the interior of the ice sheet and rapid thinning occurs (Figure 3.10).

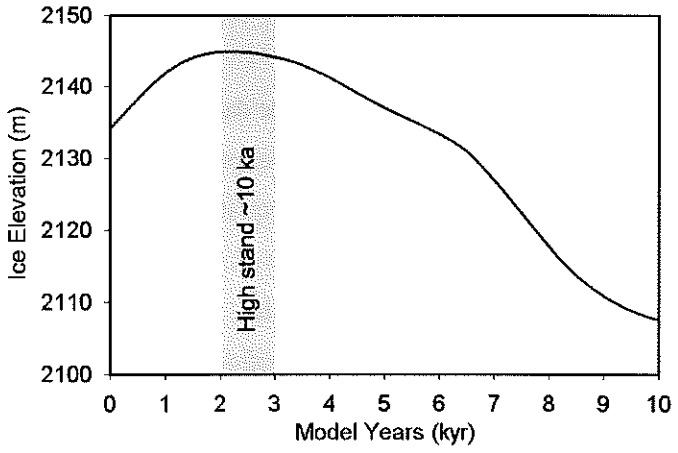

Figure 3.9 Elevation changes at Mt. Waesche generated by the ice sheet model tuned to the existing chronology from the Ross Embayment (see text). Model years are time since the start of deglaciation. Maximum ice elevations occur over 2000 years after the start of deglaciation in the Ross Sea (14-11 ka). The model elevations are for the 20 x 20 km grid unit containing Mt. Waesche, not necessarily the elevation at the sample sites; the relative elevation change is more significant than the absolute elevations. The timing and magnitude of ice elevation changes at Mt. Waesche are similar to the glacial geologic evidence.

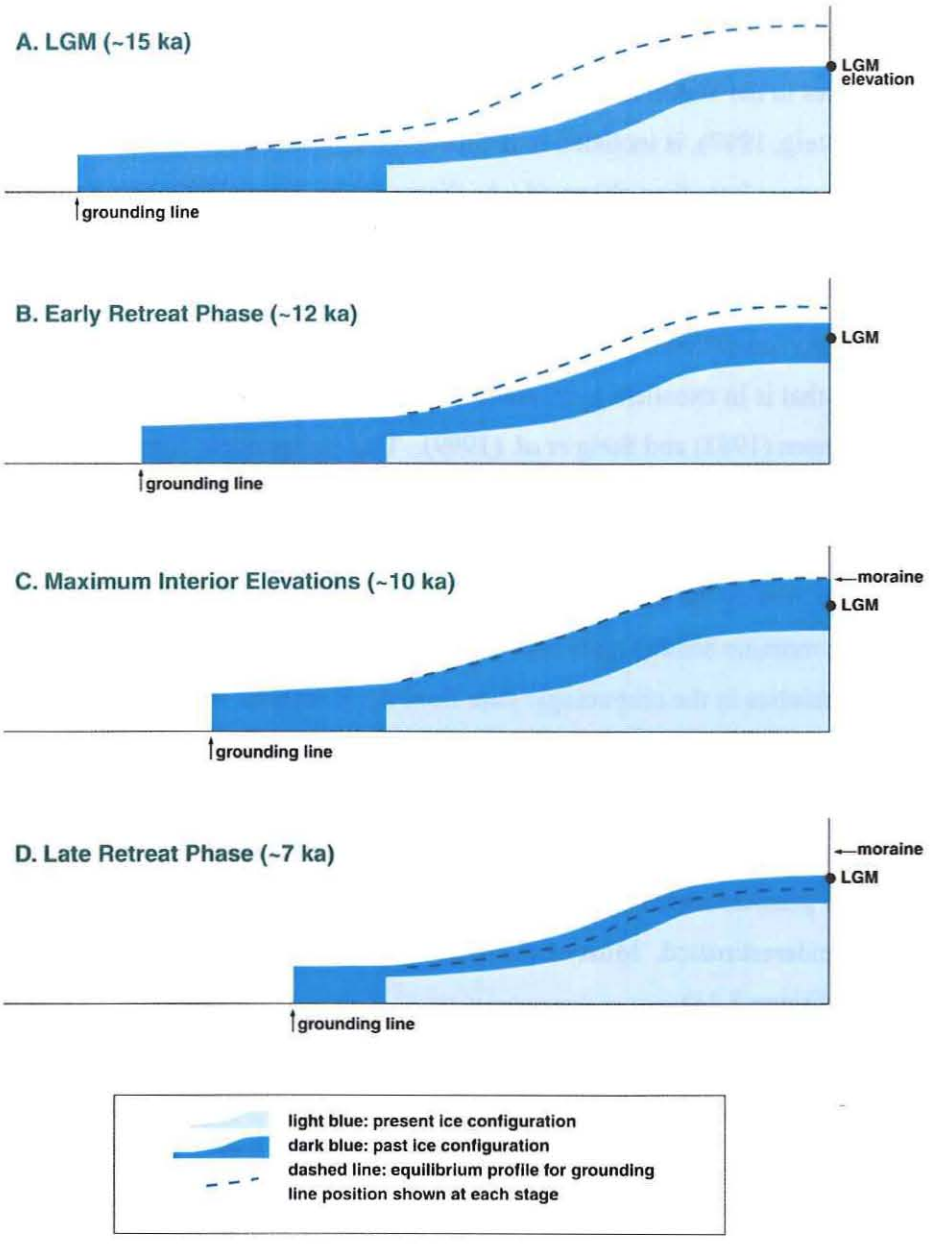

Figure 3.10 Cartoon showing elevation changes of the interior of WAIS during the last deglaciation. A) Ice sheet profile during the LGM, just prior to retreat of the grounding line in response to sea level rise. The ice profile is not in equilibrium with the extended grounding line. B) Ice profiles during early retreat phase. The equilibrium profile is still higher than the actual profile so ice thickening continues in the interior. C) Ice profiles when maximum elevations occur in interior. The initial wave of thinning has reached the interior; equilibrium and actual profiles coincide. Deposition of boulders on uppermost part of the lower moraine band occurs. D) Ice profiles during late retreat phase. Equilibrium profile is lower than actual profile. Interior elevations lower due to grounding line retreat. Deposition of boulders on lower moraine band continues.

The model results are remarkably consistent with the glacial geologic evidence at Mt. Waesche. This result may be somewhat serendipitous: if a factor-of-two change in snow accumulation rates in the WAIS interior between the LGM and the Holocene, as indicated by ice core data (*e.g.*, Steig, 1997), is included in the model, maximum elevations are lower and occur several thousand years later than observed. As discussed by Steig (1999) this implies that the current version of the model may overestimate the ice-dynamics response time to changes in boundary conditions, likely because of unrealistic simulation of ice stream dynamics. On the other hand, with accumulation held constant, the model produces an elevation history for interior West Antarctica that is in excellent agreement with elevation changes inferred for the Byrd ice core both by Jenssen (1983) and Steig *et al.* (1999). This independent corroboration of the model-derived elevation history suggests that it is substantially correct.

The model time scale (years after the start of grounding line retreat) can be converted to calendar years by pinning the maximum ice elevations predicted at Mt. Waesche to the age of the lower part of the moraine band (Figure 3.10). This implies that deglaciation began ~12 ka, well within the uncertainties in the chronologic data from the Ross Sea. The model results may then be used to constrain the timing and magnitude of Holocene ice volume changes in the Ross Sea sector of the WAIS. In the model, most ice volume is lost early (Figure 3.11). By ~10 ka (2000 model yrs) only ~3 m sea level equivalent (ice volume above sea level) remains. Because the model accurately predicts ice levels at Mt. Waesche, it is unlikely that the interior WAIS volume is significantly underestimated. Most of the remaining ice is released during a short pulse in the early Holocene (Figure 3.11).

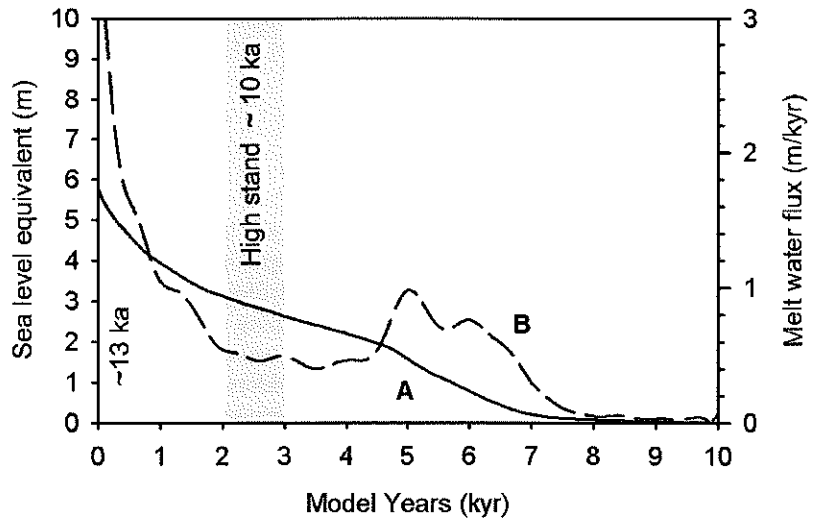

Figure 3.11 Ice volume expressed as sea level equivalent and melt water flux from the Ross Sea sector of the WAIS during deglaciation generated by the ice sheet model. Model years are time since the start of deglaciation. (A) Ice volume. Only ~3 m of sea level equivalent remains at ~10 ka. (B) Melt water flux. Maximum Holocene values are ~1 m/kyr and occur during the middle Holocene.

These results have implications for the contribution of the WAIS to eustatic sea level rise during the last termination. The WAIS has been suggested as the source of the two melt water pulses responsible for the abrupt rises in sea level recorded in the Barbados coral record (Fairbanks, 1989). Clark (1996) attributed the first melt water pulse to Antarctica through a process of elimination of potential Northern Hemisphere sources. The ice mass responsible for meltwater pulse 1B is located in Antarctica in global models of deglaciation based upon geophysical predictions of post-glacial relative sea level change (ICE-3G and ICE-4G) (Peltier, 1994; Tushingham and Peltier, 1991). Melt water pulse 1B, is a ~28 m of sea level rise in 1000 yrs centered on 11 ka. The results presented here suggest that there is insufficient ice volume in the WAIS for it to be the primary source of either melt water pulse 1A or 1B. This conclusion is not strongly dependent on the ice sheet model. The glacial chronology places an upper limit on ice thickness near a dome of the WAIS and constrains the magnitude of interior ice draw down during the Holocene. The potential contribution of the EAIS to the meltwater pulses needs to be explored.

Upper moraine band: Evidence for earlier ice sheet high stands

Most of the surface exposure ages on the upper moraine band fall within stadials in the marine isotope record (Figure 3.12), and the others fall within interglacial cool periods. Evidence for earlier advances of the WAIS is found in McMurdo Sound (Brook *et al.*, 1995; Denton *et al.*, 1989b) (Chapter 5) and along outlet glaciers of the Transantarctic Mountains (Bockheim *et al.*, 1989; Denton *et al.*, 1989a; Mercer, 1968) (Chapter 4). In the McMurdo area the penultimate glaciation dates to stage 6 (Denton *et al.*, 1989b; Kurz and Ackert, 1996). Given that earlier expansions of the WAIS have occurred, evidence of earlier ice sheet high stands at Mt. Waesche is expected. Cold-based ice frozen to its bed can override surfaces without causing significant disturbance, even leaving desert pavements intact (Bockheim *et al.*, 1989). It is tentatively concluded that the upper part of the moraine band was deposited during multiple, overlapping glacial advances.

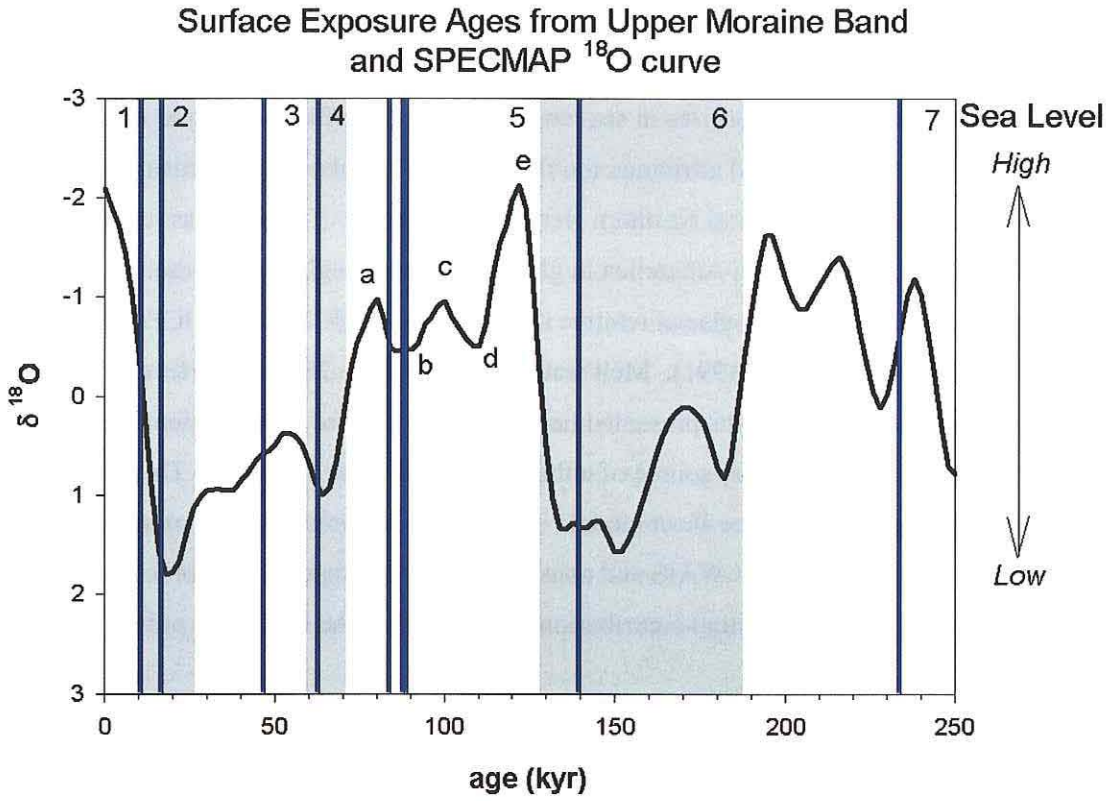

Figure 3.12 Comparison of surface exposure ages from the upper part of the moraine band with the Specmap oxygen isotope record (Imbrie *et al.*, 1982). Stages are numbered; glacial stages are shaded. The thin bars indicate the calculated exposure ages and do not encompass the uncertainty which is ~10%. All ages fall near relative maxima in $\delta^{18}O$ (larger global ice volume, lower sea levels). Sea level during stage 5b is estimated to be 60 m lower than present.

The distribution of exposure ages is consistent with expansions of the WAIS during glacial stages but also suggests that expansions occurred during interglacial stages as well. It is striking that all of the exposure ages fall on relative maxima in the marine $\delta^{18}O$ record. Two ages fall near the end of stage 6, analogous to samples from the lower moraine band. One sample falls within stage 3 and another within stage 4. Three ages fall within interstadial 5b. In contrast to other locations where the surface exposure ages scatter, all of the interstadial 5b ages are from a single location (WA-4B). This location is a well-developed ridge within the upper moraine that is interpreted as an ice margin position. The ages form a tight cluster with a mean of 86.3 ± 2.7 ka. Sea levels were roughly 65 m below present at that time (Chapman and Shackleton, 1999; Shackleton, 1987). Thus, an ice sheet high stand during interstadial 5b is also consistent with models in which sea level controls WAIS extent. Because the WAIS probably never obtains an equilibrium profile, interior ice sheet elevations may not correlate directly with grounding line

position which presumably was less advanced during interstadial 5b than during the LGM. Prior ice sheet history and accumulation rates will also effect dome elevations, so higher interior ice levels during stage 5b than during stage 2 are conceivable. Nunataks such as Mt. Waesche may preserve a more complete record of WAIS fluctuations than areas near the ice sheet margin, where only the largest expansions of the ice sheet are preserved.

If all the surface exposure ages from the upper moraine band record past ice margins, sample WA-3A-2, may indicate that WAIS elevations were up to 85 m above the present ice surface at Mt. Waesche ~10 ka. The age of this sample falls within the age range of samples from the lower part of the moraine band and is comparatively unweathered. In this case, the ice sheet elevation determined from the lower moraine band is underestimated. However, the main conclusions regarding WAIS chronology and ice volume would be unchanged. Further work to determine the depositional processes on the upper part of the moraine band is required to resolve this issue.

3.5 Conclusions

Lateral moraine bands at Mt. Waesche gauge past ice levels in interior West Antarctica. Ice levels recorded by the lower moraine band reached elevations at least 45 m above the present ice surface ~10 ka, several thousand years after maximum ice extent was reached in the Ross Embayment. Similar results are produced by a non-equilibrium ice sheet model tuned to existing deglaciation chronologies in the Ross Sea. The combined results indicate that the glacial chronology at Mt. Waesche is consistent with other data for the Ross Embayment and with the WAIS being out of equilibrium during the LGM. The calculated Holocene contribution of the WAIS to sea level rise is ~3 m, significantly less than that commonly assumed in most deglaciation models.

The upper moraine band likely records multiple earlier WAIS high stands. The surface exposure ages are widely scattered, but fall within glacial periods in the marine isotope record consistent with models in which sea level controls WAIS extent. Although the data is sparse, it appears that expansions of the WAIS occurred during both interglacial and glacial stages. The best evidence for an earlier high stand, a cluster of ages from a single location, occurs during interstadial 5b.

Paired ^{3}He and ^{36}Cl ages are concordant with low erosion rates. The isotope pair is well suited to basaltic lithologies and can constrain erosion rates on samples as young as 10 ka.

References

Anderson, J.B., Shipp, S.S., Bartek, L.R., and Reid, D.E., 1992, Evidence for a grounded ice sheet on the Ross Sea continental shelf during the late Pleistocene and preliminary paleodrainage reconstruction, *in* Kennett, J.P., and Warnke, D.A., eds., *The Antarctic Paleoenvironment: A perspective on global change*, Volume 57: Antarctic Research Series: Washington, D. C., American Geophysical Union, p. 39-62.

Behrendt, J.C., LeMasurier, W.E., and Cooper, A.K., 1992, The West Antarctic rift system -- A propagating rift "captured" by a mantle plume, *in* Kaminuma, K., and Yoshida, Y., eds., *Recent progress in Antarctic Earth Science*: Tokyo, Terra, p. 315-322.

Bockheim, J.G., Wilson, S.C., and Denton, G.H., 1989, Late Quaternary ice-surface fluctuations of Hatherton Glacier, Transantarctic Mountains: *Quaternary Research*, **v. 31**, p. 229-254.

Brook, E.J., Kurz, M.D., Ackert, R.P., Jr., Denton, G.H., Brown, E.T., Raisbeck, G.M., and Yiou, F., 1993, Chronology of Taylor Glacier advances in Arena Valley, Antarctica, using *in situ* cosmogenic ^{3}He and ^{10}Be: *Quaternary Research*, **v. 39**, p. 11-23.

Brook, E.J., Kurz, M.D., Ackert, R.P., Jr., Raisbeck, G., and Yiou, F., 1995, Cosmogenic nuclide exposure ages and glacial history of late Quaternary Ross Sea Drift in McMurdo Sound, Antarctica: *Earth and Planetary Science Letters*, **v. 131**, p. 41-56.

Brown, E.T., Edmond, J., Raisbeck, G.M., Yiou, F., Kurz, M.D., and Brook, E.J., 1991, Examination of surface exposure ages of Antarctic moraines using *in-situ* produced ^{10}Be and ^{26}Al: *Geochimica et Cosmochimica Acta*, **v. 55**, p. 2269-2283.

Cerling, T.E., and Craig, H., 1994, Cosmogenic ^{3}He production rates from 39°N to 46°N latitude, western USA and France: *Geochimica Cosmochimica Acta*, **v. 58**, p. 349-255.

Chapman, M.R., and Shackleton, N.J., 1999, Global ice-volume fluctuations, North Atlantic ice-rafting events, and deep ocean circulation changes between 130 and 70 ka: *Geology*, **v. 27**, p. 795-798.

Clark, P.U., Alley, R.B., Keigwin, L.D., Licciardi, J.M., Johnsen, S.J., and Wang, H., 1996, Origin of the first global meltwater pulse following the last glacial maximum: *Paleoceanography*, **v. 11**, p. 563-577.

Denton, G.H., Bockheim, J.G., Wilson, S.C., Leide, J.E., and Anderson, B.G., 1989a, Late Quaternary ice-surface fluctuations of Beardmore Glacier, Transantarctic Mountains: *Quaternary Research*, **v. 31**, p. 189-209.

Denton, G.H., Bockheim, J.G., Wilson, S.C., and Stuiver, M., 1989b, Late Wisconsin and early Holocene glacial history, inner Ross Embayment, Antarctica.: *Quaternary Research*, **v. 31**, p. 151-182.

Denton, G.H., Prentice, M.L., and Burkle, L.H., 1991, Cainozoic history of the Antarctic ice sheet, *in* Tingey, R.J., ed., *The Geology of Antarctica: Oxford*, Clarendon Press, p. 365-419.

Domack, E.W., Jacobson, E.A., Shipp, S., and Anderson, J.B., 1999, Late Pleistocene/Holocene retreat of the West Antarctic Ice Sheet: Part 2- Sedimentologic and stratigraphic signature.: *Geological Society of America Bulletin*, **v. 111**, p. 1517-1536.

Dunbar, N.W., Esser, R.P., and McIntosh, W.C., 1999, Englacial tephra layers in West Antarctica: Implications for the history of the West Antarctic Ice Sheet: Antarctic Journal of the United States, review 1998, v. in press.

Fairbanks, R.G., 1989, A 17,000-year glacio-eustatic sea level record: Influence of glacial melting rates on the Younger Dryas event and deep-ocean circulation: *Nature*, **v. 342**, p. 637-642.

Fastook, J.L., and Prentice, M., 1994, A finite-element model of Antarctica: sensitivity test of meteorological mass-balance relationships: *Journal of Glaciology*, **v. 40**, p. 167-175.

Gosse, J.C., Klein, J., Evenson, E.B., Lawn, B., and Middleton, R., 1995, Beryllium -10 dating of the last Pinedale glacial sequence: *Science*, **v. 268**, p. 1329-1333.

Grootes, P., and Stuiver, M., 1986, Ross Ice Shelf oxygen isotopes and West Antarctic climate history: *Quaternary Research*, **v. 26**, p. 49-67.

Hall, B.L., and Denton, G.H., 1999, Radiocarbon chronology of Ross Sea drift, eastern Taylor Valley, Antarctica: Evidence for a grounded ice sheet in the Ross Sea at the LGM: *Geografiska Annaler*, v. in press.

Huybrechts, P., 1990a, A 3-D model for the Antarctic Ice Sheet: A sensitivity study on the glacial-interglacial contrast: *Climate Dynamics*, **v. 5**, p. 79-92.

Huybrechts, P., 1990b, The Antarctic ice sheet during the last glacial-interglacial cycle: A three dimensional experiment: *Annals of Glaciology*, **v. 5**, p. 115-119.

Imbrie, J., Hays, J.D., Martinson, D.G., McIntyre, A., Mix, A.C., Morley, J.J., Pisias, N.G., Prell, W.L., and Shackleton, N.J., 1982, The orbital theory of Pleistocene climate: Support from a revised chronology of the marine $\delta^{18}O$ record, *in* Berger, A., Imbrie, J., Hays, J., Kukla, G., and Saltzman, B., eds., *Milankovitch and Climate*: Boston, D. Reidel.

Jenssen, D., 1983, Elevation and climate hanges from total gas content and stable isotopic measurements, *in* Robin, G.d.Q., ed., *The climate record in polar ice sheets*: London, Cambridge University Press, p. 138-144.

Kurz, M.D., 1986, *In situ* production of terrestrial cosmogenic helium and some applications to geochronology: *Geochimica et Cosmochimica Acta*, **v. 50**, p. 2855-2862.

Kurz, M.D., and Ackert, R.P., Jr., 1996, Ice volume in the Ross Sea during Glacial Maximum: Geochronological Evidence from Mt. Morning , Antarctica: *EOS, Trans. AGU*, **v. 76**, p. F182.

Lal, D., 1991, Cosmic ray labeling of erosion surfaces: *In situ* nuclide production rates and erosion models: *Earth and Planetary Science Letters*, **v. 104**, p. 424-439.

LeMasurier, W., and Kawachi, Y., 1990, Mt. Waesche, *in* LeMasurier, W., and Thompson, J.W., eds., *Volcanoes of the Antarctic plate and Southern Oceans, Volume 48: Antarctic Research Series*: Washington D. C., American Geophysical Union, p. 208-211.

LeMasurier, W., and Rex, D.C., 1989, Evolution of linear volcanic ranges in Marie Byrd Land , West Antarctica*: Journal of Geophysical Research*, **v. 94**, p. 7223-7236.

Licciardi, J.M., Kurz, M.D., and Clark, P.U., 1999, Calibration of cosmogenic ^{3}He production rates: Results from Holocene lava flows: *Earth and Planetary Science Letters*, **v. 172**, p. 261-271.

Licht, K.J., Dunbar, N.W., Andrews, J.T., and Jennings, A.E., 1999, Distinguishing subglacial till and glacial marine diamictons in the western Ross Sea, Antarctica: Implications for last glacial maximum grounding line: *Geological Society of America Bulletin*, **v. 111**, p. 91-103.

Licht, K.J., Jennings, A.E., Andrews, J.T., and Williams, K.M., 1996, Chronology of late Wisconsin ice retreat from the western Ross Sea, Antarctica: *Geology*, **v. 24**, p. 223-226.

Liu, B., Phillips, F.M., Fabryka-Martin, J.T., Fowler, M.M., and Stone, W.D., 1994, Cosmogenic ^{36}Cl accumulation in unstable landforms1. Effects of the thermal neutron distribution: *Water Resources Research*, **v. 30**, p. 3115-3125.

MacAyeal, D.R., 1992, Irregular oscillations of the West Antarctic ice sheet: *Nature*, **v. 359**, p. 29-32.

Martinerie, P., Raynaud, D., Etheridge, D.M., Barnola, J., and Mazaudier, D., 1992, Physical and climatic parameters which influence the air content in polar ice: *Earth and Planetary Science Letters*, **v. 112**, p. 1-13.

Mercer, J.H., 1968, Glacial geology of the Reedy Glacier Area, Antarctica: *Geological Society of America Bulletin*, **v. 79**, p. 471-486.

Mercer, J.H., 1978, West Antarctic ice sheet and the CO_2 greenhouse effect: A threat of disaster: *Nature*, **v. 271**, p. 321.

Nishiizumi, K., Kohl, C.P., Arnold, J.R., Klein, J., and Fink, D., 1991, Cosmic ray produced ^{10}Be and ^{26}Al in Antarctic rocks: Exposure and erosion rates: *Earth and Planetary Science Letters*, **v. 104**, p. 440-454.

Oppenheimer, M., 1998, Global warming and the stability of the West Antarctic Ice Sheet: *Nature*, **v. 393**, p. 325-332.

Peltier, W.R., 1994, Ice Age Paleotopography: *Science*, **v. 265**, p. 195-201.

Phillips, F.M., and Plummer, M.A., 1996, CHLOE: A program for interpreting *in situ* cosmogenic nuclide data for surface exposure dating and erosion studies. (abstr.): *Radiocarbon*, **v. 38**, p. 98.

Phillips, F.M., Zreda, G.M., Gosse, C.J., Klein, J., Evenson, E.B., Hall, R.D., Chadwick, O.A., and Sharma, P., 1997, Cosmogenic ^{36}Cl and ^{10}Be ages of Quaternary glacial and fluvial deposits of the Wind River Range, Wyoming: *Geological Society of America Bulletin*, **v. 109**, p. 1453-1463.

Phillips, F.M., Zreda, M.G., Benson, L.V., Plummer, M.A., Elmore, D., and Sharma, P., 1996a, Chronology for fluctuations in Late Pleistocene Sierra Nevada Glaciers and Lakes: *Science*, **v. 274**, p. 749-751.

Phillips, F.M., Zreda, M.G., and Flinsch, M.R., 1996b, A reevaluation of cosmogenic ^{36}Cl production rates in terrestrial rocks: *Geophysical Research Letters*, **v. 23**, p. 949-952.

Raynaud, D., and Lebel, B., 1979, Total gas content and elevation of polar ice sheets: *Nature*, **v. 281**, p. 289-291.

Raynaud, D., and Whillans, I.M., 1982, Air content of the Byrd Core and past changes in the West Antarctic Ice Sheet: *Annals of Glaciology*, **v. 3**, p. 269-273.

Schäfer, J.M., Ivy-Ochs, S., Wieler, R., Leya, I., Baur, H., Denton, G.H., and Schlüchter, C., 1999, Cosmogenic noble gas studies in the oldest landscape on earth: surface exposure ages of the Dry Valleys, Antarctica: *Earth and Planetary Science Letters*, **v. 167**, p. 215-226.

Shackleton, N.J., 1987, Oxygen isotopes, ice volume and sea level: *Quaternary Science Reviews*, **v. 6**, p. 183-190.

Shipp, S., Anderson, J.B., and Domack, E.W., 1999, Late Pleistocene/Holocene Retreat of the West Antarctic Ice-sheet System in the Ross Sea: *Geological Society of America Bulletin*, **v. 111**, p. 1486-1516.

Sowers, T., and Bender, M., 1995, Climate records covering the last deglaciation: *Science*, **v. 269**, p. 210-213.

Steig, E.J., 1997, How well can we parameterize past accumulation rates in polar ice sheets?: *Annals of Glaciology*, **v. 25**, p. 418-422.

Steig, E.J., Fastook, J.L., Ackert, R.P., Jr., White, J.W.C., Licht, K.L., Zweck, C., and Goodwin, I., 1999, West Antarctic Ice Sheet elevation changes, *Antarctic Research Series, American Geophysical Union*, p. in press.

Stone, J.O., 1999, Air pressure and cosmogenic isotope production: *Journal of Geophysical Reviews*, p. in review.

Tushingham, A.M., and Peltier, W.R., 1991, Ice-3G: A new global model of late Pleistocene deglaciation based upon geophysical predictions of post-glacial relative sea level change: *Journal of Geophysical Research*, **v. 96**, p. 4497-4523.

Appendix 3.1 Sample Data from Mt. Waesche

Sample	Lithology	Minerology	Elev. (m)	Latitude (S)	Longitude (W)
Supraglacial debris					
DB-94-1	black basalt	plag, ol, cpx, crustal xeno	1935	77° 14.85'	127° 01.19'
BIT-252	black basalt	plag, ol, cpx	1935	77° 14.85'	127° 01.19'
Transect 4, moraine boulders					
WA-4D-1	black vesicular basalt	ol, cpx, plag	2010	77° 12.05'	127° 07.47'
WA-4D-3	black vesicular basalt	ol, cpx, plag	2010	77° 12.05'	127° 07.47'
WA-4C-1	black vesicular basalt	ol, cpx, plag	2015	77° 12.04'	127° 07.09'
WA-4C-2	black vesicular basalt	ol, cpx, plag	2015	77° 12.04'	127° 07.09'
WA-4B-1	black vesicular basalt	ol, cpx, plag	2035	77° 12.08'	127° 06.73'
WA-4B-2	dark grey basalt	rare plag	2035	77° 12.08'	127° 06.73'
WA-4B-3	black vesicular basalt	ol, cpx, plag	2035	77° 12.08'	127° 06.73'
WA-4A-1	basalt	plag, sparce large ol	2040	77° 12.13'	127° 06.29'
WA-4A-2	dark grey basalt	sparce plag	2040	77° 12.13'	127° 06.29'
Transect 3, moraine boulders					
WA-3E-1	gray basalt	large plag; sparce ol, cpx	1945	77° 13.30'	127° 04.36'
WA-3D-1	gray basalt	large plag; sparce ol, cpx	1985	77° 13.30'	127° 04.36'
WA-3D-2	gray basalt	large plag; sparce ol, cpx	1985	77° 13.30'	127° 04.36'
WA-3B-1	gray basalt	large plag; sparce ol, cpx	2025	77° 13.18'	127° 03.67'
WA-3B-2	gray basalt	large plag; sparce ol, cpx	2025	77° 13.18'	127° 03.67'
WA-3A-1	dark grey basalt	plag, ol, crustal xeno	2035	77° 13.18'	127° 03.39'
WA-3A-2	black vesicular basalt	ol, cpx, plag	2035	77° 13.18'	127° 03.39'
Isolated moraine patch					
WA-2-1	basalt	plag, sparce large ol	1975	77° 13.89'	126° 55.07'
Lava Flow					
WA-11	black vesicular basalt	rare large ol, plag	2055	77° 13.67'	126° 54.84'
WA-5	black vesicular basalt	rare large ol, plag	2055	77° 13.67'	126° 54.84'

ol = olivine; cpx = clinopyroxene; plag = plagioclase; xeno = xenoliths
Latitude and longitude determined by GPS. Elevations are by altimeter

Appendix 3.2 Major and trace element concentration of ^{36}Cl samples

Sample	SiO_2	Al_2O_3	CaO	MgO	Na_2O	K_2O	Fe_2O_3	MnO	TiO_2	P_2O_5	Sm	B	Gd
	%	%	%	%	%	%	%	%	%	%	ppm	ppm	ppm
WA-4A-2	53.0	17.6	6.10	2.03	6.25	2.14	11.00	0.25	1.600	0.57	12.1	15.0	08.0
WA-4B-2	51.8	17.1	6.16	2.28	6.17	2.10	11.00	0.23	1.821	0.66	13.1	16.5	08.0
WA-4C-1	44.8	13.5	10.50	10.80	2.49	0.78	14.20	0.22	2.476	0.42	07.2	14.0	07.0
WA-4D-1	44.6	13.4	10.50	10.70	2.54	0.80	14.00	0.21	2.447	0.40	07.8	10.5	07.0

Major elements measured by XRF. B and Gd measured by prompt gamma and Sm by NNA.
All measurements made at XRAL Laboratories, Don Mills, Ontario

CHAPTER 4

Plio/Pleistocene fluctuations of the Antarctic Ice sheets: Surface exposure geochronology from the Beardmore Glacier

4.1 Introduction

The history of the Antarctic ice sheets is of fundamental importance due to their role in global climate. Reconstructions of the past geometry of the ice sheets are key inputs to global climate models and a knowledge of past Antarctic ice volume is important for interpreting marine oxygen isotope and sea level records. Well-dated glacial chronologies provide constraints for ice sheet models used to reconstruct past ice sheet geometries. Projected anthropogenic warming during the next century could conceivably cause the collapse of parts of the Antarctic ice sheets with dramatic effects on global sea level. The response of the Antarctic ice sheets to the last glacial/interglacial transition is of particular interest.

The Transantarctic Mountains (TAM) separate the largely terrestrial East Antarctic Ice Sheet (EAIS) from the marine West Antarctic Ice Sheet (WAIS) (Figure 4.1). Outlet glaciers of the EAIS flow through the mountains into the Ross Ice Shelf or the Ross Sea. Because they are located in the interior and link both ice sheets, the glacial deposits adjacent to outlet glaciers in the southern TAM potentially record fluctuations of the elevation of both the East and West Antarctic ice sheets. The extent of the WAIS is determined principally by sea level which controls the grounding line position of the ice sheet. During the Pleistocene, sea level is driven primarily by the growth and decay of Northern Hemisphere ice sheets. Therefore, in spite of the fact that Milankovitch forcing in the Southern Hemisphere is out of phase with that of the north (Crowley and North, 1991), it is thought that the WAIS fluctuated synchronously with the Northern Hemisphere ice sheets (Hollin, 1962). The EAIS, grounded largely above sea level, is thought to be less sensitive to changes in sea level. However, even relatively small advances on the margins of the EAIS over the continental shelf may result in significant ice volume changes due to the long length of the margin. In contrast to the periphery of the ice sheet, the chronology of ice sheet fluctuations in interior Antarctica is poorly constrained. Knowledge of the timing and magnitude of the interior ice elevation changes is necessary to constrain ice volumes and the response times of the ice sheet. Knowledge of ice sheet behavior during previous glacial periods is even more uncertain.

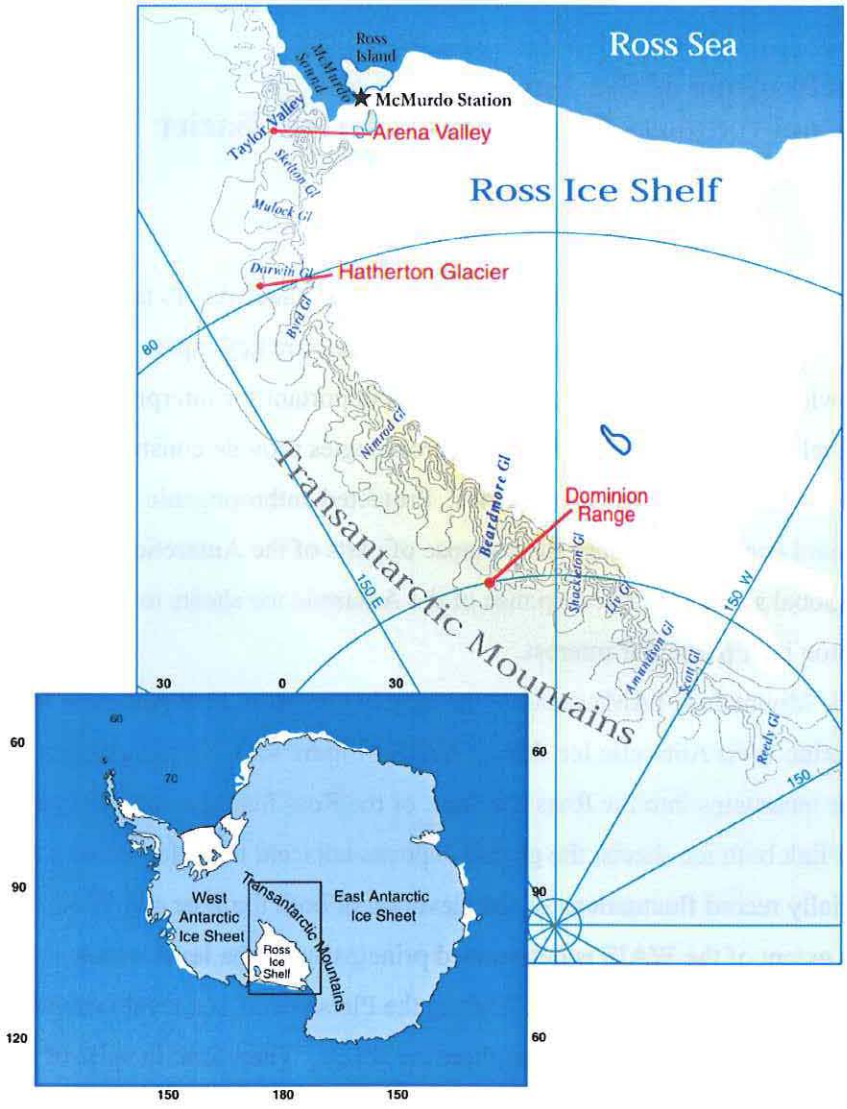

Figure 4.1 Location Map of Antarctica and the Transantarctic mountains showing key locations mentioned in text.

The Dominion Range, at the head of the Beardmore Glacier (Figure 4.2), contains a well-preserved moraine sequence which is inferred on the basis of rock weathering studies to range in age from the Holocene through the Pliocene (Denton *et al.*, 1989a; Mercer, 1972). The moraines preserve a detailed record of past fluctuations of the upper Beardmore Glacier. Because the Beardmore Glacier connects the Ross Ice Shelf and the EAIS, a chronology of the moraines provides insight to the behavior and interaction between the East and West Antarctic ice sheets. In addition, the moraines overlie Sirius Group sediments which are important due to the presence of *in situ Nothofagus* (Southern Beech) as well as marine microfossils. The co-occurrence of these fossils has been used to infer significantly warmer Pliocene temperatures in Antarctica and

a dynamic EAIS. Faults which displace these Sirius deposits are used to infer over 1000 m of tectonic uplift of this block of the TAM since their deposition (McKelvey *et al.*, 1991). However, the Pliocene age of these deposits is in dispute because the age-diagnostic microfossils are reworked. It is suggested based on geomorphic arguments that the Sirius sediments are much older (*e.g.,* Clapperton and Sugden, 1990). The age of the oldest overlying moraines provide an independent minimum age for the key Sirius sediments.

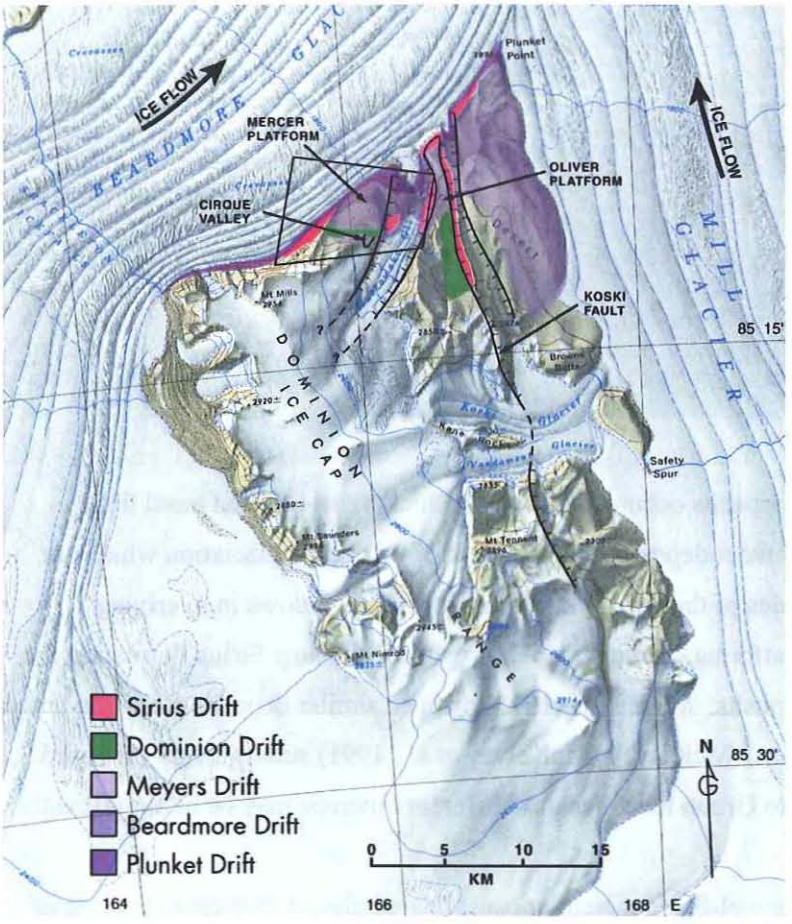

Figure 4.2 Map of Dominion Range at the confluence of the Beardmore and Mill Glaciers showing glacial drifts, faults and location names. The grounding line is 150 km to the north. Base map is part of the Plunket Point 1;250,000 series topographic maps published by the U.S.G.S. Box shows location of Figure 4.8.

4.2 Geological background

Introduction

The bedrock of the Dominion Range is composed of flat-lying Permian Buckley Formation and Triassic Fremouw Formation of the Beacon Super Group Sandstones which are intruded by Jurassic Ferrar Dolerite sills (Elliot *et al.*, 1974; Oliver, 1964). Two broad benches

occur adjacent to the Beardmore Glacier on the northern side of the range. The benches are separated by a trough containing the Rutkowski Glacier, which drains an ice cap on the Dominion Range (Figure 4.2). Southwest (up glacier) of the benches, steep cliffs up to 500 m high supply debris to the glacier surface (Figure 4.3).

Figure 4.3 Photograph of Mercer Platform, looking down glacier (northeast). The steep cliffs in the foreground supply debris to the Beardmore Glacier.

Two types of glacial deposits occur. The first are thick, semi-lithified basal tills, stratified sediments and ice-contact deposits characteristic of wet-based glaciation which are exposed in bluffs along the sides of the Beardmore Glacier and in windows in overlying unconsolidated drift on the platforms. Mercer (1972) proposed the name Sirius Formation for these semi-lithified glacial deposits. Mayewski (1975) mapped similar deposits along the length of the Transantarctic Mountains. McKelvey (McKelvey *et al.*, 1991) subsequently proposed raising the stratigraphic rank to Group level because different outcrops may be of significantly different age.

The second type are gravel-boulder rich, unconsolidated glacial drift characteristic of cold-based glaciation which overlies Sirius drift and bedrock. This drift typically consists of bouldery lateral moraine ridges up to several meters high and thinner intervening drift sheets which record fluctuations of the Beardmore and Rutkowski Glaciers. Near the present Beardmore Glacier, the drift is commonly ice-cored. The chronology of these unconsolidated glacial drifts is the subject of this chapter.

Lateral moraines

The benches in the northern Dominion Range are overlain by a remarkably well-preserved series of moraine ridges and thin glacial drift composed of boulders and gravel (Denton *et al.*, 1989a; Mercer, 1972) (Figure 4.4). These drifts record expansions of the Beardmore Glacier as well as the Rutkowski Glacier. The moraines are composed of sandstone and dolerite, with rare limestone conglomerate and granite erratics. The drift covers the Meyer Desert, Oliver Platform, and the platform to the southwest of the Rutkowski Trough, here informally referred to as the Mercer Platform (Figure 4.2). The younger, proximal drift, and moraines conformably overlie small fault scarps, while some older moraines are cut by them.

In contrast to the Sirius deposits, the drift lacks a glacial-fluvial component and was laid down in the absence of meltwater. The drift is typical of that deposited by polar glaciers that are frozen to the underlying bed. However, striated clasts and boulders are common. The eroding cliffs of Sirius Group tillites which occur along the margin of the Beardmore Glacier to the west are probably the source of many of the striated boulders (Figure 4.3). Alternatively, some may be derived from the base of the contemporaneous Beardmore glacier because striated clasts occur on the glacier surface further west than the observed Sirius outcrops suggesting that the thicker parts of the glacier are wet-based.

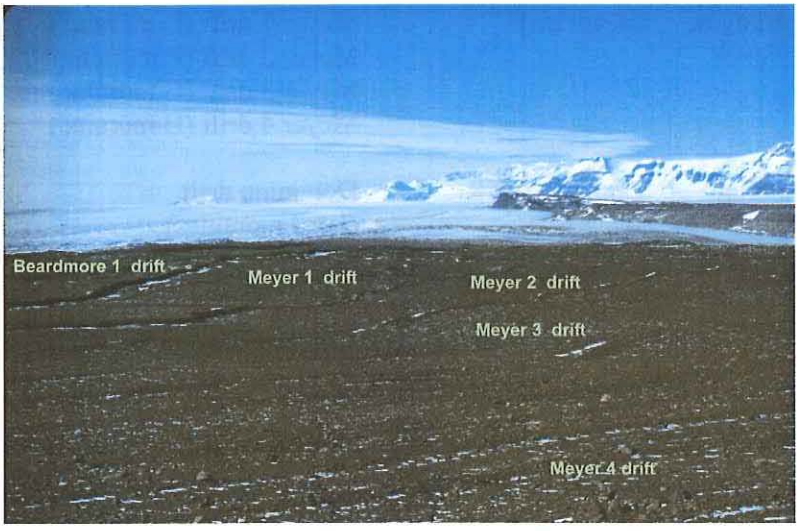

Figure 4.4 Photograph of well-preserved lateral moraines on the Mercer Platform. The moraines are sub parallel ridges composed of boulder to gravel sized debris. Glacial drifts are bounded by a distinct moraine.

The gravel drift has been mapped and subdivided by various authors (Denton *et al.*, 1989a; Mayewski and Goldthwait, 1985; Mercer, 1972) (Table 4.1). Mercer (1972) used the

relative degree of rock weathering to subdivide lateral moraine ridges in the Dominion Range into four groups. On Beardmore I (oldest), cavernous weathering of fine grained dolerite is well advanced, and sandstone boulders are disintegrated. On Beardmore II, cavernous weathering on dolerite is incipient, but is well-developed on sandstone boulders. On Beardmore III, dolerite boulders are stained with ferrous oxides and sandstone is only slightly weathered. The youngest moraine adjacent to the glacier is unweathered. Past longitudinal glacier profiles were reconstructed by correlating moraines along the margins of the Beardmore Glacier. The profile corresponding to the youngest moraine parallels the present glacier surface. The older Beardmore I-III profiles indicate that the greatest thickening of the outlet glacier occurred toward the Ross Ice Shelf and that relatively little thickening occurred near the head; similar profiles were reconstructed for the Reedy Glacier to the south (Mercer, 1968).

Table 4.1 Correlation of Drift Sheets mapped in the Beardmore Glacier Region

Mercer (1972)	Mayewski *et al.* (1985)	Denton *et al.* (1989)	This Work
"Youngest moraine"	Low moraine	Plunket drift	Plunket drift (A moraine)
Beardmore III	Low moraine	Beardmore drift	Beardmore 1 (B moraine) Beardmore 2 (C moraine)
Beardmore II	Middle moraine	Meyer drift	Meyer 1 drift (D moraine) Meyer 2 drift (E moraine) Meyer 3 drift (G moraine) Meyer 4 drift (H moraine)
Beardmore I	High moraine	Dominion drift	Dominion drift (I & J moraines)

In addition, Mercer (1972) noted that the Beardmore III lateral moraines in the Dominion Range cross-cut terminal moraines of the Rutkowski Glacier indicating that advances of the Rutkowski and thickening of the upper Beardmore Glacier were out-of-phase (Figure 4.5). These results were interpreted as damming of the outlet glaciers by an expanded WAIS in the Ross Sea and reduced accumulation leading to alpine glacier retreat in the interior. Mercer (1972) considered this to be strong evidence in support of the hypothesis that the WAIS is controlled by sea level and inferred that the Beardmore III drift corresponds to the last glacial maximum (LGM;

marine isotope stage 2). A cartoon of the present and inferred LGM configuration of the Beardmore Glacier is shown in Figure 4.6.

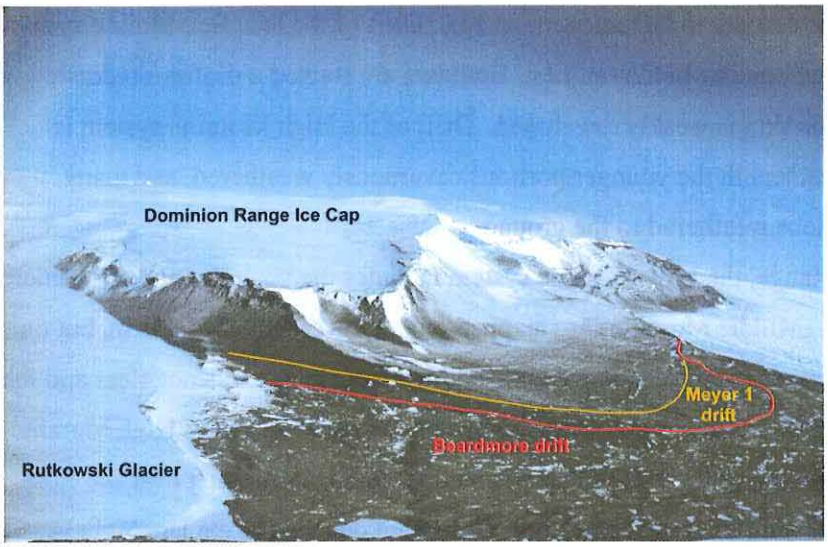

Figure 4.5 Photograph of Mercer Platform, looking up glacier (southwest). The Beardmore 1 and Meyer 1 drifts project into the Rutkowski Trough and are overlain by the Rutkowski Glacier.

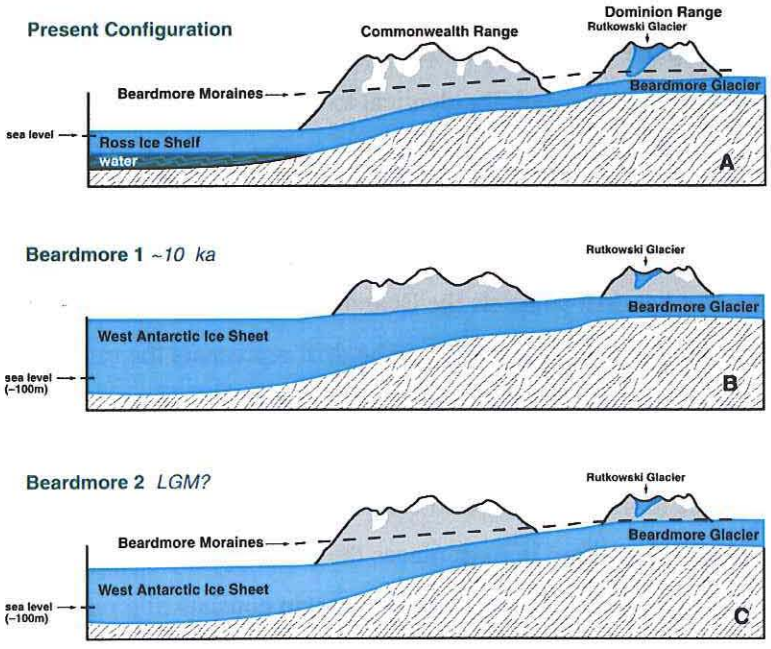

Figure 4.6 Cartoon showing the response of the Beardmore Glacier to expansion of the WAIS during the LGM. A) The present configuration; the Beardmore Glacier flows into the floating Ross Ice Shelf which controls the elevation of the glacier. The elevation of lateral moraines above the present ice surface increases down glacier. Alpine glaciers are advancing over the lateral moraines. B) ~10 ka; the WAIS is grounded at the mouth of Beardmore Glacier and the ice surface is at the Beardmore 1 lateral moraines. Alpine glaciers, starved of precipitation, are retracted. C) Speculative configuration during the LGM. The WAIS is grounded at the mouth of Beardmore Glacier, but maximum ice elevations have yet to occur. A wave of thickening has propagated up glacier. Alpine glaciers are retreating.

Mayewski (1985), working on the inland (western) side of the central Transantarctic Mountains and using rock and soil weathering criteria, also mapped three moraine systems (Table 4.1). The Low Moraine system which is unweathered, commonly ice-cored, and parallels the present glacier surface, was thought to be Holocene in age. Drift of the Middle Moraine system typically includes a series of boulder-belt moraines. Boulders are stained a uniform reddish brown and cavernous weathering is weakly developed. Drift of the High Moraine system is deeply weathered, with boulders in the younger portions cavernously weathered, and many boulders in the oldest portions weathered to the ground.

At the Dominion Range, the Low Moraine system includes the youngest and Beardmore III drifts of Mercer (1972). Middle Moraines are mapped on the lower Oliver Platform, but on the Mercer Platform the boundary between the Middle and High Moraines was not clear and the two drifts were not differentiated. The profiles reconstructed for the Middle and High Moraine systems show greater thickening of the polar plateau with only minor thickening near the Ross Ice Shelf. Through tenuous long-distance correlation with dated deposits in the Dry Valleys Region the age of the High and Middle Moraines was estimated to lie between 1.6 Myr and 49 kyr. None of the moraine systems were correlated with the LGM in this scheme.

Denton *et al.* (1989a) used soil development and rock weathering to map the gravel drifts along the Beardmore Glacier, including the Mercer Platform to the southwest of the Rutkowski Trough (Figure 4.2). Their conclusions were essentially identical to those of Mercer (1972); the glacial deposits were divided into four drifts and a slightly different nomenclature used (Table 4.1). The Plunket drift occurs nearest to the glacier, is unweathered, and ice-cored. The drift is up to 10 m above the present ice level, thins toward the glacier, and grades into the supraglacial debris on the present glacier. The Plunket drift parallels the Beardmore Glacier margin and generally extends less than 250 m from the active glacier ice. The drift represents the most recent thickening of the glacier, at some point during the Holocene.

The Beardmore drift is slightly weathered and hummocky and is presumed ice-cored in some locations. This drift corresponds to the Beardmore III drift of Mercer (1972). The character of the drift margin varies with location. In most places the drift is bounded by a bouldery gravel-rich moraine ridge. On the Mercer Platform, the margin consists of a ramp up to 10 m high at the angle of repose (Figure 4.7). A 1 to 2 m high ridge occurs on top of the scarp. The elevation of the Beardmore drift above the present ice surface increases down glacier. Through correlations based on soil-development with ^{14}C-dated deposits in the Hatherton Glacier

Area (Bockheim *et al.*, 1989) and Dry Valleys (Denton *et al.*, 1989b), Denton *et al.* (1989a) assigned a LGM age to the Beardmore Drift.

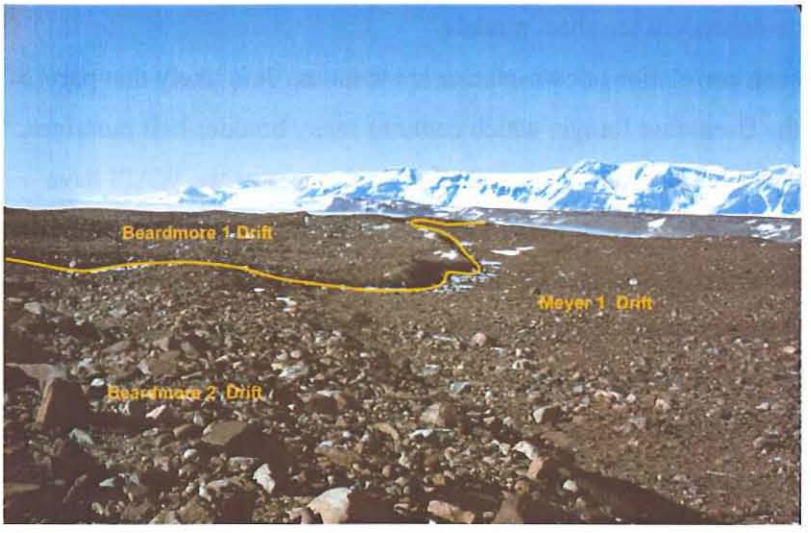

Figure 4.7 Photograph of the margin of the Beardmore drift. Beardmore 2 drift (foreground) is overlain by Beardmore 1 drift. There is a distinct contrast in weathering between the Beardmore and Meyer drifts.

The Meyer drift consists of thin weathered drift and boulder moraines outboard of the Beardmore drift at several locations along the Beardmore Glacier. At the Dominion Range, Meyer drift corresponds to the Beardmore II drift of Mercer (1972) on the Oliver Platform and the undifferentiated Middle-High moraines of Mayewski and Goldthwait (1985) on the Mercer Platform. Because it parallels the Beardmore drift, it is also thought to record damming by grounded ice in the Ross Embayment and is correlated with stage 6 deposits (Marshall drift) in McMurdo Sound. Prentice *et al.* (1986) mapped Dominion drift, a series of moraines in the Dominion range, beyond the Meyer drift margin and extending up to 2500 m on upper Oliver Platform. Denton *et al.* (1991) attributed the uppermost moraines of the Dominion Drift to an ancient thick, cold-based ice sheet which nearly submerged the TAM. These moraines show extreme weathering and correspond to the Beardmore III and High moraines (Table 4.1). The moraines are considered pre-Quaternary in age.

In summary, previous mapping of the glacial deposits in the Dominion Range is consistent. Four distinct drifts are distinguished on the basis of rock weathering and soil development. Although the Mercer-Denton conceptual model of ice sheet configuration along the TAM during the LGM appears well supported, (Mayewski did not work in the lower reaches of the glacier where the ice thickening is most apparent) absolute dating of deposits is lacking.

The correlations with distant, dated deposits are based on relative weathering criteria and lithologic and local climatic effects are difficult to rule out. Certainly, for even the younger drifts, the relative chronology is not able to determine precise dates for local glacial maxima, data which is necessary to test time-dependent ice sheet models.

For the older drifts, even correlations down-glacier are tenuous. It is likely that parts of the extensive Meyer drift in the Dominion Range, which contains many boulder-belt moraines, are older than stage 6. In the McMurdo Sound Region, multiple advances of the WAIS have occurred prior to the last glaciation (Ackert and Kurz, 1994) (Chapter 5). Lastly, it is not clear that all moraines in the Dominion Range record damming of the Beardmore Glacier. During interglacial periods, increased precipitation due to warmer temperatures and the proximity of open ocean is expected to result in increased accumulation and thickening of outlet glaciers. This response is shown by the Taylor Glacier in the Dry Valleys (Figure 4.1). The Taylor Glacier is presently advancing and the youngest moraines were deposited during the last interglacial (stage 5) (Brook *et al.*, 1993; Denton *et al.*, 1989b; Hendy *et al.*, 1979; Marchant *et al.*, 1994). The objectives of this study were to test the previous models with absolute dating of the lateral moraines and to provide minimum ages for the underlying Sirius deposits.

4.3 Surface exposure dating

In surface exposure dating, the abundance of cosmogenic nuclides in surficial rocks is used to determine the length of time that the rock has been exposed to cosmic rays. The technique has been used to develop glacial chronologies where chronologic controls were previously unobtainable (*e.g.*, Gosse *et al.*, 1995; Phillips *et al.*, 1990). The technique is well suited to Antarctica where low erosion rates have resulted in the preservation of abundant ancient glacial deposits. The principles of surface exposure dating with cosmogenic nuclides are discussed in detail in Chapter 1. A brief summary is included here.

In rocks, cosmogenic nuclides are produced primarily by spallation reactions between cosmic rays and major elements. The concentration of cosmogenic nuclides in a rock is directly related to the time the sample has been exposed to cosmic rays. In practice, this simple relation is complicated in several ways. The production rate varies as a function of depth in the rock, and with altitude, because the cosmic ray flux is attenuated by interaction with matter. At depths greater than two meters, rock is effectively shielded from cosmic rays capable of causing spallation reactions. Corrections for mass shielding are straightforward and do not add significant

uncertainty to the calculated exposure age. A fundamental assumption when applying surface exposure dating to glacial moraine boulders is that erosion has rapidly exhumed the rocks from shielded depths and the accumulation of cosmogenic nuclides begins when the boulder is deposited on a moraine.

Production rates also vary with latitude. The galactic cosmic ray flux at the top of the atmosphere consists primarily of charged particles (protons). At low latitudes, where the lines of the Earth's magnetic field are perpendicular to the flux, particles with insufficient energy (< cut-off rigidity) are deflected. This effect is greatest at the equator and decreases toward the poles. Above 60° latitude the cosmic ray flux is unaffected by the Earth's magnetic field. Lal (1991) summarized star production rate data (Lal and Peters, 1967) in polynomial form which is used to scale production rates from calibration sites to the appropriate altitude and latitude. Because the strength of the Earth's magnetic dipole varies on 10,000 year time scales, production rates at low latitudes are time-dependent. In contrast, productions rates at high (>60°) latitude are constant (assuming the galactic cosmic ray flux is constant and integrated over the solar cycle). However, to date, published production rates have been calibrated at low latitudes on surfaces less than 20 kyr; when scaled to high latitudes using present day scaling, some systematic error likely results. These uncertainties are minimized at older, higher latitude calibration sites (Chapter 2).

An additional scaling correction is required for Antarctica. Anomalously low atmospheric pressure over the continent means that there is effectively less atmospheric shielding at a given altitude than at the corresponding altitude at 60° latitude (Stone, 1999). This correction varies with altitude and may be up to 25 percent compared to sites at 60° latitude. Previous surface exposure studies in Antarctica did not account for this effect and thus likely overestimate the age of the samples. However, a ~20 percent overestimate of the ^{10}Be and ^{21}Ne production rates used in earlier work largely compensates for the error in those isotope systems (Clark *et al.*, 1995). Corrections for this effect are made using the formulation of Stone (1999) (Chapter 1). Total uncertainty in production rates and scaling is difficult to quantify; uncertainties in surface exposure dates are estimated to be 10 to 15 percent (Clark *et al.*, 1995) but may be significantly less (Chapter 2) and an estimate of less than 10 percent is assumed here.

The concentration of cosmogenic nuclides can be interpreted either as a minimum exposure age or a maximum erosion rate (Lal, 1991). When erosion is at steady state, the removal of cosmogenic nuclides by erosion (and radioactive decay) is equal to production and maximum erosion rates can be calculated (Chapter 1). In general, this assumption is more likely

to be valid for cosmogenic nuclides with relatively short half lives and where erosion rates are high (^{26}Al, ^{36}Cl). However, due to the great age of some Antarctic surfaces, this technique can be applied to stable isotopes as well. Erosion rates can also be determined by use of paired radioactive cosmogenic nuclides such as ^{10}Be and ^{26}Al (Brown *et al.*, 1991). Previous work in the Dry Valley Region established that maximum erosion rates are very low, less than about $1x10^{-5}$ g/cm^2/yr (.05 mm/kyr) (Brown *et al.*, 1991; Nishiizumi *et al.*, 1991). Therefore, for young samples the erosion rate is often assumed to be zero. However, for old samples (>250 kyr) this effect is not negligible and zero-erosion ages will underestimate the true exposure age.

A final issue is whether the sample has remained a closed system during exposure. For the noble gases, diffusion could result in loss of the cosmogenic nuclides. Diffusion rates of ^{3}He in clinopyroxene (cpx) and olivine, are very low compared to the time periods of interest (Trull *et al.*, 1991). Experimentally determined diffusion rates in quartz suggested that quartz would also retain helium over time scales useful for exposure dating (Trull *et al.*, 1991). However, ^{3}He loss due to diffusion has been shown to occur in quartz (Brook and Kurz, 1993; Cerling, 1990; Staudacher and Allegre, 1991) and is strongly dependent on grain size (Brook and Kurz, 1993). On the basis of the concordance of paired ^{3}He and ^{10}Be ages up to ~100 kyr, Brook (1993) and Brook *et al.* (1995) tentatively concluded that diffusion in quartz is slow enough in Antarctica to have minimal effect on young (<100 kyr) samples. However, these conclusions were based on scaled ^{3}He production rates which are probably too low (see above). When scaled for Antarctic elevations and quartz composition, the ages are generally 20 to 30 percent lower than the ^{10}Be ages of the samples, even for samples as young as 14 kyr. Thus, it appears ^{3}He exposure ages determined in quartz should be considered minimum ages for all samples. On the other hand, concordant ^{21}Ne and ^{10}Be ages in quartz up to 2 Ma indicate diffusion is not a problem for ^{21}Ne (Bruno *et al.*, 1997; Staudacher and Allegre, 1991).

Surface exposure dating has been successfully applied to glacial deposits in the Antarctic. In the Dry Valleys, the results are consistent with relative chronologies and other independent dating techniques. Brook (1993) and Brook *et al.*, (1993) developed a chronology for the Taylor Glacier (Figure 4.1) which drains the McMurdo dome of the East Antarctic Ice Sheet by measuring ^{3}He and ^{10}Be exposure ages on sandstone boulders on the well-preserved lateral moraines in Arena Valley, an ice-free tributary to the Taylor Glacier drainage. The mean ^{10}Be ages of 122 ± 29 kyr (114 ± 25 with new scaling and production rate) on the youngest (lowest elevation) moraine are consistent with Th/U ages on associated lake carbonates down valley

(Hendy *et al.*, 1979). The ^{10}Be exposure ages of the oldest moraines (~2 Ma) are also consistent with ^{40}Ar/^{39}Ar and K-Ar ages of volcanics interbedded with correlated moraines down valley (Denton *et al.*, 1971; Wilch *et al.*, 1993). As discussed above, the ^{3}He ages are consistently lower than the ^{10}Be ages, probably due to diffusion.

Brook *et al.* (1995) used the ^{3}He technique with supplemental ^{10}Be data to date the youngest Ross Sea drift (Stuiver *et al.*, 1981b) in the McMurdo Sound Region. In that study, olivine and clinopyroxene were the primary mineral phases measured. The ages show considerable scatter and range from 6 to 105 kyr. The younger exposure ages show a normal distribution and are consistent with the ^{14}C dates (Denton *et al.*, 1989b; Hall and Denton, 1999; Stuiver *et al.*, 1981a) which date to 12 to 14 ka . The older ages represent either earlier unrecognized glacial advances or the reworking of previously exposed boulders. In addition, Brook *et al.* (1995) showed that similar drift sheets which extend beyond the limit of Ross Sea drift are significantly older and can be distinguished using surface exposure dating. Subsequently, Kurz *et al.*, (1994) used ^{3}He to date drift limits interbedded with lava flows in southern McMurdo Sound to stages 2, 4 and 6. Ackert and Kurz (1994) (Chapter 5) used similar techniques to show that at least four glaciations in the Ross Sea occurred prior to the deposition of Ross Sea drift in southern McMurdo Sound.

4.4 Methods

Field work and sample preparation

Field work on the Mercer Platform in the Dominion Range was carried out from December 2-14, 1995, with helicopter support from the United States Antarctic Program (USAP) remote camp at Shackleton Glacier. The emphasis was on sampling for surface exposure dating of previously described deposits. Samples were collected with hammer and chisel from the tops of boulders. Detailed field descriptions were made of each sample which include elevation, GPS coordinates, lithology, size, local geomorphology, deposit type, and shielding of the sample (Appendix 4.1). Elevations were determined relative to the base camp with altimeters. Differential GPS was used to tie the camp and selected moraine elevations to the global reference frame. Detailed surficial geologic maps of moraines and drift on Oliver and Mercer Platforms were made on high resolution air photographs (Figure 4.8).

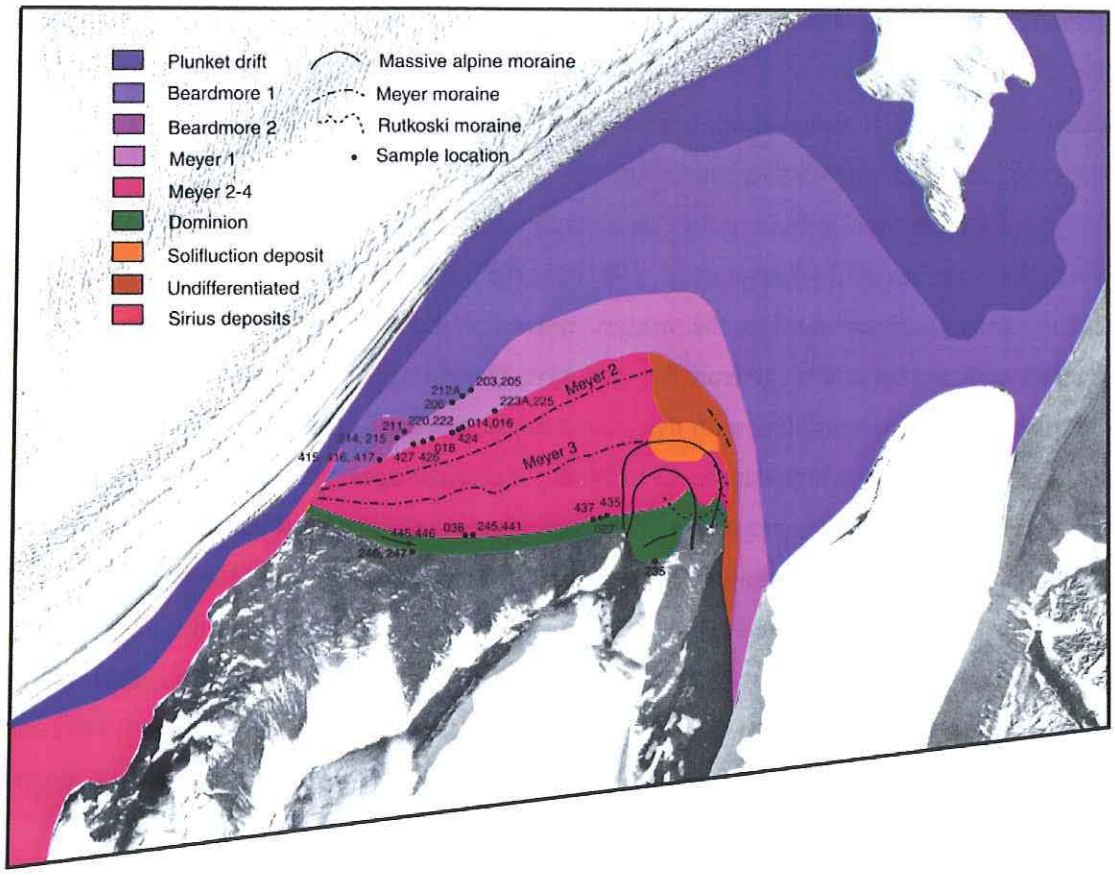

A

Figure 4.8A Surficial geologic map of the Mercer Platform, Dominion Range.

The degree of boulder weathering on the moraines was used to establish the relative ages of moraines. Rock weathering was also used to evaluate erosion, stability of blocks and the potential for prior exposure of individual boulders. The thickness of quartz weathering rinds and degree of cavernous weathering on sandstone boulders increases with exposure age and proved a useful tool (Weed and Ackert, 1986). Various dolerite lithologies also follow characteristic weathering processes. Mineral grain size apparently controls the weathering rate; fine-grained lithologies are the most resistant. In general, pitting and desert varnish increases with age allowing relative age estimates.

In some coarse-grained lithologies, distinctive types of cavernous weathering occur. One, "horn and hollow" weathering, consists of intersecting, vertical circular pits, ~10 cm in diameter with intervening horns (these are tafoni pits of Mercer (1972). Because the depth of the

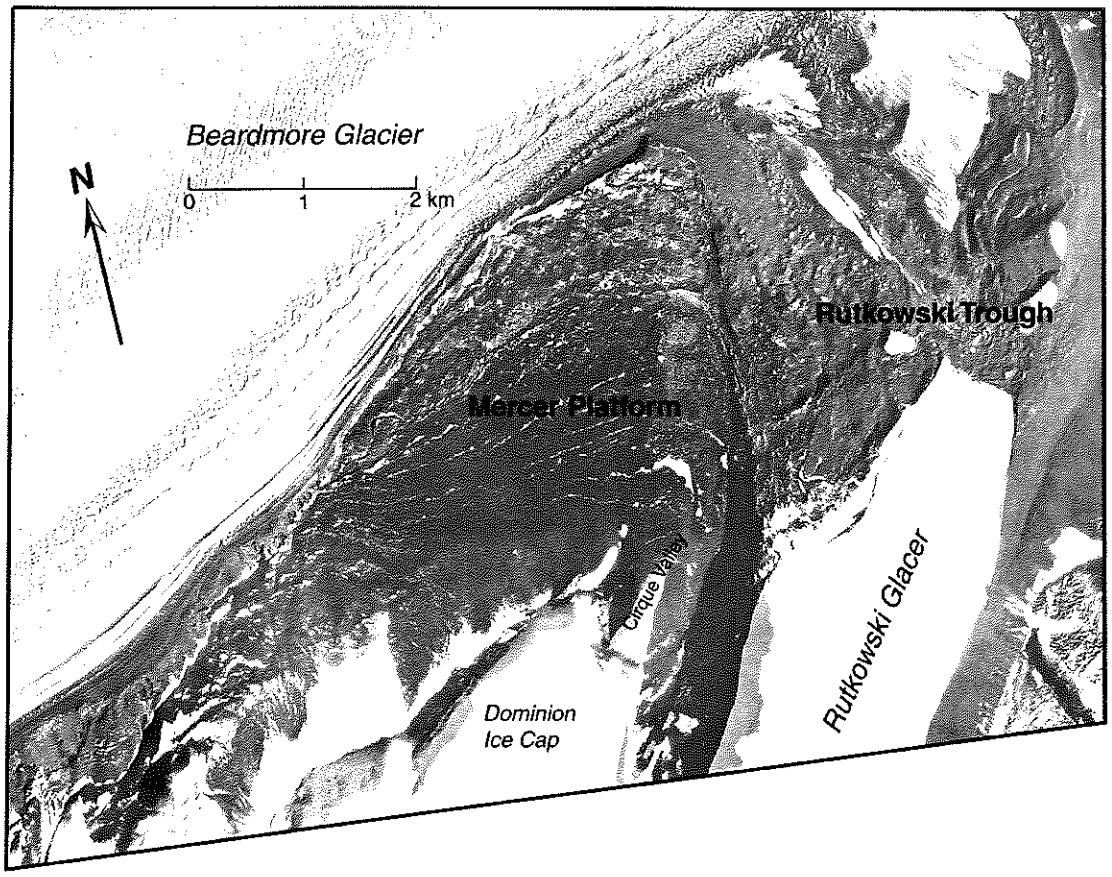

B

Figure 4.8B Vertical aerial photograph mosaic (TMA 2736; 3-073, 3-071, TMA 2737 V; 3-092, TMA 2738 V; 3-162, H 22800 , 1/14/85) on which the map is based.

pits apparently increases faster than the diameter, pit depth is a useful relative age indicator. Another lithology weathers preferentially along curvilinear surfaces (joints?) resulting in "puzzle rocks" consisting of large (10's of cm) intricately fitted pieces (Figure 4.9). In early stages, the joint surfaces are weathered several cm deep but the boulder remains intact. Later, the deepening weathering fronts intersect. These blocks eventually disaggregate, but the blocks remain recognizable as parts of a single larger block for some time. As the individual pieces continue to weather by spalling and pitting, it become impossible to recognize disaggregated blocks.

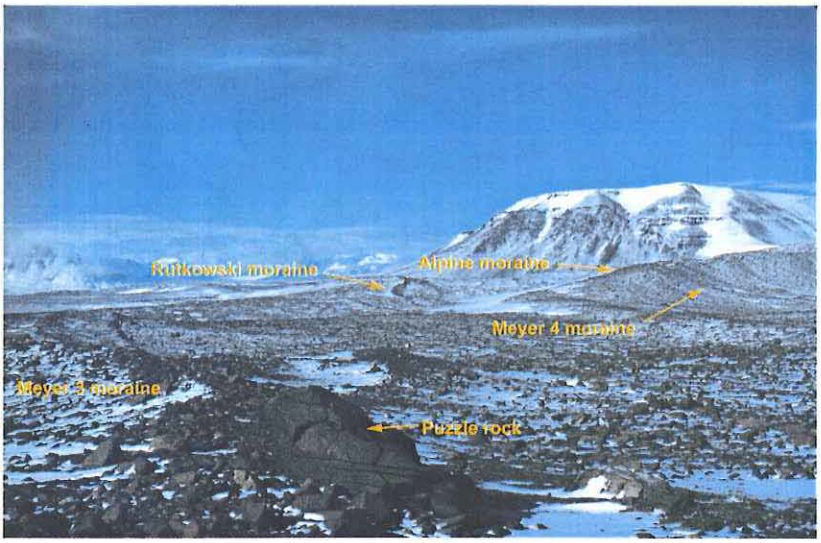

Figure 4.9 Photograph of Meyer 3 moraine. A large puzzle rock occurs in the foreground. Note "missing" piece. Large alpine moraines overlain by a Rutkowski Glacier boulder moraine occur in the background.

As will be shown below, many distinct drift sheets occur on the Mercer platform. The Beardmore Glacier overrode older drift sheets each time it advanced, depositing thin drift and moraines on top of the older deposits. In order to sample boulders representative of the drifts, only the crests of the most distal moraine of each drift sheet were sampled. In the field, the sampled moraines were given letter designations A-J, with increasing distance from the present glacier margin (Table 4.1). The F moraine was not sampled because it was later realized not to be a drift edge. The B moraine corresponds to the margin of the Beardmore drift while the H moraine corresponds to the Meyer drift limit. The I and J moraines are the lowest (youngest) moraines in the Dominion drift. At least twelve samples for surface exposure dating were collected from each sampled moraine ridge in the Meyer and Beardmore drifts.

Coarse-grained sandstones and dolerite were collected to facilitate mineral separation. Most sandstone lithologies in the moraines were fine-grained; most sampled boulders were either a poorly-sorted olive green sandstone with rare beds of 0.5 to 4 mm quartz grains or a white medium- to coarse-grained sandstone. Both lithologies are assumed to crop out in the cliffs up-glacier from the study area. The same lithologies occur in the supraglacial debris on the present glacier and within the underlying Sirius deposits.

Sub samples were broken off the collected samples using a hydraulic splitter. Sandstone and dolerite samples were ground and sieved to remove the fine (<5 mm) fraction and the course (>2 mm) fraction. Mineral separates free of adhering ground mass or cements were picked from the .5 to 1 mm and/or 1 to 2 mm fractions. In both lithologies, adhering material is likely to be non-retentive of helium leading to underestimates of the exposure age. In dolerite, plagioclase

which is not retentive for helium, commonly adheres to the pyroxene grains. In some samples it was necessary to pick pyroxene from the .4 to .5 mm fraction in order to obtain clean grains.

In the sandstones, the adhering material is microcrystalline silica cement; diffusion rates increase with smaller grain size. The sandstone cement also seemed a likely site of impurities (often the adhering material was stained reddish brown). In most samples only conchoidally fractured grains were selected because whole rounded grains typically had some adhering cement. In some cases, an alternate procedure was employed. Quartz grains were physically abraded in an air abrasion chamber. Such grains were subsequently cleaned in weak nitric acid to remove adhering stainless steel and rinsed and sonicated in water and acetone. Comparisons of measurements on abraded and conchoidally fractured grains showed no significant difference (Tables 4.2 and 4.3a).

Measurements of cosmogenic isotopes

Measurements of cosmogenic ^{3}He were made on pyroxene from dolerite and measurements of ^{3}He and ^{21}Ne were made on quartz from sandstones. Most ^{3}He measurements were made on the WHOI helium isotope mass-spectrometer (MS 2) (Kurz et al., 1987). Helium and neon isotopes were measured by step heating of 10 quartz samples. The automated gas extraction line includes a titanium sponge getter, a SAES getter and a cryogenic charcoal trap for separating noble gases (cooled to 7°K, He released at 35°K, Ne released a 70°K). Extracted gas was analyzed for isotopic composition on a MAP215-50 mass spectrometer with a Nier type source. All neon isotopes and ^{3}He were measured with an electron multiplier and ^{4}He was measured with a Faraday collector. The samples were progressively heated to 300, 600,and 1500 °C. A blank was analyzed for each temperature step, and air standards were analyzed between each sample and blank run. Because Ne has three isotopes and the isotopic ratio of air-neon and cosmogenic neon are significantly different, mixing relationships can be evaluated on isotope ratio plots. Figure 4.10 shows that the data are consistent with simple two-component mixing between an air-like and a cosmogenic end member.

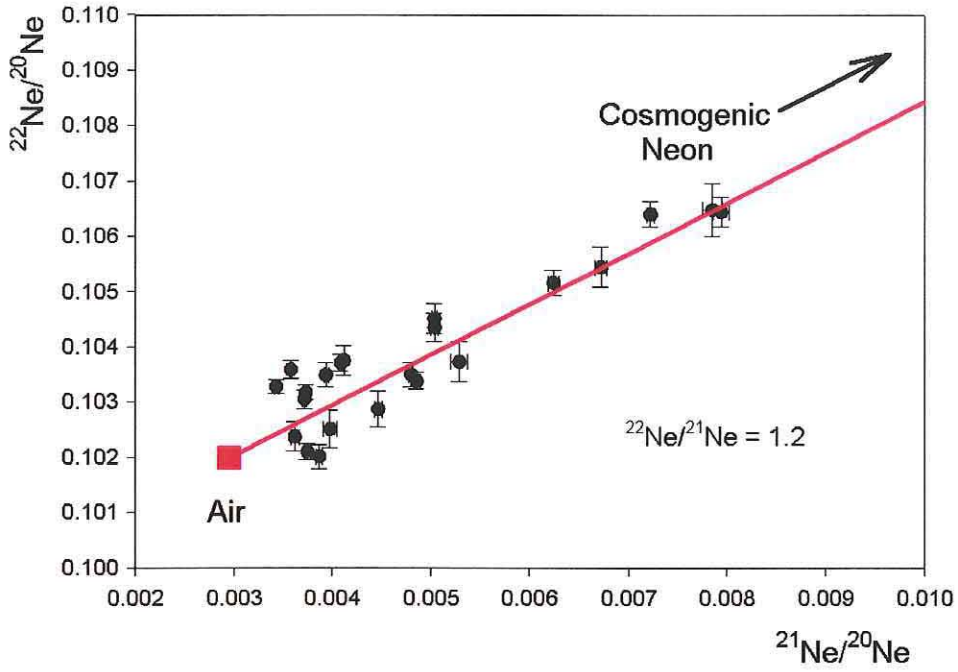

Figure 4.10 Neon isotope ratio plot. Square is air composition. The data determine a line which passes through the air composition and the cosmogenic composition. The measured neon ratios can be explained by simple two component mixing between these end members. 1.2 is the cosmogenic $^{22}Ne/^{21}Ne$ production ratio in quartz (Bruno *et al.*, 1997).

The cosmogenic ^{3}He component is calculated by subtracting the inherited component from the total ^{3}He measured. For young extrusive volcanic phenocrysts (olivine and cpx) the inherited component is primarily magmatic helium which can be released from fluid and melt inclusions by crushing the sample (Kurz, 1986). Typically, about 90 percent of the gas is released in the crushing step. The $^{3}He/^{4}He$ measured on crushing is multiplied by the ^{4}He concentration measured when the sample is melted to determine the initial concentration. This value is then subtracted from the total ^{3}He measured on melting the sample (Chapter 1). This calculation assumes that there is no radiogenic helium (^{4}He atoms are stopped α particles) in the sample and that all the ^{4}He is magmatic. For young olivine samples (<1 Ma) which have low U and Th concentrations the assumptions are valid. Even in olivine, implanted radiogenic ^{4}He from the ground mass may be important for samples older than ~1 Ma.

For the old rocks measured in this study, radiogenic helium is a significant component and other methods must be used to determine the cosmogenic ^{3}He concentration. A simple approach is to assume all the ^{3}He is cosmogenic. This assumption is appropriate if the magmatic and nucleogenic ^{3}He components are negligible. Nucleogenic ^{3}He can be produced by the

reaction Li (α,n) T$\rightarrow{}^{3}$He and for the assumption to be valid, Li, Th and U concentrations must be low. This approach gives reasonable results for quartz (Brook *et al.*, 1993) and is justified by determinations of the inherited component using step heating and measurement of low Li, Th and U concentrations (Trull *et al.*, 1991). Shielded samples which have no cosmogenic component can also be used to test this assumption.

In contrast to young olivine, the inherited helium component in clinopyroxene from the Ferrar Dolerite (176 Ma) is dominated by radiogenic helium. Crushing the clinopyroxene yields only 8 to 15 percent of the total gas and inconsistent, poorly constrained $^{3}He/^{4}He$. The initial ^{3}He concentration was determined from three well-shielded samples from Taylor Valley (Figure 4.1). It is assumed that the Ferrar Dolerite is uniform in the distribution of Li, Th and U and results from the shielded samples are applicable to other distant samples. The weighted mean $^{3}He/^{4}He$ of three shielded samples is .0100 ± .0004 R/R_a (R_a is the $^{3}He/^{4}He$ of air = 1.384×10^{-6}). This value is a factor of 2 to 3 lower than crush values and indicates that some cosmogenic ^{3}He is released by crushing. Details of these experiments are presented in Chapter 2.

Crushing quartz releases a significant fraction of the cosmogenic helium (Brook and Kurz, 1993). The variety of sandstone lithologies sampled makes finding equivalent shielded samples unfeasible. However, cosmogenic ^{3}He in quartz is released by heating to 600° C and estimates of the initial $^{3}He/^{4}He$ can be made by step heating (Trull *et al.*, 1991). A value of .011 ± .04 R/R_a was determined by melting the step-heated quartz grains, consistent with that calculated from the measured Li, Th and U concentrations of the sample (Trull *et al.*, 1991). In this study, helium isotopes were measured in gas aliquots from 6 samples which were incrementally heated to 300, 600 and 1500° C. Almost all ^{3}He is released in the 300° and 600° steps. The quartz grains are melted in the 1500° step. Very little ^{3}He remains in the 1500° step although more than half of ^{4}He is typically released (Chapter 2). The weighted mean of the 6 samples in which the ^{3}He concentration was above blank levels in the 1500° step is .003 ± .0004 R/R_a. These results (Chapter 2) support the assumption that the contribution of non-cosmogenic ^{3}He is negligible.

A sea level, high latitude ^{3}He production rate of 129 ± 3 atoms/g/yr obtained from olivine from the Cerro Volcán lava flow in Patagonia was used (Chapter 2). The flow is dated to 125 ± 4 ka, by K-Ar and $^{40}Ar/^{39}Ar$. This production rate is slightly higher than the average ^{3}He production rate of 115 ± 4 atoms/g/yr in olivine (Cerling and Craig, 1994) applied in most earlier studies utilizing ^{3}He for exposure dating. The Patagonian production rate is used in this work

because the calibration age of that lava flow is closer to the age of most of the Antarctic surfaces, and scaling of the production rate to high latitude involves less uncertainty than scaling from the calibration sites of Cerling and Craig (1994) (see Chapter 2 for additional discussion).

The Patagonian production rate of ^{3}He in olivine (Fo_{85}) was scaled for the composition of the Antarctic samples. Calculations of ^{3}He production rates based on proton excitation functions (Lal, 1991) suggest that the production rate could be as much as 8 percent higher in quartz than in olivine (Fo_{80}) because the elemental production rate of Fe is a factor of 2 to 3 lower than the other common silicate rock elements. More recent calculations (Masarik and Reedy, 1995; Masarik and Reedy, 1996) underestimate ^{3}He production rates measured in the Cerro Volcán lava flow by about 20 percent, but accurately predict the relative difference between the clinopyroxene and olivine ^{3}He production rates (see Chapter 2). The elemental production rates of Masarik and Reedy (1996) are therefore used to scale production rates measured at Cerro Volcán for quartz and pyroxene in this study. The composition of Ferrar Dolerite clinopyroxene was taken from Schäfer *et al.* (1999) who measured the composition of ten samples from six localities in the Dry Valleys. A 6 percent variation in production rates within that sample set is predicted based on the 6 to 14 weight percent variation in the Fe content of the pyroxene. The production rate scaled for composition is 140 atoms/g/yr in quartz and 127 atoms/g/yr in pyroxene.

In contrast to ^{3}He, the production rate of ^{21}Ne is more strongly dependent on the major element composition of the sample. In quartz, cosmogenic ^{21}Ne is produced only by spallation reactions on Si. A ^{21}Ne/^{26}Al production ratio of 0.65 and a ^{21}Ne production rate of 21 atoms/g/yr (at sea level high latitude) (Niedermann *et al.*, 1994) were determined from aliquots of samples used to determine ^{10}Be and ^{26}Al production rates in the Sierra Nevada (Nishiizumi *et al.*, 1989). However, like the ^{10}Be and ^{26}Al calibration, an exposure age of 11 ka for the glaciated surface and the present geomagnetic latitude of 44° was assumed. Subsequently, Clark (1995) showed that deglaciation of the Sierra Nevada was substantially earlier (13-14 ka) and suggested that the geographic latitude was a better estimate of the average geomagnetic latitude. Their revised ^{10}Be and ^{26}Al production rates using the data of (Nishiizumi *et al.*, 1989) were ~20 percent lower and in good agreement with production rates determined from the Laurentide moraine in New Jersey.

Earlier data supporting the higher production rate of Nishiizumi (1989) from Antarctica (Brown *et al.*, 1991; Nishiizumi *et al.*, 1991) do not take into account the anomalous low atmospheric pressure which results in higher production rates for a given altitude. When the data are scaled to sea level using a formulation based on Antarctic atmospheric data (Stone, 1999) they

are consistent with the Clark (1995) production rates. A ^{21}Ne production rate in quartz of 17.5 atoms/g/yr, consistent with revised ^{26}Al production rates is used in this study. For a more complete discussion of production rates see Chapter 2.

4.5 Results

Field relationships

The observed distribution of Sirius Group deposits agrees with that of McKelvey (1991). Sirius deposits are exposed in bluffs at the northern end of the Mercer Platform along the Beardmore Glacier (Figure 4.3). Sirius deposits are also exposed at Oliver Bluffs and in the Koski fault along the eastern side of Oliver Platform (Figure 4.2) where up to 185 m of Sirius Group deposits and the underlying glacial erosion surface are exposed (Elliot *et al.*, 1974). The erosion surface exhibits a valley-in-valley profile reflecting progressive glacial erosion by the ancestral Beardmore Glacier (McKelvey *et al.*, 1991). The inner valley wall corresponds to the steep bedrock slope which divides the upper and lower benches of Oliver Platform (Figure 4.2). The same general morphology and elevations occur at the Mercer Platform and thus it is likely the Mercer platform is also underlain by Sirius drift which pinches out against the slope south of the platform.

A small cirque-headed valley, with a small snow field against the headwall, occurs adjacent to the Rutkowski Trough in the southeast corner of the Mercer platform (Figures 4.2 and 4.5). Two previously undescribed massive alpine lateral moraines (30 m high) occur near the mouth of the valley on the eastern side (Figure 4.11). In paired stereoscopic air photographs, it is observed that the lateral moraines are connected to two subdued terminal moraine loops enclosing the mouth of the valley. No other evidence of ice flowing out of the cirque was observed even though that part of the Dominion Range ice cap terminates above the cirque headwall and a snowfield occupies the headwall (Figures 4.2 and 4.5).

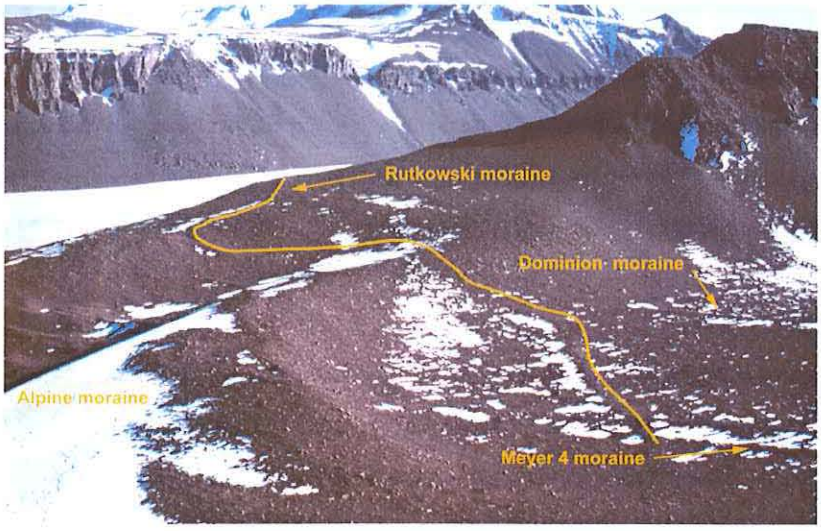

Figure 4.11
Photograph of massive alpine moraines deposited by ice flowing out of the small valley adjacent to the Rutkowski Glacier. Moraines from the Rutkowski and Beardmore Glaciers overlie the massive moraines. Note cross-cutting relation between the Rutkowski and Meyer 4 moraines.

The alpine moraines are overlain by a complex set of cross-cutting boulder-belt moraines. One set of moraines was deposited by ice spilling out of the Rutkowski Trough. These previously undescribed moraines rise in elevation and turn toward the south indicating that they were deposited by ice flow down Rutkowski Trough from the Dominion Range ice cap (Figure 4.11). The other set consists of lateral moraines deposited by the Beardmore Glacier. The outermost of these moraines extend into the cirque valley and wrap around the crests of the large alpine lateral moraines. Near the mouth of the cirque valley, the outermost Rutkowski moraine cross cuts the Beardmore lateral moraines at ~ 60° (Figure 4.11). The Beardmore lateral moraines are the outermost moraines of the series mapped as Meyer drift by Denton *et al.* (1989a). The lateral moraines fan out over the platform from an origin along the bluffs at the northwest corner of the platform. The angle between the lateral moraines and the cliffs along the glacier increases with relative age of the moraines. This relationship suggests that significant erosion of the cliffs has occurred since the deposition of the oldest Beardmore lateral moraines. The younger lateral moraines can be traced into the Rutkowski Trough, indicating that a lobe of the Beardmore Glacier projected into the trough (Denton *et al.*, 1989a; Mercer, 1972) (Figures 4.5 and 4.8).

On the basis of rock weathering and overall morphology, the lateral moraines on the Mercer Platform are here divided into three drifts. The division is similar to that of earlier work and the nomenclature of Denton (1989a) is retained (Table 4.1). The Plunket drift is composed of ice-cored moraines which grade into supraglacial debris. The drift parallels the present ice

surface and records recent expansion of the Beardmore Glacier. The boulders consist of angular to rounded and striated sandstone and dolerite. The sandstone is unweathered; some of the dolerite is stained. The drift is similar to that observed in the youngest moraines (Figure 4.12). The source for the trails of debris on the present glacier can be traced to the base of the steep cliffs of Sirius Group sediments and sandstone and dolerite bedrock exposed along the Beardmore Glacier to the south (Figure 4.3). Because of the lithologic similarity of the supraglacial debris, Plunket drift, and the material composing the older moraines, a similar source for the samples collected for exposure dating is inferred. The lack of weathered debris on the glacier and in the Plunket drift suggests that prior exposure is minimal.

Figure 4.12
Photograph of supraglacial debris on the Beardmore Glacier. Drift is unweathered except for staining on some dolerite boulders.

On the Mercer Platform, the Beardmore drift is differentiated from the older Meyer drift by the relative lack of weathering, silty gray matrix material, abundant striated and molded clasts, massive relief, and hummocky surface. In the Rutkowski Trough, the Beardmore drift overlies moraines of the Rutkowski Glacier and is overlain by the present Rutkowski Glacier terminus (Figures 4.5 and 4.8). At their western extent, the Beardmore drift margins are semi-parallel to the bluffs exposing Sirius Drift immediately up-glacier, indicating that the Beardmore Glacier was banked up against the cliffs when the moraines were deposited. These cliffs are a likely source of the striated boulders and muddy matrix found in the Beardmore drift.

The Beardmore drift is subdivided into two units provisionally termed the Beardmore 1 (overlying) and Beardmore 2 (underlying) (Table 4.1). Beardmore 2 drift is only exposed in the

northwest corner of the Mercer Platform, near where the moraines originate along the edge of the bluff (Figure 4.8). A clear cross-cutting relationship between the two drifts occurs (Figure 4.7). Apparently, the earlier ice advance filled what had been a topographic depression with thick (ice-cored?) drift and the subsequent ice margin was deflected around the new topographic high. The surface of the Beardmore 2 drift is less hummocky than the overlying Beardmore 1 drift and the boulders have a little more desert varnish giving the underlying drift a slightly darker color. These field observations suggest that the drifts record distinct glacial advances rather than a terminal and recessional position from one advance.

The Meyer drift is composed of thin drift sheets and associated boulder-belt moraines (Figures 4.4, 4.8 and 4.9). The moraines are 1 to 4 m high, consisting of a network of boulders with interstitial gravel and cobbles. Four drifts, provisionally termed the Meyer 1 (innermost adjacent to the Beardmore drifts) through Meyer 4 (outermost forming the distal edge of the Meyer drift), are distinguished. The distal edge of each drift is bounded by a prominent moraine ridge with an increase in boulder weathering on the distal side. Each ice advance overrode drift sheets deposited during earlier advances without substantially altering the underlying topography. Consequently, many of the subdued moraine ridges within a mapped drift sheet may actually be from earlier advances. The moraines are nearly parallel; cross-cutting relationships are rare. The Meyer 1 and 2 moraines are overlain by the Beardmore 2 drift in the northwest corner of the platform. The other older Meyer moraines are cut by the cliff along the glacier (Figure 4.8).

In contrast to the Beardmore drift, the relative percentage of sandstone boulders is less on the Meyer drift (Denton *et al.*, 1989a) and the dolerite boulders have thick desert varnish. Overall, the drift is a deep reddish brown. Because boulder weathering is well advanced, weathering differences between the drifts are subtle and previous studies based on relative dating techniques did not subdivide these drifts although a range of ages was implied (Denton *et al.*, 1989a; Mayewski, 1975; Mercer, 1972). Increases in the degree of boulder weathering from the Meyer 1 drift to the Meyer 4 drift are observed in this study. The percentage of sandstone boulders decreases from Meyer 1 to Meyer 4 and the sandstone boulders are progressively cavernously weathered. On the Meyer 1 moraine, horned and hollow dolerite boulders do not occur and striated dolerite boulders are common. Horned and hollow boulders occur on the Meyer 2 drift adjacent to the Meyer 1 drift as well as the other distal drifts. Development of puzzle rocks dolerite is incipient on Meyer 1. On Meyer 2 and 3 development is complete with the boulders retaining their shape, and on Meyer 4 the boulders have largely disaggregated. The

Meyer 3 drift cross-cuts older Meyer moraines and is less weathered than the adjacent drift surfaces.

The Meyer 1 moraine follows the trend of the Beardmore drifts and also projects into the Rutkowski Trough (Figures 4.5 and 4.8). The Meyer 2 moraine is truncated by a small depression. The Meyer 1 moraine can be traced across the same depression indicating the formation of the depression may have occurred between deposition of the Meyer 1 and 2 drifts. A hummocky deposit covers the Meyer 3 drift (Figure 4.13). Well-developed patterned ground on this deposit suggests ice cement at shallower depths than in the adjacent Meyer drift. The deposit slopes upward toward the Rutkowski Trough and is bounded by a Rutkowski moraine ridge to the south. This deposit is tentatively identified as solifluction (soil creep) lobes which originated from morainal material deposited when the Rutkowski Glacier stood at the edge of the trough. The adjacent basin may be eroded by ice marginal drainage from the same or a similar ice advance, a collapse feature resulting from melting of a buried ice core, or the result of local slump faulting.

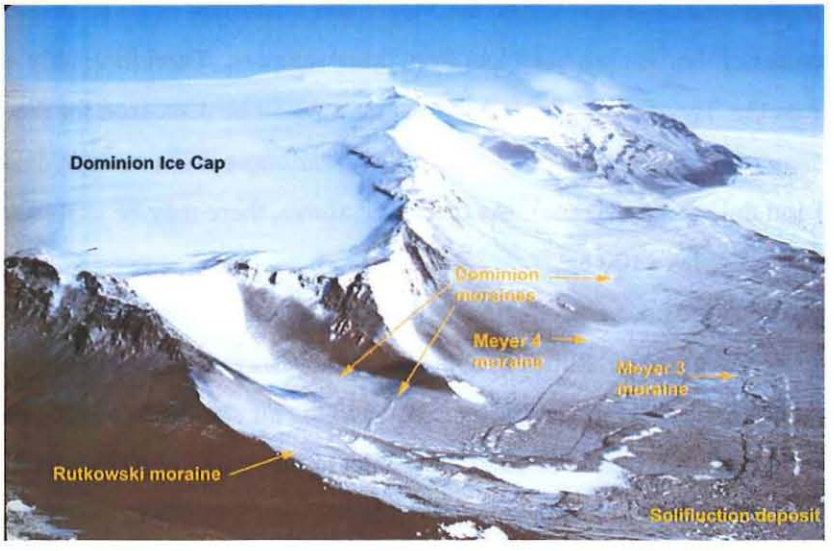

Figure 4.13 Photograph of moraines on Mercer Platform looking south. The hummocky solifluction deposit characterized by patterned ground appears in the lower right corner. This deposit truncates the Meyer 3 moraines and is related to an advance of the Rutkowski Glacier, indicating a warmer climate than at present. The Dominion moraines in the cirque valley, the highest Rutkowski moraine, and the Meyer 4 moraine are conspicuous after the light snowfall.

The Meyer 4 moraine forms the distal boundary of the Meyer drift and marks the boundary between continuous drift cover and more scattered glacial deposits. The Meyer 4 moraines overlie wider sinuous moraines which are probably related to the older Dominion drift. In places, the moraine is partially buried by scree from the steep bedrock slope at the southern side of the Mercer Platform. The weathering of the boulders is noticeably more developed than

the Meyer 1 moraine. Horned and hollow dolerite is common and the sandstone boulders are deeply cavernously weathered and have greater than 1 mm quartz rinds.

The Dominion drift on the Mercer Platform consists of two moraines which are preserved in the floor of the small cirque valley and on the hills at the southwest corner of the Platform (Figure 4.13). The moraines cannot be traced across the steeper intervening slopes. The moraines are extremely subdued, in some places discernible only by the scattering of sandstone erratics. The larger sandstone boulders are cavernously weathered into grotesque shapes. Most are weathered to the ground surface or small cobbles. These are the oldest lateral moraines on the Mercer Platform. Their age places minimum age constraints on the alpine glaciation associated with the massive alpine moraines and the underlying Sirius deposits.

Surface exposure ages

The ^{3}He and ^{21}Ne data are presented in Tables 4.2 and 4.3. The neon data is limited to 10 sandstone boulders from the older moraines. Diffusion of cosmogenic helium from quartz is demonstrated by the variable $^{3}He/^{21}Ne$ of samples from the Meyer and Dominion drifts (Table 4.4). Between 10 and 50 percent of the ^{3}He has been lost from these samples. Therefore, only the surface exposure ages from the ^{3}He of pyroxene and ^{21}Ne of quartz will be discussed for the Meyer and Dominion drift samples. The ^{3}He exposure ages of the Beardmore drifts include data on both sandstones (quartz) and dolerite (pyroxene). As discussed above, there may be problems with diffusion in quartz even in samples <100 ka.

This problem is apparent in the poor reproducibility of replicate quartz samples from the Beardmore drift (Table 4.2). The large uncertainties in some (early) measurements is due to very low $^{3}He/^{4}He$ of the samples inlet to the mass spectrometer relative to the air standard aliquot. For other (later) samples, larger standard and sample aliquots were inlet to maximize the ^{3}He signal. Crushed samples (powders) typically gave higher cosmogenic ^{3}He concentrations than mineral grains. This paradoxical result is an artifact of the method used to calculate cosmogenic ^{3}He. A significant fraction of the ^{4}He is released by crushing. The inherited ^{3}He calculated by multiplying the initial $^{3}He/^{4}He$ by total ^{4}He released by melting the powder is underestimated, leading to a higher calculated cosmogenic ^{3}He (see Chapter 1, Equations 9-11). This effect was observed in both quartz and pyroxene and is related to the fact that the ^{4}He is radiogenic rather than magmatic (Table 4.2 and 4.3a). In order to calculate mean exposure ages for the moraine

boulders, only measurements on whole grains were used. In cases were there are replicates with acceptable uncertainties the higher measured ^{3}He is used.

Table 4.2 Helium isotopic data for Beardmore Drift

Sample	type	lith.	elev.	depth	^{4}He $x10^{-6}$	±1 sig	$^{3}He/^{4}He$	±1 sig	^{3}He cosmo $x10^{6}$	±1 sig	Age	±1 sig
			(m)	(cm)	ccSTP/g		(melt)		atoms/g		(kyr)	(kyr)
Beardmore 2 Drift												
SAK95-210	grains	SS	1810	2.0	2.90	0.006	0.386	0.004	41.3	0.6	48.7	0.8
SAK95-210	abraded	SS	1810	2.0	1.29	0.002	0.899	0.008	43.1	0.4	**50.8**	0.6
SAK95-211	abraded	SS	1810	0.5	2.12	0.003	0.108	0.002	8.26	0.35	9.5	0.4
SAK95-211	powder	SS	1810	0.5	1.92	0.004	0.158	0.005	11.1	0.5	12.7	0.6
SAK95-211	grains	SS	1810	0.5	21.0	0.021	0.017	0.011	10.9	9.1	12.6	10.5
SAK95-211	grains	SS	1810	0.5	6.20	0.014	0.032	0.002	6.69	1.03	7.7	1.2
SAK95-211	grains	SS	1810	0.5	0.92	0.001	0.264	0.012	8.89	0.43	**10.2**	0.5
SAK95-214	grains	SS	1810	1.5	0.33	0.000	2.871	0.014	34.8	0.2	**40.7**	0.3
SAK95-214	powder	SS	1810	1.5	1.92	0.003	0.248	0.006	17.5	0.5	20.5	0.6
SAK95-214	abraded	SS	1810	1.5	7.65	0.015	0.162	0.002	45.3	1.3	52.9	1.6
SAK95-214	dirty	SS	1810	1.5	6.44	0.009	0.123	0.005	28.8	1.5	33.6	1.8
SAK95-215	grains	SS	1810	2.5	1.76	0.002	0.306	0.005	19.8	0.4	**23.6**	0.5
SAK95-217	grains	SS	1810	3.0	1.41	0.003	0.219	0.005	11.3	0.3	**13.6**	0.4
SAK95-415	powder	Dol	1810	2.0	3.76	0.020	0.126	0.003	16.2	0.4	21.1	0.6
SAK95-415	grains	Dol	1810	2.0	4.79	0.009	0.101	0.003	16.2	0.5	**21.1**	0.7
SAK95-416	grains	SS	1810	1.5	2.65	0.002	0.048	0.001	4.44	0.11	5.2	0.1
SAK95-417	powder	Dol	1810	1.5	0.96	0.005	0.341	0.014	11.9	0.5	15.3	0.7
SAK95-417	grains	Dol	1810	1.5	2.23	0.004	0.131	0.002	10.0	0.2	**12.9**	0.2
Beardmore 1 Drift												
SAK95-203	grains	SS	1800	2.0	3.80	0.005	0.064	0.007	8.62	1.14	**10.3**	1.4
SAK95-205	powder	SS	1800	1.5	6.18	0.010	0.064	0.007	14.0	1.9	16.5	2.2
SAK95-205	grains	SS	1800	1.5	27.68	0.021	0.025	0.006	22.7	7.4	26.7	8.8
SAK95-205	grains	SS	1800	1.5	2.16	0.002	0.086	0.003	6.66	0.40	**7.8**	0.5
SAK95-206	grains	SS	1800	2.5	0.71	0.003	0.268	0.004	6.96	0.15	**8.3**	0.2
SAK95-209	grains	Dol	1800	2.0	5.49	0.013	0.059	0.002	10.0	0.4	**13.1**	0.6
SAK95-212A	grains	SS	1795	2.0	0.41	0.000	0.314	0.006	4.76	0.11	5.7	0.1
SAK95-404	grains	SS	1800	1.5	4.05	0.007	0.038	0.001	5.28	0.62	**6.2**	0.7
SAK95-405	grains	SS	1800	3.0	2.09	0.003	0.084	0.002	6.30	0.35	**7.6**	0.4
SAK95-407	grains	SS	1800	3.0	1.69	0.003	0.114	0.003	6.98	0.31	**8.4**	0.4
SAK95-408	grains	Dol	1800	5.0	19.64	0.048	0.016	0.001	9.50	0.79	**13.1**	1.1
SAK95-409	grains	SS	1800	2.0	3.70	0.008	0.049	0.002	6.33	0.62	**7.5**	0.7
SAK95-413	grains	Dol	1800	2.0	7.28	0.016	0.042	0.001	8.67	0.29	**11.4**	0.4

Age uncertainties are propagated analytical uncertainties only. Only ages in bold type are used to calculate mean ages and plotted in figures. Production rate and scaling uncertainties are assumed <10%. ^{3}He sea level production rates of 140 at/g/yr (quartz) and 127 at/g/yr (pyroxene) are scaled for elevation using the formulation of Stone (1999). Initial $^{3}He/^{4}He$ is assumed to be .010 (pyroxene) and .003 (quartz). See text for explanation. SS=sandstone; Dol=dolerite. Abraded = quartz grains which were processed in an air abrasion chamber to remove adhering cement. Powder = samples were crushed *in vacuo* prior to melting. Grains = mineral grains. Dirty = grains with adhering cement.

The exposure ages of samples from the Beardmore 1 drift range from 5.7 to 13.1 ka with a mean value of 9.4 ± 2.4 ka (Table 4.2). The weighted mean (8.8±0.1 kyr) differs slightly from the mean and the uncertainty is less because the oldest and youngest samples have the largest analytical uncertainties. Sample 212A was not included in the mean calculation because it is a

large block in front of the moraine. Given the young age of the sample (5.7 ka) compared to the others it is likely this boulder rolled off the moraine to a new orientation some time after deposition of the moraine. The age distribution of the samples is plotted in Figure 4.14. The ages of the sandstones have a roughly normal distribution. However, the ages of the dolerite samples are consistently older. The weighted mean of the sandstone boulders is 8.15 ± 0.14, while that of the dolerite is 12.0 ± 0.3. A t-test shows that the sandstone and dolerite ages represent different populations at the 95 percent confidence interval

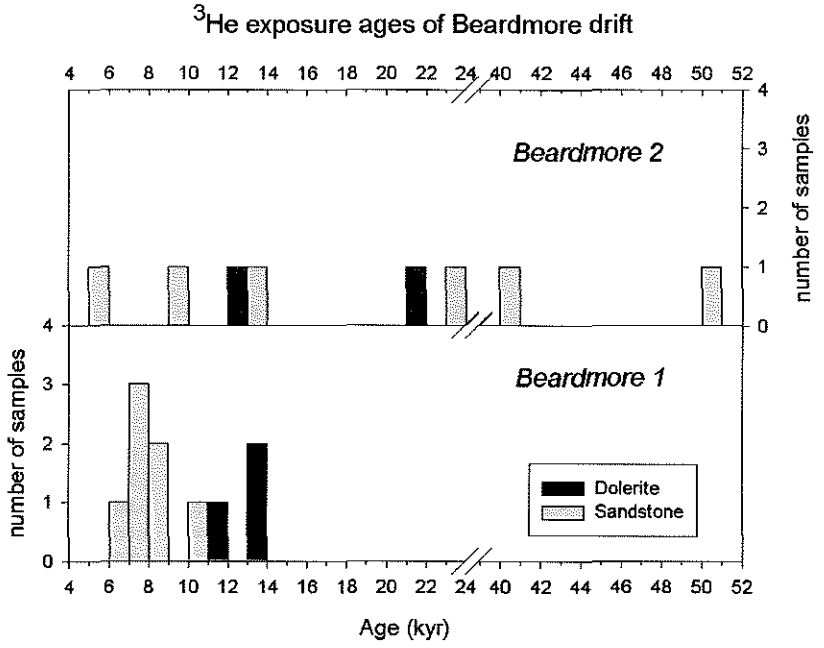

Figure 4.14 Histogram of ^{3}He surface exposure ages of boulders from Beardmore drift. The ages from Beardmore 1 drift are clustered between 6 and 14 ka and record maximum ice elevations of the WAIS in this region during the last glacial cycle. In contrast, the ages from the Beardmore 2 drift are widely scattered, but overlap those of the Beardmore 1 moraine. The older ages are likely due to prior exposure. The drift most likely records an earlier thickening of the Beardmore Glacier during the LGM.

This offset could result for a number of reasons. The scaling for elemental composition may be incorrect. Better agreement is obtained when the same production rate is used for both minerals, but use of a common production rate would require no dependence of the ^{3}He production rate on composition, which seems unlikely. There could be differences in prior exposure of the two lithologies. For example, two of the dolerite boulders are angular and were presumably derived from bedrock cliffs. The sandstones are well rounded and, in most cases, striated, indicating that they are derived from the more rapidly eroding semi-lithified Sirius

sediments or from beneath the Beardmore Glacier where prior exposure might be less. There may be a larger inherited ^{3}He component in the dolerites than those in the Taylor Valley, so that the initial ^{3}He concentrations assumed for the dolerite may be too low. Finally, there may have been diffusive loss from the quartz even over these short exposure times. Comparison with ^{10}Be is necessary to evaluate this possibility, but reevaluation of limited data from Brook *et al.* (1995) suggests that diffusion is possible. Given these uncertainties, the best age estimate of the Beardmore 1 drift is the mean age of the samples (9.4 ± 2.4 kyr).

The surface exposure ages of the Beardmore 2 drift are widely scattered, ranging from 5.2 to 56 kyr with no cluster of ages (Figure 4.14). The ages are consistent with the stratigraphic and weathering observations indicating an older age than the Beardmore 1 drift. Scatter in surface exposure ages can arise from erosion, prior exposure of the samples, and/or variable diffusive loss of quartz. In Antarctica, low erosion rates minimize the likelihood of post-depositional erosion for such young surfaces and increase the likelihood of prior exposure. Because prior exposure is a more likely source of scatter than pervasive erosion or disturbance of the samples, it is unlikely the drift is as old as the oldest exposure samples. Similar wide ranges of exposure ages in the Ross Sea drift on Mt. Morning in the McMurdo Sound Region have been demonstrated to reflect prior exposure (Kurz and Ackert, 1996). The youngest exposure age (5 kyr) is from a very friable sandstone lithology which may have experienced significant erosion. If this anomalous sample is omitted, the youngest ages of the Beardmore 2 drift overlap with the oldest ages from the Beardmore 1 drift. The age of the Beardmore 2 drift likely falls within the loose cluster of ages from 12 to 24 ka obtained by excluding the extreme outliers. The stratigraphic relationship with the Beardmore 1 drift places a minimum age of the Beardmore 2 drift of ~10 ka. Because observable weathering occurred between deposition of these drifts, a tentative age of 15 to 24 ka (LGM) is assigned to the Beardmore 2 drift.

Meyer drift

Helium and neon isotopic data from boulders in the Meyer and Dominion moraines appear in Table 4.3. Surface exposure ages were measured on boulders from the Meyer 1 (innermost) and Meyer 4 (outermost) moraines in order to constrain the age range of the Meyer drifts. The ^{3}He exposure ages of four angular dolerite boulders and the ^{21}Ne age of a sandstone boulder from the Meyer 1 moraine are plotted in Figure 4.15. The surface exposure ages calculated for no erosion and erosion rates of .05 and .10 mm/kyr appear in Table 4.4. The ages

of three dolerite boulders overlap at the 2σ analytical uncertainties and have a mean age of 564 ± 12 ka. The ^{21}Ne age (625 ka) is older and one dolerite ^{3}He age is significantly younger (349 ka). However, in this age range the assumption of no erosion is not likely valid and these should be interpreted as minimum ages.

Table 4.3 a Helium isotopic data from Meyer and Dominion drift.

Sample	type	lith.	elev. (m)	depth (cm)	^{4}He x10^{-6} ccSTP/g	±1 sig	$^{3/4}$ He (melt)	±1 sig	^{3}He cosmo x10^{6} atoms/g	±1 sig
Dominion Drift										
SAK95-235	abraded	SS	1785	2.0	1.62	0.003	4.02	0.03	242	2
SAK95-246	abraded	SS	1930	1.5	38.6	0.088	0.17	0.00	243	7
SAK95-246		SS	1930	1.5	10.4	0.016	0.66	0.01	256	3
SAK95-247		SS	1930	3.0	0.059	0.000	49.2	0.2	109	1
SAK95-445	abraded	SS	1910	1.5	0.909	0.001	14.5	0.06	489	2
SAK95-446	abraded	SS	1910	3.0	0.895	0.002	10.2	0.10	340	3
Meyer 4 Drift										
SAK95-027		Dol	1785	1.0	3.58	0.011	5.45	0.03	725	5
SAK95-036		SS	1850	1.5	0.37	0.001	12.3	0.0	170	1
SAK95-245A		SS	1850	1.5	1.68	0.013	11.5	0.1	715	9
SAK95-435		SS	1785	1.5	2.26	0.007	1.04	0.01	86.9	0.8
SAK95-437		Dol	1785	3.0	9.47	0.026	1.77	0.01	620	5
SAK95-441	abraded	SS	1850	2.0	1.98	0.003	1.17	0.01	86	1
Meyer 1 Drift										
SAK95-014		SS	1790	3.0	0.30	0.001	12.1	0.1	137	1
SAK95-016		SS	1790	5.0	0.46	0.001	10.2	0.0	175	1
SAK95-018		Dol	1790	3.0	7.05	0.020	1.62	0.01	422	4
SAK95-220	abraded	SS	1790	1.5	0.67	0.001	8.33	0.04	206	1
SAK95-222	powder	Dol	1790	1.5	2.10	0.009	3.76	0.02	294	2
SAK95-222	grains	Dol	1790	1.5	2.52	0.005	2.76	0.01	258	1
SAK95-223A		SS	1790	1.5	2.34	0.002	1.84	0.01	160	1
SAK95-225		SS	1790	1.5	5.34	0.008	0.59	0.01	117	1
SAK95-424		Dol	1790	3.0	5.86	0.016	1.89	0.02	410	4
SAK95-426		Dol	1790	3.0	6.33	0.021	1.82	0.01	427	3
SAK95-427	abraded	SS	1790	3.0	1.07	0.002	3.41	0.02	135	1

Initial ^{3}He/^{4}He is assumed to be .010 (pyroxene) and .003 (quartz). SS = sandstone; Dol = dolerite. Abraded = samples which were physically abraded to remove adhering cement. Powder = samples were crushed *in vacuo* prior to melting. All other samples were whole mineral grains.

Table 4.3 b Neon isotopic data from Meyer and Dominion drifts.

Sample	lith.	elev. (m)	depth (cm)	heating step °C	$^{20}Ne/^{22}Ne$	±1 sig	$^{21}Ne/^{22}Ne$	±1 sig	^{20}Ne $x10^{-11}$ ccSTP/g	±1 sig	^{21}Ne cosmo $x10^{8}$ atoms/g	±1 sig
Dominion Drift												
SAK95-235	SS	1785	2.0	300	9.80	0.02	.0379	.0003	5.25	.041	0.15	0.01
				600	9.69	0.01	.0362	.0002	41.7	0.3	1.02	0.06
				1500	9.68	0.01	.0332	.0002	65.8	0.5	0.98	0.08
SAK95-246	SS	1930	1.5	300	9.77	0.03	.0353	.0003	8.38	.090	0.17	0.02
				600	9.57	0.02	.0482	.0003	23.4	0.3	1.48	0.05
				1500	9.64	0.03	.0397	.0002	12.3	0.1	0.44	0.02
SAK95-247	SS	1930	3.0	600	9.70	0.02	.0361	.0001	54.4	0.3	1.24	0.05
				1500	9.65	0.02	.0345	.0001	54.7	0.3	1.01	0.05
SAK95-445	SS	1910	1.5	300	9.39	0.04	.0737	.0009	1.34	.003	0.17	0.00
				600	9.40	0.02	.0678	.0004	13.4	0.0	1.50	0.02
				1500	9.51	0.02	.0593	.0005	7.31	.016	0.63	0.01
SAK95-446	SS	1910	3.0	300	9.64	0.03	.0510	.0008	1.75	.014	0.18	0.01
				600	9.39	0.02	.0746	.0007	6.51	.052	1.44	0.05
				1500	9.48	0.03	.0638	.0006	3.33	.027	0.55	0.02
Meyer 4 Drift												
SAK95-036	SS	1850	1.5	300	9.52	0.04	.0580	.0005	1.73	.012	0.16	0.00
				600	9.52	0.01	.0598	.0003	7.93	.055	0.77	0.02
				1500	9.68	0.02	.0399	.0002	5.31	.037	0.18	0.01
SAK95-245A	SS	1850	1.5	600	9.58	0.02	.0483	.0003	22.0	0.3	1.15	0.05
				1500	9.64	0.01	.0394	.0002	43.6	0.6	1.24	0.08
SAK95-435	SS	1785	1.5	300	9.72	0.03	.0435	.0004	2.05	.020	0.12	0.01
				600	9.66	0.02	.0463	.0002	11.0	0.1	0.77	0.03
				1500	9.66	0.02	.0381	.0002	9.48	.094	0.35	0.02
SAK95-441	SS	1850	2.0	300	9.95	0.04	.0397	.0003	5.02	.035	0.14	0.01
				600	9.65	0.01	.0472	.0002	13.6	0.1	0.72	0.02
				1000	9.81	0.03	.0376	.0003	6.32	.044	0.15	0.01
				1500	9.62	0.10	.0477	.0011	0.02	.000	0.00	0.00
Meyer 1 Drift												
SAK95-016	SS	1790	5.0	300	9.76	0.03	.0389	.0006	8.38	.090	0.05	0.00
				600	9.67	0.01	.0470	.0003	23.4	0.3	0.44	0.01
				1500	9.79	0.01	.0367	.0003	12.3	0.1	0.14	0.01

Cosmogenic ^{21}Ne is calculated in a manner similar to cosmogenic ^{3}He. See Chapter 1. All ^{20}Ne is assumed to be from air with an initial $^{21}Ne/^{20}Ne$ of (.00295).

$^{21}Ne_{initial} = {}^{21}Ne/^{20}Ne_{initial} \times {}^{20}Ne_{total}$;

$^{21}Ne_{total} = {}^{21}Ne/^{20}Ne_{measured} \times {}^{20}Ne_{total}$; $^{21}Ne_{cosmo} = {}^{21}Ne_{total} - {}^{21}Ne_{initial}$

Table 4.4 Surface exposure ages of Meyer and Dominion drifts.

Sample	lith.	elev. (m)	depth (cm)	^{3}He cos x 10^6 atom/g	±1 sig	Age e=0 (kyr)	±1 sig	Age e=.05 (kyr)	Age e=.10 (kyr)	^{21}Ne cosmc x10^8 atoms/g	±1 sig	Age e=0 (kyr)	±1 sig	Age e=.05 (kyr)	Age e=.10 (kyr)	^{3}He/^{21}Ne atoms/g
Dominion Drift																
SAK95-235	SS	1785	2.0	242	2	291	2	295	299	2.14	0.10	**2045**	97	2262	2555	1.13
SAK95-246	SS	1930	1.5	243	7	260	8	263	266	2.09	0.06	**1778**	52	1939	2147	1.16
SAK95-247	SS	1930	3.0	109	1	119	1	120	121	2.25	0.07	**1956**	63	2153	2416	0.48
SAK95-445	SS	1910	1.5	489	2	531	2	544	558	2.30	0.02	**1986**	23	2190	2463	2.13
SAK95-446	SS	1910	3.0	340	3	379	4	385	392	2.17	0.05	**1915**	48	2104	2353	1.56
Meyer 4 Drift																
SAK95-027	Dol	1785	1.0	725	5	**944**	6	987	1035							
SAK95-036	SS	1850	1.5	170	1	193	1	195	196	1.11	0.02	**1003**	17	1051	1107	1.53
SAK95-245A	SS	1850	1.5	715	9	811	10	842	877	2.39	0.09	**2161**	85	2405	2742	2.99
SAK95-435	SS	1785	1.5	86.9	0.8	104	1	104	105	1.24	0.04	**1171**	34	1238	1317	0.70
SAK95-437	Dol	1785	3.0	620	5	**836**	6	870	907							
SAK95-441	SS	1850	2.0	85.8	0.6	98	1	99	99	1.02	0.02	**925**	20	966	1012	0.84
Meyer 1 Drift																
SAK95-014	SS	1790	3.0	137	1	167	1	168	170							
SAK95-016	SS	1790	5.0	175	1	221	1	224	226	0.63	0.02	**625**	16	644	664	2.78
SAK95-018	Dol	1790	3.0	422	4	**567**	5	582	598							
SAK95-220	SS	1790	1.5	206	1	245	1	248	251							
SAK95-222	Dol	1790	1.5	258	1	338	2	343	349							
SAK95-223A	SS	1790	1.5	160	1	190	1	192	193							
SAK95-225	SS	1790	1.5	117	1	138	2	139	140							
SAK95-424	Dol	1790	3.0	410	4	**551**	5	566	581							
SAK95-426	Dol	1790	3.0	427	3	**574**	5	589	606							
SAK95-427	SS	1790	3.0	135	1	165	1	166	168							

Age uncertainties are propagated analytical uncertainties only. Only ages in bold type were used to calculate mean ages and plotted in figures. Production rate and scaling uncertainties are assumed <10%. Sea level ^{3}He production rates of 140 atoms/g/yr (quartz) and 127 atoms/g/yr (pyroxene) and ^{21}Ne production rate 17.5 atom/g/yr (quartz) are scaled for elevation using the formulation of Stone (1999). SS = sandstone; Dol = dolerite. E = erosion rate (mm/kyr). Samples were whole mineral grains.

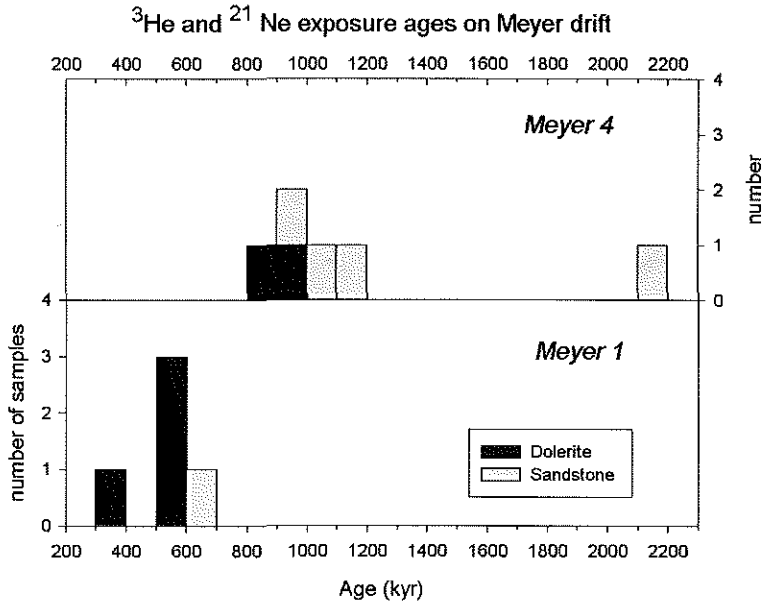

Figure 4.15 Histogram of surface exposure ages of boulders from Meyer drift. Ages of dolerite boulders were determined using ^{3}He. Ages of sandstone boulders were determined using ^{21}Ne. The ages of Meyer 1 drift cluster around 600 ka. The ages of Meyer 4 drift cluster around 900 ka and are clearly distinguished from those of Meyer 1 drift, indicating that Meyer drift was deposited during multiple glaciations during the mid Pleistocene. The dolerite (^{3}He) ages are consistently younger than the sandstone (^{21}Ne) ages suggesting the ^{21}Ne production rate is slightly low relative to the ^{3}He production rate.

The youngest age is from a "puzzle rock;" the sample was a small piece which was in place but had weathered free of the boulder (Figure 4.16). Although this boulder appears older than the others measured based on the degree of weathering, it apparently has a higher *weathering rate*. The lower ^{3}He concentration of this sample could result from recent removal of a 30 cm thick "puzzle piece" which had until recently been overlying the sample (Figure 4.9). Alternatively it could result from a more constant erosion rate of ~1.0 mm/kyr. The maximum erosion rate assuming steady state is 1.3 cm/kyr, but this high value is impossible (>4 m of erosion in 300 kyr). Erosion rates of even ~1.0 mm/kyr are a factor of 20 higher than the typical maximum erosion rates measured on dolerite boulders in Antarctica assuming steady state erosion (Kurz and Ackert, 1997; Schäfer *et al.*, 1999) although values as high as 0.20 to 0.35 mm/kyr were measured on bedrock samples from the Dry Valleys (Schäfer *et al.*, 1999). Maximum dolerite erosion rates calculated from the samples with the highest cosmogenic nuclide concentration in this study are ~5 mm/kyr suggesting that none of the samples are at steady state erosion.

Figure 4.16
Photograph of sample SAK95-222 from the Meyer 1 drift. Although the advanced weathering makes this boulder appear older than others on the moraine, the surface exposure age is younger. The boulder is a "puzzle rock" preferentially weathered along joint surfaces. A puzzle "piece" which had shielded the sample has apparently slid off, resulting in the young apparent age.

The extremely low steady state rates measured on old (>1 Ma) surfaces may be considered *minimum* values for erosion rates of boulders because sampling is biased toward resistant lithologies. Boulders with higher erosion rates will have disappeared or be much smaller (and therefore not sampled) on the old (>1 Ma) surfaces used to calculate steady state erosion rates. In this case, erosion rates of ~1 mm/kyr would result in loss of ~58 cm of rock over the

exposure period. This is more than half the remaining thickness of the block implying that this rock will be completely eroded within 1 Myr.

Complete erosion of ~1 m boulders on such time scales is consistent with the morphology of the Dominion drift moraines which consist of very subdued moraine ridges and lines of erratic blocks. If those moraines started with morphology similar to that of the Meyer moraines, most boulders have disintegrated. As discussed below, these moraines have exposure ages ~2 Ma. Moraines with similar morphology in Arena Valley (Figure 4.1) have similar exposure ages (Brook *et al.*, 1993; Brown *et al.*, 1991). Lithology dependent erosion rates are also consistent with the typical large variation in degree and type of dolerite weathering observed on individual moraine crests. The mineral grain size of the dolerite seems to control the weathering style and rate. In conclusion, it is not unreasonable to attribute the anomalous lower exposure age to variable erosion rates and to expect age scatter due to these effects when sampling multiple lithologies.

Although some prior exposure cannot be ruled out, the cluster of ages from different locations on the moraine suggests that the moraine is at least ~560 ka. This value represents a minimum age because there has been some erosion. Using the maximum value measured for dolerite boulder erosion of 0.1 mm/kyr (Schäfer *et al.*, 1999; Kurz and Ackert, 1997), the exposure ages range from 581 to 606 ka (Table 4.4). Because this erosion rate is higher than most measured, these exposure ages place loose upper limits on the moraine age. The ^{21}Ne age of the sandstone boulder is slightly older but agrees within analytical uncertainty of the erosion corrected age of the oldest dolerite sample.

The exposure ages of samples from the Meyer 4 moraine form a cluster of ages centered on ~1.0 Ma (Figure 4.15). There is one outlier at ~2 Ma. Excluding this sample, the mean exposure age of the samples is 976 ± 124 ka. The mean age using an erosion rate of 0.1 mm/ kyr is 1076 ± 153 ka. The age of the outlier is similar to ages obtained on boulders from the Dominion drift (below) and likely represents a boulder reworked from those deposits or simply sticking through the Meyer 4 moraine. This was the largest boulder on the moraine, over 3 m high and 5 m long.

The ^{21}Ne ages and the ^{3}He ages overlap demonstrating that the production rates used are broadly consistent. However, as was the case for the Meyer 1 ages, the dolerite (^{3}He) ages are generally younger than the sandstone (^{21}Ne) ages. This discrepancy could result from greater average prior exposure of the sandstone samples, underestimates of dolerite erosion rates, or

small inconsistencies in the production rates. The ^{21}Ne production rate was determined on a younger (~13 ka) surface than that used for the ^{3}He production rate (~125 ka) and could well be low relative to the ^{3}He production rates. Additional data is needed to test these possibilities.

Dominion drift

The results for the Dominion drift appear in Figure 4.17. Measurements were made on both mapped moraines; there was no discernible difference in the degree of weathering, which is extreme in both cases. No dolerite boulders were sampled due to the difficulty in unambiguously distinguishing moraine boulders from talus derived from the dolerite bedrock slopes above. The two samples from the proximal Dominion moraine have the same age ~1.9 Ma. The age of the distal Dominion moraine range from 1.8 to 2.0 Ma. The two moraines cannot be distinguished on the basis of the exposure ages. The mean age of all the samples is 1.94 ± .10 Ma (no erosion) and 2.39 ± 15 Ma (erosion = .1 mm/kyr). The Dominion drift is clearly distinguished from the oldest Meyer drift by the exposure ages and is about 1 million years older. As noted above, the outlier in the Meyer 4 ages falls within the exposure ages of the Dominion drift.

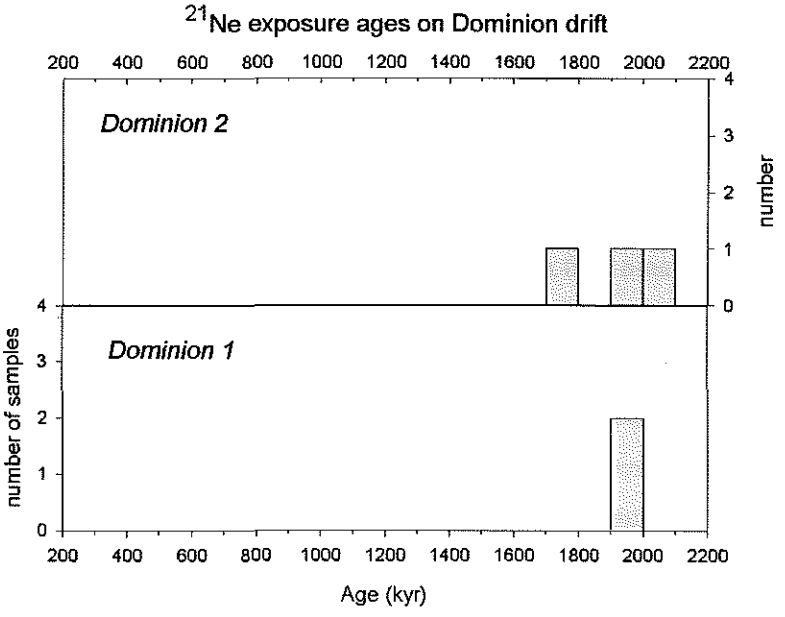

Figure 4.17 Histogram of surface exposure ages of boulders from two moraines of the Dominion drift. The moraines cannot be distinguished on the basis of surface exposure ages. Ages were determined using ^{21}Ne. The ages cluster between 1.9 and 2.0 Ma. Note the outlier in Meyer 4 drift (Figure 4.15) also falls within this age range.

4.6 Discussion

Beardmore drift: Last glacial maximum

The age of the Beardmore 1 moraine in the Dominion Range is constrained by the surface exposure data to 9.4 ± 2.4 ka. The question arises as to whether these ages are applicable to other outcrops of the Beardmore drift. Because the Beardmore 2 drift is only exposed in a small outcrop at the northwestern end of the Mercer platform, Beardmore 1 drift most likely correlates with the outer margin of Beardmore drift at other locations mapped by Denton *et al.* (1989a). In this case, the age of the Beardmore 1 drift constrains the time of maximum thickening of the WAIS at the mouth of the Beardmore Glacier. However, because the distal margins of the two drifts are so close, and rock weathering so similar, it is possible that the Beardmore 2 drift forms the outer limit at other locations and the age of this drift should be used to constrain the timing of maximum ice elevations down glacier. Mercer (1972) reports evidence for a readvance of ice within his equivalent Beardmore III drift (Table 4.1). Locations are not given by Mercer, but similar ice profiles are implied. It is not known whether these ice margins correspond to Beardmore 1 and 2 or Beardmore 1 and another younger drift. In either case, the surface exposure ages are consistent with earlier inferences that the Beardmore drift records thickening of the WAIS during the LGM.

Support for using the age of the Beardmore 1 drift to constrain the most recent expansion of the WAIS comes from the ages of deposits along the Hatherton Glacier, an outlet glacier to the north (Figure 4.1). There, a similar glacial drift occurs which is correlated with the Beardmore drift (Denton *et al.*, 1989b). This Britannia drift is subdivided into two units (I & II) by Bockheim (1989). Both drifts increase in elevation above the Hatherton Glacier toward the Ross Ice Shelf. At Lake Wellman, which is located in an ice-free tributary valley about half way down the Hatherton Glacier, a series of ^{14}C dates on blue green algae which grew in ice-dammed or kettle lakes along the Hatherton Glacier provide minimum ages for the underlying Britannia drift. The two Britannia drifts cannot be distinguished here, but they are separable in the next valley up glacier where their respective elevations preclude the younger Britannia drift from forming the most distal part of the Britannia drift in Wellman Valley.

The ^{14}C dates range in age from 10.6 to 12 ka at the outer margin of the drift to as old as 6.8 ka near the present lake (Bockheim *et al.*, 1989; Conway *et al.*, 1999). The ^{14}C ages are clearly minimum ages for the Britannia II drift in that they date overlying lakes. However, if the

lakes were small and ice-dammed, similar to the present lake Wellman, the dates may also constrain the ice margin. This interpretation is supported by the fact that the ages decrease down slope and that the algae was found *under* boulders suggesting a contemporaneous ice margin at that elevation. Thus, the ^{14}C dates of correlative drift at the Hatherton glacier are consistent with the surface exposure dates of the Beardmore 1 drift. The more conservative interpretation of the dates as minimum ages is consistent with the ages of both Beardmore 1 and 2 drifts. Although resolution of this issue awaits surface exposure dating of Beardmore drift at other locations, the age of the Beardmore 1 drift (9.4±2.4 ka) is assumed to record the maximum ice elevations in the Beardmore Glacier during the LGM. This interpretation is supported by results from Mt. Waesche near a dome of the WAIS in Marie Byrd Land indicating the last high stand of the WAIS also occurred at ~10 ka (Chapter 3).

The exposure age of the Beardmore 1 drift is considerably younger than 14 to 15 ka which is estimated for the maximum extent of the WAIS in the McMurdo Sound Region (Denton *et al.*, 1989b; Hall *et al.*, 1999; Stuiver *et al.*, 1981a). Chronologic data from the Ross Embayment indicates that the WAIS advanced across the Ross Sea during the LGM and that grounding line retreat was well underway by ~11 ka (Domack *et al.*, 1999; Licht *et al.*, 1999; Licht *et al.*, 1996). Grounding line retreat probably began as early as 14 ka, in response to sea level rise resulting from the melting of Northern Hemisphere ice sheets.

Delayed maximum ice elevations in interior parts of the WAIS are predicted by both non-equilibrium ice sheet models and models which incorporate twofold accumulation increases during the early Holocene (Steig *et al.*, 1999). The maximum is later and lower in the model with increased accumulation. The non-equilibrium ice sheet model is a quasi-3D ice sheet model of the WAIS tuned to fit the available chronology of ice advance and deglaciation from the Ross Embayment. The model provides a finite element solution of a 2-D (map-plane) time dependent mass continuity equation that integrates ice flow in a vertical column of ice (Fastook and Prentice, 1994; Steig *et al.*, 1999).

Ice sheet growth and decay in this model are driven solely by changes in calving rates, which roughly simulates the effects of sea level change. This simple approach is justified by results from more complex 3-D time-dependent thermomechanical ice sheet models which suggest that eustatic sea level is the primary control on the configuration of the WAIS (Huybrechts, 1990a). An important result of the model is that the WAIS does not have sufficient time to equilibrate with its extended grounding line position during the LGM, consistent with the

model of Huybrechts (1990b). As a consequence, interior elevations continue to thicken during grounding line retreat until the initial wave of thinning reaches the interior of the ice sheet. The delay in maximum ice elevation relative to maximum ice extent in the Ross Sea is several thousand years. The model results agree well with the glacial chronology at Mt. Waesche, as well as interpretations of the oxygen isotope record from the Byrd ice core (Steig *et al.*, 1999).

The Dominion Range is a similar distance along flow line from the inferred LGM margin of the WAIS as the domes of the ice sheet in West Antarctica. Given that the Beardmore Glacier flowed into the WAIS, a similar delay in maximum ice elevations along the glacier would be expected. Thus, relatively young surface exposure ages obtained for the Beardmore 1 drift are consistent with older dates (^{14}C and surface exposure) obtained from the McMurdo Sound Region and can be used to test or tune time-dependent ice sheet models.

This conclusion leaves the interpretation of the ages obtained on the Beardmore 2 drift problematic. If the Beardmore 1 drift records the maximum ice levels at the Dominion Range during the LGM, what does the older Beardmore 2 drift record? Many of the ages obtained fall within the LGM. The explanation is likely tied to the position of the grounding line of the WAIS during stage 3. The response time of the Beardmore Glacier to changes in sea level are shorter than that of the WAIS. Unlike the domes of West Antarctica, the Dominion Range is close (160 km) to the present grounding line. As long as the WAIS grounding line is south of the mouth of Beardmore Glacier, ice profiles must stay similar to those at present.

This suggests two scenarios: 1) If the grounding line of the WAIS was south of the Beardmore Glacier during stage 3, as sea level was further drawn down by growth of Northern Hemisphere ice sheets early in stage 2, the grounding line of the Beardmore Glacier would have advanced. A wave of thickening would then have propagated up glacier. If accumulation dropped by a factor of 2 during the LGM as been suggested (*e.g.*, Steig, 1997), a transient ice maximum could have occurred at the head of the glacier. Eventually, thickening due to damming of the Beardmore by grounding of the Ross Ice Shelf would have propagated up glacier leading to a second maximum in the Dominion Range. 2) Alternatively, if the grounding line of WAIS advanced north of the Beardmore prior to stage 2, higher ice levels at the Dominion Range could have occurred earlier. The most likely period for this is stage 4 which is consistent also with the oldest surface exposure dates measured on the Beardmore 2 drift (Ackert and Kurz, 1997). However, as discussed above, this interpretation would require anomalously high erosion rates or pervasive reworking of the samples to explain the scatter of younger ages.

An ice core from the Dominion Range ice cap that spans the last 30 kyr provides an independent record of environmental conditions in the Dominion Range which can be compared to the glacial chronology (Mayewski *et al.*, 1995). Oxygen isotopes from this core and others (Ciais *et al.*, 1994) show that warming following the LGM reached a maximum around 10 ka and that the early Holocene was relatively warm. Despite the chronological uncertainties, it is unlikely that the thickening of the upper Beardmore Glacier was in response to an accumulation increase associated with peak Holocene temperatures. The Rutkowski Glacier, which drains the Dominion Range ice cap (Fig 4.2) and presumably has a faster response time than the EAIS, was more retracted at 10 ka when the Beardmore was at a maximum than at present. However, the readvance reported by Mercer (1972) within the Beardmore drift and the younger Britannia drift at the Hatherton Glacier (Bockheim *et al.*, 1989) might be related to the Holocene temperature maximum.

There is no conspicuous event in the Dominion ice core record which correlates with the Plunket drift. Maximum values for chemical species indicating relatively strong influences of marine source air masses occur around 7000 ka. However, the contemporaneous increase in terrestrial salts indicative of ice-free terrain suggests the increased moisture expected with these air masses was deposited elsewhere and there is no significant change in the oxygen isotope record. The only significant change in oxygen isotopes is a decrease between 900 and 1000 ka. This event correlates with an increase in methane-sulfonic acid which is produced in the atmosphere by reaction of dimethylsulfide (DMS). DMS is produced by phytoplankton and is linked to greater sea ice extent, consistent with cooler temperatures. Because the surface of the Beardmore Glacier is an ablation zone throughout its length, ice levels may be more sensitive to changes in ablation rates on the glacier than in accumulation rates on the EAIS. Ablation (by sublimation) decreases with lower temperatures. The Plunket drift may record a recent thickening of the Beardmore Glacier in response to this cold event.

Meyer 1 drift: Stage 16

The surface exposure ages indicate the age of the Meyer 1 drift is ~600 ± 60 ka. This value is significantly older than the isotope stage 6 age proposed by Denton *et al.* (1989a and 1989b) for the Meyer drift. That age was based on the similarities of the ice profiles obtained from the Meyer and Beardmore drifts which imply that earlier thickening of the Beardmore Glacier was also due to damming by the WAIS. The Meyer drift was correlated with glacial-

lucustrine deposits in the McMurdo Sound Region dammed by an expanded WAIS which has been dated to stage 6 (Denton *et al.*, 1989b). The new field mapping in the Dominion Range confirms the similarities of the Beardmore and Meyer 1 ice margins, in particular, that they both project into the Rutkowski Trough which was free of alpine ice when the drifts were deposited (Figures 4.5 and 4.8). Taken together, these data suggest that the Mercer-Denton model can be applied to the Meyer 1 drift.

Assuming the surface exposure ages provide a good estimate of the age of the moraine, they are compared with the marine isotope record (Figure 4.18). The surface exposure ages encompass stages 15 and 16. In this age range, glacial and interglacials cannot be resolved using more conservative age uncertainties (±10%) which estimate scaling and erosion rate uncertainties. When the similarities of the Meyer 1 and Beardmore 1 ice margins are considered along with field evidence for a greatly expanded Rutkowski Glacier at other times (discussed below), it is unlikely that the Meyer 1 drift records the peak interglacial conditions of stage 15. Extending the Mercer-Denton conceptual model, the Meyer 1 drift likely dates to stage 16. It is significant in this regard that stage 16 is one of four Pleistocene stadials characterized by greater than usual $\delta^{18}O$ depletion which is interpreted as increased ice volume (the others are stages 2, 6, and 12). This "excess" ice is a characteristic of the last 900 kyr when the 100 kyr climate cycle dominates the marine isotope record (Raymo, 1997). If the correlation with this isotope stage is correct, the implication is that the ^{3}He production rate used is somewhat high or that substantial erosion or cover has occurred.

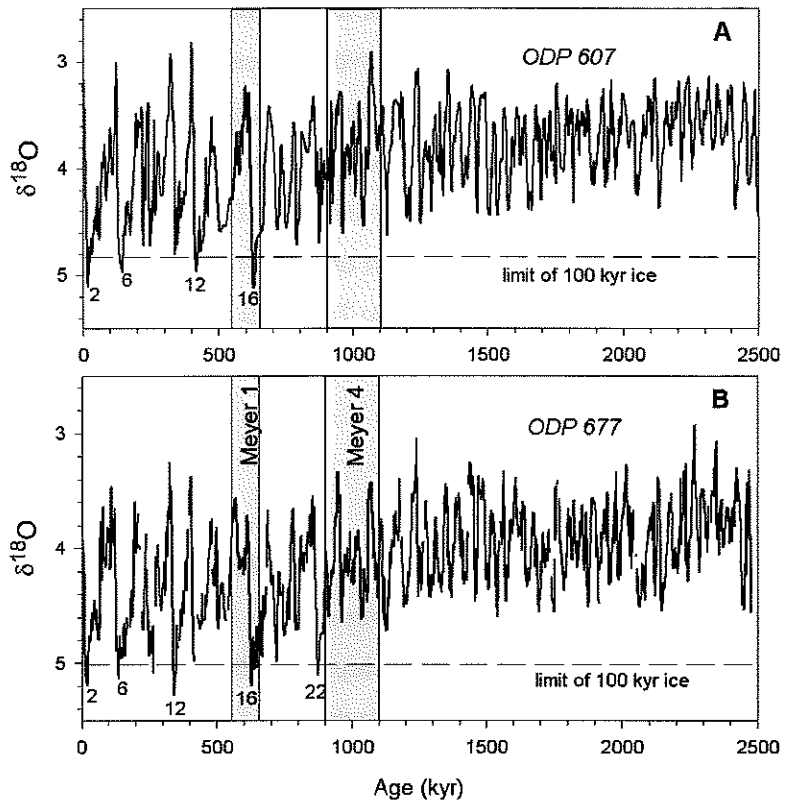

Figure 4.18 Oxygen isotope records for the last 2 Ma compared with glacial chronology from the Dominion Range. The oxygen isotope records are proxies for global ice volume. A) Record from benthic foraminifera from ODP 607 in the North Atlantic. B) Record from benthic foraminifera from ODP 677 in the eastern equatorial Pacific. Differences in the records reflect different relative contributions of temperature to the isotopic signal. Stage 16 is characterized by extreme $\delta^{18}0$ enrichment (greater ice volume and lower sea levels) in virtually all $\delta^{18}0$ records. In contrast, stage 22 and maxima in $\delta^{18}0$ around 2 Ma are most prominent in equatorial Pacific cores.

The surface exposure data are incompatible with the earlier stage 6 age assignment for Meyer drift unless the surface exposure ages are dominated by pervasive prior exposure. As discussed above, the tight cluster of dates suggests that this is unlikely. However, it could be argued that five dates may not be sufficient to accurately characterize the exposure age distribution. In this regard the ^{3}He data from five additional sandstone boulders are instructive (Table 4.4). These ages must be considered minimum ages because diffusive loss of helium from quartz clearly occurs in this age range. For example, the paired ^{3}He and ^{21}Ne data in this study indicate only 35 percent retention. Revised age estimates from the paired ^{3}He and ^{10}Be data presented by Brook (1993), using the present, best estimates for production rates, indicate greater than 25 percent ^{3}He loss from samples ~100 ka. Thus, although some of the ^{3}He ages fall within stage 6, when diffusive loss is considered, all ten samples indicate an age older than stage 6.

In addition to the reasons outlined above, the stage 6 age assignment of Meyer drift by Denton (1989b) was made by comparing the degree of soil development on Meyer drift with that of Taylor II and III drifts exposed in Arena Valley (Figure 4.1). Meyer soil development fell

between that of Taylor II (stage 5) and Taylor III (stage 7) which were dated by correlation with U/Th dated drifts farther down Taylor Valley (Denton *et al.*, 1989b). Subsequent surface exposure dating has confirmed the stage 5 age of the Taylor II moraine and indicates that the Taylor III moraine is >350 kyr (Brook, 1993). The degree of soil development on Meyer drift is significantly greater than that of Taylor II and only slightly less than that of Taylor III. Therefore the relative age data are also consistent with an age of the Meyer drift older than stage 6. The apparently younger soil development of Meyer drift compared to Taylor III may be attributed to the colder, dryer climate at the Beardmore and implies that it is not possible to resolve the relative ages of deposits in this age range using soil development.

Meyer 4 drift: Stage 22?

In contrast to the Meyer 1 drift, the Meyer 4 drift cannot be traced into the Rutkowski Trough. Rather, the outer moraine ends near the crest of the outer massive alpine moraine at the edge of the trough. Although a continued out-of-phase relationship seems likely, it is not possible to determine conclusively whether local ice flowing out of the Rutkowski Trough expanded in phase with the Beardmore Glacier at that time or not. The trends and character of all the Meyer drifts are similar, suggesting similar local ice dynamics. The few Rutkowski alpine moraines which drape over the outer massive alpine moraine also show evidence of out-of-phase behavior. The best defined alpine moraine, which can be traced over both massive alpine lateral moraines, cross-cuts the Meyer 4 moraine at a sharp angle (Figure 4.8 and 4.11). Thus, it appears that during deposition of this older Rutkowski moraine, the Beardmore Glacier was not as extensive as when the older Meyer drifts were deposited. These relationships are consistent with a continued out-of-phase relationship between Beardmore and Rutkowski ice during deposition of the Meyer 4 drift.

The significant age difference between the Meyer 1 and 4 drifts suggested by boulder weathering is corroborated by the surface exposure ages of the boulders from the Meyer 4 moraine which average ~1.00 ± 0.15 Ma (Table 4.4). Comparison with the marine isotope record is more speculative than for the Meyer 1 drift. The surface exposure ages do not provide unambiguous correlation with a specific isotope stage because the uncertainty in a surface exposure age determination in this age range will always overlap glacial and interglacial stages in the oxygen isotope record (Figure 4.18).

The field relationships justify tentatively attributing a glacial stage to the Meyer 4 drift. The surface exposure age includes stage 22 which is characterized in tropical Pacific benthic and planktonic records by $\delta^{18}O$ depletions comparable to those of the late Pleistocene 100 kyr glaciations (Raymo, 1997). In such records it is also where the dominant period in time series of climate proxies changes from 41 kyr to the 100 kyr (Figure 4.18) (Berger *et al.*, 1994). This transition has been termed the mid-Pleistocene revolution. Other field evidence in the Dominion Range is consistent with a stage 22 age assignment. The correlation of the Meyer 1 and 4 drifts with stages 16 and 22 respectively implies the occurrence of two intervening stadials (stages 18 and 20). This corresponds with the number of drift sheets mapped between the Meyer 1 and 4 drifts (Meyer 2 and 3). Finally, as discussed below, the outer Meyer 4 moraine marks a distinct geomorphic boundary implying a change in climatic regime. The mid-Pleistocene revolution marks a fundamental shift in the Earth's climate system with major shifts in the global carbon budget (Berger *et al.*, 1994; Raymo *et al.*, 1997).

These conclusions imply that the WAIS has been extant and fluctuating synchronously with the Northern Hemisphere ice sheets for about the last million years and that the WAIS is intimately connected with the development of the 100 kyr cycle. If tectonic effects are minimal (as discussed below), the results imply similar maximum ice volumes in the WAIS and EAIS for the last one million years. Therefore, it is unlikely that the WAIS accounted for a significantly greater fraction of the global ice volume earlier in the Pleistocene. This indicates that the WAIS has acted as an amplifier of the $\delta^{18}O$ signal generated by the Northern Hemisphere ice sheets during the Pleistocene and that WAIS ice volume is a critical component of the "excess ice" characterizing the 100 kyr glaciations.

Although it was argued that the Beardmore drift at the Dominion Range is correlative with units mapped by Denton *et al.* (1989a) down glacier, this may not hold true for the Meyer drift. There are many more moraines (and drifts) exposed in the Meyer drift at the Dominion Range than in Meyer drift outcrops down glacier. The stage 6 age assigned by Denton *et al.* (1989a) may well hold for some Meyer drift outcrops. If this is the case, it could provide problems for stratigraphic terminology in the future. As the Meyer Desert of the Dominion Range is the informal type section for Meyer drift (Denton *et al.*, 1989a), this nomenclature has been retained here. Should the Meyer drift at other locations prove to be younger than that of the Dominion Range a new name and type section will be required.

Lack of stage 6 and 12 drifts in the Dominion Range

Given the remarkable preservation of the glacial record at the Dominion Range and accepting the Mercer-Denton model, the absence of moraines of stage 6 and stage 12 at the Dominion Range is perplexing. In the McMurdo Sound Region, stage 6 glacial deposits are more extensive than those of stage 2 (Denton *et al.*, 1989b; Kurz and Ackert, 1996). The glacial chronology at the Dominion Range indicates that during deposition of the Meyer drift each glaciation was successively less extensive. Assuming similar ice sheet volumes, this pattern could result from glacial erosion deepening the Beardmore Trough (or the Ross Embayment) or from slow tectonic up lift of the Dominion Range, both of which are possible in the geologic setting. The pattern of successively less extensive glaciation may have continued after deposition of the Meyer 1 drift. Glacial drifts deposited during stages 6 and 12 probably underlie the Beardmore drift. If so, the pattern must have changed with the deposition of the Beardmore drift, but the reason is not clear. It seems unlikely that ice extent simply was greater during stage 2 than the preceding glaciations. Maximum glacial conditions (lowest sea levels) in the isotope record were comparatively short during stage 2. This is reflected in the non-equilibrium behavior of the WAIS discussed in Chapter 3.

A speculative scenario is presented here. Down faulting of the northern margin of the Mercer Platform along the Beardmore Glacier could result in locally greater ice extent during stage 2. There is abundant evidence for recent faulting at the Dominion Range. While the larger faults strike parallel to the Mill Glacier, defining Oliver Platform and Rutkowski Trough (Figure 4.2), smaller faults cut across the Oliver Platform parallel to the Beardmore Glacier. Structural control of the Beardmore Glacier has been inferred in the past (Grindley and Laird, 1969; Kadmina *et al.*, 1983). Non-tectonic slope failure due to oversteeping of the Beardmore Trough by glacial erosion is also possible. In this regard, it is suggested that the bluffs exposing Sirius deposits along the Beardmore Glacier may be fault scarps. The overlying Beardmore and Meyer drifts were deposited by cold-based ice which preserved underlying topography; active glacial erosion of the cliffs is not consistent with this observation. This interpretation does not exclude erosion at the base of the Beardmore Glacier which is probably wet-based. This scenario is supported by the differences in the morphology of the Beardmore and Meyer drifts. The presence of a significant ice core in the Beardmore drift on the Mercer Platform implies a thicker debris mantle and increased debris input to the glacier, consistent with newly exposed fault scarps.

Dominion drift

Dominion drift consists of isolated moraine ridges on the slopes above the Meyer drift. The mapping of the Dominion drift moraines shows that the Beardmore ice margin had a similar surface profile to that of the Meyer drifts but was up to 80 m thicker. Due to the greater thickness, the ice margin was influenced by the topography of the slopes forming the southern side of the platform. The ice projected into the mouth of the small cirque-headed valley which was ice-free. Although extremely weathered, the moraine morphology is similar to that of the Meyer moraines; the Dominion drift also consists of boulder belts draped over the underlying topography. There is no evidence of running water; the moraines were deposited by cold-based ice under conditions similar to the present.

The moraines overlie colluvium derived from the steep slopes of the Dominion Range which border the southern side of the platform. The moraines are not preserved on the steeper slopes of the Dominion Range indicating that slope processes have probably been active since deposition of the moraines. Colluvium is overflowing the Meyer 4 moraine in some places beneath the steep slopes, indicating some activity since the deposition of that moraine. However, the preservation of the Dominion moraines on the moderate slopes at the southwest corner of the platform indicate that soil creep (solifluction) has been minimal there.

The relationship of the Beardmore Glacier and locally derived ice in the Rutkowski Trough during deposition of the Dominion drift is not clear. However, the ice profiles are similar to those of the younger glacial advances. The surface exposure ages indicate that the Dominion drifts are about 2 Ma ,which falls within a period of global cooling in the marine isotope record (Raymo *et al.*, 1989). Large Northern Hemisphere ice sheets are believed to have formed about 2.4 Ma and again after 2.1 Ma (Raymo *et al.*, 1989). Therefore, it is possible these moraines also record expansion of the WAIS in response to lower glacial-eustatic sea levels. Maxima in $\delta^{18}O$ of planktonic foraminifera in the Western Pacific (ODP 806) occur at about this time (Berger *et al.*, 1994). Similar values do not occur again until stage 22. This observation is consistent with the lack of moraines in the Dominion Range preserved from this interval.

Alpine moraines: A record of local glaciation

The presence of moraines recording advances of the Rutkowski Glacier significantly beyond the present terminus indicates periods during the last one million years when climatic conditions were more favorable to local ice accumulation in the Dominion Range than those at

present. Following the reasoning of Denton *et al.* (1989b), Marchant *et al.*, (1994) and Mercer (1968), these conditions most likely occurred during interglacial periods due to warmer temperatures and closer proximity to the open ocean moisture source. Because the alpine glacial moraines record significantly larger ice extent than present, and by extension conditions more favorable for ice accumulation, the Rutkowski moraines may indicate a more reduced WAIS than present. It is possible some of the moraines are an indirect record of collapse of the WAIS. Evidence for Pleistocene collapse of the WAIS from sediment recovered from beneath the ice sheet is presented by Scherer *et al.* (1998). During one of the Rutkowski Glacier advances, temperatures warm enough to thaw surficial sediments are suggested by the hummocky solifluction deposit which truncates the Meyer 3 drift (Figure 4.13). Mercer (1968) reports two inactive solifluction flows at the Reedy Glacier to the south. These flows are undated but older than moraines attributed to the LGM. The flow at the Dominion Range is younger than the Meyer 3 drift (<1 Ma) and older than the Beardmore drift. The stratigraphic relationship with the Meyer 1 drift is not clear, but the deposit could easily be younger. Several earlier advances are recorded by boulder belt moraines overlying the outer large alpine moraine.

In contrast to the overlying boulder belts characteristic of deposition by cold-based ice, the massive alpine moraines record evidence of a different glacial regime. Although the basal ice conditions are not known, the debris input was much greater, suggesting warmer climatic conditions. Rather than the boulder belts and thin drift typically deposited by polar glaciers, the moraine morphology is similar to that commonly deposited by temperate and subpolar wet-based alpine glaciers. Such morphology is unknown in the Pleistocene alpine glacier record of Antarctica, but similar pairs of massive alpine moraines of Pliocene age occur in Wright Valley in the Dry Valleys (Hall *et al.*, 1993). Although striated stones and silty matrix are present within the Wright Valley moraines, Hall *et al.* (1993) concluded that these components were reworked from older basal tills and that the alpine glaciers were cold-based. In any case, the contrast with the younger boulder belt moraine loops which occur within the older massive moraines indicates a significant change in glacier dynamics most likely related to warmer climate.

Correlations with glacial deposits in the Dry Valleys

The geomorphology and geographic setting of the Meyer and Dominion drifts bear a striking resemblance to the well-studied moraines of the Taylor Glacier in Arena Valley, an ice-free tributary near the head of the Taylor Glacier in the Dry Valleys (Figures 4.1 and 4.19a)

(Denton *et al.*, 1989b; Marchant *et al.*, 1994). The Taylor Glacier is also an outlet glacier of the EAIS, but it does not presently reach the Ross Sea. The degree of rock weathering on the Meyer 4 and Dominion moraines, in particular the thickness of quartz rinds (several mm) on sandstone boulders resembles that of the Taylor IVa and IVb moraines in Arena Valley (Weed and Ackert, 1986). The Meyer 4 drift and the Taylor IVa drift exhibit similar morphology, consisting of numerous moraine ridges and continuous, but thin drift extending far beyond the present glacier margin. As is the case at the Dominion Range, two older moraines (Taylor IVb) occur outboard of the Taylor IVa drift. The Taylor IVa and IVb moraines overlie colluvium derived from the steep valley slopes which has remained largely inactive since deposition of the moraines (Marchant *et al.*, 1994). Exposure ages of these moraines of ~1 and ~2 Ma respectively (Brook *et al.*, 1993; Brown *et al.*, 1991; Staudacher and Allegre, 1991) provide a quantitative basis for correlating the moraines (Table 4.5). Synchronous behavior of two EAIS outlet glaciers in the Transantarctic Mountains over 800 km apart, demonstrates that the glacial records at both locations have regional significance.

Table 4.5 ^{10}Be exposure ages from Arena Valley

sample	Elevation (m)	Age e=0 (kyr)	±1 sig	Age e=.05 (kyr)	Age e=.10 (kyr)
Taylor IVa					
KBA89-45-1	1160	920	220	950	990
KBA89-47-2	1160	890	50	930	960
KBA89-94	1140	1100	60	1150	1210
Taylor IVb					
SCW87-3-1	1600	1520	100	1630	1770
KBA89-25	1320	1660	100	1800	1980
AA86-14	1310	2230	150	2530	2990
AA86-15	1340	1950	130	2150	2450
BW84-105	1300	1680	120	1830	2020

Exposure ages are calculated using the scaling of Stone (1999) and a ^{10}Be production rate of 5 atoms/g/yr (Clark *et al.*, 1995). ^{10}Be data is from Brook (1993).

The fundamental difference between the Taylor and Beardmore Glaciers is that the Taylor Glacier presently does not reach the Ross Sea (Figure 4.19a). Therefore, the fluctuations of the Taylor Glacier are presently decoupled from direct influence of the WAIS and controlled by accumulation rates at the nearby Taylor Dome. This situation has resulted in an out-of-phase relationship with the WAIS over the last glacial cycle (Denton *et al.*, 1989b; Marchant *et al.*,

1994). The Taylor Glacier is presently advancing (Robinson, 1984) and exposure ages of the youngest moraine fall within the last interglacial (stage 5) (Brook *et al.*, 1993). The older moraines are generally assumed to also have been deposited during interglacial stages but, as discussed above, the exposure ages are not precise enough to distinguish between glacial and interglacial intervals in the marine isotope record and thereby test this model. In contrast, the Meyer drifts in the Dominion Range are correlated here with glacial intervals in the marine isotope record. If the older Taylor and Dominion Range drifts do correlate with each other, one of the conceptual models is incorrect.

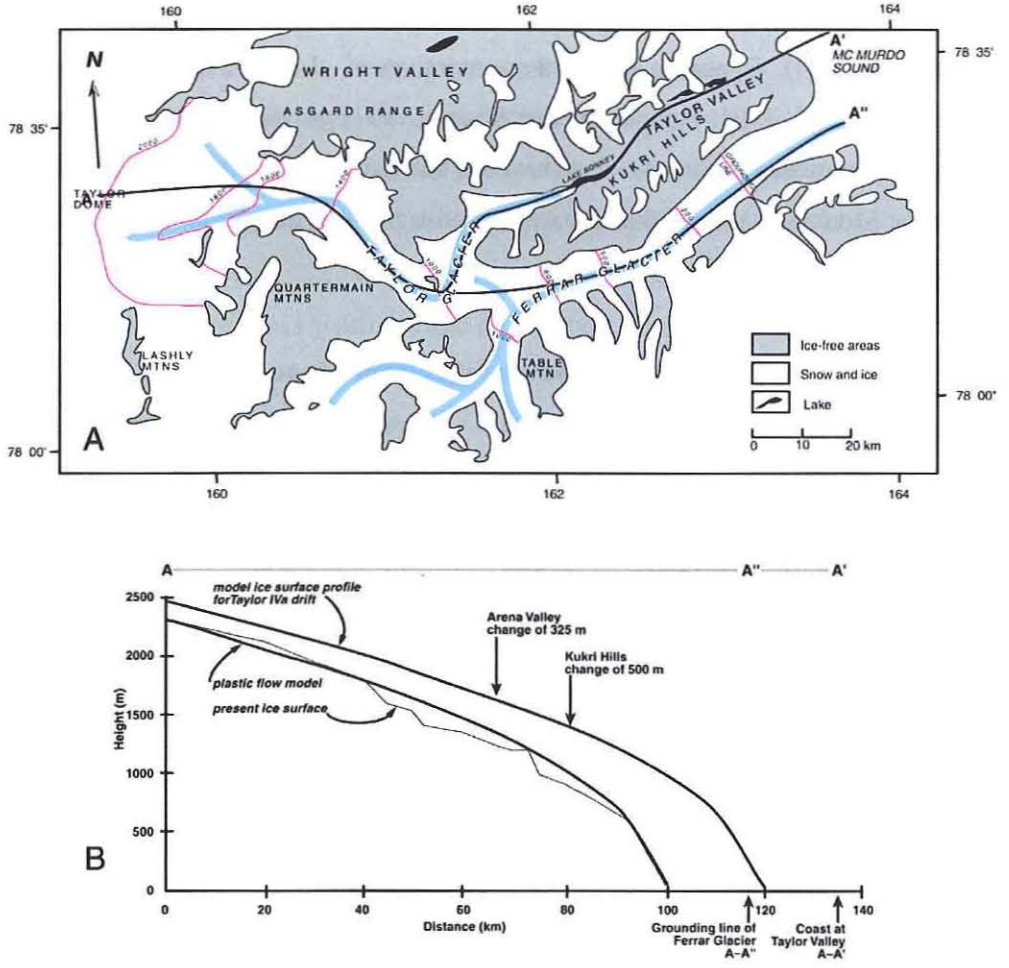

Figure 4.19 A) Map of the Taylor and Ferrar Glaciers. At present all ice from the upper Taylor Glacier flows into Taylor Valley. B) Present and reconstructed profiles of the Taylor Glacier during deposition of the Taylor IVa moraines in Arena Valley. While Taylor IVa ice would not have reached the coast in Taylor Valley, the reconstructed profile extends beyond the present grounding line in the Ferrar Valley. Because the plastic flow model over-estimates the profile for tidewater glaciers and ice flux would have to more than double to support the additional ice flow down the Ferrar, grounded ice in McMurdo Sound is required to explain the height of the Taylor IVa moraines in Arena Valley. The Taylor IV moraines probably were deposited during glacial, rather than interglacial, stages.

The correlation of the older drifts in Arena Valley with interglacial conditions is based on a simple extension of the most recent ice dynamics into the past (Denton *et al.*, 1989b). This assumption implies that the Taylor Glacier has not interacted with grounded ice in McMurdo Sound for the last two million years. Apparent support for this assumption comes from calculated glacier profiles which are tied to the elevation of the moraines in Arena Valley and projected down Taylor Valley (Marchant *et al.*, 1994). Those profiles indicate the Taylor IVa advance would have terminated short of the coast (Figure 4.19B). However, these calculations ignore the unusual relationship of the Taylor and Ferrar drainages which are connected west of the Kukri Hills (Figure 4.19a). In contrast to the Taylor Glacier, the Ferrar Glacier presently calves into McMurdo Sound. Casual inspection of Figure 4.19A suggests that much of the ice of the upper Taylor Glacier flows down the Ferrar Valley. In fact, at present, all of the ice flows into the Taylor Valley, deflected by a sill across the head of the Ferrar and ice from the Emmanuel Glacier (Robinson, 1984).

The reconstructed glacier profiles for the Taylor IVa moraine indicate that ice levels were 500 m higher than present at the junction of the Taylor and Ferrar Valleys (Figure 4.19b). At that level, a significant fraction of the ice must have flowed down the Ferrar Valley. Projecting the reconstructed Taylor IVa profile down the Ferrar Valley results in a glacier terminus beyond the present grounding line (Figure 4.19B). In addition, the simple plastic flow model used for the ice profile reconstruction is inappropriate for a tidewater glacier (it results in a convex rather than concave profile). It appears that Taylor IVa ice levels in Arena Valley could not be maintained in the absence of grounded ice in McMurdo Sound blocking the mouth of the Ferrar Valley. The argument is even more convincing for the higher Taylor IVb moraines and if there has been any Plio-Pleistocene tectonic uplift of the Dry Valleys tectonic block. If the topography was lower, the grounding line would be farther up glacier (closer to Arena Valley). Moderate uplift during the Pliocene is inferred by marine sediments in drill holes from the mouth of Taylor Valley (Ishman and Rieck, 1992), but is limited to <300 m since 2.5 Ma by subaerial volcanics exposed in Taylor Valley (Wilch *et al.*, 1993).

Thus, correlation of the Meyer 4 drift with the Taylor IVa moraines is consistent with an interpretation that they both record grounded ice in the Ross Embayment. A similar case can be made for the Taylor IVb and Dominion drift. The implication is that expansion of the WAIS, with grounding lines north of McMurdo Sound, occurred as long ago as 2 Ma. This date is later than the initiation of Northern Hemisphere glaciation (Raymo *et al.*, 1989) and so could

conceivably reflect a response to glacial eustatic sea level similar to that envisioned for the younger moraines. Between ~2 and ~1 Ma the WAIS was apparently less extensive, with grounding lines probably south of the Beardmore Glacier. After ~1 Ma the WAIS has fluctuated synchronously with the Northern Hemisphere ice sheets and was a component of the excess ice characterizing the 100 kyr cycle. Recent evidence of extremely warm interglacial conditions with open seaways across West Antarctica at some time between 1.11 and .83 Ma was recently presented by Scherer (1999). These results are consistent with the glacial history described above in that they occur between the inferred glaciations in West Antarctica.

As stated above, the massive alpine moraines in the Dominion Range are similar to pairs of Pliocene alpine moraines fronting glaciers in Wright Valley (Hall *et al.*, 1993). Correlation of moraines by morphology alone is tenuous, but similar moraines are not described elsewhere in the glacial record of Antarctica. The ages of those moraines have been bracketed by the presence or absence of $^{40}Ar/^{39}Ar$ dated volcanic debris. The older moraines are >3.7 Ma and the younger are <3.5 Ma (Hall *et al.*, 1993). Correlation of these moraines with the massive moraines at the Dominion Range is consistent with the exposure ages of overlying Dominion drift and suggests the age of the inner alpine moraine is between 2 and 3.5 Ma. Thus, the first evidence for a significantly different (warmer) climate in the Dominion Range probably occurs within this interval. This is consistent with marine isotope records which record warmer global temperatures and less ice volume prior to 2 Ma (Raymo *et al.*, 1989).

Implications for the tectonic history of the Dominion Range

Significant uplift of the Beardmore Region has been suggested to explain the presence of Pliocene Sirius Group glacial marine sediments at up to 1000 m at the Cloudmaker (Webb *et al.*, 1996). The uppermost marine unit at the Cloudmaker is correlated with the lowermost Sirius group deposits at the Dominion range (McKelvey *et al.*, 1991; Webb and Harwood, 1991) implying over 1800 m of uplift. Uplift in the Dominion Range had previously been called on to explain the occurrence of *Nothofagus* flora at 1800 m. The presence of the Koski Fault and the more numerous smaller faults were cited as evidence supporting recent tectonism. The proposed uplift has been linked to evidence of recent rifting in the Ross Sea (Behrendt and Cooper, 1991).

The overall tectonic pattern in the Dominion Range is one of extension, as evidenced by normal faulting. The Oliver Platform is bounded to the east by the Koski fault (Elliot *et al.*, 1974; Webb and Harwood, 1991). This fault is one side of an asymmetrical graben which offsets the

surface topography of the Meyer Desert (Figure 4.2). It is proposed that the similar steep western slope of the Oliver Platform (eastern wall of Rutkowski Trough) is also a fault, and that the Rutkowski Trough is also a graben, although offset bedrock was not observed. The lack of talus or fault gouge at the base of the Koski Fault indicates that the fault plane is close to that of the scarp. Although the Dominion Range may be uplifting as a block, in a local sense, the normal motion on the faults combined with the fault planes parallel to the scarps requires that the floors of the grabens have dropped relative to the adjacent platforms. The throw on these faults (<300 m) is small compared to the proposed uplift. Although the faulting is consistent with regional uplift, it does not require it. The faulting is also consistent with more local extension of the Dominion Range due to over steepening of the flanks of the range by glacial erosion or faulting along the Beardmore and Mill Glaciers. The glacial chronology can place some constraints on the style and timing of uplift and local faulting in the Dominion Range.

One line of evidence comes from the cirque valley in the southeast corner of the Mercer Platform. Cooler, dryer climatic conditions alone are not sufficient to explain the absence of glacial deposits younger than the massive moraines originating from within the cirque. The steep valley walls are a ready source of debris, so non-deposition is not a likely explanation. Boulder moraines overlying the alpine moraines indicate that thick ice from the Dominion ice cap filled the adjacent Rutkowski Trough repeatedly after deposition of the alpine moraines. Why did ice not also flow out of the cirque at this time? One possibility is that the formation of the Rutkowski Trough (graben), which projects into the Dominion Range ice cap, diverted ice flow away from the cirque valley and into the nascent Rutkowski Glacier. The faulting must have occurred prior to ~2 Ma, the exposure age of the Dominion moraines which project into an ice free valley and which are not overlain by subsequent moraines deposited by ice from the cirque. If the age assignment of the massive alpine moraines is correct, the inferred faulting is younger than 3.5 Ma.

The surface exposure ages (Tables 4.2 and 4.4) have been calculated assuming no uplift during exposure of the samples. For the Beardmore drift this is a reasonable assumption. However, for the Meyer and Dominion drifts this assumption must be evaluated. If significant uplift has occurred during exposure of the samples, the calculated exposure ages will underestimate the true age and correlations with the marine isotope record are potentially erroneous. The consistency of the trend and character of the moraines on the Mercer Platform argues against significant uplift during their deposition. Moreover, there is no significant change

in the ice profiles on the Mercer Platform over this period. If significant uplift occurred it did not involve significant tilt as predicted by flexural and rift shoulder models (Stern and ten Brink, 1989). As stated above, slight uplift (<150 m) may have contributed to the preservation of the older moraines. Less than 150 m in elevation separates the youngest and oldest moraines on the Mercer Platform and at least four glaciations occur between them. It is unlikely that increases in EAIS thickness would so closely match uplift rates >500 m/Ma over 2 Ma. If the correlation of the Meyer 4 and Dominion moraines with the Taylor IV moraines in Arena Valley is accepted, it would also require differential thickening of the EAIS because uplift in the Dry Valleys Block is constrained to <100 m /Ma.

The biostratigraphic age of the Sirius deposits at the Dominion Range is less than 3.8 Ma, but might be as young as less than 3.1 Ma if correlation with other Sirius group sediments containing a younger assemblage of diatoms is correct (Webb *et al.*, 1996). If the inference that the profiles and ages of lateral moraines on the Mercer Platform indicate that the Dominion Range has been stable for 2 Ma is correct, and depending on which (if any) biostratigraphic age of the Sirius Group sediments is accepted, there remains only 1.1 to 1.8 Myr in which the uplift can occur. This constraint requires uplift rates of 1200 to 740 m/ Ma at the Cloudmaker and rates of 1640 to 1000 m/Ma at the Dominion Range. The timing of uplift under this scenario is consistent with the inferred formation of the Rutkowski graben, however, the uplift rates are extremely high.

In summary, the glacial chronology at the Dominion Range is consistent with the biostratigraphic age of the Sirius Group deposits there, but they do not preclude it being older. All of the surface exposure ages of overlying deposits are younger than 2 Ma. If the inferred age of the massive alpine moraines is correct, they would be broadly contemporaneous with the biostratigraphic age inferred for the Sirius deposits. Their morphology is consistent with the inferred environmental conditions. The inferred age of formation of the Rutkowski graben is also consistent with an age of < 3.1 Ma for the Sirius deposits which they offset. The apparent stability of the Mercer Platform over the last 2 Ma suggests that either uplift occurred between 2 and 3 Ma and was very rapid, or that some uplift occurred earlier. The uplift rates are based on correlation of the upper glacial-marine units at the Cloudmaker and the Dominion Range and assume they are not much younger than the overlying terrestrial members which contain the reworked Pliocene diatoms and *Nothofagus*. Perhaps the hiatus which occurs between the terrestrial and marine members is large. The present altitude of the *Nothofagus* bearing member

does not *require* uplift; it has been *assumed* that the *Nothofagus* grew near sea level. This minimizes the temperature increase required to support the flora, but there is no direct evidence for lower elevations.

4.7 Conclusions

The glacial chronology at the Dominion Range spans more than 2 million years and is divided into four drifts. The Plunket drift which parallels the present glacier margin is Holocene age. Comparison with the Dominion ice core suggests a possible age of ~1000 yrs. The Beardmore drift records damming of the Beardmore glacier by grounded ice in the Ross Embayment. The exposure age of the Beardmore 1 drift (~10 ka) lags behind the glacial maximum in the McMurdo Sound region by several thousand years. A delayed maximum is predicted by a non-equilibrium ice sheet model and is in good agreement with exposure ages on moraines at Mt. Waesche in Marie Byrd Land. The results confirm the model, first proposed by Mercer, that the outlet glaciers thicken when the grounding line of the WAIS advances across the continental shelf in response to glacial eustatic sea level lowering. The Beardmore 2 drift occurs only as a small window in the overlying Beardmore 1 drift. The exposure ages show wide scatter from 6 to 56 ka, which is attributed to prior exposure. The best estimate of the age of the moraine is 15 to 24 ka. The early thickening of the Beardmore Glacier relative to the WAIS probably reflects the shorter response time of the outlet glacier to an advance of its grounding line as sea level dropped during the LGM.

The Meyer drift is subdivided into four drifts which span 300 kyr. On the basis of field relationships, it appears that the Meyer drifts also record damming of the Beardmore Glacier by an expanded WAIS. The youngest Meyer 1 drift is ~600 ka and is correlated with marine isotope stage 16. The oldest Meyer 4 drift is ~1 Ma and is correlated with MIS 22. This stage marks the mid-Pleistocene revolution and the onset of dominance of the 100 kyr cycle in climate records. Thus, it appears that advances of the WAIS are partly responsible for the excess ice associated with these climate cycles. Because the Beardmore and Meyer drifts occur at similar elevations, earlier expansions of the WAIS were not significantly greater than that of the LGM, indicating that for the last 1 million years the WAIS was only an amplifier of the larger Northern Hemisphere ice sheets signal. The Dominion moraines are ~2 Ma. The profiles of the moraines are similar to that of the younger moraines, suggesting that they also represent damming by the WAIS, but the relationship is not clear as is the case for the Meyer 1 drift.

The Meyer 4 moraine and Dominion moraines are correlated with the Taylor IVa and IVb moraines in Arena Valley on the basis of morphology and exposure ages. This implies that the Taylor Glacier moraines also record damming by the WAIS. Although the recent Taylor Glacier has not reached the coast and exhibits an out-of-phase relationship with the WAIS, analysis of model ice profiles indicates that the out-of-phase relationship was not likely when ice levels stood at Taylor IV levels. Synchronous thickening of the Beardmore and Taylor Glaciers indicates that the grounding line was north of McMurdo Sound and provides additional evidence that these earlier advances of the WAIS were similar in extent to that of the LGM.

The Meyer and Dominion moraines overlie a pair of massive alpine moraines deposited by an outlet glacier of the Dominion Ice Cap flowing out of the small cirque at the edge of the Meyer Platform. On the basis of morphology and stratigraphic position, these moraines are correlated with the paired alpine moraines of Wright Valley which are dated to <3.5 Ma and >3.7 Ma. The massive moraines record evidence of warmer climates than those which obtained during deposition of the lateral drifts by the Beardmore Glacier. The lack of subsequent ice advances from the cirque is tentatively attributed to formation of the Rutkowski graben by normal faulting and capture of the ice cap drainage by the Rutkowski Glacier between 2 and 3.5 Ma.

The parallel profiles and similar trends of the lateral moraines over the last 2 million years is evidence for tectonic stability of the Dominion Range over that period. Significant uplift of Sirius Group glacial marine sediments must have occurred prior to 2 Ma. If the Pliocene biostratigraphic age of these sediments is correct, it requires extremely high uplift rates. The glacial chronology of the Mercer Platform is consistent with a late Pliocene age for the underlying Sirius group sediments containing *Nothofagus* but provides only a minimum age.

References

Ackert, R.P., Jr., and Kurz, M.D., 1997, Late Quaternary glacial chronology of the Beardmore Glacier, Antarctica: Evidence for expansion of the West Antarctic Ice Sheet during Marine Isotope Stage 2 and 4: *Eos, transactions, AGU*, **v. 78**, p. F249.

Behrendt, J.C., and Cooper, A., 1991, Evidence of rapid Cenozoic uplift of the shoulder escarpment of the Cenozoic West Antarctic rift system and a speculation on possible climate forcing: *Geology*, **v. 19**, p. 315-319.

Berger, W.H., Yasuda, M.K., Bickert, T., Wefer, G., and Takayama, T., 1994, Quaternary time scale for the Ontong Java Plateau: Milankovitch template for Ocean Drilling Program Site 806: *Geology*, **v. 2**, p. 463-467.

Bockheim, J.G., Wilson, S.C., and Denton, G.H., 1989, Late Quaternary ice-surface fluctuations of Hatherton Glacier, Transantarctic Mountains: *Quaternary Research*, **v. 31**, p. 229-254.

Brook, E.J., 1993, Surface exposure geochronology using cosmogenic nuclides; applications in Antarctic glacial geology, MIT/WHOI.

Brook, E.J., and Kurz, M.D., 1993, Surface-exposure chronology using *in situ* cosmogenic ^{3}He in Antarctic quartz sandstone boulders: *Quaternary Research*, **v. 39**, p. 1-10.

Brook, E.J., Kurz, M.D., Ackert, R.P., Jr., Denton, G.H., Brown, E.T., Raisbeck, G.M., and Yiou, F., 1993, Chronology of Taylor Glacier advances in Arena Valley, Antarctica, using *in situ* cosmogenic ^{3}He and ^{10}Be: *Quaternary Research*, **v. 39**, p. 11-23.

Brook, E.J., Kurz, M.D., Ackert, R.P., Jr., Raisbeck, G., and Yiou, F., 1995, Cosmogenic nuclide exposure ages and glacial history of late Quaternary Ross Sea Drift in McMurdo Sound, Antarctica: *Earth and Planetary Science Letters*, **v. 131**, p. 41-56.

Brown, E.T., Edmond, J., Raisbeck, G.M., Yiou, F., Kurz, M.D., and Brook, E.J., 1991, Examination of surface exposure ages of Antarctic moraines using *in-situ* produced ^{10}Be and ^{26}Al: *Geochimica et Cosmochimica Acta*, **v. 55**, p. 2269-2283.

Bruno, L.A., Baur, H., Graf, T., Schlücter, C., Signer, P., and Wieler, R., 1997, Dating of Sirius Group tillites in the Antarctic Dry Valleys with cosmogenic ^{3}He and ^{21}Ne: *Earth and Planetary Science Letters*, **v. 147**, p. 37-54.

Cerling, T.E., 1990, Dating Geomorphic Surfaces Using Cosmogenic ^{3}He: *Quaternary Research*, **v. 33**, p. 148-156.

Cerling, T.E., and Craig, H., 1994, Cosmogenic ^{3}He production rates from 39°N to 46°N latitude, western USA and France: *Geochimica Cosmochimica Acta*, **v. 58**, p. 349-255.

Ciais, P., Jouzel, J., Petit, J.R., Lipenvov, V., and White, J.W.C., 1994, Holocene temperature variations inferred from six Antarctic ice cores: *Annals of Glaciology*, **v. 20**, p. 427-436.

Clapperton, C.M., and Sugden, D.E., 1990, Late Cenozoic glacial history of the Ross Embayment, Antarctica: *Quaternary Science Reviews*, **v. 9**, p. 253-272.

Clark, D.H., Bierman, P.R., and Larsen, P., 1995, Improving *in situ* cosmogenic chronometers: *Quaternary Research*, **v. 44**, p. 367-377.

Conway, H., Hall, B.L., Denton, G.H., Gades, A.M., and Waddington, E.D., 1999, Past and future grounding-line retreat of the West Antarctic Ice Sheet: *Science*, **v. 286**, p. 280-283.

Crowley, T.J., and North, G.R., 1991, *Paleoclimatology*: New York, Oxford University Press.

Denton, G.H., Armstrong, R.L., and Stuiver, M., 1971, The late Cenozoic glacial history of Antarctica, *in* Turekian, K.K., ed., *The Late Cenozoic Glacial Ages*: New Haven, Yale University Press.

Denton, G.H., Bockheim, J.G., Wilson, S.C., Leide, J.E., and Anderson, B.G., 1989a, Late Quaternary ice-surface fluctuations of Beardmore Glacier, Transantarctic Mountains: *Quaternary Research*, **v. 31**, p. 189-209.

Denton, G.H., Bockheim, J.G., Wilson, S.C., and Stuiver, M., 1989b, Late Wisconsin and early Holocene glacial history, inner Ross Embayment, Antarctica.*:* *Quaternary Research*, **v. 31**, p. 151-182.

Denton, G.H., Prentice, M.L., and Burkle, L.H., 1991, Cainozoic history of the Antarctic ice sheet, *in* Tingey, R.J., ed., *The Geology of Antarctica: Oxford*, Clarendon Press, p. 365-419.

Domack, E.W., Jacobson, E.A., Shipp, S., and Anderson, J.B., 1999, Late Pleistocene/Holocene retreat of the West Antarctic Ice Sheet: Part 2- Sedimentologic and stratigraphic signature.*:* *Geological Society of America Bulletin*, **v. 111**, p. 1517-1536.

Elliot, D.H., Barrett, P.J., and Mayewski, P.A., 1974, Reconnaissance geologic map of the Plunket Point Quadrangle, Transantarctic Mountains, Antarctica: Washington, D. C.: U. S. Government Printing Office, U. S. Geological Survey.

Fastook, J.L., and Prentice, M., 1994, A finite-element model of Antarctica: sensitivity test of meteorological mass-balance relationships: *Journal of Glaciology*, **v. 40**, p. 167-175.

Gosse, J.C., Klein, J., Evenson, E.B., Lawn, B., and Middleton, R., 1995, Beryllium -10 dating of the last Pinedale glacial sequence: *Science*, **v. 268**, p. 1329-1333.

Grindley, G.W., and Laird, M.G., 1969, Geology of the Shackleton Coast, Plate XIV, *in* Craddock, C.E.A., ed., Geologic maps of Antarctica(Antarctic Map Folio Ser., 12, American Geographical Society.

Hall, B.L., and Denton, G.H., 1999, Extent and chronology of the Ross Sea Ice Sheet and the Wilson Piedmont Glacier along the Scott Coast at the Last Glacial Maximum: *Geografiska Annaler*, v. in press.

Hall, B.L., Denton, G.H., and Hendy, C.H., 1999, Evidence from Taylor Valley for a grounded ice sheet in the Ross Sea: *Geografiska Annaler*, v. in press.

Hall, B.L., Denton, G.H., Lux, D.R., and Bockheim, J.G., 1993, Late Tertiary Antarctic paleoclimate and ice sheet dynamics inferred from surficial deposits in Wright Valley: *Geografiska Annaler*, **v. 75A**, p. 239-268.

Hendy, C.H., Healy, T.R., Rayner, E.M., Shaw, J., and Wilson, A.T., 1979, Late Pleistocene glacial chronology of the Taylor Valley, Antarctica, and the global climate: *Quaternary Research*, **v. 11**, p. 172-184.

Hollin, J.T., 1962, On the glacial history of Antarctica: *Journal of Glaciology*, **v. 4**, p. 173-195.

Huybrechts, P., 1990a, A 3-D model for the Antarctic Ice Sheet: A sensitivity study on the glacial-interglacial contrast: *Climate Dynamics*, **v. 5**, p. 79-92.

Huybrechts, P., 1990b, The Antarctic ice sheet during the last glacial-interglacial cycle: A three dimensional experiment: *Annals of Glaciology*, **v. 5**, p. 115-119.

Ishman, S.E., and Rieck, H.J., 1992, A late Neogene Antarctic glacio-eustatic record, Victoria Land Basin, Antarctica, *in* Kennett, J.P., and Warnke, D.A., eds., The Antarctic Paleoenvironment: A perspective on global change, 1: *Antarctic Research Series*, **vol 56**: Washington D. C., American Geophysical Union.

Kadmina, I.N., Kurinin, R.G., Masolov, V.N., and Grikurov, G.E., 1983, Antarctic crustal structure from geophysical evidence, *in* Oliver, R.L., R., J.P., and Jago, J.B., eds., *Antarctic Earth Science*: Canberra, Australian Academy of Science, p. 498-502.

Kurz, M.D., 1986, *In situ* production of terrestrial cosmogenic helium and some applications to geochronology: *Geochimica et Cosmochimica Acta*, **v. 50**, p. 2855-2862.

Kurz, M.D., and Ackert, R.P., Jr., 1996, Ice volume in the Ross Sea during Glacial Maximum: Geochronological Evidence from Mt. Morning , Antarctica: *EOS, Trans. AGU*, **v. 76**, p. F182.

Kurz, M.D., and Ackert, R.P., Jr., 1997, Stability of the East Antarctic Ice Sheet?: New Chronological evidence from Bennett Platform, Antarctica: *EOS, Transactions*, AGU spring meeting, **v. 78**, p. S185.

Kurz, M.D., Ackert, R.P., and Brook, E.J., 1994, Surface chronology from cosmogenic nuclides: the Antarctic glacial record, *in* Lampher, M.A., Dalrymple, G.B., and Turrin, B.D., eds., ICOG-8, Volume U.S. Geol. Surv. Circ. 1107: Berkeley, CA, U.S. Geological Survey.

Kurz, M.D., Colodner, D., Trull, T.W., Moore, R.B., and O'Brien, K., 1990, Cosmic ray exposure dating with *in situ* produced cosmogenic ^{3}He: results from young Hawaiian lava flows: *Earth and Planetary Science Letters*, **v. 97**, p. 177-189.

Kurz, M.D., Gurney, J.J., Jenkins, W.J., and Lott, D.E., 1987, Helium isotope variability within single diamonds from the Orapa kimberlite pipe: *Earth and Planetary Science Letters*, **v. 86**, p. 57-68.

Lal, D., 1991, Cosmic ray labeling of erosion surfaces: *In situ* nuclide production rates and erosion models: *Earth and Planetary Science Letters*, **v. 104**, p. 424-439.

Lal, D., and Peters, B., 1967, Cosmic ray produced radioactivity on the Earth, *in* Flügge, S., and Sitte, K., eds., *Encyclopedia of physics*, Volume XLVI/2: New York, Springer-Verlag, p. 551-612.

Licciardi, J.M., Kurz, M.D., and Clark, P.U., 1999, Calibration of cosmogenic ^{3}He production rates: Results from Holocene lava flows: *Earth and Planetary Science Letters*, **v. 172**, p. 261-271.

Licht, K.J., Dunbar, N.W., Andrews, J.T., and Jennings, A.E., 1999, Distinguishing subglacial till and glacial marine diamictons in the western Ross Sea, Antarctica: Implications for last glacial maximum grounding line: *Geological Society of America Bulletin*, **v. 111**, p. 91-103.

Licht, K.J., Jennings, A.E., Andrews, J.T., and Williams, K.M., 1996, Chronology of late Wisconsin ice retreat from the western Ross Sea, Antarctica: *Geology*, **v. 24**, p. 223-226.

Marchant, D.R., Denton, G.H., Bockheim, J.G., Wilson, S.C., and Kerr, A.J., 1994, Quaternary changes in the level of upper Taylor Glacier, Antarctica: Implications for paleoclimate and ice-sheet dynamics: *Boreas*, **v. 23**, p. 29-43.

Masarik, J., and Reedy, R.C., , 136 (3-4), p. ,, 1995, Terrestrial cosmogenic-nuclide production systematics calculated from numerical simulations: *Earth and Planetary Science Letters*, **v. 136**, p. 381-395.

Masarik, J., and Reedy, R.C., 1996, Monte Carlo simulation of the *in-situ*-produced cosmogenic nuclides: *Radiocarbon*, **v. 38**, p. 163.

Mayewski, P.A., 1975, Glacial geology and late Cenozoic history of the Transantarctic Mountains, Antarctica: Columbus, Ohio State University.

Mayewski, P.A., and Goldthwait, R.P., 1985, Glacial events in the Transantarctic Mountains: a record of the East Antarctic ice sheet, *in* Turner, M.D., and Splettstoesser, J.F., eds., Geology of the Transantarctic Mountains, Volume 36: *Antarctic Research Series*: Washington D. C., American Geophysical Union, p. 275-274.

Mayewski, P.A., Lyons, W.B., Zielinski, M., Twickler, M., Whitlow, S., Dibb, J., Grootes, P., Taylor, K., Whung, P.-Y., Fosberry, L., Wake, C., and Welch, K., 1995, An Ice-core-based, late Holocene history for the Transantarctic Mountains, Antarctica, *Antarctic Research Series*, Volume 67, American Geophysical Union, p. 33-45.

McKelvey, B.C., Webb, P.N., Harwood, D.M., and Mabin, M.C.G., 1991, The Dominion Range Sirius Group: a record of the late Pliocene- early Pleistocene Beardmore Glacier, *in* Thomson, M.R.A., Crame, J.A., and Thomson, J.W., eds., *Geological Evolution of Antarctica*: Cambridge, Cambridge University Press, p. 675-682.

Mercer, J.H., 1968, Glacial geology of the Reedy Glacier Area, Antarctica*: Geological Society of America Bulletin*, **v. 79**, p. 471-486.

Mercer, J.H., 1972, Some observations on the glacial geology of the Beardmore Glacier area, *in* Adie, R.J., ed., Antarctic Geology and Geophysics: Oslo, *Universitetsforlaget*, p. 427-433.

Niedermann, S., Graf, T., Kim, J.S., Kohl, C.P., Marti, K., and Nishiizumi, K., 1994, Cosmic-ray-produced ^{21}Ne in terrestrial quartz; the neon inventory of Sierra Nevada quartz separates: *Earth and Planetary Science Letters*, **v. 125**, p. 341-355.

Nishiizumi, K., Kohl, C.P., Arnold, J.R., Klein, J., and Fink, D., 1991, Cosmic ray produced ^{10}Be and ^{26}Al in Antarctic rocks: Exposure and erosion rates: *Earth and Planetary Science Letters*, **v. 104**, p. 440-454.

Nishiizumi, K., Winterer, E.L., Kohl, C., P., Klein, J., Middleton, R., Lal, D., and Arnold, J.R., 1989, Cosmic ray production rates of 10-Be and 26-Al in quartz from glacially polished rocks: *Journal of Geophysical Research*, **v. 94**, p. 17907-17915.

Oliver, R.L., 1964, Geological observations at Plunket Point, Beardmore Glacier, *in* Adie, R.J., ed., *Antarctic Geology*: Amsterdam, North-Holland Publishing Company.

Phillips, F.M., Zreda, M.G., Smith, S.S., Elmore, D., Kubik, P.W., and P., S., 1990, Cosmogenic chorine-36 chronology for glacial deposits at Bloody Canyon, Eastern Sierra Nevada: *Science*, **v. 248**, p. 1529-1532.

Prentice, M.L., Denton, G.H., Lowell, T.V., Conway, H.T., and Heusser, L.E., 1986, Pre-late Quaternary glaciation of the Beardmore Glacier region, Antarctica: *Antarctic Journal of the United States*, **v. 21**, p. 95-98.

Raymo, M.E., 1997, The timing of major climate terminations: *Paleoceanography*, **v. 12**, p. 577-585.

Raymo, M.E., Oppo, D.W., and Curry, W., 1997, The mid Pleistocene climate transition: A deep sea carbon isotopic perspective: *Paleoceanography*, **v. 12**, p. 546-559.

Raymo, M.E., Ruddiman, W.F., Backman, J., Clement, B.M., and Martinson, D.G., 1989, Late Pliocene variation in Northern Hemisphere ice sheets and North Atlantic deep water circulation: *Paleoceanography*, **v. 4**, p. 413-446.

Robinson, P.H., 1984, Ice dynamics and thermal regime of Taylor Glacier, South Victoria Land, Antarctica: *Journal of Glaciology*, **v. 30**, p. 153-160.

Schäfer, J.M., Ivy-Ochs, S., Wieler, R., Leya, I., Baur, H., Denton, G.H., and Schlüchter, C., 1999, Cosmogenic noble gas studies in the oldest landscape on earth: surface exposure ages of the Dry Valleys, Antarctica: *Earth and Planetary Science Letters*, **v. 167**, p. 215-226.

Scherer, R., 1999, Proximal evidence of past deglacial events in West Antarctica, WAIS meeting: Washington D. C.

Scherer, R.P., Aldahan, A., Tuoaczyk, S., Possnert, G., Engelhardt, H., and Kamb, B., 1998, Pleistocene Collapse of the West Antarctic Ice Sheet: *Science*, **v. 281**, p. 82-85.

Staudacher, T., and Allegre, C.J., 1991, Cosmogenic Neon in ultramafic Nodules from Asia and in Quartzite from Antarctica: *Earth and Planetary Science Letters*, **v. 106**, p. 87-102.

Steig, E.J., 1997, How well can we parameterize past accumulation rates in polar ice sheets?: *Annals of Glaciology*, **v. 25**, p. 418-422.

Steig, E.J., Fastook, J.L., Ackert, R.P., Jr., White, J.W.C., Licht, K.L., Zweck, C., and Goodwin, I., 1999, West Antarctic Ice Sheet elevation changes, *Antarctic Research Series*, American Geophysical Union, p. in press.

Stern, T.A., and ten Brink, U.S., 1989, Flexural uplift of the Transantarctic Mountains: *Journal of Geophysical Research*, **v. 94**, p. 10,315-10,330.

Stone, J.O., 1999, Air pressure and cosmogenic isotope production: *Journal of Geophysical Reviews*, p. in review.

Stuiver, M., Denton, G.H., Hughes, T.J., and Fastook, J.L., 1981, History of the marine ice sheet in West Antarctica during the last glaciation, a working hypothesis, *in* Denton, G.H., and Hughes, T.J., eds., *The Last Great Ice Sheets*: New York, Wiley-Interscience, p. 319-436.

Stuiver, M., and Reimer, P.J., 1993, Extended ^{14}C data base and revised Calib 3.0 ^{14}C age calibration program: *Radiocarbon*, **v. 25**, p. 215-230.

Trull, T.W., Kurz, M.D., and Jenkins, W.J., 1991, Diffusion of cosmogenic ^{3}He in olivine and quartz: implications for surface exposure dating: *Earth and Planetary Science Letters*, **v. 103**, p. 241-256.

Webb, P.-N., and Harwood, D.M., 1991, Late Cenozoic glacial history of the Ross Embayment, Antarctica: *Quaternary Science Reviews*, **v. 10**, p. 215-223.

Webb, P.-N., Harwood, D.M., Mabin, M.G.C., and McKelvey, B.C., 1996, A marine and terrestrial Sirius Group succession, middle Beardmore Glacier-Queen Alexandra Range, Transantarctic Mountains, Antarctica: *Marine Micropaleontology*, **v. 27**, p. 273-297.

Weed, R., and Ackert, R.P.J., 1986, Chemical weathering of Beacon Supergroup sandstones and implications for Antarctic glacial chronology: *South African Journal of Science*, **v. 82**, p. 513-516.

Wilch, T.I., Lux, D.R., Denton, G.H., and McIntosh, W.C., 1993, Minimal Pliocene-Pleistocene uplift of the dry valleys sector of the Transantarctic Mountains: A key parameter in ice-sheet reconstructions: *Geology*, **v. 21**, p. 841-844.

Appendix 4.1 Sample data from the Dominion Range, Beardmore Glacier

Sample	Deposit	Drift	Rock type	Elev.	Depth	Latitude (S)		Longitude (E)	
				(m)	(cm)	degrees	minutes	degrees	minutes
SAK95 -014	D moraine	Meyer 1	sandstone	1790	3.0	85	9.642	165	59.167
SAK95 -016	D moraine	Meyer 1	sandstone	1790	5.0	85	9.642	165	59.167
SAK95 -018	D moraine	Meyer 1	dolerite	1790	3.0	85	9.645	165	58.457
SAK95 -027	H moraine	Meyer 4	dolerite	1785	1.0	85	10.058	166	4.742
SAK95 -036	H moraine	Meyer 4	sandstone	1850	1.5	85	10.128	165	59.370
SAK95 -203	B moraine	Beardmore 1	sandstone	1800	2.0	85	9.431	165	59.849
SAK95 -205	B moraine	Beardmore 1	sandstone	1800	1.5	85	9.431	165	59.849
SAK95 -206	B moraine	Beardmore 1	sandstone	1800	2.5	85	9.423	165	59.438
SAK95 -209	B moraine	Beardmore 1	dolerite	1800	2.0	85	9.523	165	57.958
SAK95 -210	C moraine	Beardmore 2	sandstone	1810	2.0	85	9.622	165	56.295
SAK95 -211	C moraine	Beardmore 2	sandstone	1810	0.5	85	9.622	165	56.295
SAK95 -212	B moraine	Beardmore 1	sandstone	1810	1.5	85	9.436	165	58.419
SAK95 -214	C moraine	Beardmore 2	sandstone	1795	2.0	85	9.663	165	55.821
SAK95 -215	C moraine	Beardmore 2	sandstone	1810	2.5	85	9.663	165	55.821
SAK95 -217	C moraine	Beardmore 2	sandstone	1810	3.0	85	9.648	165	56.253
SAK95 -220	D moraine	Meyer 1	sandstone	1790	1.5	85	9.608	165	59.498
SAK95 -222	D moraine	Meyer 1	dolerite	1790	1.5	85	9.608	165	59.498
SAK95 -223	D moraine	Meyer 1	sandstone	1790	1.5	85	9.634	165	59.715
SAK95 -225	D moraine	Meyer 1	sandstone	1790	1.5	85	9.634	165	59.715
SAK95 -235	J moraine	Dominion 2	sandstone	1785	2.0	85	10.483	166	8.432
SAK95 -245	H moraine	Meyer 4	sandstone	1850	1.5	85	10.127	166	59.701
SAK95 -246	J moraine	Dominion 2	sandstone	1930	1.5	85	10.189	165	54.689
SAK95 -247	J moraine	Dominion 2	sandstone	1930	3.0	85	10.189	165	54.689
SAK95 -404	B moraine	Beardmore 1	sandstone	1800	1.5	85	9.354	166	0.545
SAK95 -405	B moraine	Beardmore 1	sandstone	1800	3.0	85	9.466	165	58.638
SAK95 -407	B moraine	Beardmore 1	sandstone	1800	3.0	85	9.466	165	58.638
SAK95 -408	B moraine	Beardmore 1	dolerite	1800	5.0	85	9.492	165	58.859
SAK95 -409	B moraine	Beardmore 1	sandstone	1800	2.0	85	9.553	165	57.879
SAK95 -413	B moraine	Beardmore 1	dolerite	1800	2.0	85	9.508	165	58.048
SAK95 -415	C moraine	Beardmore 2	dolerite	1810	2.0	85	9.704	165	55.406
SAK95 -416	C moraine	Beardmore 2	sandstone	1810	1.5	85	9.954	165	55.582
SAK95 -417	C moraine	Beardmore 2	dolerite	1810	1.5	85	9.954	165	55.582
SAK95 -424	D moraine	Meyer 1	dolerite	1790	3.0	85	9.611	165	58.743
SAK95 -426	D moraine	Meyer 1	dolerite	1790	3.0	85	9.658	165	58.155
SAK95 -427	D moraine	Meyer 1	sandstone	1790	3.0	85	9.658	165	58.155
SAK95 -435	H moraine	Meyer 4	sandstone	1785	1.5	85	10.106	166	5.451
SAK95 -437	H moraine	Meyer 4	dolerite	1785	3.0	85	10.147	166	4.480
SAK95 -441	H moraine	Meyer 4	sandstone	1850	2.0	85	10.129	165	59.800
SAK95 -445	I moraine	Dominion 1	sandstone	1910	1.5	85	10.122	165	54.541
SAK95 -446	I moraine	Dominion 1	sandstone	1910	3.0	85	10.119	165	54.568

CHAPTER 5

Chronology of older Ross Sea drift: Results from southern McMurdo Sound

5.1 Introduction

Reconstructions of Antarctic Ice Sheet geometry are important inputs to global climate models. Knowledge of Antarctic ice volume is required for interpreting marine oxygen isotope records and other climatic records and the timing and extent of Antarctic Ice Sheet fluctuations are key to understanding the cause of the Pleistocene Ice Ages. The marine-based West Antarctic Ice Sheet (WAIS) is potentially unstable and there is concern that global warming could trigger collapse of the WAIS (Mercer, 1978; Oppenheimer, 1998). An understanding of WAIS behavior during the last glacial cycle provides a context for evaluating future response of the ice sheet.

The size of the West Antarctic Ice Sheet is determined principally by sea level (Hollin, 1962; Huybrechts, 1990; Mercer, 1968; Stuiver *et al.*, 1981), which is driven by the growth and decay of Northern Hemisphere Ice sheets. Therefore, it is thought that the WAIS fluctuated synchronously with the Northern Hemisphere ice sheets during the Pleistocene (Denton *et al.*, 1971; Denton *et al.*, 1989b; Denton *et al.*, 1991; Hollin, 1962; Mercer, 1968; Mercer, 1972). Although the grounding line of the WAIS in the Ross Sea during the last glacial maximum (LGM, stage 2) is now known within about 100 km (Domack *et al.*, 1999; Licht *et al.*, 1999; Licht *et al.*, 1996; Shipp *et al.*, 1999), the volume of the ice sheet and the timing of deglaciation of the WAIS are less well determined (Chapter 3). Knowledge of WAIS extent during the penultimate glaciation (stage 6) is fragmentary (Denton *et al.*, 1991) and knowledge of the behavior of the WAIS during earlier glacial periods is almost nonexistent.

In contrast to the WAIS, alpine glaciers and marginal domes of the East Antarctic Ice Sheet (EAIS) are thought to be driven primarily by variations in accumulation (Denton *et al.*, 1989b; Marchant *et al.*, 1994a). Lower air temperatures and a greater distance to open water during glacial periods are expected to lower accumulation rates and lead to ice thinning and retreat during glacial periods. Conversely, these glaciers expand during interglacial periods. Thus, expansions of the WAIS are out-of-phase with expansions of the EAIS and alpine glaciers. These relationships are incorporated in the *dual control* model of ice sheet behavior (Denton *et al.*, 1971; Denton *et al.*, 1991; Stuiver *et al.*, 1981).

The Dry Valleys/McMurdo Sound Region is the largest ice-free area in Antarctica. Glacial deposits recording advances of the EAIS, WAIS, and alpine glaciers are well-preserved

and constitute a detailed record of Antarctic glaciation spanning millions of years. In McMurdo Sound, Ross Sea drift records the most recent expansion of the WAIS (Denton *et al.*, 1989b; Hall and Denton, 1999a; Hall *et al.*, 1999; Stuiver *et al.*, 1981). This drift has been used to constrain the position of the grounding line of the WAIS during the LGM (Denton *et al.*, 1989b; Hall and Denton, 1999b). At many locations in McMurdo Sound, glacial drift that is older and more extensive than Ross Sea drift records earlier expansions of the WAIS (Denton *et al.*, 1971; Stuiver *et al.*, 1981). However, drift limits are generally poorly preserved. Marshall drift, which includes carbonate glacial-lucustrine sediments deposited in lakes dammed by an earlier expansion of the WAIS, has been dated by the U/Th method to the penultimate glaciation (stage 6) (Denton *et al.*, 1989b).

Surface exposure dating measures the abundance of cosmogenic nuclides in surficial rocks to determine the time that the rock has been exposed to cosmic rays. The technique has proved useful in dating Antarctic glacial deposits. Brook (1993a) used ^{3}He, ^{10}Be and ^{26}Al exposure ages on well-preserved lateral moraines in Arena Valley to develop a chronology for the Taylor Glacier which drains the Taylor dome of the East Antarctic Ice Sheet. The ^{10}Be ages on the youngest (lowest elevation) moraine averaged 122 ± 29 ka, demonstrating that the most recent advance occurred during the last interglacial (stage 5). The older moraines in Arena Valley have surface exposure ages of ~1 Ma and ~2 Ma. Brook (1995) used the technique to date the Ross Sea drift mapped by Stuiver *et al.* (1981). The surface exposure ages show wide scatter. The younger ages are consistent with the ^{14}C dates reported by Denton (1989b). The older ages were thought to record either earlier unrecognized glacial advances or the reworking of previously exposed boulders. In addition, Brook *et al.* (1995) showed that the similar drift sheets which extend beyond the limit of Ross Sea drift are significantly older (up to 575 ka) and can be distinguished from Ross Sea drift using surface exposure dating.

In most locations, drift limits relating to the older drift are poorly preserved, precluding reconstruction of the associated ice sheet profiles. However, well-defined lateral drift limits occur at several locations in southern McMurdo Sound. On the Dromedary Platform (a bench on the flank of Mount Dromedary) and the Bulwark (a bedrock knob adjacent to the Koettlitz Glacier) at least four distinct ice limits older than Ross Sea drift are preserved (Figure 5.1). The presence of Pleistocene volcanic cones and lava flows (Blank *et al.*, 1962) provides stratigraphic and chronologic control on the older moraines. In addition, the younger drift margins can be traced into the adjacent Walcott Valley where cross-cutting relationships allow differentiation of

the deposits (Stuiver *et al.*, 1981). These younger moraines are correlated with dated deposits elsewhere in McMurdo Sound. The independent age control allows evaluation of the wide range of surface exposure ages obtained from moraine boulders from individual drift margins.

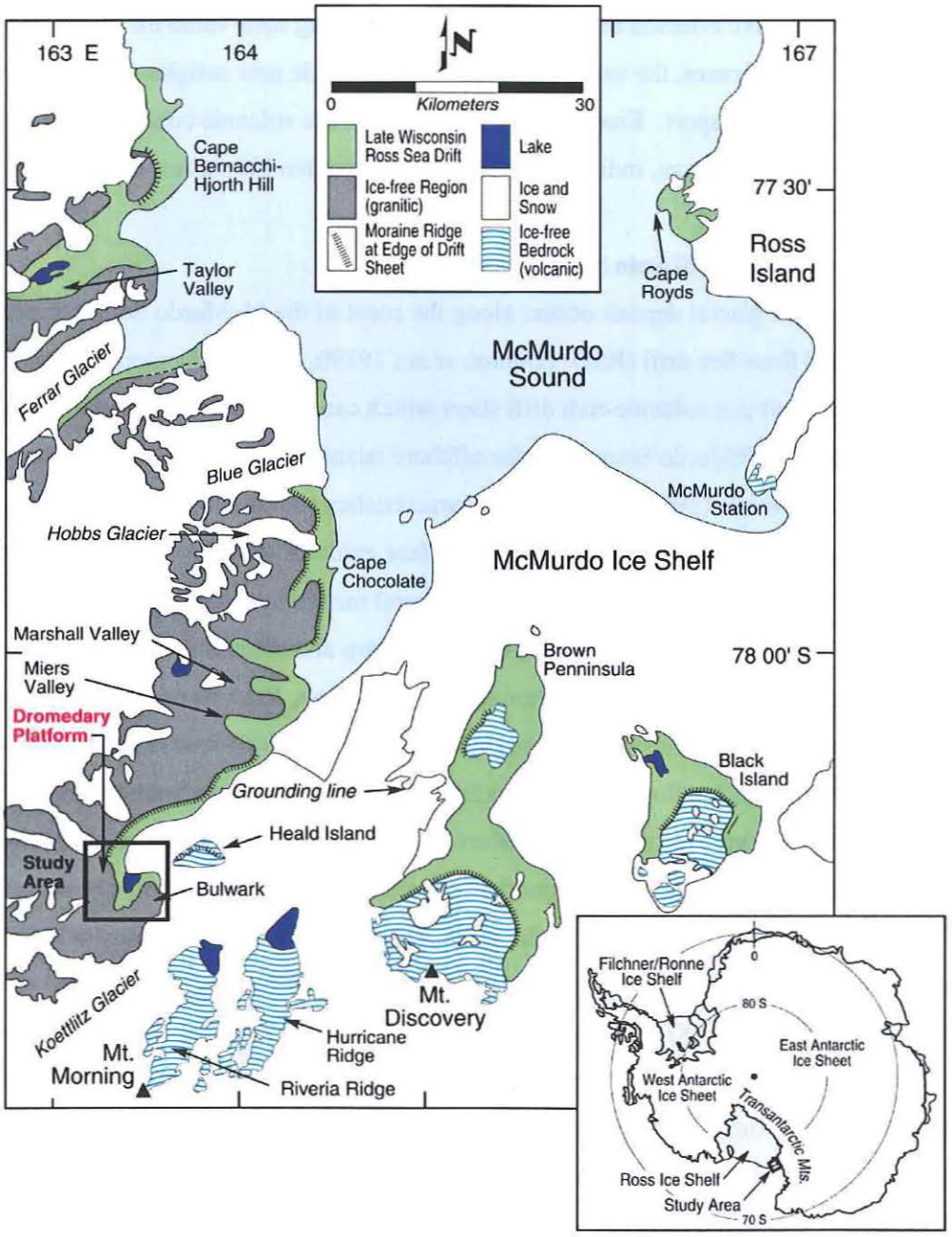

Figure 5.1 Location map of Antarctica (inset) and the McMurdo Sound Region showing locations mentioned in text. The study area is shown in box. The Ross Sea drift was deposited by grounded ice in McMurdo Sound during the last glacial maximum.

This chapter reports the results of geological mapping of the moraines in the Dromedary Platform area, coupled with surface exposure ages and $^{40}Ar/^{39}Ar$ ages of associated volcanics. The data demonstrate that expansions of the WAIS as large as that obtained during the LGM occurred at least four times during the Pleistocene. The results also demonstrate that prior exposure and cover have effected some of the samples, limiting their value for glacial chronology. In several cases, the surface exposure ages provide new insights into landform evolution and glacial transport. Erosion rates for a Pleistocene volcanic cone, obtained from the $^{40}Ar/^{39}Ar$ age and exposure age, indicate that erosion of these landforms is relatively rapid.

5.2 Glacial geology of McMurdo Sound

A distinctive glacial deposit occurs along the coast of the McMurdo Sound Region. Informally named Ross Sea drift (RSD) (Denton *et al.*, 1989b; Hall and Denton, 1999a; Stuiver *et al.*, 1981), the deposit is a volcanic-rich drift sheet which can be traced nearly continuously along the western shore of McMurdo Sound and the offshore islands (Figure 5.1). Stuiver *et al.*, (1981), and Denton *et al.*, (1989) describe the characteristics and distribution of Ross Sea drift in detail. The drift is commonly ice-cored and the surface exhibits kettle holes and debris bands. It is composed of till and stratified sediments up to several meters thick and is largely unweathered (Stuiver *et al.*, 1981). On headlands, the drift limit is sharp and commonly marked by a moraine ridge up to four meters high. In the intervening ice-free valleys, Ross Sea drift consists of glacial-lacustrine sediments deposited in proglacial lakes (Clayton-Greene *et al.*, 1988; Denton *et al.*, 1989b; Judd, 1986). Ice flow around Ross Island and into McMurdo Sound from the Ross Sea is indicated by kenyte erratics on the western shore of the sound (Stuiver *et al.*, 1981). The only possible source of the kenyte, a distinctive volcanic rock type, are outcrops on Ross Island.

The elevations of Ross Sea drift along the west coast of McMurdo Sound and on the offshore volcanic islands are used to reconstruct the ice sheet surface during the LGM (Denton *et al.*, 1989b; Stuiver *et al.*, 1981) (Figure 5.2). The reconstruction indicates that a lobe of an expanded WAIS flowed around Mount Discovery and Ross Island into McMurdo Sound. White Island, Black Island, and Brown Peninsula protruded as nunataks. Near the Koettlitz Glacier, ice elevations were lower than those of today. Ross Sea drift limits are overlain by the Koettlitz Glacier at Heald Island, the Bulwark, and Riviera Ridge (Figure 5.1). Algae and carbonate layers within glacial-lacustrine sediments have ^{14}C ages ranging from 12.3 to 23.8 ^{14}C yr BP in Taylor Valley (Hall and Denton, 1999b; Stuiver *et al.*, 1981) and 10.3 to 23.0 ^{14}C yr BP in Miers Valley

(Clayton-Greene *et al.*, 1988) (Figure 5.1). These ages fall with the last glacial maximum (LGM-isotope stage 2) and indicate that the grounding line of the WAIS had expanded north of McMurdo Sound at that time, most likely due to lower eustatic sea level. Surface exposure ages on the Ross Sea drift from moraines on the headlands cluster around 12 ka, consistent with the ^{14}C chronology, but many older ages were also obtained from the drift (Brook *et al.*, 1995). The older ages were attributed to either prior exposure, a long-lived stable ice margin or multiple age drifts exposed on the headlands.

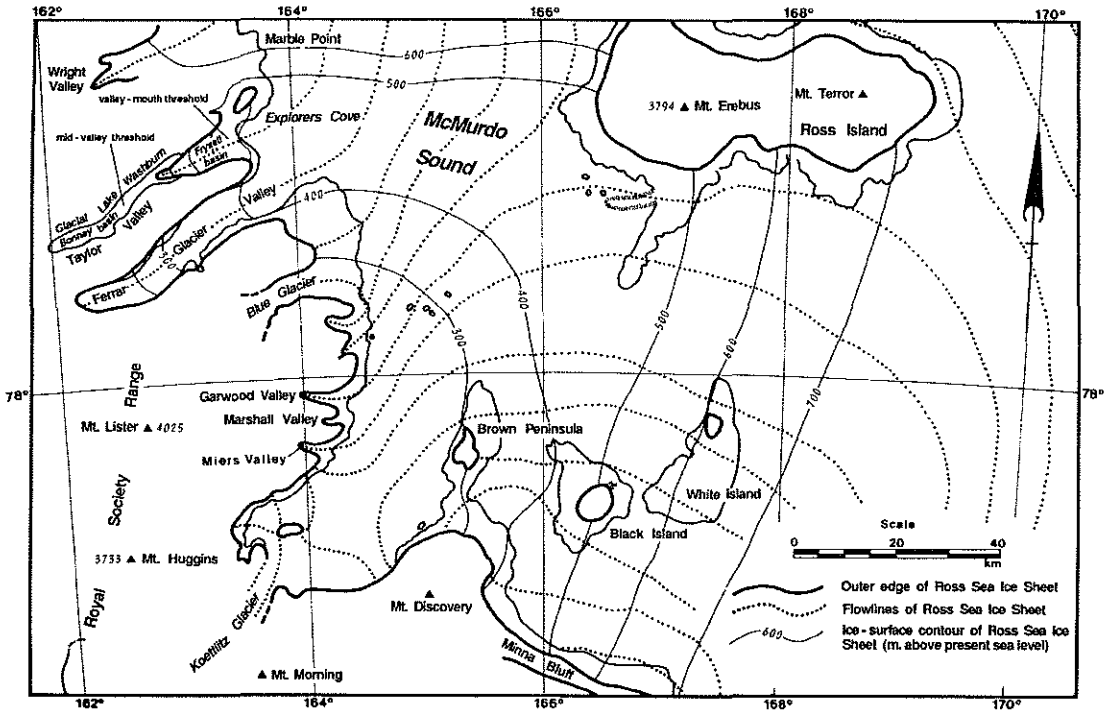

Figure 5.2 Reconstruction of ice surface in McMurdo Sound during deposition of Ross Sea drift. Dotted lines are flow lines; solid lines are surface contours in meters (from Stuiver *et al.*, 1981).

An older drift is overlain by, and exposed beyond, the margin of the Ross Sea drift. The older drift roughly parallels the younger Ross Sea drift but is discontinuous and rarely has a well-defined upper limit. Because the lithology and geometry are similar, the older drift is thought to record earlier expansion(s) of the WAIS into McMurdo Sound (Stuiver *et al.*, 1981). The older drift is not ice-cored and the drift surface is more subdued than that of the overlying Ross Sea drift (Stuiver *et al.*, 1981). Many surface boulders are cavernously weathered and have desert varnish. Drift of the Walcott, Howchin, and Canada alpine glaciers overlies the older drift but

underlies the Ross Sea drift (Stuiver *et al.*, 1981). The older drift includes deposits of several ages but has only been differentiated in Taylor Valley (Stuiver *et al.*, 1981), Wright Valley (Bockheim, 1978; Hall *et al.*, 1993; Nichols, 1971), and at the Bulwark (Denton *et al.*, 1971; Stuiver *et al.*, 1981).

The age of the older drifts is poorly constrained. Better chronologic control would help address questions relating to the role of sea level in controlling the size of the WAIS prior to the LGM and the extent of earlier WAIS advances. A chronology from the McMurdo Sound Region would complement pre-LGM chronologies being developed in the interior parts of the ice sheet (Chapters 3 and 4). In Marshall Valley (Figure 5.1), U/Th dates on carbonate layers (stratigraphically below the younger Ross Sea drift) range between 130 and 190 ka and indicate that the youngest part of the older drift dates to the penultimate glaciation (stage 6) (Denton *et al.*, 1989b). At Hurricane Ridge (Figure 5.1), the age of an older drift limit is constrained to stage 6 by surface exposure ages on erratics and ice contact lava flows (Kurz and Ackert, 1996). Surface exposure ages on the older drift along the western coast of McMurdo Sound range from 167 to 572 ka (Brook *et al.*, 1995). The surface exposure ages suggest that parts of the older drift are older than stage 6 and that the older drift is composed of multiple age deposits.

5.3 Principles of surface exposure dating

The basic principle of surface exposure dating with cosmogenic nuclides is simple. The concentration of cosmogenic nuclides in a rock is directly related to the amount of time the sample has been exposed to cosmic rays. Because rock at ~2 m depth is effectively shielded from cosmic rays, geologic processes, such as glaciation, which exhume and deposit debris with no prior exposure are ideally suited to surface exposure dating. The surface exposure age is determined from the production rate and concentration of the cosmogenic nuclide. For a full discussion and references see Chapter 1. In practice, this simple relationship is more complicated because many factors determine the production rate at any specific location.

The production rate varies as a function of altitude and latitude because the cosmic ray flux is attenuated by interaction with matter and modulated by the Earth's magnetic field (Lal, 1991). Correction for elevation and latitude (scaling) is made using star production rates combined with neutron monitor data (Lal, 1991; Lal and Peters, 1967). At latitudes greater than 60° the galactic cosmic ray flux and sea level production rates are approximately constant. The scaling factors, which include the effects of altitude based on the Standard Atmosphere (Lide,

1998-9) accurately predict (±5%) measured variations in production rates of cosmogenic nuclides with elevation (Zreda *et al.*, 1991). In Antarctica, an additional correction for elevation is necessary due to anomalous low atmospheric pressure over the continent (Stone, 1999). Correction for depth of the sample in the rock is made using measured attenuation lengths (Kurz, 1986).

The concentration of cosmogenic nuclides is also effected by surface erosion which exhumes rock with lower cosmogenic nuclide concentrations. If erosion has occurred but is assumed to be negligible, the surface exposure age will be younger than the formation age of the surface. Antarctic rock surfaces in which cosmogenic nuclide concentrations have reached steady state indicate that erosion rates are very low, only 4 to 10 cm/Myr (Brown *et al.*, 1991; Nishiizumi *et al.*, 1991; Schäfer *et al.*, 1999). Therefore, the erosion rate is often assumed to be zero. While this approximation is appropriate for young (<100 ka) samples, for older samples the true exposure age will be underestimated .

A fundamental assumption in obtaining surface exposure ages of glacial deposits is that exposure to cosmic rays began upon deposition of the boulder (no prior exposure) and that exposure has not been interrupted (the sample has remained stable and has not been shielded from cosmic rays). Consistent ages of multiple samples from the same moraine are a good indication that this assumption is valid. Because processes which might violate the assumptions are expected to operate somewhat randomly, coherence of multiple ages is convincing evidence that the assumptions have been met and that outliers may be rejected. In some cases stratigraphic relationships can be used to identify outliers.

Low erosion rates in Antarctica increase the likelihood of prior exposure because surfaces with long exposure are common. Even vertical cliffs often erode slowly enough to build up substantial inventories of cosmogenic nuclides (Chapter 2). Prior exposure of glacial boulders is clearly demonstrated on Mount Morning (Figure 5.1) where most of the exposure ages on erratic boulders (Ross Sea drift) overlying a lava flow are substantially older than the surface exposure age (~ 26 ka) of the flow (Kurz and Ackert, 1996). Although prior exposure is not a substantial problem in all locations (Brook *et al.*, 1993b)(see also Chapter 3 and 4), previous studies have indicated it is a problem in the McMurdo Sound area (Brook *et al.*, 1995; Kurz and Ackert, 1996).

5.4 Methods

Samples for surface exposure dating were collected during the austral summers of 1992-93, 1993-94 and 1996-7 in conjunction with surficial mapping of the glacial deposits and volcanic rocks. Three to twelve samples were collected from each moraine or drift segment. Lava flows were sampled in areas of intact outcrop, but original surfaces were generally not preserved on the lava flows. Sample locations were recorded by GPS and marked on air photographs, which also served as the base map for the geologic map. Sample lithologies are primarily basalt containing olivine or clinopyroxene (cpx). Dolerite containing pyroxene and quartz-rich granites, gneiss and sandstones were also sampled. Generally, samples were collected from the tops of boulders greater than 25 cm in diameter on moraine crests or benches. In cases where drift limits were not marked by a distinct moraine, boulders near the edge of the drift sheet were sampled. When large boulders of appropriate lithology were not present, smaller clasts (15-20 cm) were collected.

Sample location, lithology and size appear in Appendix 5.1. The elevations of the samples relative to a fixed point at the camp were measured using altimeters. The camp elevation and the elevation of many moraine segments are tied to a local benchmark with conventional surveying techniques (Appendix 5.2). Measurements were made to quantify shielding of cosmic rays by topography; shielding was in all cases less than 15° and no corrections were made.

The exposure data presented is almost exclusively from basalt samples. Samples bearing olivine or clinopyroxene were selected for ^{3}He measurements because those minerals retain ^{3}He quantitatively (Trull *et al.*, 1991) and the technique is well-established (Kurz, 1986; Kurz *et al.*, 1996). ^{3}He measurements were also made on two quartz-bearing samples. Sub-samples were detached using a hydraulic jaw press and the depth relative to the rock surface noted. The sub-samples were then crushed in a jaw crusher and sieved to isolate phenocrysts for hand picking. Individual mineral grains without adhering ground mass were handed-picked from the .5 to 1 mm or 1 to 2 mm fraction using a binocular microscope. Cosmogenic ^{3}He was measured using the noble gas mass spectrometer at the Woods Hole Oceanographic Institution using previously described techniques (Kurz, 1986; Kurz *et al.*, 1990). Corrections for inherited ^{3}He were made in most samples by measuring the $^{3}He/^{4}He$ in fluid and melt inclusions released by crushing the sample (Chapter 1)(Kurz, 1986). An inherited $^{3}He/^{4}He$ of 7 R/R_a was assumed for olivine samples which were not crushed.

The olivine ^{3}He production rate used here is 129 ± 4 atoms/g/yr (at sea level and high latitude) determined from the 125 ka Cerro Volcán lava flow in Patagonia (Chapter 2). This is

similar to, but slightly higher than, the commonly employed ^{3}He production rate (determined at the 17.8 ka Tabernacle Hill lava flow in Utah (121 ± 4 atoms/g/yr) (Cerling, 1990; Licciardi *et al.*, 1999). The Cerro Volcán production rate minimizes uncertainties introduced by scaling from mid latitudes and integrates over a time period which is more appropriate for the age range of the samples. Two samples from volcanic rocks interbedded with moraines were submitted for ^{40}Ar/^{39}Ar analyses in order to determine the eruptive age of the flows.

5.5 Glacial geology of Dromedary Platform and the Bulwark

The Dromedary Platform is a bedrock bench on the western flank of Mount Dromedary, (2300 m) a peak in the Royal Society Range southwest of McMurdo Sound (Figure 5.1). Four valleys separated by sharp east-west ridges open on the platform from the east. The northernmost valley is ice-free and is formed by a bifurcation of the west ridge of Mount Dromedary. The Dromedary Glacier, an alpine glacier originating on the west face of Mount Dromedary, occupies the valley immediately to the south. The southernmost valleys are occupied by small rock glaciers (Figure 5.3). Dromedary Platform is separated from the Koettlitz Glacier to the west by the Bulwark, a bedrock knob adjacent to the glacier, and Pyramid Trough, an ice-free glacial trough between the Bulwark and Dromedary Platform. The Koettlitz Glacier is a large alpine glacier which originates between Mount Morning and the Royal Society Range and flows north to McMurdo Sound where it feeds the western part of the McMurdo Ice Shelf (Figure 5.1). The grounding line is situated about 10 km north of Dromedary Platform. The Koettlitz Glacier overlies Ross Sea drift on the Bulwark and on Mount Morning, indicating that the glacier was less extensive during deposition of Ross Sea drift.

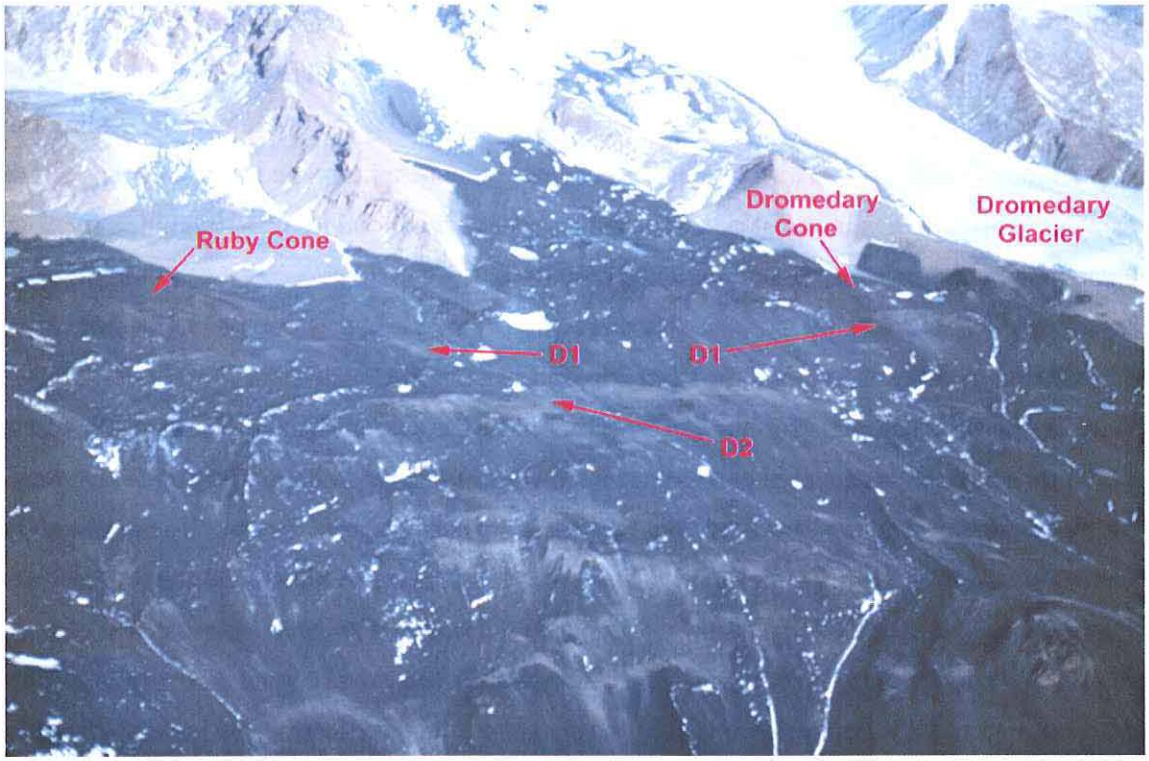

Figure 5.3 Photograph of Dromedary Platform taken from a helicopter over the Bulwark. Quaternary volcanics mantle the platform. Glacial moraines (D1 and D2), composed largely of light colored felsic rocks, are conspicuous on the volcanics. Lava flows originating under the Dromedary Glacier and from the adjacent valley overlie the D1 moraine. The margin of the later flow is a steep curvilinear embankment several meters high where it contacts the Dromedary Cone. This morphology indicates substantial erosion of the Dromedary Cone since deposition of the lava flow. Local down-slope movement of glacial debris is indicated by streaks of light colored material.

The basement rocks underlying Dromedary Platform are Precambrian to Cambrian granite and meta-sediments (Blank *et al.*, 1962). These rocks are overlain by basaltic volcanic cones and lava flows of the McMurdo Group Volcanics (Wright, 1980). The prominent volcanic cones were assigned informal names in the field. Ruby Cone is a well-preserved agglutinate cone on the southern end of the platform. Dromedary Cone and Condor Cone are deeply eroded and occur just south and north of the Dromedary Glacier terminus. Lava flows completely mantle the platform; the basement rocks crop out only on the adjacent ridges and the walls of Pyramid Trough. The volcanics are overlain by, and in some cases interbedded with, lateral moraines and drift sheets.

A new map of the surficial geology of the Dromedary Platform Area appears in Figure 5.4. Four glacial drifts attributed to expansions of grounded ice in McMurdo Sound were previously differentiated on the Bulwark (Denton *et al.*, 1971) and Ross Sea drift was mapped in

the Pyramid Trough (Stuiver *et al.*, 1981). However, the higher elevation moraines on Dromedary Platform have not been previously differentiated. These moraines are provisionally labeled Dromedary 0 through Dromedary 6 (D0 - D6). This scheme was adopted for simplicity in the field. The elevation of the moraines ranges from 780 m (D0) to 350 m (D6) (Figures 5.3 and 5.4; Table 5.1). The higher elevation (older) moraines (D0 - D4) are discontinuous, however the lowest (younger) moraines (D5 and D6) can be traced continuously across the platform and into the Walcott Valley to the north. In general, the elevations of the moraines decrease from south to north, consistent with the ice flow direction of the Koettlitz Glacier (Figure 5.5). The exception is the lowest moraine (D6), which delineates an ice tongue flowing into the Pyramid Trough from the north, similar to, but more extensive than, the lobe of the present day Koettlitz Glacier (Figure 5.5). The D6 moraine corresponds to the Ross Sea drift limit mapped by Stuiver (1981).

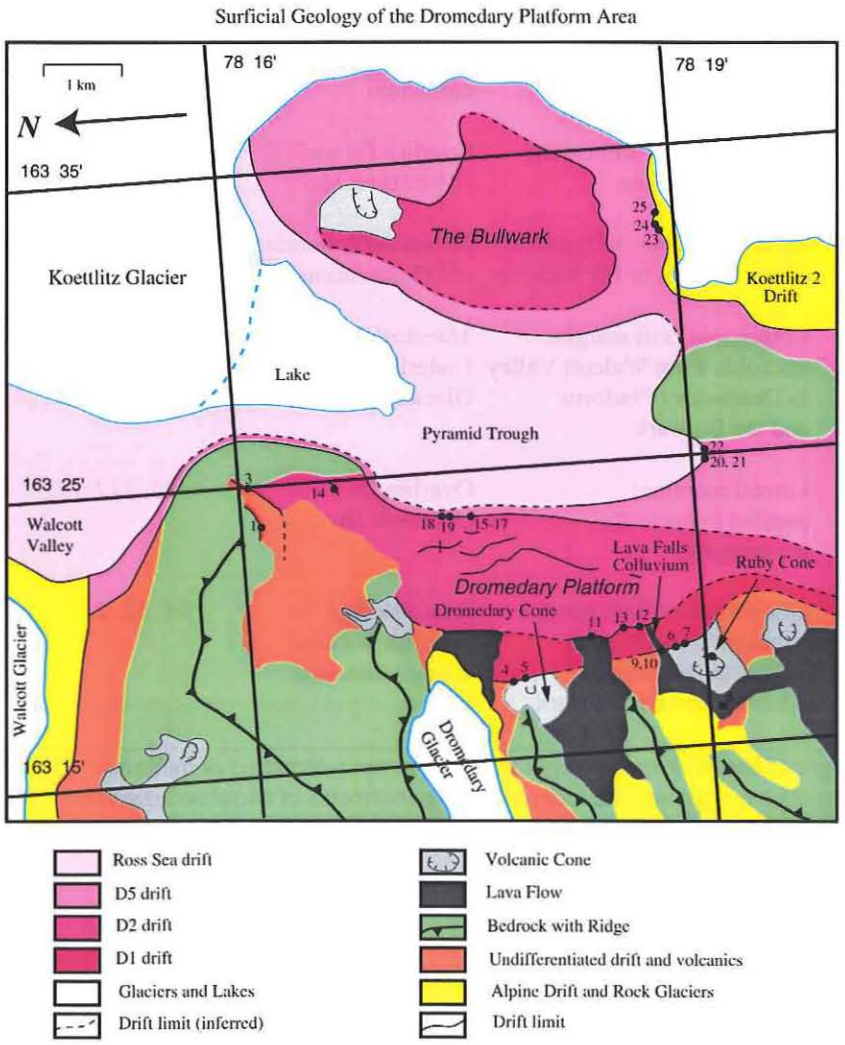

Figure 5.4 Surficial geological map of Dromedary Platform and the Bulwark showing drift sheets, selected volcanic rocks, and sample locations.

Table 5.1 Stratigraphic relationships and exposure ages of glacial and volcanic deposits on Dromedary Platform

Unit	Elevation (m)	Deposit type	Stratigraphy	Exposure Age (ka)
D0 moraine	720	Volcanic-rich drift Highest elevation drift	Oldest glacial deposit overlies bedrock	**479**
Ruby Cone	760-780	Unglaciated volcanic cone and associated lava flows	Underlies D1 *(1.68±0.13 Ma)*	**854**
D1 moraine	680-775	Thin drift and small lateral moraines	Overlies Ruby Cone Underlies volcanic colluvium	**402**, 320, 271 185, 164
Dromedary Cone	750-800	Eroded Volcanic Cone	Overlies D1	
D2 moraine	675-740	Large lateral moraine	Deflects Lava Falls colluvium	**351**, 221, 191
Lava Falls Colluvium	715-760	Basaltic debris originating SW of Ruby Cone	Overlies D1 and D2 *(<9.8±0.10 Ma)*	422, 412, 278
D3-D4 moraine	450-650	Lateral moraines with similar characteristics to D2 moraine	Recessional moraines of D2 glaciation?	106
D5 moraine *(stage 6)*	380-410	Continuous drift margin, traceable from Walcott Valley to Dromedary Platform and the Bulwark	*Marshall drift* Underlies Walcott Glacier moraines	280, 262, ***159*** 105, 94
Walcott Glacier and K2 moraines *(stage 5)*	400	Lateral moraines parallel to present ice margins	Overlies D5 Underlies D6	185, ***117***, 22,
D6 moraine *(stage 2)*	340-390	Discontinuous drift margin, traceable from Walcott Valley to Dromedary Platform and the Bulwark	*Ross Sea drift* Overlies Walcott Glacier moraines	94, 62, ***23***

Ages in italics are $^{40}Ar/^{39}Ar$ ages of basalt. Exposure ages in bold type are interpreted as minimum ages. Exposure ages in bold italic type are consistent with independent age estimates of correlated deposits. Helium isotope data appears in Table 5.2.

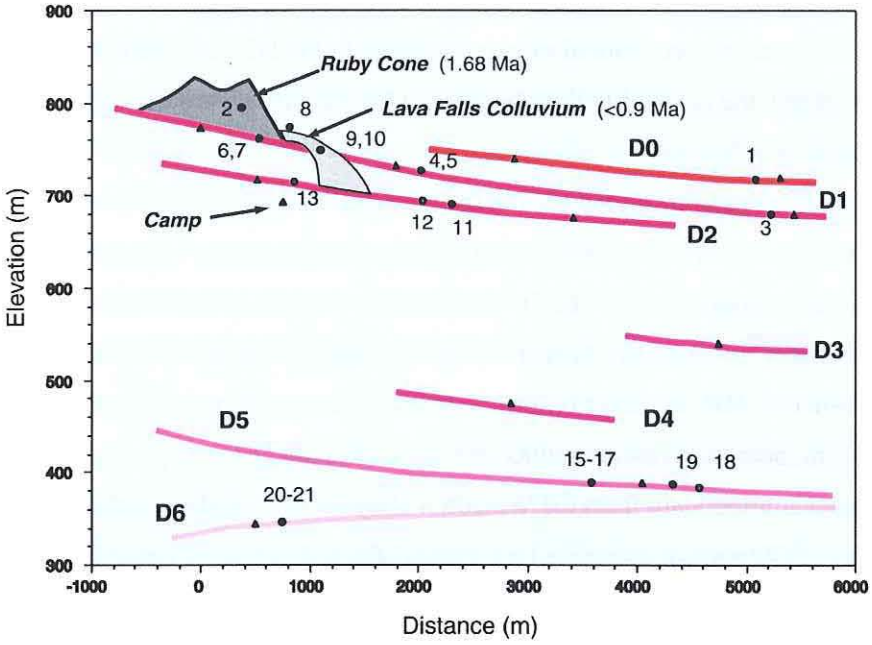

Figure 5.5 Elevation of moraines and the sampled volcanic features on Dromedary Platform projected onto a vertical plane. Note that the D6 moraine slopes in the opposite direction to the higher moraines. Horizontal distances are measured from location 7 (See Figure 5.3). Triangles are surveyed locations (See Appendix 5.2). Dots are sample locations.

The morphology of the glacial drift varies from distinct moraine ridges 5 to 6 m high with distinct crests (D2) to drift-sheet margins one boulder thick (D1). Boulders larger than 0.5 m are rare although large blocks (>10 m^3) occur locally on the D2 moraine. The D3 and D4 moraines show similar morphology to D2, but are more discontinuous and occur at lower elevations. Streaks of light-colored felsic debris in gullies indicate down-slope movement of moraine material where slopes are steep (Figure 5.4). Moraine material on lower angle slopes between gullies appears stable. Glacial erratics at higher elevation than the D1 moraine were observed in several locations between the Dromedary Glacier and Ruby Cone (Figure 5.3). The erratic boulders occur in "windows" in younger flows which expose older lava flows.

The D1 through D6 moraines are largely composed of light-colored felsic rocks and are conspicuous on the underlying basalt (Figure 5.3). Observed lithologies include metasediments, gneiss, granites, pegmatites, sandstones, and dolerite, as well as erratic basalt. In contrast, the D0 drift is composed of volcanic-rich debris. The degree of rock weathering as indicated by ventifaction, cavernous weathering, and desert varnish, decreases from the D0 moraine to the D6 moraine. Striations occur on protected rock faces on the D5 and D6 moraines, but are absent on surface boulders on the D0 through D4 moraines.

The geomorphic observations indicate that the moraines on Dromedary Platform generally decrease in age from higher to lower elevations. However, it is not possible to

determine the age relationships between the D2, D3, and D4 moraines. Although it is likely that the D3 and D4 moraines are younger recessional moraines related to the D2 glacial advance, given the subdued morphology, the possibility that the D3 and D4 moraines were overridden by a younger D2 advance cannot be ruled out.

The D5 and D6 moraines can be traced around the headland to the north into the Walcott Valley (Figure 5.4 and 5.6). In the Walcott Valley, D6 (Ross Sea drift) overlies a lateral moraine of the Walcott Glacier (Stuiver *et al.*, 1981). The D5 drift limit is overlain by the Walcott moraine (Table 5.1 and Figures 5.4 and 5.6). This cross-cutting relationship demonstrates that the ice advances which deposited the D5 and D6 moraines are out-of-phase with advances of the Walcott Glacier. At present, both the Wolcott and Koettlitz Glaciers are advancing. The Ross Sea drift (D6) can be traced continuously from the Walcott Valley to Miers Valley to the north (Figure 5.1) where ^{14}C and U/Th ages of associated proglacial lake sediments are dated between 10 and 23 ka (Clayton-Greene *et al.*, 1988).

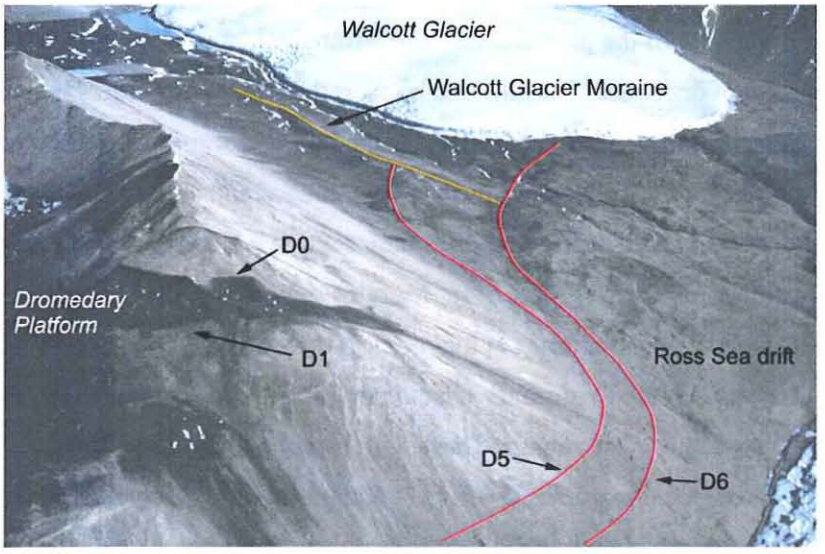

Figure 5.6 Photograph taken from over Pyramid Valley showing the bedrock shoulder between Dromedary Platform and the Walcott Valley and the D0 (dark) and D1 (light) drift limits. The cross-cutting relationships of the D5 and D6 moraines with the Walcott alpine moraines are also visible.

The elevation of the D5 moraine is similar to that of a drift limit at Hurricane Ridge on Mount Morning on the other (east) side of the Koettlitz Glacier (Figure 5.1). Surface exposure ages of boulders on the drift and ice contact lava flows fall within stage 6 (Kurz and Ackert, 1996). The D5 moraines are correlated with pro-glacial lake sediments underlying Ross Sea drift

in Marshall Valley to the north of Miers Valley which have stage 6 U/Th ages (Denton *et al.*, 1989b) (Figure 5.1).

The D5 and D6 moraines also occur on the Bulwark (Figure 5.4). The D6 moraine occurs on the western wall of Pyramid Trough and passes under the Koettlitz Glacier on the northeast side (Stuiver *et al.*, 1981). The D5 drift limit can be traced around the Bulwark indicating that it was a nunatak. Distinct drift limits occur on the volcanics at the north and south ends of the Bulwark. The elevations decrease to the north and parallel the D5 drift limit on the Dromedary Platform. Drift patches and erratics which occur above the D5 moraine indicate the Bulwark was overridden during earlier glacial advances, consistent with the ice thickness indicated by the elevation of the higher moraines on the Dromedary Platform.

The Koettlitz 1 (K1) and Koettlitz 2 (K2) moraines occur along the margin of the Koettlitz Glacier on the Bulwark (Figure 5.4). The inner moraine (K1) is ice-cored and unweathered and can be traced continuously along the glacier to the north side of the Bulwark where it overlies Ross Sea drift (D6). This moraine is inferred to be Holocene age. The outer moraine (K2) occurs on the south side of the Bulwark above the D6 drift limit and extends along the Koettlitz Glacier to the south overlying D5 drift. The K2 moraine is not ice-cored and the surface boulders show cavernous weathering and staining. There is not a distinct difference in surface weathering of boulders on the K2 moraine and the adjacent D5 drift. The K2 moraine represents an expansion of the Koettlitz Glacier younger than the D5 drift.

5.6 Volcanic/glacial stratigraphy and $^{40}Ar/^{39}Ar$ chronology

Stratigraphic relationships between lava flows and moraines occur at several locations on the Dromedary Platform. The D1 moraine overlies Ruby Cone at the south end of the platform (Figures 5.4 and 5.7). The D1 moraine is overlain by at least two lava flows. One originates under the Dromedary Glacier and the other in the valley south of Dromedary Glacier. In addition, volcanic colluvium overlies the D1 moraine just north of Ruby Cone. The lava flows are in turn overlain by the D2 moraine (Figures 5.3, 5.4, and 5.7 and Table 5.1). The lava flows can be traced down-slope below the D2 moraines and do not show evidence of interaction with an ice margin, demonstrating ice-free conditions at Dromedary Platform between deposition of the D1 and D2 moraines. The volcanic colluvium is informally named the Lava Falls colluvium. Down slope creep of the colluvium subsequent to deposition of the D2 moraine is indicated by ponding of the colluvium behind the moraine.

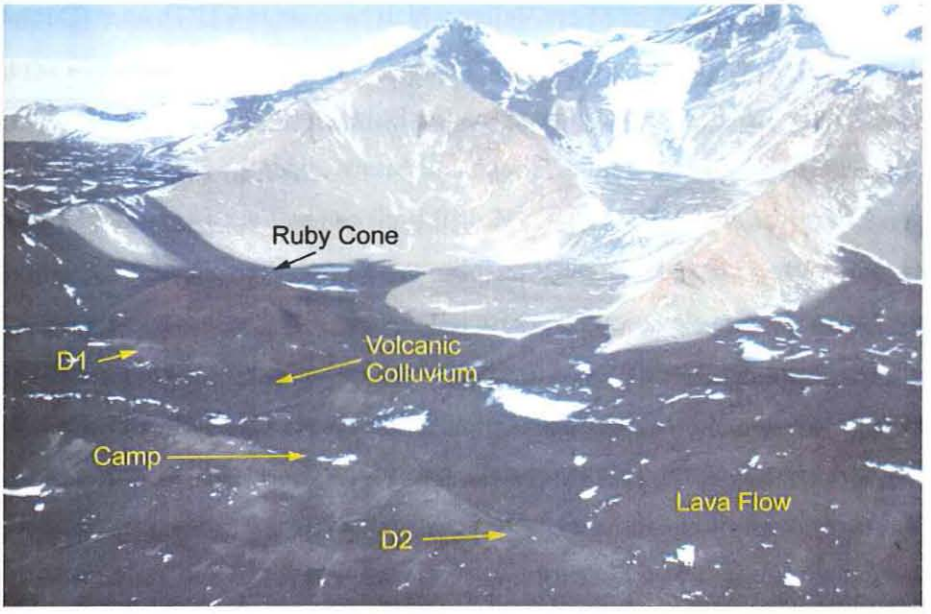

Figure 5.7 Photograph of Ruby Cone on Dromedary Platform. The Cone is only minimally eroded. The D1 moraine overlies the flank of the cone. The age of the cone (1.68± 0.13 Ma) provides a maximum age for the D1 moraine. Younger volcanic colluvium overlies the D1 and is deflected by the D2 moraines.

The Lava Falls colluvium was initially interpreted as an extremely degraded, but *in situ*, lava flow that had been extensively reworked by periglacial processes. The landform is composed of a distinctive gray olivine-rich basalt that can be traced continuously up slope to the basin behind Ruby Cone. The basin is filled with volcanic debris of similar lithology derived from the Lava Falls flow. However, the landform has very low relief and lacks channels, levees, or other distinctive lava flow morphology. The landform surface is smooth, has active sand-wedge polygons, and thins to a feather edge (Figure 5.8). Similar subdued surface morphology occurs in the basin. The thin drift that makes up the D1 moraine occurs on both sides of (but not on) the landform, indicating that the volcanic debris composing the landform overlies the D1 moraine. This "lava flow" was selected for $^{40}Ar/^{39}Ar$ dating because it appeared older than the other overlying flows (which have clear flow morphology preserved) and would therefore provide a better age constraint on the underlying D1 moraine. As discussed below (Section 5.7), this landform is now inferred to be colluvium derived from a lava flow which moved down slope after deposition of the D2 moraine. The key difference in these interpretations is that the volcanic debris is not *in situ* and the $^{40}Ar/^{39}Ar$ age of the basalt does not constrain the age of the underlying D1 moraine.

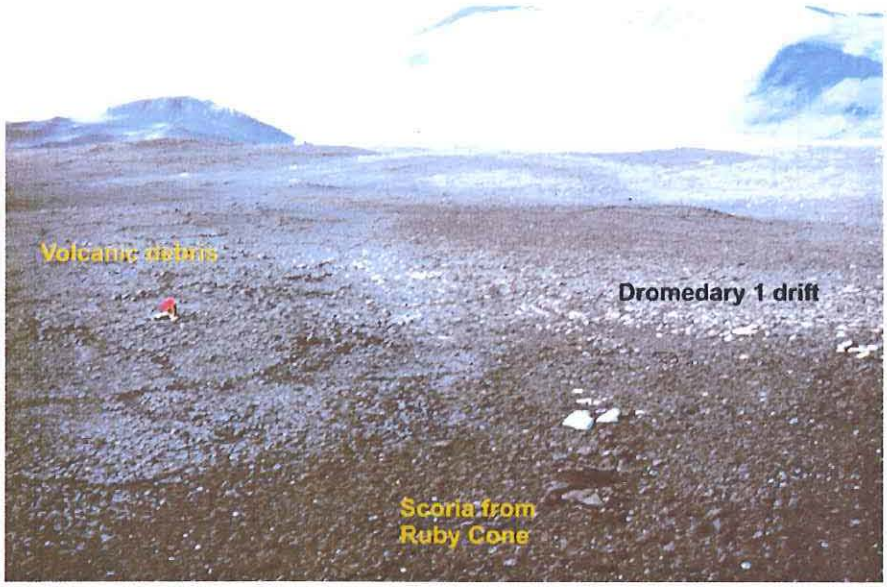

Figure 5.8 Photograph of the D1 moraine at Ruby Cone. The moraine overlies scoria from Ruby Cone and consists of erratic boulders. The moraine is truncated by a thin sheet of volcanic debris. The debris is interpreted as colluvium (periglacial debris which has crept down slope) younger than the moraine. T. Kenna in red parka provides scale.

$^{40}Ar/^{39}Ar$ measurements of samples from Ruby Cone (MK92-245-2) and the Lava Falls colluvium (KAK93-430) were made at the New Mexico Geochronological Research Laboratory using the incremental heating technique. The resulting age spectra show well-defined plateaus (Figure 5.9A and B). However, the plateaus are slightly saddle shaped, and the intercept of the isochron for Ruby Cone is slightly elevated, suggesting the presence of minor excess ^{40}Ar. The weighted mean plateau ages and isochron ages agree within 2σ; the isochron ages are considered the best age estimate. Similar amounts of excess ^{40}Ar occur in other Quaternary basalts from the Dry Valleys Region. The isochron ages are considered accurate eruption ages (Wilch *et al.*, 1993). The results indicate that the Ruby Cone is 1.68 ± 0.13 Ma. This $^{40}Ar/^{39}Ar$ age provides a maximum age for the D1 moraine. The $^{40}Ar/^{39}Ar$ age of the basalt composing the Lava Falls colluvium is 0.92 ± 0.10 Ma and provides a maximum age of the Lava Falls colluvium and the D2 moraine. Unfortunately, the age of the volcanic debris does not constrain the age of the D1 moraine.

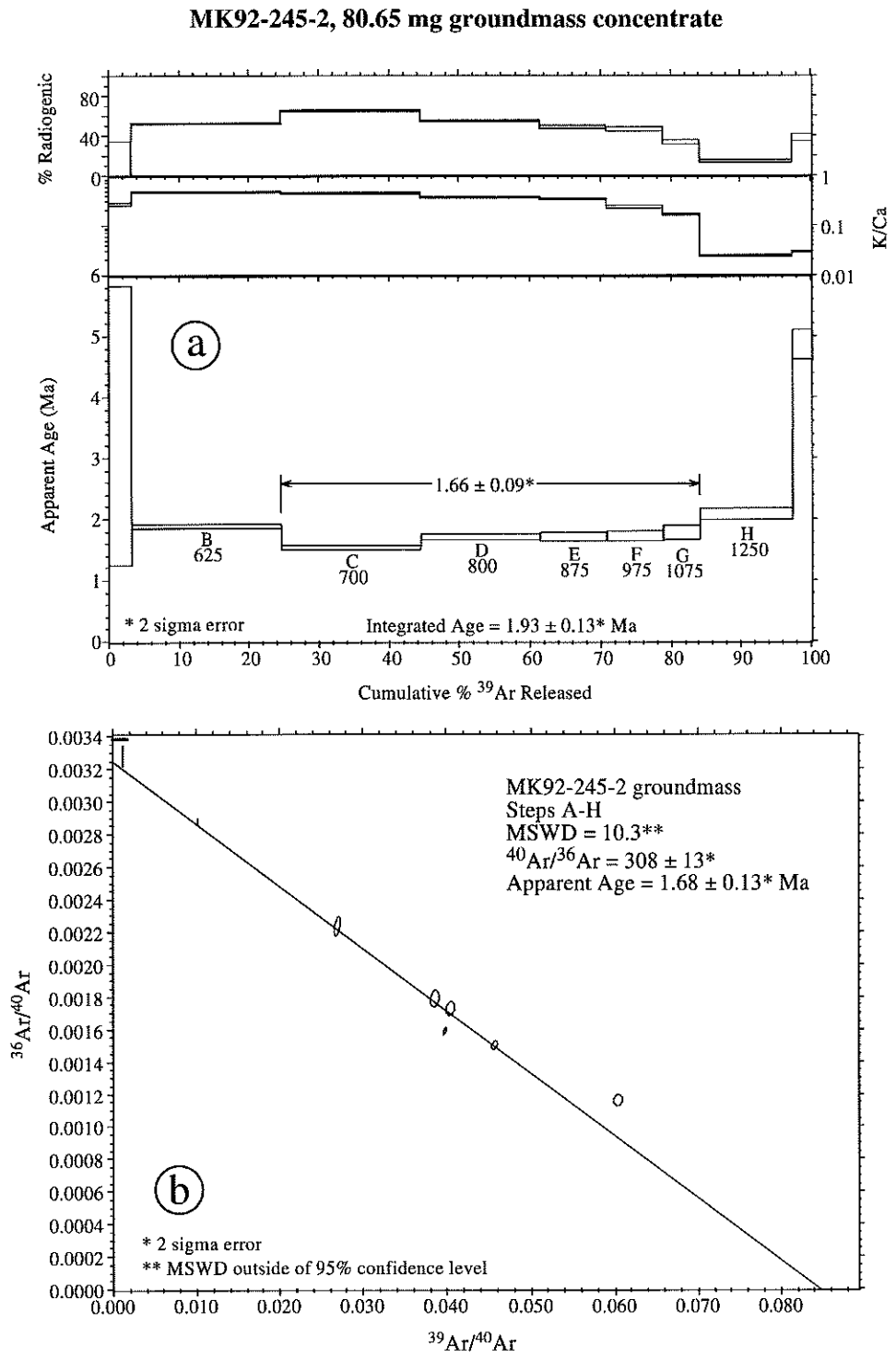

Figure 9A

Figure 5.9A $^{40}Ar/^{39}Ar$ data from Ruby Cone (MK92-245-2) on Dromedary Platform. The isochron age is the preferred age for the samples. a) Age spectrum and b) inverse isochron.

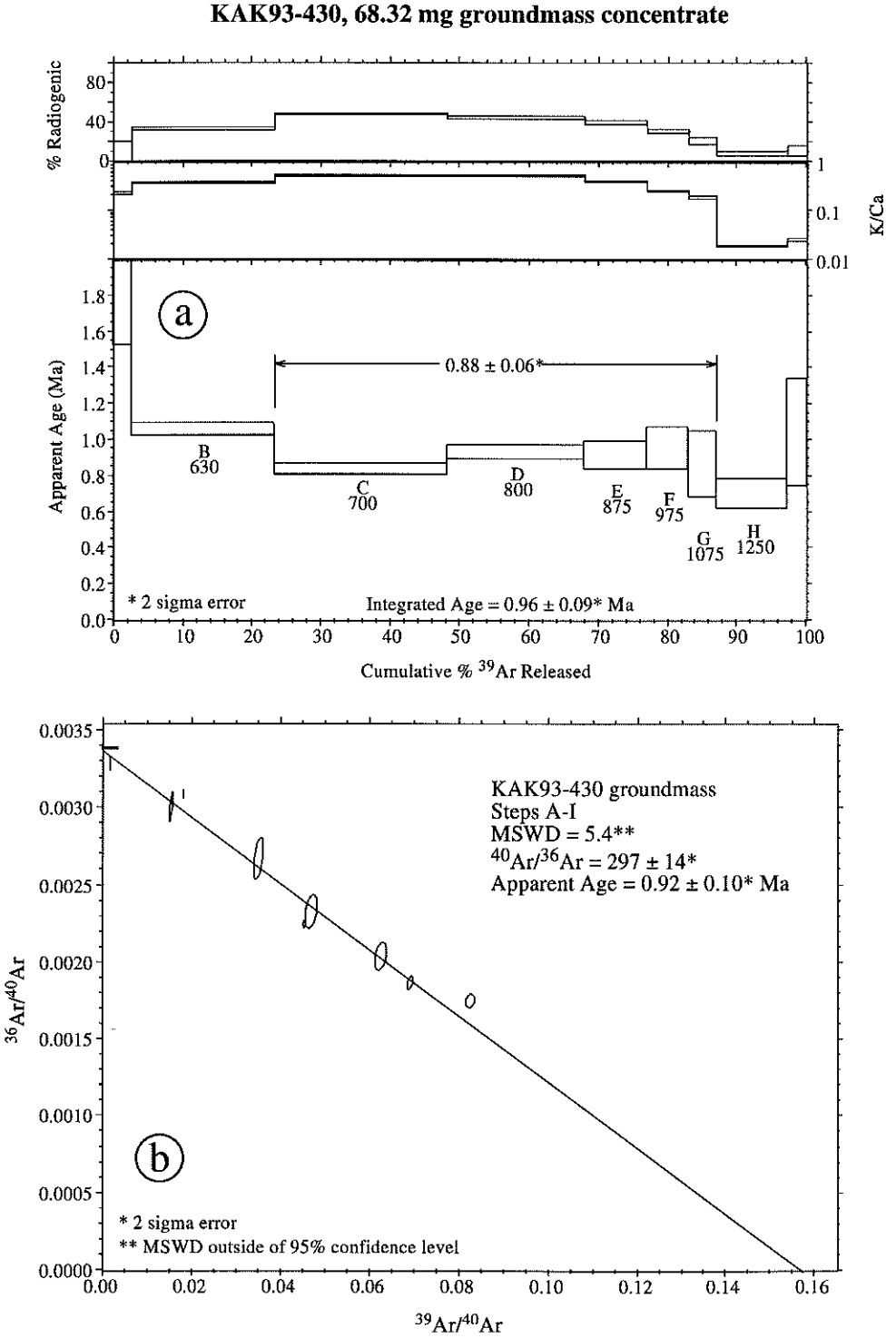

Figure 9B

Figure 5.9B $^{40}Ar/^{39}Ar$ data from volcanic debris (KAK93-430) on Dromedary Platform. The isochron age is the preferred age for the samples. a) Age spectrum and b) inverse isochron.

5.7 ^{3}He surface exposure ages

Introduction

The helium isotope data and ^{3}He surface exposure ages appear in Table 5.2 and assume no erosion or tectonic uplift. The surface exposure ages from each moraine show significant scatter (Figure 5.10). In some cases, it is possible to evaluate the scatter because there is independent stratigraphic or chronologic control on the moraines. There is evidence for cover, erosion, and prior exposure of some samples. The ^{40}Ar/^{39}Ar ages provide maximum ages for the D1 and D2 moraines. The D6 moraine is part of the Ross Sea drift and dates to the last glacial maximum (Stage 2) (Stuiver *et al.*, 1981). The D5 moraine is correlated with dated deposits of stage 6 age in Marshall Valley and on Hurricane Ridge (Denton *et al.*, 1989b; Kurz and Ackert, 1996).

Table 5.2 Helium isotope data and surface expoure ages from Dromedary Platform

Sample	Location	Elev. (m)	3He/4He R/Ra (crush)	1sig	4He ccSTP/g x10e-9	±1 sig	3/4 R/Ra (melt)	±1 sig	3He atoms/g x10e7	±1 sig	Age (ka)	±1 sig
Dromedary 0												
MK92-225	1	730	7.00	1.00	6.08	0.12	675	4	15.12	0.32	479	10
Ruby Cone												
MK92-245-1	2	765	11.1	0.2	2.03	0.04	3694	37	27.85	0.63	854	20
Dromedary 1												
MK92-228	3	703	8.48	0.25	5.03	0.10	671	4	12.39	0.26	402	9
MK92-238	4	770	7.00	1.00	85.19	1.71	23.9	0.1	5.36	0.16	164	5
MK92-239	5	770	6.87	0.10	5.99	0.12	280	1	6.08	0.13	185	4
KAK93-431-1	6	727	7.00	1.00	15.57	0.31	155	2	8.55	0.22	271	7
KAK93-034	7	727	7.00	1.00	68.34	1.37	46.7	0.9	10.09	0.33	320	11
Lava Falls Colluvium												
KAK93-035	8	762	7.00	1.00	24.29	0.49	107	1	9.03	0.20	278	6
KAK93-429	9	727	7.00	1.00	11.20	0.22	326	2	13.30	0.29	422	9
KAK93-430	10	727	7.00	1.00	5.12	0.10	689	3	12.99	0.27	412	9
Dromedary 2												
MK92-233	11	727	7.00	1.00	3.96	0.08	480	3	6.97	0.15	221	5
MK92-235	12	727	7.00	1.00	1.85	0.04	1614	11	11.07	0.23	351	8
KAK93-054-1	13	727	0.011	0.004	331.17	6.63	4.89	0.03	6.01	4.21	191	4
MK92-242	14	578	7.27	0.17	10.91	0.22	79.1	0.7	2.92	0.07	106	3
Dromedary 5												
RA92-012-1	15	389	7.03	0.12	9.00	0.18	116	2	3.64	0.10	159	5
RA92-012-2	16	386	8.32	0.77	3.11	0.06	216	2	2.40	0.06	105	3
RA92-013	17	386	7.37	0.09	13.50	0.27	126	2	5.98	0.17	262	8
RA92-014-1	18	386	7.00	0.05	5.14	0.10	120	1	2.15	0.05	94	2
MK92-216	19	385	7.15	0.11	8.57	0.17	207	1	6.38	0.14	280	6
Dromedary 6												
RA92-039	20	345	6.74	0.15	2.08	0.04	184	2	1.37	0.03	62	1
RA92-040	21	345	7.08	0.06	13.29	0.27	17.5	0.2	0.51	0.02	23	1
RA92-041	22	345	7.16	0.12	3.14	0.06	185	3	2.07	0.06	94	3
Koetlitz 2												
RAK96-019	23	454	0.011	0.004	570.87	0.46	0.26	0.01	0.54	0.01	22	1
RAK96-018	24	454	5.53	0.14	2.65	0.00	294	3	2.84	0.03	117	1
RAK96-214	25	454	6.93	0.05	34.74	0.03	41.8	0.2	4.50	0.02	185	1

Helium isotope data and surface exposure ages from Dromedary Platform. R_a is the ^{3}He/^{4}He of air = 1.384 x 10^{-6}. R is the measured ^{3}He/^{4}He. Surface exposure ages are calculated using a sea level high latitude ^{3}He production rate of 129±4 atoms/g/yr. The data is scaled for altitude using the approach of Stone (1999). The surface exposure age uncertainty is propagated analytical uncertainty only. Estimated uncertainty in production rate and scaling is 5-10%. An initial ^{3}He/^{4}He of 7.0 R_a was assumed for samples which were not crushed.

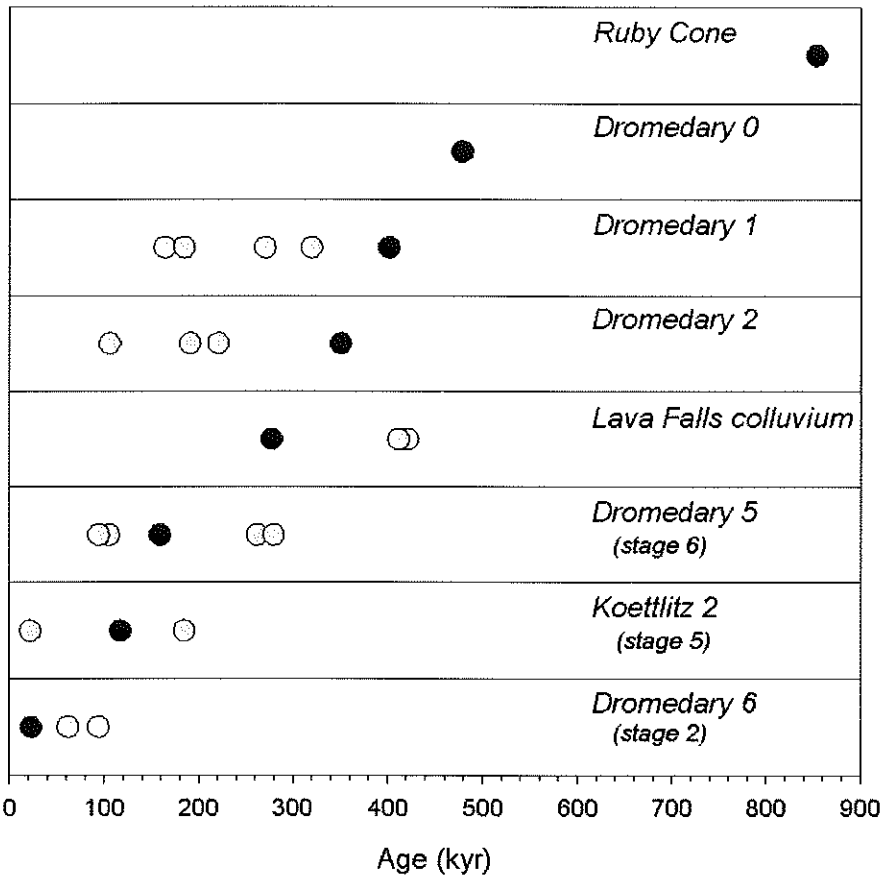

Figure 5.10 Plot of surface exposure ages obtained from moraines and volcanics on Dromedary Platform and the Bulwark. Black circles are the exposure ages of samples which are inferred to be the best age estimate for the deposit. For the D6, K2, and D5 moraines, the age of the samples corresponding to the black circles agrees with independent age determinations on correlative drift. For older deposits the samples corresponding to the black circles are taken as minimum ages. Gray circles to the right of open circles are samples inferred to have prior exposure. Gray circles to the left of open circles are samples inferred to have had substantial erosion or cover. The plot shows wide scatter in the exposure ages for individual moraines. However, the ages corresponding to the black circles fall in stratigraphic order.

Surface exposure ages and erosion rates of Ruby Cone and Lava Falls colluvium

The oldest exposure age obtained is from a lava flow exposed on the flank of Ruby Cone (Table 5.2). This exposure age (854 ka) is substantially younger than the $^{40}Ar/^{39}Ar$ age (1.68±0.13 Ma), consistent with geomorphic evidence for some erosion of Ruby Cone. A mean erosion rate of 60 to 75 cm/Myr is required to increase the exposure age to that of the $^{40}Ar/^{39}Ar$ age of the flow assuming constant erosion (Lal, 1991, Chapter 1). Erosion of ~100 to 125 cm of overlying material is reasonable given the morphology of the cone and the friable nature of the welded scoria/agglutinate. The higher erosion rate assumes most of the shielding material was

probably similar to the more erodable and lower density (~2 g/cm^3) scoria/agglutinate spatter exposed in the rim of Ruby Cone rather than basalt (density ~2.8 g/cm^3).

The exposure ages of samples from the Lava Falls colluvium which overlies the D1 moraine near Ruby Cone are 422 and 412 ka. The samples were collected at the same location and agree within error, suggesting that processes effecting the surface acted uniformly over distances of a few meters. The exposure ages are substantially younger than the $^{40}Ar/^{39}Ar$ age (920±10 ka) of the basalt debris composing the landform. The younger exposure ages require erosion rates of the landform greater than 100 cm/Myr if the dated material is *in situ.* This erosion rate is unlikely because it is higher than that inferred for the adjacent agglutinate volcanic cone.

The preferred interpretation of the landform is that it is colluvium which flowed over the D1 moraine well after eruption of the basalt debris. There is abundant evidence of downslope movement of debris on the Dromedary Platform. Streaks of felsic debris occur in gullies below moraines (Figure 5.4). Down slope creep of the basalt debris composing the landform is indicated by ponding of the debris behind the D2 moraine. The D2 moraine has slumped down slope at the location where it is in contact with the ponded debris. Given evidence for active periglacial processes and the unreasonably high erosion rates required by the $^{40}Ar/^{39}Ar$ age data, the landform is more likely colluvium which was active significantly later than the eruptive age of the basalt. This interpretation is consistant with the surface exposure ages on the adjacent D1 moraine discussed below which also require unreasonably high erosion rates if the moraine is older than 920±10 ka, as required if the landform is an *in situ* lava flow. In general, surface exposure ages poorly constrain the age of colluvium deposits because the deposits may be active for long periods or episodically active. In this case, the colluvium may have prior exposure to cosmic rays before and during transport down slope. Burial and re-exposure during down slope movement is also possible.

An additional exposure age (278 ka) was obtained from the source area of the Lava Falls colluvium in the basin west of Ruby Cone. The surface is composed of fractured basalt of similar lithology to the colluvium sampled at Ruby Cone and has similar morphology. Sand-wedge polygons are well-developed. This surface is also interpreted as volcanic colluvium. The younger exposure age may result from exhumation by frost heaving from depth.

Surface exposure age of the D0 drift

The single exposure age (480 ka) on the D0 moraine is interpreted as a minimum age. Assuming an associated ice profile parallel to the D1 moraine, D0 ice would have covered Ruby Cone and the Lava Falls Colluvium (Figure 5.5). Although a few erratics occur on isolated lava flow surfaces above the D1 moraine, they do not occur on Ruby Cone or on the volcanic debris overlying the D1 moraine, indicating the moraine may be older than those volcanics (>1.68 Ma). In that case, the much younger exposure age implies cover or erosion rates greater than 130 cm/Myr. Both alternatives seem unlikely. D0 drift may not be preserved at the south end of the platform or the assumed ice profile may be incorrect.

The drift is predominantly composed of basalt of similar lithology with only rare non-volcanic rocks. The D0 drift thins rapidly but can be traced into the ice-free valley immediately to the south where the upper limit is determined by basalt erratics on the bedrock. A volcanic rich drift above the D1 occurs adjacent to (underlying?) the Condor Cone north of Dromedary Glacier (Figure 5.4). Similar volcanic rich drift near the Howchin Glacier (Figure 5.1) contains abundant hyaloclastite, a volcanic rock type characteristic of interaction of water and lava during an eruption. The Howchin drift and the D0 drift may have been derived from volcanics erupted onto or through ice. If this is the case, prior exposure would be minimal and $^{40}Ar/^{39}Ar$ dates on the volcanics should closely date the associated glaciation.

Surface exposure ages of the D1 moraine

Two boulders from the D1 drift limit on the eastern slope of Ruby Cone have exposure ages of 272 and 321 ka. If the $^{40}Ar/^{39}Ar$ age of the overlying basalt debris is taken as the minimum age (assuming the landform is an *in situ* lava flow), erosion rates of 150 to 200 cm/Ma are required. The exposure ages would imply that the D1 drift limit which now consists of small (<30 cm) erratic boulders is the remains of a much thicker drift sheet which originally was similar in morphology to the D2 moraine. However, these erosion rates are two orders of magnitude higher than those measured on moraine boulders elsewhere in Antarctica (Brown *et al.*, 1991; Nishiizumi *et al.*, 1991) and would imply that basalt moraine boulders had eroded or been exhumed faster than the underlying agglutinate volcanic cone. This conclusion is contradicted by field observations of relative weathering rates of moraines and volcanic landforms and by the erosion rate calculated here for Ruby Cone. Therefore, the exposure ages of the moraine boulders imply that the overlying basalt is not *in situ.* The exposure ages of the moraine boulders are

interpreted as minimum ages for the D1 ice advance. Cover and exhumation of the moraine boulders by material from Ruby Cone, as discussed below, is possible but would have had to occur prior to deposition of the adjacent Lava Falls colluvium, because there is no agglutinate debris from Ruby Cone on the Lava Falls colluvium.

The exposure ages of samples from the D1 moraine segment near the Dromedary Glacier are considerably younger (164 and 186 ka) than those at Ruby Cone (Table 5.2). The D1 drift limit near the Dromedary Glacier is a distinct arcuate ridge. The moraine contains abundant boulders larger than 30 cm, and has a generally less-weathered appearance than the D1 drift at Ruby Cone (Figure 5.11). The surface between the boulders is largely composed of scoria derived from the eroded Dromedary Cone immediately up slope from the moraine. The younger ages are attributed to cover of the moraine by scoria from the Dromedary Cone.

Figure 5.11 Photograph of the D1 moraine at Dromedary Glacier. The moraine forms a distinct ridge and the boulders are larger and more abundant than those of the D1 moraine at Ruby Cone. The scoria between the boulders is derived from Dromedary Cone directly up slope. The moraine is inferred to have been buried by scoria and subsequently exhumed. The surface exposure ages of the boulders are younger than those on the D2 moraine down slope which is known from stratigraphic relationships to be younger, providing additional evidence for a disturbed exposure history of the D1 boulders here. M. Kurz provides scale.

Stratigraphic relationships with the lava flow that overlies the D1 moraine between Ruby and Dromedary Cones demonstrate that Dromedary Cone is younger than the D1 moraine (Figure 5.3). The margin of the flow facing the Dromedary Cone is an embankment several meters high. The embankment forms a nearly circular arc around the center of the Dromedary Cone on the southwest side (Figures 5.3 and 5.4). The lava flow was deflected by the Dromedary Cone when the cone was much larger. The D1 moraine falls well within the inferred radius of the original volcanic cone. Because the lava flow overlies the D1 moraine, the moraine was deposited prior to erosion of the cone. Evidently, the moraine was covered by scoria during eruption of Dromedary Cone and was subsequently exhumed. The younger exposure ages of the moraine boulders relative to those at Ruby Cone are the result of shielding from cosmic rays by scoria. The difference in exposure ages between the two locations implies that they were shielded for at least 86 kyr. These conclusions also imply that weathering rates of volcanic cones in Antarctica are strongly dependent on lithology. The younger Dromedary Cone is substantially more eroded than the older Ruby Cone, presumably due to a higher relative percentage of scoria compared to lava flows and welded agglutinate.

The single exposure age of the D1 moraine on the shoulder at the north end of the platform is 403 ka. The moraine occurs on a broad bench and the exposure history of the sample is unlikely to be complicated by substantial erosion or cover. The exposure age is interpreted as a minimum age for the D1 moraine assuming prior exposure is minimal.

Surface exposure age of the D2 and D3 drifts

The three exposure ages on the D2 moraine show wide scatter. The youngest age of 191 ka (KAK93-054) is measured on quartz which has likely had some diffusive loss of ^{3}He (Brook and Kurz, 1993). The other samples (351 and 221 ka) provide a minimum age for the moraine, assuming the samples did not have prior exposure. The age of the oldest sample on the D2 moraine is older than all but the oldest age from the D1 moraine. All the D2 ages are older than the ages from the D1 moraine near Dromedary Glacier, consistent with inferences of burial of those samples. The surface exposure ages are younger than the ages from the Lava Falls colluvium, which was active after deposition of the D2 moraine, indicating the likelihood of prior exposure of the colluvium samples. A maximum age of the moraine will be obtained when $^{40}Ar/^{39}Ar$ ages of the underlying lava flows are available. The single age (106 ka) from the D3

moraine is consistent with it being younger than the D2 moraine, but the age is also less than the exposure ages of samples from the D5 moraine which is younger than the D3.

Surface exposure ages of the D5 drift

As was the case for the higher elevation moraines, the surface exposure ages from the D5 moraine show wide scatter (94-280 ka). Independent chronologic control for the age of the moraine comes from correlative drift in other locations. Because the D5 moraine lies immediately beyond the Ross Sea drift (D6), it is correlated with drift underlying Ross Sea drift in Marshall Valley (Figure 5.1). U/Th dates on carbonate in associated glacial lacustrine sediments span isotope stage 6 (130-190 kyr) (Denton *et al.*, 1989b). Surface exposure ages of drift and associated ice contact volcanic landforms at similar elevation at Hurricane Ridge on Mount Morning also have stage 6 ages (Kurz and Ackert, 1996). Therefore, the D5 moraine is assumed to date to the penultimate glaciation. However, only one of the exposure ages (159 ka) falls within stage 6. Two fall within stage 8 (262 and 280 ka) and the two youngest ages (94 and 105 ka) fall within stage 5 (Table 5.2). If the correlation of the D5 moraine with stage 6 deposits is correct, the older samples must have substantial prior exposure. The similar ages and correspondence with stage 8 of the older samples suggests the possibility that the correlation of D5 with stage 6 deposits is incorrect. On the other hand, the older samples may be reworked from the deposits of the previous glaciation (stage 8) (Brook, 1993; Brook *et al.*, 1993b). The stage 5 ice limit of the Koettlitz Glacier is mapped at a much lower elevation; the younger ages must be due to erosion or exhumation by frost heaving.

Surface exposure ages of the D6 drift

The surface exposure ages on the D6 moraine (23, 62 and 94 ka) fall within the range of previous surface exposure measurements on Ross Sea drift (Brook *et al.*, 1995) consistent with the mapping of the D6 moraine as Ross Sea drift (Stuiver *et al.*, 1981). Only the age of the youngest sample falls within stage 2. The older ages are attributed to prior exposure. Brook (1995) suggests that prior exposure is unlikely in Ross Sea drift because most of the glacial debris was assumed to be derived subglacially from the Ross Sea. Subsequent work on Hurricane Ridge showed that the surface exposure ages of Ross Sea drift boulders overlying a lava flow were older than those on the underlying well-preserved lava flow, demonstrating that prior exposure is common on the Ross Sea drift at that location (Kurz and Ackert, 1996). The results from

Dromedary Platform are also consistent with prior exposure. Apparently, in the southern part of McMurdo Sound, the volcanic component of Ross Sea drift is largely material derived from previously exposed surfaces. The volcanic Black Island and Brown Peninsula protruded above the LGM ice surface as nunataks and are potential sources of previously exposed debris (Figure 5.2).

Surface exposure ages of the K2 drift

The surface exposure ages from the K2 moraine show scatter similar to that observed on the Dromedary moraines. The youngest age (22 ka) is from a quartz vein in gneiss which potentially has lost cosmogenic ^{3}He. The geometry of the D6 moraine and the K2 moraine requires that the K2 moraine is older than the D6 moraine (Ross Sea drift). The K2 moraine lies within the D5 drift limit and is thus younger than the penultimate glaciation. Because the moraine records Koettlitz Glacier ice levels larger than present and the moraine morphology and boulder weathering are most similar to the D5 moraine, the K2 moraine is inferred to date to the last interglacial (stage 5). One sample has a surface exposure age (117 ka) consistent with this interpretation. The older sample (184 ka) records prior exposure. Additional samples are necessary in order to constrain the age of this moraine.

Summary

The surface exposure ages from Dromedary Platform demonstrate the need for many samples to characterize the age of glacial deposits. Although problems of prior exposure erosion and cover are demonstrated, some "reasonable" exposure ages were obtained on the younger D5, K2, and D6 moraines (Figure 5.10), suggesting that the ages of all of the moraines could be better constrained with a larger data set. The exposure ages from the D6 moraine indicate prior exposure of ~70 kyr is possible. If the stage 6 age assignment of the D5 moraine is correct, two samples on that moraine have prior exposure of ~100 kyr. In the absence of other evidence to the contrary, prior exposure of this magnitude may be present in the samples from the older moraines and the uncertainty in the ages is assumed to be ~100 kyr.

In addition to problems with prior exposure, some of the older samples apparently have been covered by scoria during or after volcanic eruptions and later exhumed by erosion. This is almost certainly the case for the D1 moraine near Dromedary Glacier where exposure ages are younger than those from the stratigraphically younger D2 moraine and there is good geomorphic

evidence for cover and subsequent erosion of the Dromedary Cone. Cover may partly explain the relatively young ages of D1 drift at Ruby Cone although there is no evidence of prior cover. If a substantial period of exposure occurred prior to burial, the duration of burial could be determined by measuring a radioactive cosmogenic nuclide such as ^{36}Cl or ^{26}Al. A radioactive nuclide will give younger ages than ^{3}He due to radioactive decay while the sample is shielded from cosmic rays.

5.8 Discussion

Implications of the glacial record on Dromedary Platform for Antarctic glacial history

The implications for Antarctic glacial chronology of the older glacial record on Dromedary Platform depend on the interpretation of the moraines and drift older than the D6 moraine (Ross Sea drift). Do the D0 through D5 moraines reflect expansions of the Koettlitz Glacier due to higher accumulation rates or damming of the Koettlitz Glacier by grounded ice in McMurdo Sound? Evidence for thickening of glaciers due to both processes occurs in the Transantarctic Mountains. If the moraines record expansions of the Koettlitz Glacier, the glacial chronology should be similar to that of Arena Valley, where moraines record an advance of the Taylor Glacier during the last interglacial period (Brook *et al.*, 1993b; Denton *et al.*, 1989b; Marchant *et al.*, 1994b). In contrast, grounded ice in McMurdo Sound is required if the moraines record damming of the Koettlitz Glacier. Outlet glaciers to the south of McMurdo Sound were dammed when the WAIS advanced across the Ross Sea in response to lower sea level (Bockheim *et al.*, 1989; Denton *et al.*, 1989a) (Chapter 4). The implication of grounded ice in McMurdo Sound is that the grounding line of the WAIS was north of McMurdo Sound and the Dromedary moraines would therefore record expansions of the WAIS similar to, or greater than, during the LGM.

The D5 moraine is key to distinguishing between these alternatives. On the Dromedary Platform and the Bulwark, the D5 moraines can be used to reconstruct the ice profile of an ancestral Koettlitz Glacier that flowed through the Pyramid Trough and projected into the Walcott Valley. The D5 moraine is traced continuously to the Walcott Glacier where it is cross-cut by a lateral moraine of that glacier. The cross-cutting relationship demonstrates that the D5 advance was out-of-phase with the Walcott Glacier. Because the Walcott and Koettlitz are large alpine glaciers fed by local accumulation, they are expected to have similar response to large

climate changes. This relationship, when combined with independent evidence (at Marshall Valley and Hurricane Ridge) for grounded ice in McMurdo Sound during stage 6, is compelling evidence that the D5 moraine represents damming of the Koettlitz Glacier by grounded ice in McMurdo Sound during stage 6.

In contrast to the penultimate glacial period, the lower Koettlitz Glacier was not thicker than present during the LGM. Apparently, grounded ice did not fill McMurdo Sound for long enough to allow the lower part of the Koettlitz Glacier to thicken substantially. A shorter duration of grounded ice during stage 2 compared to stage 6 is supported by independent ^{14}C dating of glacial-lacustrine deposits in the Dry Valleys (Stuiver *et al.*, 1981). Ice-dammed lakes occurred during the LGM, but there is little evidence for lakes earlier than 26 ^{14}C kyr BP; the ice damming the lakes was thinning by ~12 ^{14}C kyr BP (Hall and Denton, 1999b). Additional evidence comes from Hurricane Ridge on Mount Morning (Figure 5.1) where a lava flow with an exposure age of ~26 ka can be traced to the present ice margin (Kurz and Ackert, 1996). Therefore, immediately prior to 26 kyr, the ice levels in southern McMurdo Sound were lower than at present. In contrast, U/Th dates associated with glacial-lacustrine sediment (Denton *et al.*, 1989b) and surface exposure ages on ice-contact volcanics on Mount Morning (Kurz and Ackert, 1996) span much of stage 6 (~60 kyrs). The ages suggest that grounded ice remained in McMurdo Sound much longer, consistent with greater thickening of the Koettlitz Glacier observed at Dromedary Platform during stage 6.

The K2 moraine parallels the present Koettlitz Glacier margin and shows boulder weathering similar to that of the D5 moraine. This moraine is correlated with the Walcott alpine moraine. The K2 moraine records thickening of the Koettlitz Glacier during the last interglacial (stage 5), slightly larger than the advances that have occurred during the Holocene. The K2 and K1 moraines record ice profiles of the Koettlitz Glacier terminating in McMurdo Sound. During interglacial periods, the grounding line of the glacier is determined by sea level and the bathymetry of McMurdo Sound. The present grounding line of the Koettlitz Glacier in McMurdo Sound is only 10 km to the north of Dromedary Platform (Figure 5.1). At the grounding line, ice elevations are limited to ten percent of the water depth due to flotation and thus constrain ice thicknesses up glacier. The similar elevation of the K2 and K1 moraines is consistent with the profile of the lower Koettlitz Glacier being determined by the grounding line position. Thickening of the Koettlitz Glacier to the elevation of the D5 moraine is unlikely without grounded ice in McMurdo Sound damming the Koettlitz Glacier. Therefore, the higher moraines

on the Dromedary Platform are also inferred to record the presence of grounded ice in McMurdo Sound and substantial expansions of the WAIS.

Assuming the pattern of glaciation established since the penultimate glaciation (Stage 6) can be projected further into the past, the moraines on Dromedary Platform were deposited during glacial periods in the marine isotope record. Although correlation with specific glacial stages is not possible with the present chronologic data, the surface exposure ages are consistent with deposition of the D2 or D1 moraine during stage 12 (~425 ka), a glaciation of similar magnitude to that of stages 2 and 6.

Effects of tectonic uplift

Thicker ice resulting from longer full-glacial conditions appears insufficient to explain the older moraines on Dromedary Platform which are up to 350 m higher than those of stage 6 (D5). Grounded ice apparently remained in McMurdo Sound throughout stage 6, so it is difficult to call on a longer period of damming during earlier glaciations to raise ice levels higher. The higher elevation moraines (D0-D4) may record either higher ice profiles due to a thicker ice in McMurdo Sound or alternatively relate to tectonic uplift.

The $^{40}Ar/^{39}Ar$ age of Ruby Cone can be used to calculate maximum average uplift rates since eruption (1.68±.13 Ma). Because the cone erupted subaerially, maximum vertical displacement is the present elevation of the cone above sea level (Wilch *et al.*, 1993). For Ruby Cone, the maximum average uplift rate is 455 m/Myr. Assuming that ice profiles reached elevations similar to the D5 moraine during earlier glaciations, uplift rates less than 455 m/Myr are sufficient to account for the present elevations of the oldest moraines (D0 and D1) if the moraines are as old as 1 Ma. However, if the moraines are substantially younger, uplift rates higher than the maximum determined by Ruby Cone are required. For example, the difference in elevation between the D2 and D5 moraines is about 300 m. If the D2 moraine is assumed to be stage 12 and to record ice elevations originally similar to those of D5 (stage 6), uplift rates of greater than 1000 m/Ma are required during a short pulse in the late Quaternary. Although rapid uplift is an alternative explanation for the differing geometry of the D5 and D6 ice margins, low uplift rates in the last 120 kyr are suggested by the fact the Koettlitz moraines (K1 and K2) are at similar elevations. Lack of recent tectonic activity is also indicated by the absence of fault scarps in the area. Exposure ages older than stage 6 measured on samples from older Ross Sea drift in

several locations in McMurdo Sound north of Dromedary Platform (Brook *et al.*, 1995) provide additional evidence for earlier WAIS glaciations larger than that of stage 6.

In summary, the elevations of the older (highest) moraines may be partly attributable to tectonic uplift and, therefore, inferences about the relative extent of the WAIS during earlier glaciations would be premature. However, the vertical displacement of the D2 moraine relative to the D5 moraine requires unreasonably high uplift rates if the D2 moraine is as young as stage 12. If tectonic uplift has occurred, the exposure ages calculated on the older moraines will be underestimated. However, even recent "instantaneous" uplift (modeled by using elevations 300 m lower than measured) would not resolve the disparity between the surface exposure ages and the $^{40}Ar/^{39}Ar$ ages of the Lava Falls colluvium.

5.9 Conclusions

The most recent expansion of the WAIS into McMurdo Sound during the LGM (stage 2) is recorded by the D6 moraine on the Dromedary Platform and the Bulwark. Earlier expansions of the WAIS into McMurdo Sound dammed the lower Koettlitz Glacier at least four times prior to the LGM. The penultimate glaciation (stage 6) is recorded by the D5 moraine/drift limit on Dromedary Platform and the Bulwark. A lateral moraine of the Koettlitz Glacier (K2) which overlies D5 drift and occurs above the D6 (Ross Sea drift) limit is tentatively assigned to stage 5. At least for the last two glacial cycles, advances of grounded ice into McMurdo Sound and alpine glaciers along the coast have been out of phase.

The ice profile associated with the D6 moraine (Ross Sea drift) is unusual compared to the older moraines in that thickening of the lower Koettlitz Glacier is not observed. It is inferred that the grounding event which deposited Ross Sea drift was relatively short compared to the older events; there was not enough time for the Koettlitz Glacier to thicken substantially. Although it is not possible to assign absolute ages to the moraines older than D5, some of the expansions of the WAIS probably are older than 400 ka. These results are consistent with glacial chronologies developed at interior locations (Chapters 3 and 4) and the hypothesis that the WAIS has fluctuated synchronously with Northern Hemisphere ice sheets during the Pleistocene. The stratigraphic and spatial relationships presented here provide a framework for further refinement of the glacial chronology. Additional surface exposure ages and $^{40}Ar/^{39}Ar$ ages for the volcanics should constrain glacial chronology and place additional constraints on uplift of the Royal Society block of the Transantarctic Mountains.

The $^{40}Ar/^{39}Ar$ age of Ruby Cone is 1.68 ± 0.13 Ma. The eruption age implies an erosion rate of 60 to 75 cm/Ma for part of the volcanic cone. This rate is an order of magnitude higher than erosion rates measured on sandstone and dolerite boulders and bedrock in the Transantarctic Mountains and shows that erosion rates are lithology dependent. The high erosion rate is consistent with field observations indicating rapid erosion of these landforms. Wind blown snow often melts on the dark, solar-heated rock and refreezes beneath the surface. The porous nature of the agglutinate volcanic cones, low density of the material, and dark color makes the cones highly susceptible to frost shattering and wind erosion. This result demonstrates the utility of surface exposure dating for studying landform evolution. The $^{40}Ar/^{39}Ar$ age also constrains maximum mean uplift rates to 455 m/Myr on Dromedary Platform since eruption of Ruby Cone.

Large scatter is observed in the surface exposure ages from individual moraines. Independent stratigraphic and chronologic control on the moraines allowed evaluation of the surface exposure ages. Examples of prior exposure, erosion, and cover are present. Additional surface exposure measurements using other lithologies and other cosmogenic nuclides such as ^{10}Be and ^{36}Cl, as well as $^{40}Ar/^{39}Ar$ dates of the volcanic rocks, have the potential to further constrain the glacial chronology and provide insights into erosion rates of volcanic landforms in Antarctica.

References

Blank, H.R., Jr., Cooper, R.A., Willis, A.G., and Wheeler, R.H., 1962, *Geological Map of the Koettlitz-Blue Glacier Region, Southern Victoria Land, Antarctica*, Royal Society of New Zealand.

Bockheim, J.G., 1978, Soil weathering sequences in Wright Valley: *Antarctic Journal of the United States*, **v. 12**, p. 105-108.

Bockheim, J.G., Wilson, S.C., and Denton, G.H., 1989, Late Quaternary ice-surface fluctuations of Hatherton Glacier, Transantarctic Mountains: *Quaternary Research*, **v. 31**, p. 229-254.

Brook, E.J., 1994, Surface exposure geochronology using cosmogenic nuclides; applications in Antarctic glacial geology, MIT/WHOI.

Brook, E.J., and Kurz, M.D., 1993, Surface-exposure chronology using *in situ* cosmogenic ^{3}He in Antarctic quartz sandstone boulders: *Quaternary Research*, **v. 39,** p. 1-10.

Brook, E.J., Kurz, M.D., Ackert, R.P., and Denton, G.H., 1993a, Chronology of Taylor Glacier advances in Arena Valley using in situ produced cosmogenic helium-3: *Antarctic Journal of the United States (1991 review)*, **v. XXVI**, p. 82-85.

Brook, E.J., Kurz, M.D., Ackert, R.P., Jr., Denton, G.H., Brown, E.T., Raisbeck, G.M., and Yiou, F., 1993b, Chronology of Taylor Glacier advances in Arena Valley, Antarctica, using *in situ* cosmogenic ^{3}He and ^{10}Be: *Quaternary Research*, **v. 39**, p. 11-23.

Brook, E.J., Kurz, M.D., Ackert, R.P., Jr., Raisbeck, G., and Yiou, F., 1995, Cosmogenic nuclide exposure ages and glacial history of late Quaternary Ross Sea Drift in McMurdo Sound, Antarctica: *Earth and Planetary Science Letters*, **v. 131**, p. 41-56.

Brown, E.T., Edmond, J., Raisbeck, G.M., Yiou, F., Kurz, M.D., and Brook, E.J., 1991, Examination of surface exposure ages of Antarctic moraines using in-situ produced ^{10}Be and ^{26}Al: *Geochimica et Cosmochimica Acta*, **v. 55**, p. 2269-2283.

Cerling, T.E., 1990, Dating Geomorphic Surfaces Using Cosmogenic ^{3}He: *Quaternary Research*, **v. 33**, p. 148-156.

Clayton-Greene, J.M., Hendy, C.H., and Hogg, A.G., 1988, Chronology of a Wisconsin age proglacial lake in the Miers Valley, Antarctica, *New Zealand Journal of Geology and Geophysics*, **v. 31**, p. 353-361.

Denton, G.H., Armstrong, R.L., and Stuiver, M., 1971, The late Cenozoic glacial history of Antarctica, *in* Turekian, K.K., ed., *The Late Cenozoic Glacial Ages*: New Haven, Yale University Press.

Denton, G.H., Bockheim, J.G., Wilson, S.C., Leide, J.E., and Anderson, B.G., 1989a, Late Quaternary ice-surface fluctuations of Beardmore Glacier, Transantarctic Mountains: *Quaternary Research*, **v. 31**, p. 189-209.

Denton, G.H., Bockheim, J.G., Wilson, S.C., and Stuiver, M., 1989b, Late Wisconsin and early Holocene glacial history, inner Ross Embayment, Antarctica.: *Quaternary Research*, **v. 31**, p. 151-182.

Denton, G.H., Prentice, M.L., and Burkle, L.H., 1991, Cainozoic history of the Antarctic ice sheet, *in* Tingey, R.J., ed., *The Geology of Antarctica*: Oxford, Clarendon Press, p. 365-419.

Domack, E.W., Jacobson, E.A., Shipp, S., and Anderson, J.B., 1999, Late Pleistocene/Holocene retreat of the West Antarctic Ice Sheet: Part 2- Sedimentologic and stratigraphic signature.: *Geological Society of America Bulletin*, **v. 111**, p. 1517-1536.

Hall, B.L., and Denton, G.H., 1999a, Extent and chronology of the Ross Sea Ice Sheet and the Wilson Piedmont Glacier along the Scott Coast at the Last Glacial Maximum: *Geografiska Annaler*, in press.

Hall, B.L., and Denton, G.H., 1999b, Radiocarbon chronology of Ross Sea drift, eastern Taylor Valley, Antarctica: Evidence for a grounded ice sheet in the Ross Sea at the LGM: *Geografiska Annaler*, in press.

Hall, B.L., Denton, G.H., and Hendy, C.H., 1999, Evidence from Taylor Valley for a grounded ice sheet in the Ross Sea: *Geografiska Annaler*, in press.

Hall, B.L., Denton, G.H., Lux, D.R., and Bockheim, J.G., 1993, Late Tertiary Antarctic paleoclimate and ice sheet dynamics inferred from surficial deposits in Wright Valley: *Geografiska Annaler*, **v. 75A**, p. 239-268.

Hollin, J.T., 1962, On the glacial history of Antarctica: Journal of Glaciology, **v. 4**, p. 173-195.

Huybrechts, P., 1990, A 3-D model for the Antarctic Ice Sheet: A sensitivity study on the glacial-interglacial contrast: *Climate Dynamics*, **v. 5**, p. 79-92.

Judd, F.M., 1986, The chronology of Ross Sea glaciation, an Antarctic glaciation of Illinoisan age [M. S. thesis]: Waikato, University of Waikato.

Kurz, M.D., 1986, *In situ* production of terrestrial cosmogenic helium and some applications to geochronology: *Geochimica et Cosmochimica Acta*, **v. 50**, p. 2855-2862.

Kurz, M.D., and Ackert, R.P., Jr., 1996, Ice volume in the Ross Sea during Glacial Maximum: Geochronological Evidence from Mt. Morning , Antarctica: *EOS, Trans. AGU*, **v. 76**, p. F182.

Kurz, M.D., Colodner, D., Trull, T.W., Moore, R.B., and O'Brien, K., 1990, Cosmic ray exposure dating with in situ produced cosmogenic ^{3}He: results from young Hawaiian lava flows: *Earth and Planetary Science Letters*, **v. 97**, p. 177-189.

Kurz, M.D., Kenna, T.C., Lassiter, J.C., and DePaolo, D.J., 1996, Helium isotopic evolution of Mauna Kea Volcano: First results from the 1-km drill core: *Journal of Geophysical Research*, **v. 101**, p. 11,781-11,791.

Lal, D., 1991, Cosmic ray labeling of erosion surfaces: In situ nuclide production rates and erosion models: *Earth and Planetary Science Letters*, **v. 104**, p. 424-439.

Lal, D., and Peters, B., 1967, Cosmic ray produced radioactivity on the Earth, *in* Flügge, S., and Sitte, K., eds., *Encyclopedia of physics*, Volume XLVI/2: New York, Springer-Verlag, p. 551-612.

Licciardi, J.M., Kurz, M.D., and Clark, P.U., 1999, Calibration of cosmogenic ^{3}He production rates: Results from Holocene lava flows: *Earth and Planetary Science Letters*, **v. 172**, p. 261-271.

Licht, K.J., Dunbar, N.W., Andrews, J.T., and Jennings, A.E., 1999, Distinguishing subglacial till and glacial marine diamictons in the western Ross Sea, Antarctica: Implications for last glacial maximum grounding line: *Geological Society of America Bulletin*, **v. 111**, p. 91-103.

Licht, K.J., Jennings, A.E., Andrews, J.T., and Williams, K.M., 1996, Chronology of late Wisconsin ice retreat from the western Ross Sea, Antarctica: *Geology*, **v. 24**, p. 223-226.

Lide, D.R., 1998-9, CRC Handbook of Chemistry and Physics: Boca Raton, CRC Press, p. 14-16.

Marchant, D.R., Denton, G.H., Bockheim, J.G., Wilson, S.C., and Kerr, A.J., 1994a, Quaternary changes in the level of upper Taylor Glacier, Antarctica: Implications for paleoclimate and ice-sheet dynamics: *Boreas*, **v. 23**, p. 29-43.

Marchant, D.R., Denton, G.H., Bockheim, J.G., Wilson, S.C., and Kerr, A.J., 1994b, Quaternary changes in the level of upper Taylor Glacier, Antarctica: Implications for paleoclimate and ice-sheet dynamics: *Boreas*, **v. 23**, p. 29-43.

Mercer, J.H., 1968, Glacial geology of the Reedy Glacier Area, Antarctica: *Geological Society of America Bulletin*, **v. 79**, p. 471-486.

Mercer, J.H., 1972, Some observations on the glacial geology of the Beardmore Glacier area, *in* Adie, R.J., ed., *Antarctic Geology and Geophysics*: Oslo, Universitetsforlaget, p. 427-433.

Mercer, J.H., 1978, West Antarctic ice sheet and the CO_2 greenhouse effect: A threat of disaster: *Nature*, **v. 271**, p. 321.

Nichols, R.L., 1971, Glacial geology of Wright Valley, *in* Quam, L.O., ed., *Research in the Antarctic*, Volume Publication 93: Washington D. C, American Association for the Advancement of Science, p. 293-340.

Nishiizumi, K., Kohl, C.P., Arnold, J.R., Klein, J., and Fink, D., 1991, Cosmic ray produced ^{10}Be and ^{26}Al in Antarctic rocks: Exposure and erosion rates: *Earth and Planetary Science Letters*, **v. 104**, p. 440-454.

Oppenheimer, M., 1998, Global warming and the stability of the West Antarctic Ice Sheet: *Nature*, **v. 393**, p. 325-332.

Schäfer, J.M., Ivy-Ochs, S., Wieler, R., Leya, I., Baur, H., Denton, G.H., and Schlüchter, C., 1999, Cosmogenic noble gas studies in the oldest landscape on earth: surface exposure ages of the Dry Valleys, Antarctica: *Earth and Planetary Science Letters*, **v. 167**, p. 215-226.

Shipp, S., Anderson, J.B., and Domack, E.W., 1999, Late Pleistocene/Holocene Retreat of the West Antarctic Ice-sheet System in the Ross Sea: *Geological Society of America Bulletin*, **v. 111**, p. 1486-1516.

Stone, J.O., 1999, Air pressure and cosmogenic isotope production: *Journal of Geophysical Reviews*, in review.

Stuiver, M., Denton, G.H., Hughes, T.J., and Fastook, J.L., 1981, History of the marine ice sheet in West Antarctica during the last glaciation, a working hypothesis, *in* Denton, G.H., and Hughes, T.J., eds., *The Last Great Ice Sheets*: New York, Wiley-Interscaience, p. 319-436.

Trull, T.W., Kurz, M.D., and Jenkins, W.J., 1991, Diffusion of cosmogenic ^{3}He in olivine and quartz: implications for surface exposure dating: *Earth and Planetary Science Letters*, **v. 103**, p. 241-256.

Wilch, T.I., Lux, D.R., Denton, G.H., and McIntosh, W.C., 1993, Minimal Pliocene-Pleistocene uplift of the dry valleys sector of the Transantarctic Mountains: A key parameter in ice-sheet reconstructions: *Geology*, **v. 21**, p. 841-844.

Wright, A.C., 1980, Landforms of McMurdo Volcanic Group, Southern Foothills of Royal Society Range, Antarctica: *New Zealand Journal of Geology and Geophysics*, **v. 23**, p. 605-613.

Zreda, M.G., Phillips, F.M., Elmore, D., Kubik, P.W., Sharma, P., and Dorn, R.I., 1991, Cosmogenic chlorine-36 production rates in terrestrial rocks: *Earth and Planetary Science Letters*, **v. 105**, p. 94-109.

Appendix 5.1 Sample data from Dromedary Platform.

Sample	Location	Lithology	Size (cm)	Latitude (S)	Longitude (E)	Elev. (m)
Dromedary 0						
MK92-225	1	Basalt: ol	20	78 16 07	163 22 22	730
Ruby Cone						
MK92-245-1	2	Basalt: ol, cpx	400x800	78 18 52	163 18 36	765
Dromedary 1						
MK92-228	3	Basalt: ol, cpx	45	78 16 03	163 23 49	703
MK92-238	4	Basalt: ol, cpx	100x60	78 17 48	163 17 46	770
MK92-239	5	Basalt: ol, cpx	>50	78 17 48	163 17 46	770
KAK93-431-1	6	Basalt: ol	>15	78 18 49	163 18 34	727
KAK93-034	7	Basalt: ol, cpx	15x15x15	78 18 51	163 18 31	727
Lava Falls Colluvium						
KAK93-035	8	Basalt: ol,cpx,plag	20x20x8	78 19 16	163 16 41	762
KAK93-429	9	Basalt: ol	20x18x8	78 18 46	163 18 37	727
KAK93-430	10	Basalt: ol	>15	78 18 46	163 18 37	727
Dromedary 2						
MK92-233	11	Basalt: ol	15	78 18 37	163 19 43	727
MK92-235	12	Basalt: ol, cpx	150x100x50	78 18 17	163 19 21	727
KAK93-054-1	13	Shist: qtz, garnet	6x4x3 (m)	78 18 29	163 19 20	727
MK92-242	14	Basalt: ol, cpx	15x15x15	78 16 31	163 23 53	578
Dromedary 5						
RA92-012-1	15	Basalt: ol	>15	78 17 19	163 22 57	389
RA92-012-2	16	Basalt: ol	>15	78 17 19	163 22 57	386
RA92-013	17	Basalt: ol	35x24x14	78 17 19	163 22 57	386
RA92-014-1	18	Basalt: ol	>15	78 17 19	163 22 57	386
MK92-216	19	Basalt: ol	50	78 16 53	163 23 37	385
Dromedary 6						
RA92-039	20	Basalt: ol,cpx,plag	35	78 19 06	163 25 01	345
RA92-040	21	Basalt: ol	20x14	78 19 06	163 25 01	345
RA92-041	22	Basalt: ol, cpx	>15	78 19 06	163 25 01	345
Koettlitz 2						
RAK96-019	23	Granite: qtz	220x110x46	78 18 47	163 32 44	454
RAK96-018	24	Aglutinate: cpx	105x85x40	78 18 47	163 32 44	454
RAK96-214	25	Basalt: ol	20x20	78 18 45	163 33 14	454

ol=olivine; cpx=clinopyroxene; qtz=quartz plag=plagioclase.
Latitude and Longitude are given in degrees, minutes, seconds.

Appendix 5.2 Dromedary Platform Survey Data

Location (turning point)	Fore site	Back Site	Survey point	Latitude (S)	Longitude (E) (back site)	Horizontal (back site)	Distance (ft) (to back site)	Elevation (ft) (back site)
Sunny Hill	Red Hill	Pyramid		78° 20.7512'	163° 29.7586'	204° 19' 24"	5474.37	2814.6
Red Hill	Bulwark	Sunny Hill		78° 19.919'	163° 31.5780'	191° 56' 13"	9473.29	2219.81
Bulwark	Hyaloclastite Hill	Red Hill		78° 18.3714'	163° 31.6410'	268° 12' 25"	3656.99	1973.23
Hyaloclastite Hill	Bulwark	Bulwark		78° 17.270'	163° 30.945'	0-0-0	11400.8	1910.55
78°18.039' S	Bulwark	D2 moraine	1	n. a.	n. a.	146° 24' 41"	4376.47	2275.44
163° 22.289' E	Bulwark	D2 moraine	2	n. a.	n. a.	140° 24' 56"	4935.39	2352.48
	Bulwark	D1 moraine	3	n. a.	n. a.	202°15' 49"	5706.91	2404.22
	Bulwark	Condor cone	4	n. a.	n. a.	258° 55' 28"	6694.38	2295.74
	Bulwark	D0 moraine	5	78° 16.203'	163° 22.427'	282° 25' 31"	11481.77	2358.47
	Bulwark	D1 moraine	6	78° 16.195'	163° 23.478'	288° 34' 31"	11710.41	2229.01
	Bulwark	D3 moraine	7	78° 16.579'	163° 23.760'	292° 54' 28"	9380.52	1774.58
	Bulwark	D5 moraine	8	78° 16.970'	163° 23.374'	293° 36' 58"	6984.74	1275.39
	Bulwark	D4 moraine	9	78° 17.534'	163° 21.909'	277° 27' 13"	3243	1556.62
	Bulwark	D0 moraine	10	78° 17.294'	163° 18.027'	233° 53' 45"	6938.17	2426.17
	Bulwark	D1 moraine	11	78° 18.943'	163° 18.921'	133° 53' 21"	6471.09	2538.27

Pyramid is a USGS bench mark. Distance to back site is from turning point. Survey points are marked in Figure 5.3.
n.a.=not available